

University of Windsor

Scholarship at UWindor

Electronic Theses and Dissertations

Theses, Dissertations, and Major Papers

4-6-2021

Ceramic coatings on non-valve metals deposited by plasma electrolysis

Chen Zhao
University of Windsor

Follow this and additional works at: <https://scholar.uwindsor.ca/etd>

Recommended Citation

Zhao, Chen, "Ceramic coatings on non-valve metals deposited by plasma electrolysis" (2021). *Electronic Theses and Dissertations*. 8587.

<https://scholar.uwindsor.ca/etd/8587>

This online database contains the full-text of PhD dissertations and Masters' theses of University of Windsor students from 1954 forward. These documents are made available for personal study and research purposes only, in accordance with the Canadian Copyright Act and the Creative Commons license—CC BY-NC-ND (Attribution, Non-Commercial, No Derivative Works). Under this license, works must always be attributed to the copyright holder (original author), cannot be used for any commercial purposes, and may not be altered. Any other use would require the permission of the copyright holder. Students may inquire about withdrawing their dissertation and/or thesis from this database. For additional inquiries, please contact the repository administrator via email (scholarship@uwindsor.ca) or by telephone at 519-253-3000ext. 3208.

Ceramic coatings on non-valve metals deposited by plasma electrolysis

By

Chen Zhao

A Dissertation
Submitted to the Faculty of Graduate Studies
through the Department of Mechanical, Automotive & Materials Engineering
in Partial Fulfillment of the Requirements for
the Degree of Doctor of Philosophy
at the University of Windsor

Windsor, Ontario, Canada

2021

© 2021 Chen Zhao

Ceramic coatings on non-valve metals deposited by plasma electrolysis

by

Chen Zhao

APPROVED BY:

Q. Yang, External Examiner
Aerospace Research Center, National Research Council of Canada

A. Fartaj
Department of Mechanical, Automotive and Materials Engineering

V. Stoilov
Department of Mechanical, Automotive and Materials Engineering

H. Hu
Department of Mechanical, Automotive and Materials Engineering

X. Nie, Advisor
Department of Mechanical, Automotive and Materials Engineering

March 09, 2021

DECLARATION OF CO-AUTHORSHIP / PREVIOUS PUBLICATION

I. Co-Authorship

I hereby declare that this dissertation consists of materials as results of joint research. In all cases, the key ideas, primary contributions, experimental designs, data analysis and interpretation, were performed by the author and Dr. X. Nie as advisor, and the contribution of co-authors in Chapters 3 to 7 was primarily through the help with experiments. I certify that, with the above qualification, this dissertation, and the research to which it refers, is the product of my own work.

I am aware of the University of Windsor Senate Policy on Authorship and I certify that I have properly acknowledged the contribution of other researchers and have obtained written permission from each of the co-authors to include the above materials in my dissertation.

II. Previous Publication

This dissertation includes 5 original manuscripts that have been prepared or submitted for publication or published in peer reviewed journals, as follows:

Chapter 3	Study of Plasma Electrolytic Aluminating Process Using the Taguchi Experimental Design and ANOVA analysis	To be submitted
Chapter 4	Chen Zhao, Wei Zha, Ran Cai, Xueyuan Nie, and Jimi Tjong, A New Eco-friendly Anticorrosion Strategy for Ferrous Metals: Plasma Electrolytic Aluminating, <i>ACS Sustainable Chemistry & Engineering</i> , 2019, 7, 5, 5524-5531	Published

Chapter 5	Chen Zhao, Jiayi Sun, Xueyuan Nie, Jimi Tjong, D.T.A. Matthews, Anodic Plasma Electrolytic Deposition of Composite Coating on Ferrous Alloys with Low Thermal Conductivity and High Adhesion Strength, <i>Surface and Coatings Technology</i> , 2020, 398: 126081	Published
Chapter 6	Pore-sealing Treatment of Plasma Electrolytic Aluminating Coatings on Cast Iron	To be submitted
Chapter 7	Composite Coating on Cu Prepared by Plasma Electrolytic Aluminating	To be submitted

I certify that I have obtained a written permission from the copyright owner(s) to include the above published material(s) in my dissertation. I certify that the above material describes work completed during my registration as a graduate student at the University of Windsor.

III. General

I declare that, to the best of my knowledge, my dissertation does not infringe upon anyone's copyright nor violate any proprietary rights and that any ideas, techniques, quotations, or any other material from the work of other people included in my dissertation, published or otherwise, are fully acknowledged in accordance with the standard referencing practices. Furthermore, to the extent that I have included copyrighted material that surpasses the bounds of fair dealing within the meaning of the Canada Copyright Act, I certify that I have obtained a written permission from the copyright owner(s) to include such material(s) in my dissertation.

I declare that this is a true copy of my dissertation, including any final revisions, as approved by my dissertation committee and the Graduate Studies office, and that this dissertation has not been submitted for a higher degree to any other University or Institution.

ABSTRACT

A modified plasma electrolytic oxidation (PEO) treatment has been successfully developed for the non-valve metals of Fe and Cu in electrolyte containing sodium aluminate and sodium phosphate. This process could also be termed as plasma electrolytic aluminating (PEA) since the formation of passive films mainly relies on the aluminate ions. The passive film will hinder the current flow and cause charge build-up. When a critical voltage is reached, dielectric breakdown of the passive film will ignite the sparks. X-ray photoelectron spectroscopy (XPS) analyses indicate the passive film formed on the Fe consist of FeAl_2O_4 , which means iron substrate participated in the reaction. On the other hand, the copper substrate was not involved in the passive film formed on the Cu, which consists of $\text{Al}(\text{OH})_3$. The different mechanisms could be attributed to the different reduction potentials of Fe and Cu.

Taguchi analyses were used to investigate the influence of selected process parameters, including the concentration of NaAlO_2 in the electrolyte (C), the frequency (f) and duty cycle (δ) of the power supply. ANOVA analysis revealed that C has the most significant contribution to hardness, corrosion resistance and thickness. While f has significant influence on hardness and corrosion resistance, δ contributes significantly to the thickness. Higher frequency means shorter duration of a single discharge which leads to denser coating with higher hardness and corrosion resistance. Higher duty cycle represents the higher power input during the PEA treatment. Therefore, the coating's thickness increased with higher duty cycle.

The coating prepared on iron substrate mainly consists of Al_2O_3 and FeAl_2O_4 . The hardness, polarization resistance and thermal conductivity of the coating were 822 HV, $296 \text{ k}\Omega\cdot\text{cm}^2$ and $\sim 0.5 \text{ W}/(\text{m}\cdot\text{K})$, respectively. The low thermal conductivity comes from the mesopores, nano-grains and amorphous materials. After cyclic thermal shock tests, the coating retained its porous structure without spallation. Post-treatments like electroless nickel plating (EP) and sol-gel silica coating were applied to seal the open pores and cracks. Both the PEA-EP and PEA- SiO_2 hybrid coatings could retain good corrosion resistance after immersed in sodium chloride solution for five days, while the PEA coating degraded due to pitting corrosion at these open pores and cracks.

The coating deposited on pure copper consists of ceramic matrix (Al_2O_3 and Cu_2O) embedded with Cu particles. The amount of Cu particles increased with increased coating thickness, which could be attributed to intensified plasma discharges. The hardness, polarization resistance and thermal conductivity of the coating were 1050 HV, $141.7 \text{ k}\Omega\cdot\text{cm}^2$ and $\sim 5.1 \text{ W}/(\text{m}\cdot\text{K})$, respectively. The increased thermal conductivity could be attributed to the presence of metallic Cu. The coating has excellent wear and corrosion resistance, which might be used for wear-corrosion protection of copper alloys.

DEDICATION

To my grandfather,

You are always my model and the person I want to be.

To my grandmother,

Your endless love gave me the power.

To my parents,

Thank you for the support and encourage given to me in these years.

ACKNOWLEDGEMENTS

This study has been supported by the Natural Sciences and Engineering Research Council of Canada (NSERC) and Ford Motor Company of Canada Ltd.

Many thanks to my advisor, Dr. Xueyuan Nie, for excellent supervision of this project. I really appreciate the helpful comments and careful review of this work from my committee members, Dr. Amir Fartaj, Dr. Vesselin Stoilov and Dr. Henry Hu.

I would like to thank Mr. Andy Jenner, Mr. Wei Zha, Mr. Jiayi Sun, Mr. Guang Wang and Ms. Ran Cai from University of Windsor for their assistance with the experiments.

Finally, I am thankful to the faculty, staff and graduate students at the Department of Mechanical, Automotive and Materials Engineering of the University of Windsor, particularly my colleagues in the Metal Surface Engineering lab, for their support and encouragement.

TABLE OF CONTENTS

DECLARATION OF CO-AUTHORSHIP / PREVIOUS PUBLICATION	iii
ABSTRACT	vi
DEDICATION	viii
ACKNOWLEDGEMENTS	ix
LIST OF TABLES	xv
LIST OF FIGURES	xvii
1. CHAPTER 1 Introduction	1
1.1 Background	1
1.2 Objectives	2
1.3 Dissertation Outline	3
REFERENCES	4
2. CHAPTER 2 Literature Review	9
2.1 General introduction of PEO process	9
2.2 Fundamental mechanisms of PEO process	11
2.3 PEO process parameters	16
2.3.1 Electrolyte composition	16
2.3.2 Current mode	20
2.3.3 Substrate materials	24
2.3.4 Influence of processing time	26
2.4 PEO coating properties	27

2.4.1 Hardness	27
2.4.2 Wear resistance	27
2.4.3 Corrosion resistance	28
2.4.4 Thermal conductivities	28
2.5 Recent progress of PEO process on non-valve metals and their alloys	29
2.6 Summary	31
REFERENCES	32
3. CHAPTER 3 Study of Plasma Electrolytic Aluminating Process Using the Taguchi Experimental Design and ANOVA analysis	54
3.1 Introduction	54
3.2 Experimental details	55
3.2.1 Taguchi design of experiment	55
3.2.2 Analysis of variance (ANOVA)	58
3.2.3 Experimental procedures	59
3.3 Results and discussion	61
3.4 Conclusions	71
REFERENCES	72
4. CHAPTER 4 A New Eco-friendly Anti-Corrosion Strategy for Ferrous Metals: Plasma Electrolytic Aluminating	78
4.1 Introduction	78
4.2 Experimental setup	80

4.3 Results and discussion.....	81
4.4 Conclusions	95
REFERENCES.....	96
5. CHAPTER 5 Anodic Plasma Electrolytic Deposition of Composite Coating on Ferrous Alloys with Low Thermal Conductivity and High Adhesion Strength ...	101
5.1 Introduction	101
5.2 Experimental details	103
5.2.1 Plasma electrolytic aluminating (PEA) and materials characterization	103
5.2.2 Thermal conductivity measurement	105
5.2.3 Thermal shock tests	106
5.3 Results and discussion.....	107
5.4 Conclusions	119
REFERENCES.....	119
6. CHAPTER 6 Pore-sealing Treatment of Plasma Electrolytic Aluminating Coating on Cast Iron	126
6.1 Introduction	126
6.2 Experimental setup.....	128
6.2.1 Preparation of PEA coatings.....	128
6.2.2 Preparation of PEA-EP hybrid coatings	128
6.2.3 Preparation of SiO ₂ sol and PEA-SiO ₂ hybrid coatings	129
6.2.4 Materials characterization, corrosion test and thermal conductivity measurement	130

6.3 Results and discussion.....	131
6.3.1 Materials characterization of PEA, PEA-EP and PEA-SiO ₂ samples ..	131
6.3.2 Electrochemical measurements	136
6.3.3 Thermal conductivity measurements.....	142
6.3.4 Discussion.....	143
6.4 Conclusions	146
REFERENCES.....	146
7. CHAPTER 7 Composite Coating on Cu Prepared by Plasma Electrolytic Aluminating	153
7.1 Introduction.....	153
7.2 Experimental details	154
7.3 Results and discussion.....	155
7.3.1 The discharge process and surface morphology evolution analyses	155
7.3.2 Coating formation mechanism analyses	158
7.3.3 Hardness and wear tests.....	163
7.3.4 Corrosion tests	167
7.3.5 Thermal conductivities of the PEA coatings	170
7.4 Conclusions	171
REFERENCES.....	171
8. Chapter 8 Discussion, Conclusions, and Future Works	179
8.1 Discussion	179

8.1.1 Electrolyte species	179
8.1.2 Influence of substrate materials	181
8.1.3 Post-treatments	183
8.2 Conclusions	185
8.3 Future work	187
APPENDICES	188
COPYRIGHT RELEASES FROM PUBLICATIONS	188
VITA AUCTORIS	190

LIST OF TABLES

Table 2-1 Electrolyte compositions and phase compositions of the produced coatings.	19
Table 3-1 Design factors and levels.	56
Table 3-2 Designed L9 orthogonal array of experiment plans.	56
Table 3-3 Properties of deposited coatings.	61
Table 3-4 The S/N ratio of objectives and Multi-response S/N ratio.	61
Table 3-5 Results of the ANOVA for average hardness.	67
Table 3-6 Results of the ANOVA for polarization resistance.	67
Table 3-7 Results of the ANOVA for average thickness.	67
Table 3-8 The Factor's Mean multi-response S/N ratio for each level.	69
Table 3-9 Results of ANOVA for the specific multi-response case: $w_1=0.5$, $w_2=0.5$, $w_3=0$	69
Table 3-10 The S/N ratio of objectives and multi-response S/N ratio of confirmation experiments.	70
Table 4-1 Kinetic parameters obtained from the polarization curves.	91
Table 4-2 Fitted data from the equivalent circuits.	94
Table 5-1 Sample number, corresponding to PEA treatment time and substrate type (see also section 5.2.1) and the average (\pm standard deviation) of the resulting coating thicknesses and thermal conductivities.	109
Table 5-2 Surface Porosity, cross-sectional porosity, average pore size and average grain sizes for samples S1, S4, C1 and C4.	112

Table 6-1 EDS point analysis of the selected areas of the PEA-SiO ₂ coating	134
Table 6-2 Fitting parameters of the EIS curves.	138
Table 6-3 Kinetic parameters obtained from the polarization curves.	140
Table 7-1 Results of EDS point analyses on selected areas A, B and C.....	157
Table 7-2 Fitted parameters from the EIS spectra.	168
Table 7-3 Kinetic parameters obtained from the polarization curves.	169

LIST OF FIGURES

Figure 2-1 Schematic illustration of the PEO equipment layout.	10
Figure 2-2 Two kinds of current-voltage curves of plasma electrolysis processes: (a) plasma electrolytic saturation and (b) plasma electrolytic oxidation. Adapted from ¹	13
Figure 2-3 Scanning electron micrographs showing the surface of coatings formed on Zircaloy-2 alloy in an electrolyte containing 8 g/L NaAlO ₂ and 1 g/L KOH for 30 min. Adapted from ⁵²	15
Figure 2-4 Evolution of discharge events during the PEO process on Zircaloy-2 alloy in an electrolyte containing 8 g/L NaAlO ₂ and 1 g/L KOH. Adapted from ⁵²	16
Figure 2-5 Current-voltage behavior of electrolytes tested for PEO treatment of aluminum. (1) fast metal dissolution, (2) slow metal dissolution, (3) metal passivation in narrow voltage interval, (4) complex behavior of fluoride electrolytes, (5) slight passivation and (6) strong passivation of metal. Adapted from ¹	17
Figure 2-6 Various types of current modes used in PEO process. (a) alternating current (AC), (b) direct current (DC), (c) unipolar pulsed current, (d) bipolar pulsed current.	21
Figure 2-7 Scanning electron microscope images of the surface morphologies of the ceramic coating produced on ZK60 Mg alloy in electrolyte contains 8 g/L sodium phosphate, 3 g/L potassium hydroxide and 1 g/L sodium fluoride under different frequencies (bipolar current mode, duty ratio is	

0.1). (a) 100 Hz, (b) 200 Hz, (c) 500 Hz, (d) 1000 Hz. Adapted from ¹⁰⁸	23
Figure 2-8 Effect of micro discharge characteristics on the distribution of silicon. (a) high duty cycle, (b) low duty cycle. Adapted from ¹¹⁰	24
Figure 2-9 Plot of Gibbs free energy of formation against band gaps of selected oxides. Adapted from ¹¹⁵	25
Figure 2-10 (a) linear (adapted from ⁵⁹) and (b) nonlinear (adapted from ¹¹⁶) relations between the coating thickness and processing time.	26
Figure 2-11 Schematic illustration of the PEO of the carbon steel in 8 g/L NaAlO ₂ and 2 g/L NaH ₂ PO ₄ . (a) The sample before the application of anodic current. (b) The moment after the application of anodic current. (c) The deposition of an aluminum phosphates or AAP layer on the steel surface. (d) The initiation of plasma discharges through the breakdown of the dielectric layer. (e) Stable discharges at later stage of PEO. Adapted from ¹³²	30
Figure 3-1 S/N ratio graphs for (a) average hardness, (b) polarization resistance, and (c) average thickness.	65
Figure 3-2 Surface morphology of the passive layer formed in electrolyte containing (a) 20 g/L, (b) 40 g/L NaAlO ₂ . The concentration of Na ₃ PO ₄ was fixed at 5 g/L.....	66
Figure 3-3 Surface morphology of the coatings formed in electrolyte containing (a) 20 g/L, (b) 40 g/L NaAlO ₂ . The concentration of Na ₃ PO ₄ was fixed at 5 g/L.....	66

Figure 3-4 Multi-response S/N ratio graph for case: $w_1=0.5, w_2=0.5, w_3=0$. .69

Figure 4-1 (a) Voltage and (b) current density vs. time curves during the PEA process.....82

Figure 4-2 SEM images of the samples treated for (a, d) 6s, (b, e) 12s, (c, f) 100s, respectively; (g) and (h) EDS spectra from marked areas in (a) and (b), respectively.....83

Figure 4-3 (a) SEM image of the sample treated for 6s; (b-d) high resolution spectra of Fe 2p, Al 2p and O 1s, respectively.85

Figure 4-4 XRD patterns of samples treated with (a) 10 mins and (b) 6 s.86

Figure 4-5 Schematic illustration of the PEA of cast iron. (a) The system before applying current, (b) dissolution of iron into the electrolyte and migration of $Al(OH)_4^-$ anions towards the anode after applying current, (c) formation of hercynite film on the iron surface and the initiation of plasma discharge sparks, (d) growth of the hercynite-alumina composite ceramic coating via strong plasma discharge.....88

Figure 4-6 (a) SEM image and (b) hardness profile of the sample after 10 mins of PEA treatment, inset is the cross-sectional SEM image; SEM images showing wear tracks of (c) the uncoated blank sample and (d) PEA coated sample after the sliding tests.89

Figure 4-7 (a) PEA coated sample after polishing to $R_{pk}=0.22\mu m$; (b) PEA coated sample after the sliding test; (c) ultra-sonic cleaning to remove wear debris/materials transfer in (b); (d) uncoated blank sample after the sliding test.90

Figure 4-8 (a) Tafel curves of the PEA treated and blank samples; (b-c) Nyquist impedance plots, (d-e) and corresponding equivalent circuits of the blank and PEA treated samples, respectively.90

Figure 4-9 Tafel plots of various Zn alloy coated samples in a 3.5% NaCl solution at a room temperature.92

Figure 4-10 Tafel plots of the PEA coated samples test at 25°C, 40°C, 55°C and 70°C, respectively.92

Figure 4-11 Flexible hercynite-alumina composite coating deposited on (a) low-carbon-steel foil and (b) 1095 spring steel (high-carbon-steel) foil.94

Figure 5-1 Illustration of the coating deposition process.104

Figure 5-2 Experimental setup for thermal conductivity measurement..... 106

Figure 5-3 SEM plain view of selected samples (a) S1, (b) S4, (c) C1, and (d) C4. High magnification SEM images of selected samples (e) S1 and (f) C1 showing the existence of mesopores. Cross-sectional SEM images of selected samples (g) S1 and (h) S4.108

Figure 5-4 XRD patterns of selected samples(a) S1, (b) S4, (c) C1 and (d) C4. (e) Illustration of peak fitting at low angle for estimation of amorphous materials and grain size..... 111

Figure 5-5 (a) Temperature-time profile for a thermal conductivity measurement; (b) A typical steady-state thermal profile for coated ferrous metals; (c) Measured effective thermal conductivities of the coated ferrous metal samples; (d) Calculated thermal conductivities of the composite coatings.113

Figure 5-6 (a) Illustration of the adhesive tensile test; (b) A typical tensile curves of single-side coated cast iron sample; (c) Fracture surfaces after tensile test showing adhesive failure on the uncoated side..... 117

Figure 5-7 Optical images of selected samples (a) C3, (b) C6, (c) S3 and (d) S6 after 1, 25, 50 and 100 cycles (left to right) of thermal shock tests. (e) and (g) (plain views) and (f) (cross-section) are SEM images of selected sample C6 after 100 cycles of thermal shock test. Red arrows in (f) and (g) indicate the formation of small cracks after thermal shock test in the coating. The coupons in figure a-d have diameters of 25.4 mm..... 118

Figure 6-1 Illustration of the (a) electroless nickel plating and (b) sol-gel dip coating processes. 132

Figure 6-2 (a) and (b) SEM images of cross-section and surface of the PEA sample; (c) and (d) SEM images of cross-section and surface of the PEA-EP sample; (e) and (f) SEM images of cross-section of the as-sintered PEA-SiO₂ sample and surface of the polished PEA-SiO₂ sample..... 133

Figure 6-3 XRD spectra of the (a) PEA, (b) PEA-EP and (c) PEA-SiO₂ samples. 135

Figure 6-4 (a), (c) and (e) Nyquist plots of PEA, PEA-EP and PEA-SiO₂ samples after immersion in 3.5 wt.% NaCl solution for 1 hour; (b), (d) and (f) Bode plots corresponding to EIS spectra in (a), (c) and (e), respectively; (g) equivalent circuit. 136

Figure 6-5 Impedence spectra of (a) PEA (b) PEA-EP and (c) PEA-SiO₂ samples after different immersion time in 3.5 wt.% NaCl solution, (d) variation of impedance with time at different frequencies. 139

Figure 6-6 Potentiodynamic polarization curves of the PEA, PEA-EP and PEA-SiO₂ samples after immersed in 3.5 wt.% NaCl solution for 5 days. ... 140

Figure 6-7 Variation of open circuit potentials (E_{oc}) for blank cast iron and PEA-SiO₂ sample..... 142

Figure 6-8 Thermal conductivities of PEA coating and PEA-EP and PEA-SiO₂ hybrid coatings..... 143

Figure 6-9 Optical images of the PEA-EP and PEA-SiO₂ samples after thermal shock tests. 145

Figure 7-1 Average current density vs. time curve in the PEA process. 156

Figure 7-2 Surface SEM images of (a) sample 1 and (b) sample 2. 157

Figure 7-3 (a) Al 2p, (b) O 1s, (c) Cu 2p and (d) Cu LMM XPS high resolution spectra obtained from sample 1 surface..... 159

Figure 7-4 (a) Al 2p, (b) O 1s, (c) Cu 2p and (d) Cu LMM XPS high resolution spectra obtained from sample 2 surface..... 161

Figure 7-5 XRD spectrum for sample 2..... 162

Figure 7-6 SEM images of (a) surface and (b) cross-section of the sample 2. 163

Figure 7-7 Friction coefficients vs. sliding distance for the uncoated sample against a SAE52100 steel ball and coated samples against SAE52100 steel and tungsten carbide balls. 163

Figure 7-8 SEM images (BSE mode) of the wear track for (a) uncoated copper sliding against steel ball, (b) coated copper sliding against steel ball, and (c) coated copper sliding against tungsten carbide ball. (d), (e) and (f) are enlarged images of the white boxes in (a), (b) and (c), respectively. (g), (h) and (i) show the representative surfaces of the counter-balls, scale bar is 100 μm 166

Figure 7-9 (a), (b) Nyquist plots of uncoated and coated copper samples in 3.5 wt.% NaCl solution; (c), (d) Bode plots of uncoated and coated copper samples; (e), (f) equivalent circuit used for fitting the EIS spectra in (a) and (b), respectively..... 167

Figure 7-10 Potentiodynamic polarization curves of the coated and uncoated copper samples..... 169

Figure 7-11 Thermal conductivities of the coatings with different thicknesses. 170

Figure 8-1 Illustration of (a) electroless nickel plating, (b) sol-gel dipping. 185

1. CHAPTER 1 Introduction

1.1 Background

Surface engineering methods, including phosphating, metal plating and physical vapor deposition (PVD), have been applied on irons, steels and copper alloys. These treatments could improve the surface functionalities in terms of wear and corrosion resistance. However, there are still some limitations of these methods. For instance, the NO_2^- , Cr^{6+} , PO_4^{3-} and NO_3^- ions involved in the phosphating and chromium plating bath have negative influence on the human body and environment ^{1,2}. Organic painting on phosphating surface is desired for efficient corrosion protection, but it will sacrifice the surface hardness ^{3,4}. During the service of zinc plating, a lot of zinc ions would be released into eco-system and might lead to zinc pollution ⁵. Moreover, corrosion of the iron substrates will be inevitable after longtime exposure, especially to chloride ions and acidic surroundings ⁶. Therefore, post-treatment like organic coatings is also desired ⁷. The surface hardness and wear resistance of zinc plating are also low, which leads to decreased lifespan and increased cost of maintenance. PVD hard ceramic coatings could provide both the high corrosion resistance and the excellent wear resistance ⁸⁻¹⁰. However, the high cost and complex controlling of the process inhibit the wide use of these coatings. Therefore, it is urgent to develop a surface engineering method for irons, steels, and copper alloys which could realize high wear resistance, corrosion resistance, cost effectiveness and environmental friendliness simultaneously.

Plasma electrolysis for surface engineering is known as multi-functional, cost effective and environmentally friendly process. Anodic plasma electrolysis could be divided into two main categories: plasma electrolytic oxidation (PEO, a coating deposition process) and

plasma electrolytic polishing (PEP, an anodic dissolution process) ¹¹⁻¹³. PEO is thought to be suitable for the “valve metals”, while PEP dominates for the non-valve metals. For valve metals, their oxides usually are n-type semiconductors or insulators, like Al₂O₃, MgO and TiO₂, which means current cannot flow through the oxide when the metal is anode ^{13,14}. This point is critical for PEO process, since it cause the accumulation of charges and subsequent dielectric breakdown of the oxide layer, which was thought to be the origin of stable plasma discharges ¹³. The commonly known valve metals include Al, Mg, Ti, Ta, Nb, Zr and Be ¹⁴. PEO has been successfully applied on Al ^{15,16}, Mg ^{17,18}, Ti ^{19,20}, Zr ^{21,22}, Ta ^{23,24} and their alloys to realize excellent wear resistance, corrosion resistance, biocompatibility, decorative and catalytic properties.

As for the non-valve metals, PEO is normally considered not applicable because stable plasma discharges cannot be easily established in this case ¹⁴. In recent years, several papers have been published on the PEO of carbon steels and cast irons in the electrolyte contains sodium aluminate and sodium phosphate ²⁵⁻²⁷. Recent studies demonstrate that the ions in the electrolyte could help to form the passive layer (insulating ceramics) on the anode surface, which leads the stable plasma discharges ²⁸. However, detailed investigation on the process and characterization of the coating properties is still needed.

1.2 Objectives

This work focused on the preparation and characterization of ceramic coatings deposited on non-valve metals, including Fe and Cu alloys, by plasma electrolytic aluminating (PEA) process. Post-treatments were also applied to seal the pores for better corrosion performance. Following objectives were aimed to be achieved:

1. To investigate the PEA process using Taguchi experimental design and evaluate the contribution of selected process parameters, especially focusing on the concentration of the electrolyte, with ANOVA analysis.
2. To study the coating deposition mechanism of the PEA process on cast iron and investigate the wear, corrosion behaviors in detail.
3. To evaluate the thermal related properties of the PEA coatings on cast irons and steels, including thermal conductivity and thermal shock resistance.
4. To study the influence of pore-sealing post-treatment, including electroless nickel plating and sol-gel silica coating, on the corrosion resistance and thermal conductivity of the PEA coating.
5. To investigate the PEA process on Cu and characterize the deposited coatings.

1.3 Dissertation Outline

This dissertation includes a total of eight chapters:

In Chapter 1, a brief introduction was provided with the objectives and the outline of this dissertation.

In Chapter 2, a literature review related to this study was carried out. Background knowledge of the plasma electrolytic oxidation was introduced. Application of PEO process was discussed. Very few literatures of PEO process on steels were also discussed.

In Chapter 3, Taguchi analysis of the PEA process on cast iron was carried out. The hardness, polarization resistance and thickness of the coating were selected as individual responses. Contribution of process parameters was evaluated by ANOVA analysis.

In Chapter 4, the mechanism of PEA process on cast iron was investigated with scanning electron microscope (SEM), X-ray photoelectron spectroscopy (XPS) and X-ray diffraction (XRD). The wear and corrosion behaviors were also studied in detail.

In Chapter 5, the thermal conductivities of PEA coatings on cast irons and steels were measured. The relation between thermal conductivities and microstructures were discussed. The coatings' adhesion property and thermal shock resistance were also evaluated.

In Chapters 6, electroless nickel plating and sol-gel silica coating were used to seal the open pores and cracks. The purpose is to reduce the possibility of salt solution to contact the iron substrates and thus improve the long-term corrosion performance of PEA coated iron samples. The long-term corrosion behavior and thermal conductivity of the hybrid coatings were studied.

In Chapter 7, the PEA process on copper was investigated. The coating deposition mechanism was proposed based on the results of SEM, XPS and XRD analysis. The wear, corrosion and thermal behaviors of the coating were studied.

In Chapter 8, general conclusions were summarized and suggestions for future work were given.

REFERENCES

- (1) Stauffer, J. *Finishing Systems Design and Implementation: A Guide for Product Parameters, Coatings, Process, and Equipment. Society of Manufacturing Engineers, 1993.*
- (2) Conley, D. J.; Paerl, H. W.; Howarth, R. W.; Boesch, D. F.; Seitzinger, S. P.; Havens, K. E.; Lancelot, C.; Likens, G. E. Controlling Eutrophication: Nitrogen and Phosphorus. *Science* **2009**, *323* (5917), 1014–1015.
<https://doi.org/10.1126/science.1167755>.

- (3) Zubielewicz, M.; Kamińska-Tarnawska, E.; Kozłowska, A. Protective Properties of Organic Phosphate-Pigmented Coatings on Phosphated Steel Substrates. *Prog. Org. Coatings* **2005**, *53* (4), 276–285. <https://doi.org/10.1016/j.porgcoat.2005.02.008>.
- (4) Jegdić, B. V.; Bajat, J. B.; Popić, J. P.; Stevanović, S. I.; Mišković-Stanković, V. B. The EIS Investigation of Powder Polyester Coatings on Phosphated Low Carbon Steel: The Effect of NaNO₂ in the Phosphating Bath. *Corros. Sci.* **2011**, *53* (9), 2872–2880. <https://doi.org/10.1016/j.corsci.2011.05.019>.
- (5) Sprague, J. B.; Elson, P. F.; Saunders, R. L. Sublethal Copper-Zinc Pollution in a Salmon River—a Field and Laboratory Study. *Adv. Water Pollut. Res.* **1965**, 61–82. <https://doi.org/10.1016/b978-0-08-011438-5.50012-x>.
- (6) Yadav, A. P.; Nishikata, A.; Tsuru, T. Degradation Mechanism of Galvanized Steel in Wet-Dry Cyclic Environment Containing Chloride Ions. *Corros. Sci.* **2004**, *46* (2), 361–376. [https://doi.org/10.1016/S0010-938X\(03\)00153-7](https://doi.org/10.1016/S0010-938X(03)00153-7).
- (7) Martins, J. I.; Reis, T. C.; Bazzaoui, M.; Bazzaoui, E. A.; Martins, L. Polypyrrole Coatings as a Treatment for Zinc-Coated Steel Surfaces against Corrosion. *Corros. Sci.* **2004**, *46* (10), 2361–2381. <https://doi.org/10.1016/j.corsci.2004.02.006>.
- (8) Ruden, A.; Restrepo-Parra, E.; Paladines, A. U.; Sequeda, F. Corrosion Resistance of CrN Thin Films Produced by Dc Magnetron Sputtering. *Appl. Surf. Sci.* **2013**, *270*, 150–156. <https://doi.org/10.1016/j.apsusc.2012.12.148>.
- (9) Liu, C.; Bi, Q.; Matthews, A. EIS Comparison on Corrosion Performance of PVD TiN and CrN Coated Mild Steel in 0.5 N NaCl Aqueous Solution. *Corros. Sci.* **2001**, *43* (10), 1953–1961. [https://doi.org/10.1016/S0010-938X\(00\)00188-8](https://doi.org/10.1016/S0010-938X(00)00188-8).

- (10) Shan, L.; Zhang, Y. R.; Wang, Y. X.; Li, J. L.; Jiang, X.; Chen, J. M. Corrosion and Wear Behaviors of PVD CrN and CrSiN Coatings in Seawater. *Trans. Nonferrous Met. Soc. China English Ed.* **2016**, *26* (1), 175–184. [https://doi.org/10.1016/S1003-6326\(16\)64104-3](https://doi.org/10.1016/S1003-6326(16)64104-3).
- (11) Parfenov, E. V.; Mukaeva, V. R.; Farrakhov, R. G. Plasma Electrolytic Treatments for Advanced Surface Finishing Technologies. *Mater. Technol. Des.* **2019**, *1* (1), 34–41.
- (12) Belkin, P. N.; Kusmanov, S. A.; Parfenov, E. V. Mechanism and Technological Opportunity of Plasma Electrolytic Polishing of Metals and Alloys Surfaces. *Appl. Surf. Sci. Adv.* **2020**, *1*, 100016. <https://doi.org/10.1016/j.apsadv.2020.100016>.
- (13) Yerokhin, A. L.; Nie, X.; Leyland, A.; Matthews, A.; Dowey, S. J. Plasma Electrolysis for Surface Engineering. *Surf. Coatings Technol.* **1999**, *122* (2–3), 73–93. [https://doi.org/10.1016/S0257-8972\(99\)00441-7](https://doi.org/10.1016/S0257-8972(99)00441-7).
- (14) Clyne, T. W.; Troughton, S. C. A Review of Recent Work on Discharge Characteristics during Plasma Electrolytic Oxidation of Various Metals. *Int. Mater. Rev.* **2019**, *64* (3), 127–162. <https://doi.org/10.1080/09506608.2018.1466492>.
- (15) Yerokhin, A. L.; Shatrov, A.; Samsonov, V.; Shashkov, P.; Pilkington, A.; Leyland, A.; Matthews, A. Oxide Ceramic Coatings on Aluminium Alloys Produced by a Pulsed Bipolar Plasma Electrolytic Oxidation Process. *Surf. Coatings Technol.* **2005**, *199* (2-3), 150–157. <https://doi.org/10.1016/j.surfcoat.2004.10.147>.
- (16) Matykina, E.; Arrabal, R.; Skeldon, P.; Thompson, G. E. Investigation of the Growth Processes of Coatings Formed by AC Plasma Electrolytic Oxidation of Aluminium. *Electrochim. Acta* **2009**, *54* (27), 6767–6778. <https://doi.org/10.1016/j.electacta.2009.06.088>.

- (17) Arrabal, R.; Matykina, E.; Viejo, F.; Skeldon, P.; Thompson, G. E.; Merino, M. C. AC Plasma Electrolytic Oxidation of Magnesium with Zirconia Nanoparticles. *Appl. Surf. Sci.* **2008**, *254* (21), 6937–6942. <https://doi.org/10.1016/j.apsusc.2008.04.100>.
- (18) Bala Srinivasan, P.; Liang, J.; Blawert, C.; Störmer, M.; Dietzel, W. Effect of Current Density on the Microstructure and Corrosion Behaviour of Plasma Electrolytic Oxidation Treated AM50 Magnesium Alloy. *Appl. Surf. Sci.* **2009**, *255* (7), 4212–4218. <https://doi.org/10.1016/j.apsusc.2008.11.008>.
- (19) Yerokhin, A. L.; Nie, X.; Leyland, A.; Matthews, A. Characterisation of Oxide Films Produced by Plasma Electrolytic Oxidation of a Ti-6Al-4V Alloy. *Surf. Coatings Technol.* **2000**, *130* (2–3), 195–206. [https://doi.org/10.1016/S0257-8972\(00\)00719-2](https://doi.org/10.1016/S0257-8972(00)00719-2).
- (20) Shokouhfar, M.; Dehghanian, C.; Montazeri, M.; Baradaran, A. Preparation of Ceramic Coating on Ti Substrate by Plasma Electrolytic Oxidation in Different Electrolytes and Evaluation of Its Corrosion Resistance: Part II. *Appl. Surf. Sci.* **2012**, *258* (7), 2416–2423. <https://doi.org/10.1016/j.apsusc.2011.10.064>.
- (21) Xue, W.; Zhu, Q.; Jin, Q.; Hua, M. Characterization of Ceramic Coatings Fabricated on Zirconium Alloy by Plasma Electrolytic Oxidation in Silicate Electrolyte. *Mater. Chem. Phys.* **2010**, *120* (2–3), 656–660. <https://doi.org/10.1016/j.matchemphys.2009.12.012>.
- (22) Matykina, E.; Arrabal, R.; Skeldon, P.; Thompson, G. E.; Wang, P.; Wood, P. Plasma Electrolytic Oxidation of a Zirconium Alloy under AC Conditions. *Surf. Coatings Technol.* **2010**, *204* (14), 2142–2151. <https://doi.org/10.1016/j.surfcoat.2009.11.042>.

- (23) Sowa, M.; Kazek-Kęsik, A.; Socha, R. P.; Derez, G.; Michalska, J.; Simka, W. Modification of Tantalum Surface via Plasma Electrolytic Oxidation in Silicate Solutions. *Electrochim. Acta* **2013**, *114*, 627–636. <https://doi.org/10.1016/j.electacta.2013.10.047>.
- (24) Petković, M.; Stojadinović, S.; Vasilić, R.; Zeković, L. Characterization of Oxide Coatings Formed on Tantalum by Plasma Electrolytic Oxidation in 12-Tungstosilicic Acid. *Appl. Surf. Sci.* **2011**, *257* (24), 10590–10594. <https://doi.org/10.1016/j.apsusc.2011.07.055>.
- (25) Wang, Y.; Jiang, Z.; Yao, Z.; Tang, H. Microstructure and Corrosion Resistance of Ceramic Coating on Carbon Steel Prepared by Plasma Electrolytic Oxidation. *Surf. Coatings Technol.* **2010**, *204* (11), 1685–1688. <https://doi.org/10.1016/j.surfcoat.2009.10.023>.
- (26) Wang, Y.; Jiang, Z.; Yao, Z. Preparation and Properties of Ceramic Coating on Q235 Carbon Steel by Plasma Electrolytic Oxidation. *Curr. Appl. Phys.* **2009**, *9* (5), 1067–1071. <https://doi.org/10.1016/j.cap.2008.12.004>.
- (27) Yang, W.; Li, Q.; Liu, W.; Liang, J.; Peng, Z.; Liu, B. Characterization and Properties of Plasma Electrolytic Oxidation Coating on Low Carbon Steel Fabricated from Aluminate Electrolyte. *Vacuum* **2017**, *144*, 207–216. <https://doi.org/10.1016/j.vacuum.2017.08.003>.
- (28) Li, Z.; Cheng, Y.; Kang, S. hang; Tu, W.; Cheng, Y. A Re-Understanding of the Breakdown Theory from the Study of the Plasma Electrolytic Oxidation of a Carbon Steel — A Non-Valve Metal. *Electrochim. Acta* **2018**, *284*, 681–695. <https://doi.org/10.1016/j.electacta.2018.07.201>.

2. CHAPTER 2 Literature Review

Compared with classic electrolysis, plasma electrolysis provides enhanced physical-chemical reactions at the metal surface. The plasma electrolysis could be divided into cathodic processes, including plasma cleaning and plasma electrolytic saturation (PES, like nitriding and carburizing), and anodic processes, including plasma electrolytic oxidation (PEO) and plasma electrolytic polishing (PEP) ¹. PEO has been widely applied in automotive, aerospace and oil & gas industries due to the excellent multi-functionality of the coatings, including corrosion and wear resistance, chemical and thermal stability, low thermal conductivity, etc. However, PEO process cannot be readily applied on non-ferrous metals like iron and copper alloys, which are widely used in many industries. Although very few literatures have reported the PEO process on carbon steels, comprehensive process study and mechanism analysis are still needed. This chapter contains two parts: the first part covers general fundamentals and progresses of the PEO process, the second part focuses on the available literatures of PEO process on carbon steels.

2.1 General introduction of PEO process

PEO is a plasma-enhanced anodizing process for deposition of ceramic coatings on metal surface in aqueous solutions. An illustration of PEO equipment layout is shown in Figure 2-1, which consists of power supply, electrodes, electrolyte and cooling system (if needed). During the PEO process, the metal substrate is serving as the anode. Both the anode and cathode (could be a plate of graphite or just using the stainless-steel vessel) are immersed in an aqueous electrolyte. A power supply is connected to the electrodes and providing energy necessitated for the PEO process.

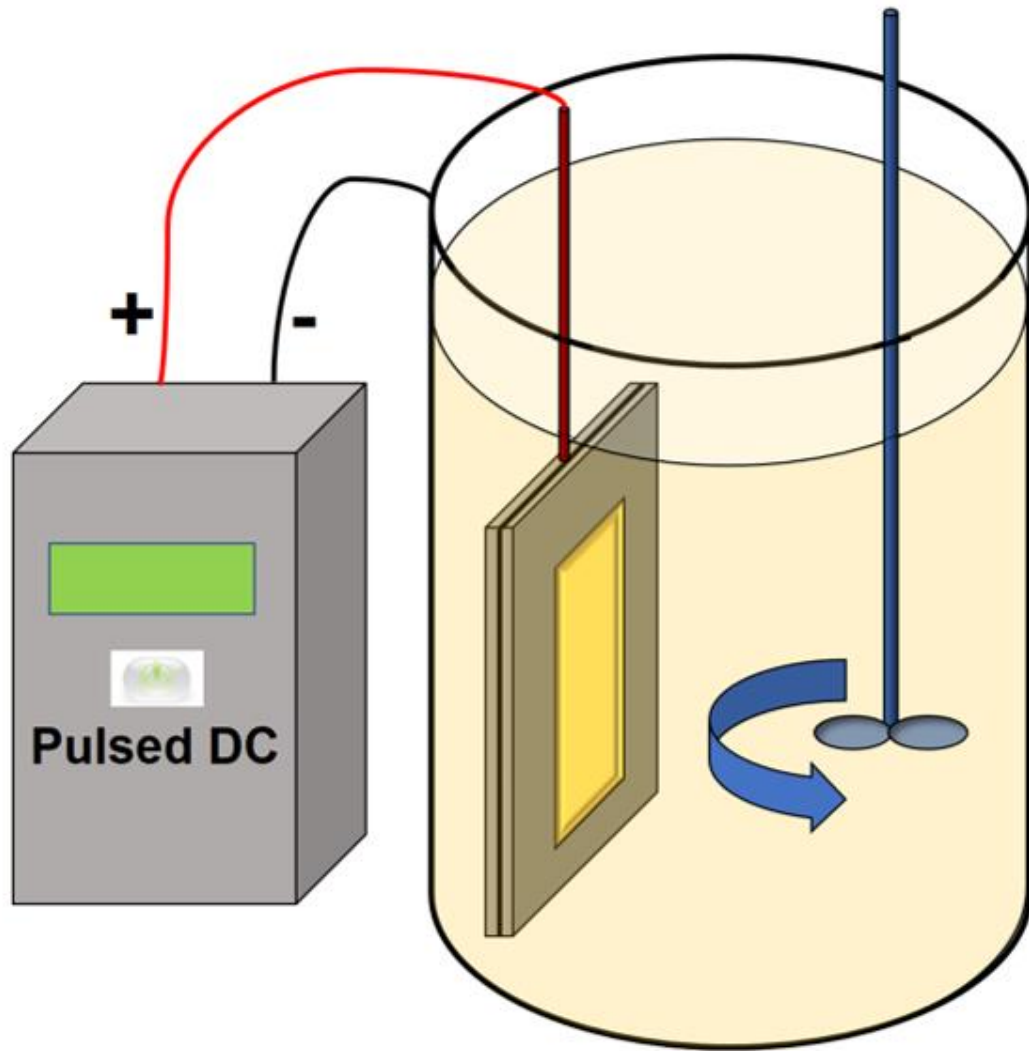


Figure 2-1 Schematic illustration of the PEO equipment layout.

While the basic equipment layout of PEO process is similar to classic anodization, a much higher voltage ($\sim 250\text{-}750\text{ V}$) is applied². Therefore, the dielectric breakdown occurs, and numerous micro plasma discharges are formed on the anode surface. Instead of continuous transport of ions through the electrolyte and thin oxide layer during classic anodization process, the metal and oxygen atoms or ions were generated simultaneously by the hot plasma and then combined to form dense oxide as they cooled during the PEO process. This mechanism promotes the growth of ceramic coatings with higher thickness and

hardness. The physical-chemical reactions involved in the PEO process are strongly enhanced by the plasma discharge events. Therefore, the physical-chemical reactions at the anode surface are complicated and accompanied with extensive gas liberation, acoustic emission and optical emission. The ongoing research of PEO treatment could be divided into two aspects, including fundamental studies of the process and characterization/optimization of the coatings' properties. In terms of scientific significance, fundamental studies focused on the phenomena during PEO process are carried out to better clarify the underlying mechanisms. For instance, the gas liberation³⁻⁵, acoustic emission⁶ and optical spectra^{5,7-10} during the PEO treatment have been characterized and investigated. To meet the requirements of various engineering applications, a lot of researches focus on characterization and optimization of specific coating properties or multi-functionalities, including tribological properties¹¹⁻¹⁶, corrosion resistance¹⁷⁻²², photocatalytic efficiency²³⁻²⁹, bioactivity³⁰⁻³⁷ and thermal properties³⁸⁻⁴³. Regarding the PEO process, numerous efforts have also been made to improve the efficiency to meet the industrial needs. PEO technology is now in the transition from lab research to engineering production. Several companies like Keronite (UK), Magoxide-coat (Germany) and Microplasmic (USA) are currently exploiting commercial usage of PEO treatments.

2.2 Fundamental mechanisms of PEO process

The plasma discharges are thought to be a result of dielectric breakdown of the oxide scale. Numerous efforts have been made to understand the discharge events. Unfortunately, the lifetime of a single discharge is very short. The plasma discharges always exist as clusters and are hard to separate, which means it is very difficult to analyze individual discharge event. Therefore, the nature of plasma discharges is not fully understood up to now. The

following reviews introduced a well-accepted mechanism of coating deposition and model of current-voltage behavior during the PEO process.

Figure 2-2 demonstrates the current-voltage behavior of a complex four-phase system, i.e. metal-dielectric-gas-electrolyte, with a number of possible phase boundaries during the plasma electrolysis process, as proposed by Yerokhin *et al*¹.

A ‘type-a’ curve represents a PES (like carburizing and nitriding) process, during which gas liberation would form a stable gas envelope on either the anode or cathode surface. Then breakdown of the gas leads to plasma discharge events. The ions with high energy could be formed inside the discharges by electron avalanche effect. These energetic ions migrate towards the electrode and combine with metal atoms to form the saturation layer, like carburizing and nitriding¹. The PES process will not be reviewed in detail in this dissertation.

The ‘type-b’ plot represents the formation of oxide films on the anode, including classic anodizing (up to U₅) and PEO (U₅-U₇). The metal-dielectric-gas-electrolyte system with a ‘type-b’ current-voltage behavior will be reviewed in detail.

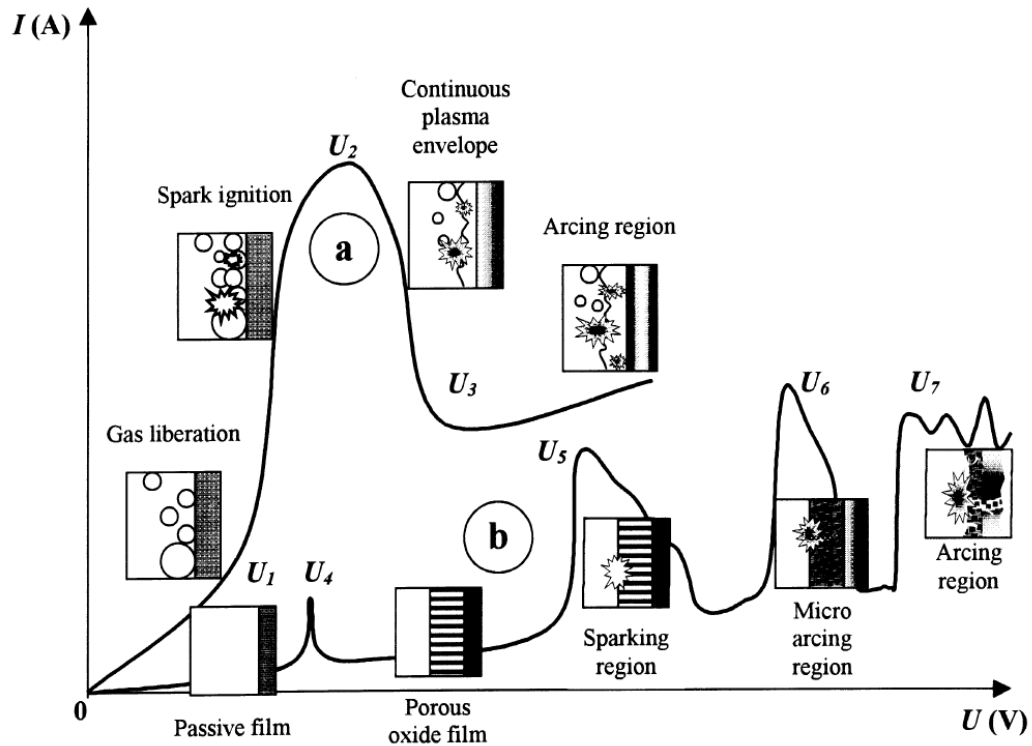


Figure 2-2 Two kinds of current-voltage curves of plasma electrolysis processes: (a) plasma electrolytic saturation and (b) plasma electrolytic oxidation. Adapted from ¹.

Firstly, the passive film (typically an oxide scale) was formed in the region 0-U₄. In this stage, the system obeys the Faraday's law and the Ohm's law. Thus, a proportional increase of current along with the rise of voltage could be observed. At U₄, the passive film begins to dissolve and thus the current is increased, as demonstrated by the current peak at this point. As the applied voltage continues to increase (U₄-U₅), a porous oxide film forms with increased thickness and thus increased impedance. Therefore, the current drops. As this stage, conventional anodizing occurs (taking titanium as an example):





At point U_5 , the electric field strength in the oxide film reaches a critical value beyond which the dielectric breakdown occurs due to impact or tunneling ionization^{44,45}. Therefore, this point marks the boundary between conventional anodizing and plasma electrolytic oxidation. In the sparking region, numerous tiny sparks moved rapidly across the surface of the oxide film, promoting the growth of the oxide film. Further increasing the voltage to U_6 , the thermal ionization could occur which could lead to short-lived but larger arcing discharges with high temperature and pressure. The metal is melted by the high temperature discharges at the metal-oxide interface. The melted metal was ejected by the high pressure through the discharge channels into the oxide-electrolyte interface where it reacts with the electrolyte species, forming metal oxides and hydroxides. The formed metal oxides and hydroxides were deposited back on the anode surface and formed circular areas. Meanwhile, the gas liberation escaped through the discharge channels, leaving holes in the centers of these circular areas like the volcano. These volcano-like morphologies are usually called as ‘pancake structure’^{46,47} or ‘crater’⁴⁸⁻⁵¹, as shown in Figure 2-3.

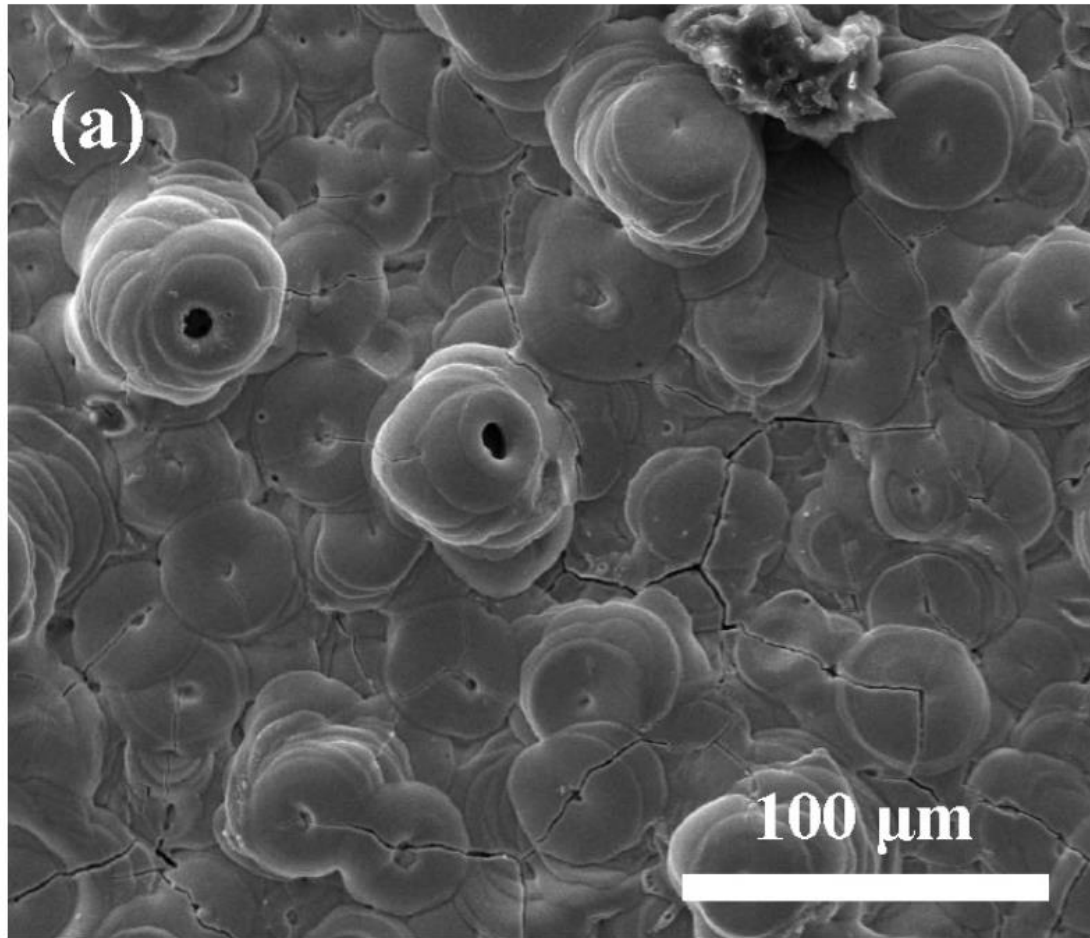


Figure 2-3 Scanning electron micrographs showing the surface of coatings formed on Zircaloy-2 alloy in an electrolyte containing 8 g/L NaAlO_2 and 1 g/L KOH for 30 min. Adapted from ⁵².

Melting and ejecting of metals, plasma assisted chemical reactions between ejected metals and electrolyte species, melting, solidification, sintering and densification of formed metal oxides simultaneously and repeatedly occurred in the relatively weak (thinner) regions of the coating during the PEO process. Therefore, the overall coating thickness is pretty uniform ⁵³⁻⁶⁰.

Above point U₇, the extremely strong arcing discharges formed throughout the coating. These arcing discharges are so strong that they might cause destructive effects such as

thermal cracking of the coating. Figure 2-4 illustrates the evolution of discharge events during the PEO process on Zircaloy-2 alloy in an electrolyte that contains 8 g/L NaAlO₂ and 1 g/L KOH ⁵².

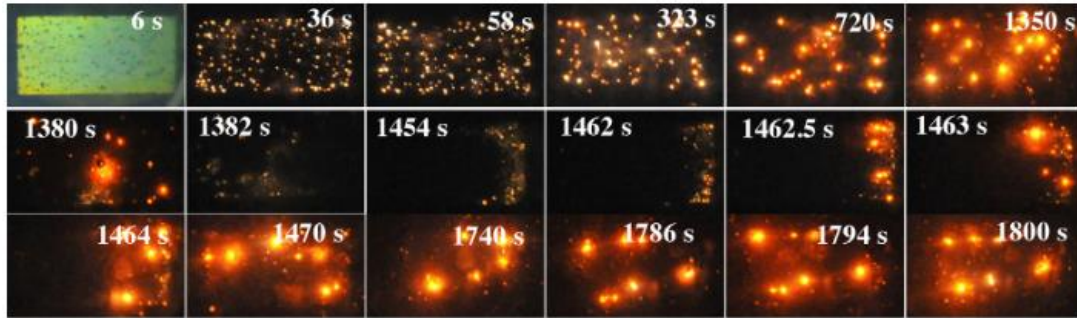


Figure 2-4 Evolution of discharge events during the PEO process on Zircaloy-2 alloy in an electrolyte containing 8 g/L NaAlO₂ and 1 g/L KOH. Adapted from ⁵².

2.3 PEO process parameters

The surface morphology and microstructure of the PEO coating are affected by many parameters including composition of electrolyte, current mode, substrate materials, processing time and so on. Here, a brief review of the studies of process parameters is given.

2.3.1 Electrolyte composition

Yerokhin ¹ has summarized six groups of electrolytes that can be used for the PEO process based on their current-voltage behavior, as shown in Figure 2-5:

1. Solutions of salts that provide fast dissolution of metals, like NaCl, NaClO₃, NaOH, NaNO₃.
2. Electrolytes providing slow metal dissolution, such as H₂SO₄, (NH₄)₂S₂O₈, Na₂SO₄.
3. Electrolytes providing metal passivation in a close range of voltages, including sodium acetate.

4. Fluoride electrolytes, which have complex behavior.
5. Electrolytes promoting slight metal passivation.
6. Electrolyte promoting strong passivation of metal, e.g., phosphoric acids, phosphates of alkaline metals (which can form polymer anions), salts of carbonic, boric acids and inorganic polymers (such as silicates, aluminates, tungstates, molybdates).

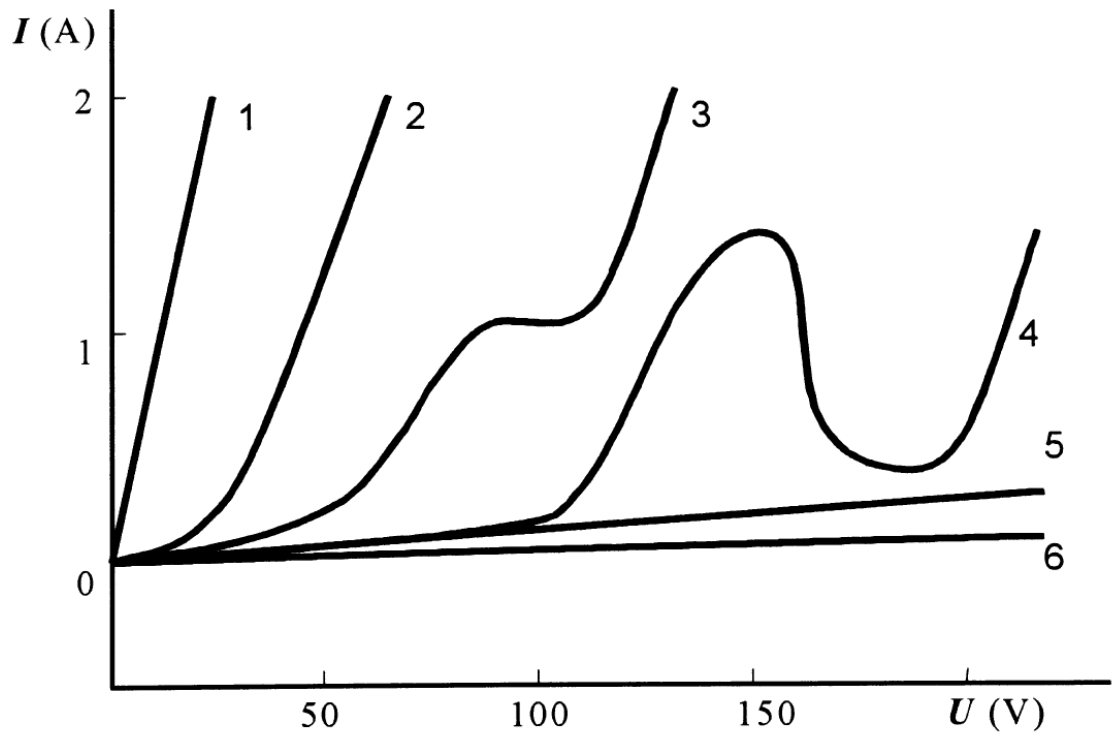


Figure 2-5 Current-voltage behavior of electrolytes tested for PEO treatment of aluminum.

(1) fast metal dissolution, (2) slow metal dissolution, (3) metal passivation in narrow voltage interval, (4) complex behavior of fluoride electrolytes, (5) slight passivation and (6) strong passivation of metal. Adapted from ¹.

From the viewpoint of contribution to the coating composition, the electrolyte could also be divided into four groups ¹:

- (a) Solutions that only provides oxygen species.

- (b) Solutions containing anionic species involved in the coating.
- (c) Solutions containing cationic components involved in the coating.
- (d) Suspensions providing cataphoretic transport of microparticles or nanoparticles that contributed to the coating composition.

Electrolytes contain silicates and phosphates, which promote strong metal passivation, are most widely used for the PEO process. These constituents decrease the breakdown voltage and increase the coating growth rate by incorporation of SiO_3^{2-} into the coatings⁶¹⁻⁶⁴. Coatings with mullite phase has been deposited on the aluminum alloys by PEO treatment in electrolyte containing sodium silicate and might be useful for thermal management application since they have very low thermal conductivities^{38,39,41}. It has been reported that the coating prepared in alkaline electrolytes containing sodium silicate (e.g., 2-20 g/L Na_2SiO_3 and 2-4 g/L KOH) had a thick and dense inner layer, which contains mainly α - and γ - Al_2O_3 phases. Complex Al-Si-O phases could also be observed in the coating. Table 2-1 summarized the effects of electrolyte compositions used in PEO process on the phase compositions of the coatings produced on aluminum alloys.

Table 2-1 Electrolyte compositions and phase compositions of the produced coatings.

Reference	Substrate	Electrolyte composition	Phase composition of produced coating
Ref ⁶⁵	Al 6082	1 g/L KOH	α -Al ₂ O ₃ and γ -Al ₂ O ₃
Ref ⁶⁶	Al 2024	20 g/L Na ₂ SiO ₃	γ -Al ₂ O ₃ dominant, α -Al ₂ O ₃ , mullite and δ -Al ₂ O ₃
Ref ⁶⁷	Al 2017A	0-8 g/L Na ₂ SiO ₃ and 2 g/L KOH	α -Al ₂ O ₃ , γ -Al ₂ O ₃ and mullite
Ref ⁶⁸	Al	30 g/L Na ₂ SiO ₃ and 10-40 g/L KOH	α -Al ₂ O ₃ , γ -Al ₂ O ₃ , mullite and Al ₂ SiO ₅

Incorporating inorganic chemical in an electrolyte sometimes could enhance the solution conductivity, promote the metal passivation, increase the stability of electrolyte and improve the coating performance. It has been reported that addition of Na₂WO₄ reduced the breakdown voltage of PEO process and produced denser, thicker and more corrosion resistant coatings ⁶⁹⁻⁷².

Micro- and nanoparticles could also be incorporated into the coatings by cataphoretic effects, i.e., particle transfer to the electrodes by strong electric fields during PEO process. Several kinds of additives, including hard and high melting point particles like SiC and ZrO₂, dry lubricants such as MoS₂ and graphene, photocatalytic particles like TiO₂ and Fe₂O₃, and coloring agents could be added into the electrolyte. For example, blue coatings on Mg-Li alloy could be achieved by adding titania sol ⁷³, black coatings were formed on aluminum alloy with K₂TiF₆ ⁷⁴.

It has been reported that coatings formed on Al and Mg alloys with incorporation of ZrO₂, CeO₂ and SiC nanoparticles have higher adhesion to the substrate, lower porosity, higher wear and corrosion resistance ^{21,63,75-82}. Carbon nanotubes and graphene/graphene oxide added into the electrolyte could also reduce the pore size and thus increase the wear and

corrosion resistance of produced coatings when compared with coatings produced in conventional electrolytes⁸³⁻⁹¹.

Incorporation of TiO₂, WO₃, SnO₂, CdS, ZnO and Fe₂O₃ nanoparticles into the PEO coating produced on titanium metals could modify the band structure and enhance charge separation property of the coating. Therefore, the photocatalytic properties of the produced coatings could be significantly improved⁹²⁻⁹⁹.

Inspired by above literature, the electrolyte chosen in the present project contains sodium aluminate and sodium phosphate, which belongs to type 6-(b). It could provide strong passivation of the iron and copper metals and the anionic species (AlO₂⁻) would also contribute to the coating composition.

2.3.2 Current mode

Current mode plays a key role in the PEO process. Various types of current mode have been applied and investigated in PEO treatment, including AC, DC and pulsed DC, as shown in Figure 2-6.

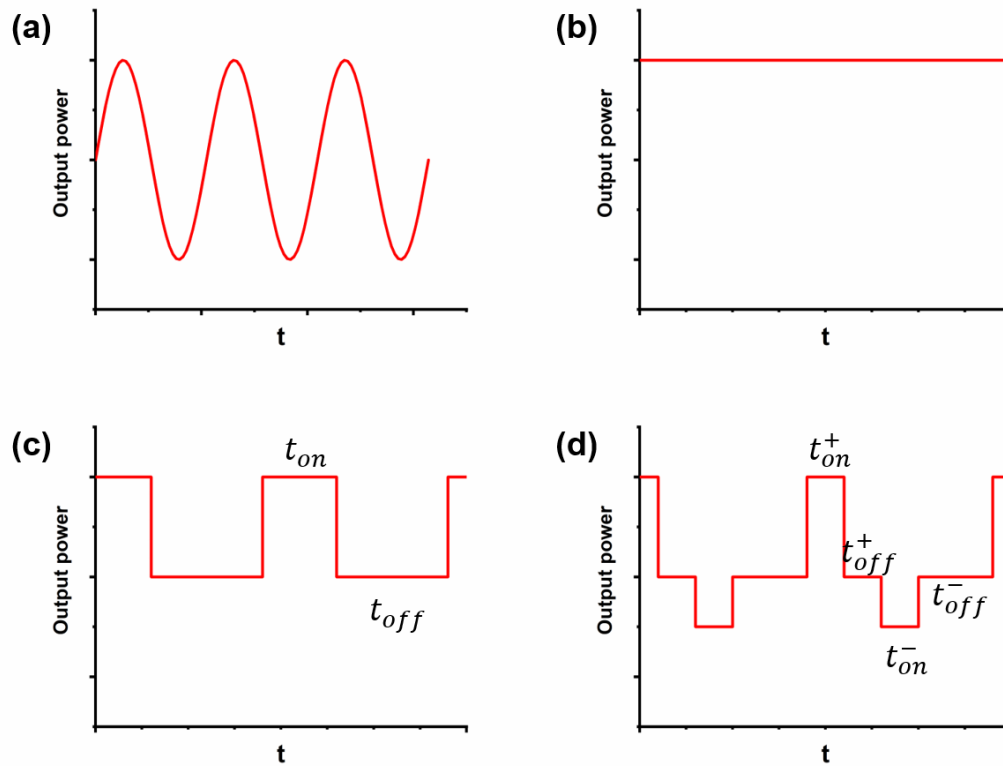


Figure 2-6 Various types of current modes used in PEO process. (a) alternating current (AC), (b) direct current (DC), (c) unipolar pulsed current, (d) bipolar pulsed current.

Here, t_{off} represents the period when the current pulse is off, t_{on}^+ and t_{on}^- represent the periods when the anodic and cathodic current pulses are on, respectively.

It is generally agreed that the coating morphologies are greatly influenced by the applied current density of DC mode. When applied current increased, the coating growth rate would increase, accompanying with increase of surface roughness²⁰. The average pore diameter and overall porosity would also increase with higher current density. Khan *et. al.*¹⁰⁰ reported that the coatings produced under higher current density (20 A/dm²) on Al alloys have higher α -Al₂O₃ phase composition when compared with coating produced at lower current density (5 A/dm²). They also reported a decreased residual stress within the

coatings as the applied current density increased. Similar results have been reported for Mg alloys ¹⁰¹.

Apart from the DC mode, AC and pulsed current mode have attracted more interest because they provide better coating quality, which should be related to the absence of long-living large discharges as found under DC mode ^{102,103}. It has been reported that under unipolar mode, the average pore size is much smaller than that under DC mode ¹⁰⁴. Xin *et. al.* ¹⁰⁵ also claimed the bond strength of the coating to the substrate was improved by the unipolar mode. Increasing corrosion resistance was also achieved by the AC and pulsed current mode ^{104,106,107}. For AC and pulsed current mode, frequency or pulse frequency is an important factor that affects the coating properties. According to Figure 2-6, the pulse frequency could be defined as:

For unipolar pulsed current mode:

$$f_u = \frac{1}{t_{off} + t_{on}} \quad (2.5)$$

or

for bipolar pulsed current mode:

$$f_b = \frac{1}{t_{on}^+ + t_{off}^+ + t_{on}^- + t_{off}^-} \quad (2.6)$$

Another important factor that will influence the coating properties is duty cycle, which could be defined as:

For unipolar pulsed current

$$\delta = t_{on} f_u \quad (2.7)$$

For positive duty cycle of bipolar pulsed current:

$$\delta_+ = t_{on}^+ f_b \quad (2.8)$$

And negative duty cycle of bipolar pulsed current:

$$\delta_- = t_{on}^- f_b \quad (2.9)$$

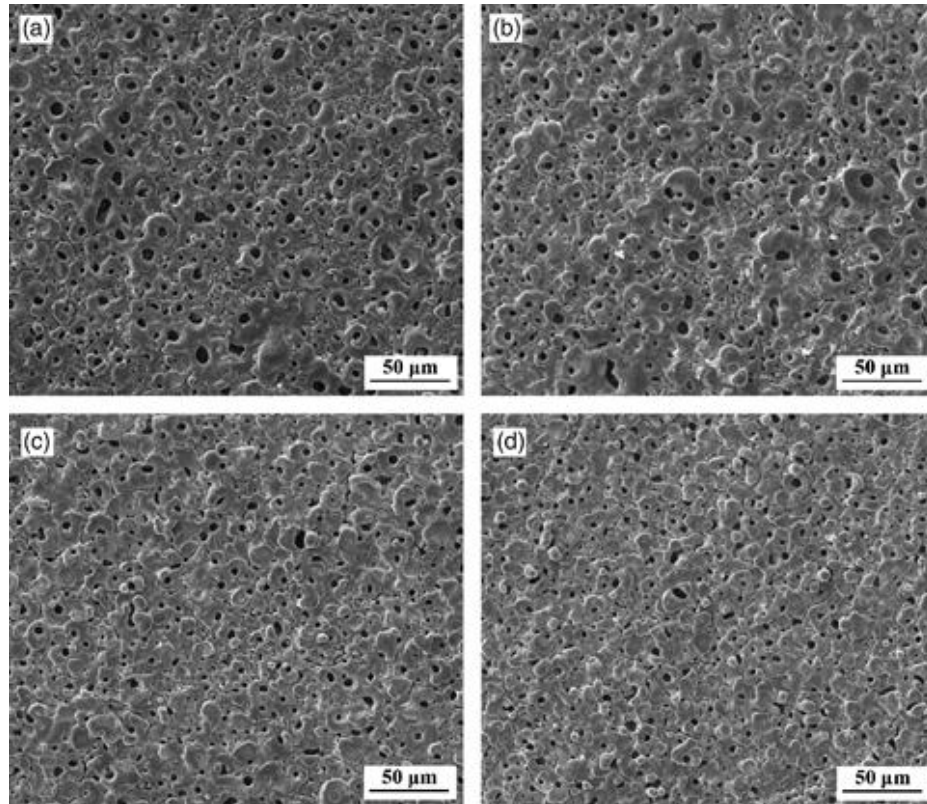


Figure 2-7 Scanning electron microscope images of the surface morphologies of the ceramic coating produced on ZK60 Mg alloy in electrolyte contains 8 g/L sodium phosphate, 3 g/L potassium hydroxide and 1 g/L sodium fluoride under different frequencies (bipolar current mode, duty ratio is 0.1). (a) 100 Hz, (b) 200 Hz, (c) 500 Hz, (d) 1000 Hz. Adapted from ¹⁰⁸.

Su *et. al.* ¹⁰⁸ have reported that the average pore size of produced ceramic coatings reduced from 10 μm under 100 Hz to 2 μm under 1000 Hz. And the corrosion resistance was also significantly enhanced as the frequency increased. Dehnavi *et. al.* ^{109,110} systematically investigated influence of frequencies and duty cycles (under unipolar current mode) of PEO treatment on Al 6061 alloy in electrolytes contains sodium silicate. They reported that low duty cycles resulted in a lower concentration on the surface but more uniform

distribution across the coating of Si, which could be attributed to the sparks of higher density but less intensity, as shown in Figure 2-8.

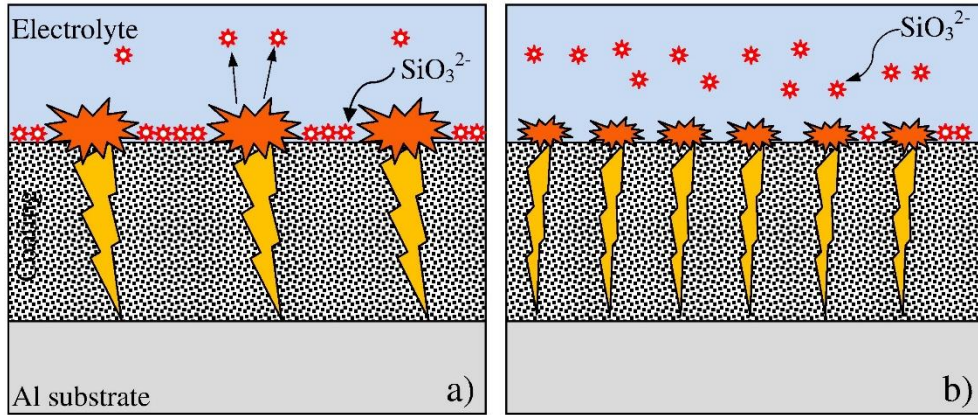


Figure 2-8 Effect of micro discharge characteristics on the distribution of silicon. (a) high duty cycle, (b) low duty cycle. Adapted from ¹¹⁰.

Increasing the pulse on time by decreasing the frequencies and increasing the duty cycles would promote the γ to α - Al_2O_3 phase transformation ¹⁰⁹. Mullite phase was formed at low frequencies, high current densities and longer treatment times. Increasing the duty cycles and lowering the frequencies would generate micro-discharges with higher intensity, which could promote absorption of Si and facilitate the formation of mullite ¹⁰⁹.

Under bipolar current mode, the negative biasing current would also influence the coating properties. Su *et. al.* ¹¹¹ has reported that a more compact and less porous coating could be produced on ZK60 magnesium alloy when the negative biasing magnitude was increased. Similar results were reported on Ti-6Al-4V alloy ¹¹², indicating this effect appears to be consistent.

2.3.3 Substrate materials

It is generally agreed that PEO processing is only applicable on ‘valve metals’ ¹¹³, which means that current can only flow in one direction in the metal-oxide-electrolyte system ¹¹⁴.

The electrons can only flow through the oxide layer in the direction from metal to electrolyte, which means the metal substrate is cathode. When the metal substrate is anode, electrons cannot flow through the oxide from the electrolyte to the metal substrate. Therefore, an electrical field might reach the dielectric breakdown point of the oxide layer, which is critical for initiation of sparks. This rectification effect at the metal-oxide junction is determined by the relative positions of the Fermi levels in the metal and semiconductor. The oxides of most ‘valve metals’ are n-type semiconductors (with large band gaps)², as shown in Figure 2-9. Their Gibbs free energies of formation are also much more negative, as illustrated in Figure 2-9.

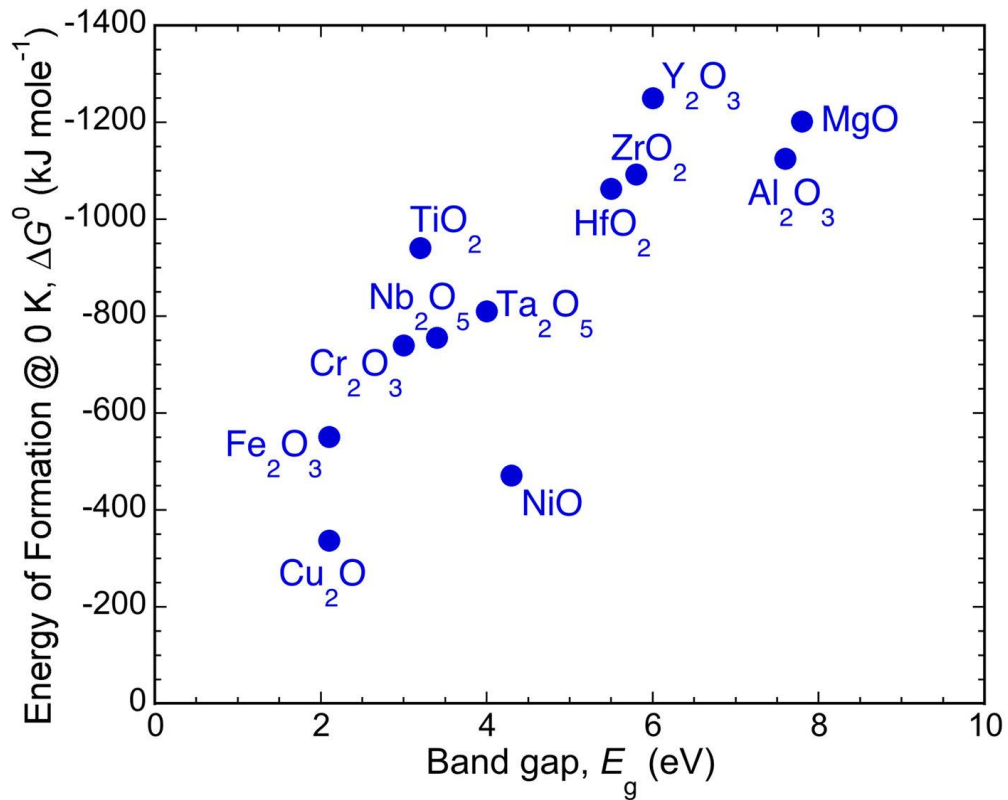


Figure 2-9 Plot of Gibbs free energy of formation against band gaps of selected oxides.

Adapted from ¹¹⁵.

Much less negative Gibbs free energies of formation of iron and copper oxides indicate less thermodynamic tendency of formation. The iron and copper oxides are p-type semiconductors with relatively small band gaps, which means electrons could flow through the oxide scale when the metal was anode. Thus, the charges would not build up across the oxide scale, which means PEO process cannot be readily applied on the iron and copper metals.

2.3.4 Influence of processing time

The influence of processing time on the coating properties has multiple aspects. The coating thickness generally increases with increased processing time. However, different increment behaviors have been observed. For example, Hussein *et. al.*⁵⁹ reported a linear relation between coating thickness and processing time, while nonlinear behavior was observed by Wang *et. al.*¹¹⁶, as shown in Figure 2-10.

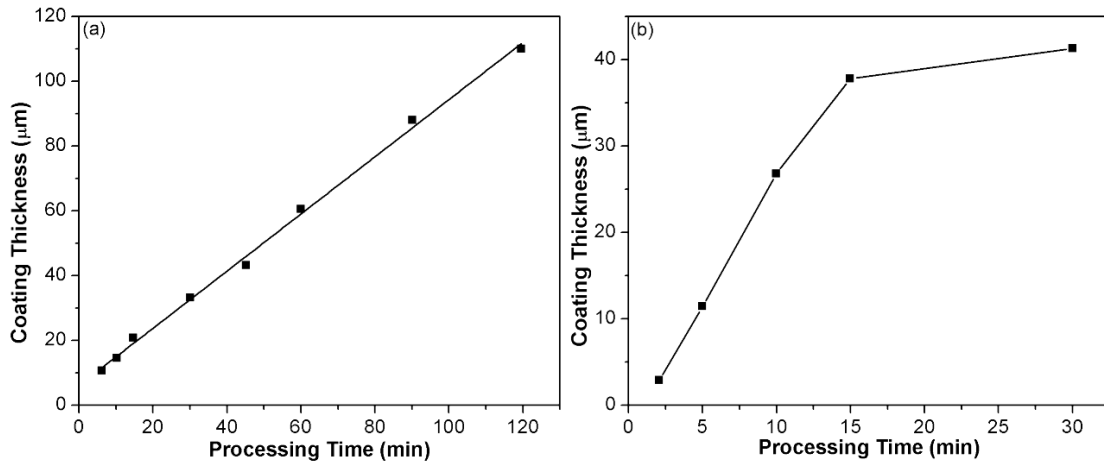


Figure 2-10 (a) linear (adapted from⁵⁹) and (b) nonlinear (adapted from¹¹⁶) relations between the coating thickness and processing time.

It has been reported that the overall porosity and average pore size of the coating generally increased as the processing time increased^{57,117}.

2.4 PEO coating properties

PEO coatings have been reported to possess high hardness, good corrosion and wear resistance, excellent adhesion to the substrate, high thermal shock resistance and low thermal conductivity. These properties, which are reviewed in detail below, make the PEO coatings suitable for automotive, aerospace, construction, oil and gas processing industries.

2.4.1 Hardness

Published studies on PEO coated aluminum alloys in alkaline electrolytes^{65-68,109} suggests that the coating consists mainly of α -Al₂O₃ and γ -Al₂O₃. Mullite phase can also be produced in electrolytes containing sodium silicate^{41,66-68,110}. By optimizing the current density, duty cycle and frequency, it is possible to promote the γ to α -Al₂O₃ (with higher hardness) phase transformation during PEO process¹⁰⁹. The hardness range of PEO coatings have been reported as 900-2000 HV^{49,102}.

2.4.2 Wear resistance

Wear resistance of the coating mainly relies on the hardness. Therefore, coatings with higher α -Al₂O₃ phase composition would demonstrate higher wear resistance¹¹⁸. A comparative study between PEO and hard anodized coatings on Al 6061 alloy shows that the wear resistance of PEO coating is much higher than that of the hard anodized coating¹¹⁹. The abrasive wear resistance of PEO coating is reported to be comparable to that of tungsten carbide composites, boride diffusion coatings¹. In recent year, PEO treatment has been applied on the aluminum cylinder to replace the cast iron liner, in order to reduce the weight of automobiles and thus decrease the fuel consumption and exhaust emissions.

2.4.3 Corrosion resistance

Light metals, like magnesium and aluminum, are susceptible to corrosion. PEO treatment can greatly enhance the corrosion resistance of these alloys. It has been reported that a three-layer structure exists in the PEO coating: (1) the dense inner layer, which could act as barrier layer for corrosion resistance; (2) the function layer with high hardness and low porosity, which could bear the load and account for the wear resistance; (3) porous outer layer. Since the corrosive medium can penetrate the pores and micro cracks of the outer layer and function layer, the corrosion resistance of the PEO coating should mainly rely on the dense barrier layer, which has been confirmed by the electrochemical impedance spectroscopy (EIS) studies on PEO coated magnesium, titanium and aluminum alloys^{19,120–123}.

In order to further improve the corrosion resistance, pores and micro cracks could be sealed by dipping the coated samples into organic sealants, like polypropylene¹²⁴, and inorganic sealants using sol-gel method^{125–127}.

2.4.4 Thermal conductivities

Curran *et. al.*^{38,41} have measured the thermal conductivities of PEO coatings on aluminum and magnesium alloys. They reported thermal conductivities of the PEO coatings are at least one order of magnitude lower than the values of corresponding bulk materials. Thermal conductivity values as low as ~ 0.8 W/(m·K) have been found for PEO coatings on magnesium³⁸. Mullite-rich coatings on aluminum alloys can be as thick as 200 μm , which might be used as thermal barrier coatings.

2.5 Recent progress of PEO process on non-valve metals and their alloys

As reviewed in section 2.3.3 substrate materials, the Gibbs free energies of formation of iron oxide and copper oxide are much less negative (less thermodynamic tendency of formation). The iron and copper oxides are p-type semiconductors with relatively small band gaps. Therefore, electrons could flow through the oxide scale when the metal was anode and the charges would not build up across the oxide scale, which means PEO process cannot be readily applied on the iron and copper metals.

One way to carry PEO process on iron alloys is to combine PEO process with the hot-aluminizing^{128,129}. That is deposit a thin layer of aluminum on the surface of iron alloys by hot-dipping or thermal spray. Then the PEO process could be carried on the aluminized iron alloys. However, PEO process in this method actually occurred on the surface of aluminum instead of iron.

Recently, a few published studies reported the direct formation of ceramic coatings on the iron alloys by PEO process in electrolytes containing sodium aluminate^{130,131}. Composite coatings consist of FeAl_2O_4 , Fe_3O_4 and Al_2O_3 have been formed. The coated samples have much higher wear and corrosion resistance when compared with the iron alloys. Li *et. al.*¹³² comprehensively investigated the PEO process, especially the mechanism for coating formation and the order of breakdown events, in dilute sodium aluminate and sodium phosphate solution (8 g/L NaAlO_2 and 2 g/L $\text{Na}_2\text{H}_2\text{PO}_4$) under extremely high voltage (> 700 V). In this paper, they have reported the initiation of plasma discharges at ~700 V with a duty cycle of 5%. After 30 mins, the final voltage reached to 800 V and the coating thickness could be as high as ~80 μm . The EDS analysis indicates that the passive film formed during the PEO process (at ~600 V) mainly consists of Al and O with small amount

of P and Fe. They proposed that the passive film should be aluminum phosphates or $\text{Al}_2\text{O}_3/\text{AlPO}_4$ and plays an important role for initiation of PEO process on carbon steel, as shown in Figure 2-11.

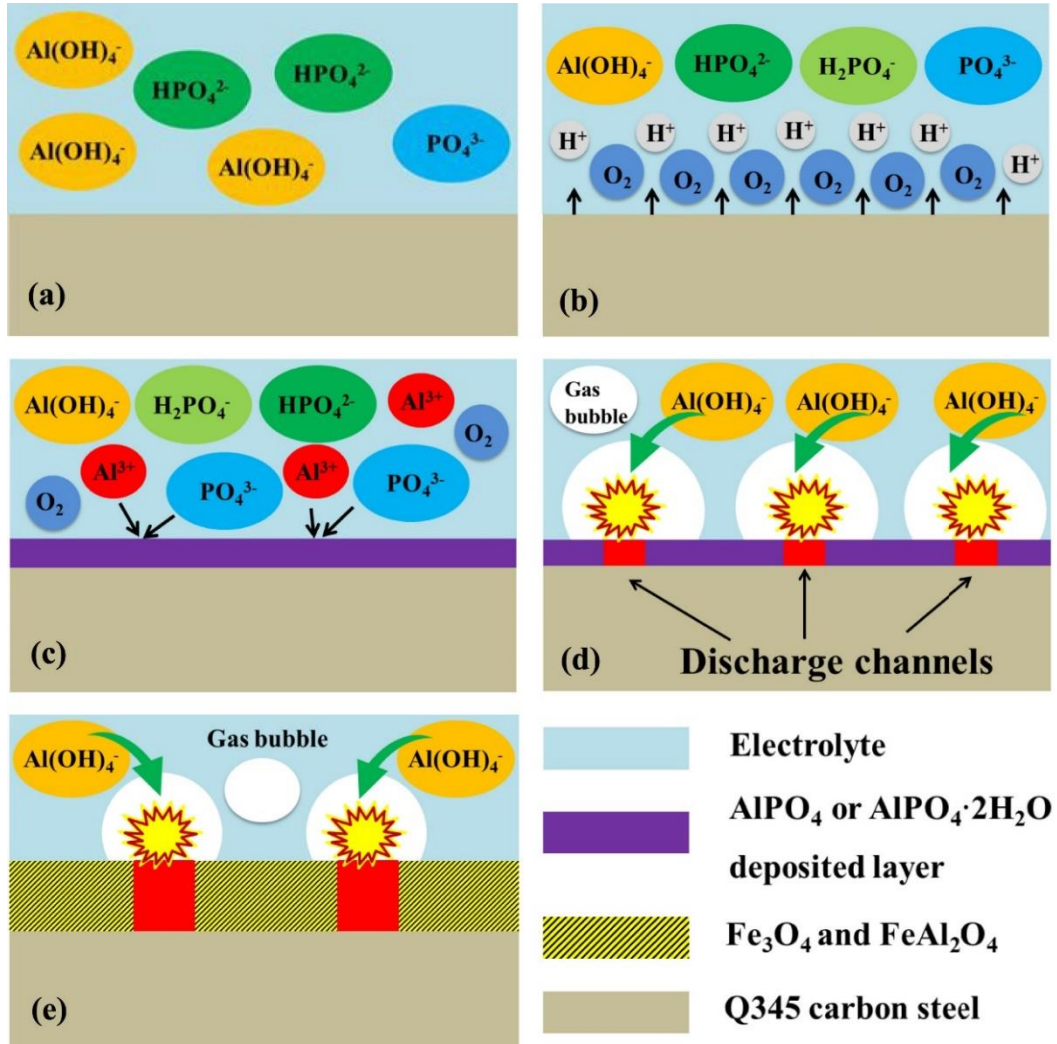


Figure 2-11 Schematic illustration of the PEO of the carbon steel in 8 g/L NaAlO_2 and 2 g/L NaH_2PO_4 . (a) The sample before the application of anodic current. (b) The moment after the application of anodic current. (c) The deposition of an aluminum phosphates or AAP layer on the steel surface. (d) The initiation of plasma discharges through the breakdown of the dielectric layer. (e) Stable discharges at later stage of PEO. Adapted from

2.6 Summary

Ferrous alloys are usually vulnerable to corrosion. The global cost of corrosion in 2013 was reported to be \$2.5 trillion, 3.4% of the global GDP. Severe business interruption always happens due to equipment and assets failure. Traditional methods to prevent corrosion include phosphating, zinc plating and chromium plating. However, the electrolyte used for phosphating process contains toxic sodium nitrite¹³³. The waste solutions contain a lot of PO_4^{3-} and NO_3^- , which have negative impact on eco-systems¹³⁴. Zinc and chromium plating would also cause environmental impacts, like zinc pollution¹³⁵. In contrast with the lack of understanding of PEO processes on ferrous alloys with medium applied voltages, the ferrous alloys are still the most widely used metallic materials in modern society.

Compared with phosphating, zinc plating and chromium plating, PEO process is eco-friendly. The prepared ceramic coatings have high chemical stability, high wear and corrosion resistance, high thermal shock resistance and low thermal conductivity. As discussed above, Li *et. al.*¹³² focused on the PEO process in dilute sodium aluminate and sodium phosphate solution under extremely high voltage (> 700 V). Such high voltages are strictly regulated in industrial production and we always want to keep the applied voltages into a medium range (< 600 V). Wang *et. al.*^{130, 131} have prepared the ceramic coating on carbon steel with medium applied voltages, but the process mechanism was not investigated, especially for the characterization of passive film formed under this condition. Therefore, it is still needed to develop a modified PEO process which can work on the ferrous alloys under medium voltages. The current-voltage behavior during the process, the passivation mechanism and the microstructure of the coating will be studied in detail.

The coating's wear, corrosion and thermal related properties are also going to be comprehensively studied.

REFERENCES

- (1) Yerokhin, A. L.; Nie, X.; Leyland, A.; Matthews, A.; Dowey, S. J. Plasma Electrolysis for Surface Engineering. *Surf. Coatings Technol.* **1999**, *122* (2–3), 73–93. [https://doi.org/10.1016/S0257-8972\(99\)00441-7](https://doi.org/10.1016/S0257-8972(99)00441-7).
- (2) Clyne, T. W.; Troughton, S. C. A Review of Recent Work on Discharge Characteristics during Plasma Electrolytic Oxidation of Various Metals. *Int. Mater. Rev.* **2019**, *64* (3), 127–162. <https://doi.org/10.1080/09506608.2018.1466492>.
- (3) Snizhko, L. O.; Yerokhin, A. L.; Gurevina, N. L.; Patalakha, V. A.; Matthews, A. Excessive Oxygen Evolution during Plasma Electrolytic Oxidation of Aluminium. *Thin Solid Films* **2007**, *516* (2–4), 460–464. <https://doi.org/10.1016/j.tsf.2007.06.158>.
- (4) Snizhko, L. O.; Yerokhin, A. L.; Pilkington, A.; Gurevina, N. L.; Misnyankin, D. O.; Leyland, A.; Matthews, A. Anodic Processes in Plasma Electrolytic Oxidation of Aluminium in Alkaline Solutions. *Electrochim. Acta* **2004**, *49* (13), 2085–2095. <https://doi.org/10.1016/j.electacta.2003.11.027>.
- (5) Cheng, Y.; Peng, Z.; Wu, X.; Cao, J.; Skeldon, P.; Thompson, G. E. A Comparison of Plasma Electrolytic Oxidation of Ti-6Al-4V and Zircaloy-2 Alloys in a Silicate-Hexametaphosphate Electrolyte. *Electrochim. Acta* **2015**, *165*, 301–313. <https://doi.org/10.1016/j.electacta.2015.03.020>.
- (6) Boinet, M.; Verdier, S.; Maximovitch, S.; Dalard, F. Plasma Electrolytic Oxidation of AM60 Magnesium Alloy: Monitoring by Acoustic Emission Technique.

Electrochemical Properties of Coatings. *Surf. Coatings Technol.* **2005**, *199* (2-3), 141–149.
<https://doi.org/10.1016/j.surfcoat.2004.10.145>.

(7) Arrabal, R.; Matykina, E.; Hashimoto, T.; Skeldon, P.; Thompson, G. E. Characterization of AC PEO Coatings on Magnesium Alloys. *Surf. Coatings Technol.* **2009**, *203* (16), 2207–2220. <https://doi.org/10.1016/j.surfcoat.2009.02.011>.

(8) Wang, L.; Chen, L.; Yan, Z.; Fu, W. Optical Emission Spectroscopy Studies of Discharge Mechanism and Plasma Characteristics during Plasma Electrolytic Oxidation of Magnesium in Different Electrolytes. *Surf. Coatings Technol.* **2010**, *205* (6), 1651–1658.
<https://doi.org/10.1016/j.surfcoat.2010.10.022>.

(9) Zhong, Y. S.; He, X. D.; Shi, L. P.; Li, M. W.; He, F. Tailored Al₂O₃/ZrO₂ Composite Oxide Layers by Bipolar Current Adjustment in the Plasma Electrolytic Oxidation (PEO) Process. *Nanosci. Nanotechnol. Lett.* **2011**, *3* (2), 209–214.
<https://doi.org/10.1166/nll.2011.1150>.

(10) Matykina, E.; Berkani, A.; Skeldon, P.; Thompson, G. E. Real-Time Imaging of Coating Growth during Plasma Electrolytic Oxidation of Titanium. *Electrochim. Acta* **2007**, *53* (4), 1987–1994. <https://doi.org/10.1016/j.electacta.2007.08.074>.

(11) Yerokhin, A. L.; Shatrov, A.; Samsonov, V.; Shashkov, P.; Pilkington, A.; Leyland, A.; Matthews, A. Oxide Ceramic Coatings on Aluminium Alloys Produced by a Pulsed Bipolar Plasma Electrolytic Oxidation Process. *Surf. Coatings Technol.* **2005**, *199* (2-3), 150–157. <https://doi.org/10.1016/j.surfcoat.2004.10.147>.

(12) Mu, M.; Liang, J.; Zhou, X.; Xiao, Q. One-Step Preparation of TiO₂/MoS₂ Composite Coating on Ti6Al4V Alloy by Plasma Electrolytic Oxidation and Its

- Tribological Properties. *Surf. Coatings Technol.* **2013**, *214*, 124–130. <https://doi.org/10.1016/j.surfcoat.2012.10.079>.
- (13) Malayoglu, U.; Tekin, K. C.; Malayoglu, U.; Shrestha, S. An Investigation into the Mechanical and Tribological Properties of Plasma Electrolytic Oxidation and Hard-Anodized Coatings on 6082 Aluminum Alloy. *Mater. Sci. Eng. A* **2011**, *528* (24), 7451–7460. <https://doi.org/10.1016/j.msea.2011.06.032>.
- (14) Durdu, S.; Usta, M. The Tribological Properties of Bioceramic Coatings Produced on Ti6Al4V Alloy by Plasma Electrolytic Oxidation. *Ceram. Int.* **2014**, *40* (2), 3627–3635. <https://doi.org/10.1016/j.ceramint.2013.09.062>.
- (15) Zhang, P.; Nie, X.; Hu, H.; Liu, Y. TEM Analysis and Tribological Properties of Plasma Electrolytic Oxidation (PEO) Coatings on a Magnesium Engine AJ62 Alloy. *Surf. Coatings Technol.* **2010**, *205* (5), 1508–1514. <https://doi.org/10.1016/j.surfcoat.2010.10.015>.
- (16) Wu, X.; Su, P.; Jiang, Z.; Meng, S. Influences of Current Density on Tribological Characteristics of Ceramic Coatings on ZK60 Mg Alloy by Plasma Electrolytic Oxidation. *ACS Appl. Mater. Interfaces* **2010**, *2* (3), 808–812. <https://doi.org/10.1021/am900802x>.
- (17) Liang, J.; Srinivasan, P. B.; Blawert, C.; Störmer, M.; Dietzel, W. Electrochemical Corrosion Behaviour of Plasma Electrolytic Oxidation Coatings on AM50 Magnesium Alloy Formed in Silicate and Phosphate Based Electrolytes. *Electrochim. Acta* **2009**, *54* (14), 3842–3850. <https://doi.org/10.1016/j.electacta.2009.02.004>.
- (18) Duan, H.; Yan, C.; Wang, F. Effect of Electrolyte Additives on Performance of Plasma Electrolytic Oxidation Films Formed on Magnesium Alloy AZ91D. *Electrochim. Acta* **2007**, *52* (11), 3785–3793. <https://doi.org/10.1016/j.electacta.2006.10.066>.

- (19) Shokouhfar, M.; Dehghanian, C.; Montazeri, M.; Baradaran, A. Preparation of Ceramic Coating on Ti Substrate by Plasma Electrolytic Oxidation in Different Electrolytes and Evaluation of Its Corrosion Resistance: Part II. *Appl. Surf. Sci.* **2012**, *258* (7), 2416–2423. <https://doi.org/10.1016/j.apsusc.2011.10.064>.
- (20) Bala Srinivasan, P.; Liang, J.; Blawert, C.; Störmer, M.; Dietzel, W. Effect of Current Density on the Microstructure and Corrosion Behaviour of Plasma Electrolytic Oxidation Treated AM50 Magnesium Alloy. *Appl. Surf. Sci.* **2009**, *255* (7), 4212–4218. <https://doi.org/10.1016/j.apsusc.2008.11.008>.
- (21) Lim, T. S.; Ryu, H. S.; Hong, S. H. Electrochemical Corrosion Properties of CeO₂-Containing Coatings on AZ31 Magnesium Alloys Prepared by Plasma Electrolytic Oxidation. *Corros. Sci.* **2012**, *62*, 104–111. <https://doi.org/10.1016/j.corsci.2012.04.043>.
- (22) Hussein, R. O.; Zhang, P.; Nie, X.; Xia, Y.; Northwood, D. O. The Effect of Current Mode and Discharge Type on the Corrosion Resistance of Plasma Electrolytic Oxidation (PEO) Coated Magnesium Alloy AJ62. *Surf. Coatings Technol.* **2011**, *206* (7), 1990–1997. <https://doi.org/10.1016/j.surfcoat.2011.08.060>.
- (23) Yao, Z.; Jia, F.; Tian, S.; Li, C.; Jiang, Z.; Bai, X. Microporous Ni-Doped TiO₂ Film Photocatalyst by Plasma Electrolytic Oxidation. *ACS Appl. Mater. Interfaces* **2010**, *2* (9), 2617–2622. <https://doi.org/10.1021/am100450h>.
- (24) He, J.; Luo, Q.; Cai, Q. Z.; Li, X. W.; Zhang, D. Q. Microstructure and Photocatalytic Properties of WO₃/TiO₂ Composite Films by Plasma Electrolytic Oxidation. *Mater. Chem. Phys.* **2011**, *129* (1–2), 242–248. <https://doi.org/10.1016/j.matchemphys.2011.04.011>.

- (25) Stojadinović, S.; Radić, N.; Vasilić, R.; Petković, M.; Stefanov, P.; Zeković, L.; Grbić, B. Photocatalytic Properties of TiO₂/WO₃ Coatings Formed by Plasma Electrolytic Oxidation of Titanium in 12-Tungstosilicic Acid. *Appl. Catal. B Environ.* **2012**, *126*, 334–341. <https://doi.org/10.1016/j.apcatb.2012.07.031>.
- (26) Stojadinović, S.; Tadić, N.; Vasilić, R. Structural and Photoluminescent Properties of ZrO₂:Tb³⁺ Coatings Formed by Plasma Electrolytic Oxidation. *J. Lumin.* **2018**, *197*, 83–89. <https://doi.org/10.1016/j.jlumin.2018.01.022>.
- (27) Akatsu, T.; Yamada, Y.; Hoshikawa, Y.; Onoki, T.; Shinoda, Y.; Wakai, F. Multifunctional Porous Titanium Oxide Coating with Apatite Forming Ability and Photocatalytic Activity on a Titanium Substrate Formed by Plasma Electrolytic Oxidation. *Mater. Sci. Eng. C* **2013**, *33* (8), 4871–4875. <https://doi.org/10.1016/j.msec.2013.08.003>.
- (28) Stojadinović, S.; Vasilić, R.; Radić, N.; Tadić, N.; Stefanov, P.; Grbić, B. The Formation of Tungsten Doped Al₂O₃ /ZnO Coatings on Aluminum by Plasma Electrolytic Oxidation and Their Application in Photocatalysis. *Appl. Surf. Sci.* **2016**, *377*, 37–43. <https://doi.org/10.1016/j.apsusc.2016.03.104>.
- (29) Lu, X.; Schieda, M.; Blawert, C.; Kainer, K. U.; Zheludkevich, M. L. Formation of Photocatalytic Plasma Electrolytic Oxidation Coatings on Magnesium Alloy by Incorporation of TiO₂ Particles. *Surf. Coatings Technol.* **2016**, *307*, 287–291. <https://doi.org/10.1016/j.surfcoat.2016.09.006>.
- (30) Krzakała, A.; Kazek-Kęsik, A.; Simka, W. Application of Plasma Electrolytic Oxidation to Bioactive Surface Formation on Titanium and Its Alloys. *RSC Adv.* **2013**, *3* (43), 19725–19743. <https://doi.org/10.1039/c3ra43465f>.

- (31) Durdu, S.; Usta, M.; Berkem, A. S. Bioactive Coatings on Ti6Al4V Alloy Formed by Plasma Electrolytic Oxidation. *Surf. Coatings Technol.* **2016**, *301*, 85–93. <https://doi.org/10.1016/j.surfcoat.2015.07.053>.
- (32) Sandhyarani, M.; Rameshbabu, N.; Venkateswarlu, K.; Sreekanth, D.; Subrahmanyam, C. Surface Morphology, Corrosion Resistance and in Vitro Bioactivity of P Containing ZrO₂ Films Formed on Zr by Plasma Electrolytic Oxidation. *J. Alloys Compd.* **2013**, *553*, 324–332. <https://doi.org/10.1016/j.jallcom.2012.11.147>.
- (33) Siu, H. T.; Man, H. C. Fabrication of Bioactive Titania Coating on Nitinol by Plasma Electrolytic Oxidation. *Appl. Surf. Sci.* **2013**, *274*, 181–187. <https://doi.org/10.1016/j.apsusc.2013.03.008>.
- (34) Sowa, M.; Piotrowska, M.; Widziółek, M.; Dercz, G.; Tylko, G.; Gorewoda, T.; Osyczka, A. M.; Simka, W. Bioactivity of Coatings Formed on Ti-13Nb-13Zr Alloy Using Plasma Electrolytic Oxidation. *Mater. Sci. Eng. C* **2015**, *49*, 159–173. <https://doi.org/10.1016/j.msec.2014.12.073>.
- (35) Krzakała, A.; Słuzalska, K.; Widziółek, M.; Szade, J.; Winiarski, A.; Dercz, G.; Kazek, A.; Tylko, G.; Michalska, J.; Iwaniak, A.; Osyczka, A. M.; Simka, W. Formation of Bioactive Coatings on a Ti-6Al-7Nb Alloy by Plasma Electrolytic Oxidation. *Electrochim. Acta* **2013**, *104*, 407–424. <https://doi.org/10.1016/j.electacta.2012.07.075>.
- (36) Aktuğ, S. L.; Durdu, S.; Yalçın, E.; Çavuşoğlu, K.; Usta, M. Bioactivity and Biocompatibility of Hydroxyapatite-Based Bioceramic Coatings on Zirconium by Plasma Electrolytic Oxidation. *Mater. Sci. Eng. C* **2017**, *71*, 1020–1027. <https://doi.org/10.1016/j.msec.2016.11.012>.

- (37) Mohedano, M.; Guzman, R.; Arrabal, R.; L6pez Lacomba, J. L.; Matykina, E. Bioactive Plasma Electrolytic Oxidation Coatings - The Role of the Composition, Microstructure, and Electrochemical Stability. *J. Biomed. Mater. Res. - Part B Appl. Biomater.* **2013**, *101* (8), 1524–1537. <https://doi.org/10.1002/jbm.b.32974>.
- (38) Curran, J. A.; Clyne, T. W. The Thermal Conductivity of Plasma Electrolytic Oxide Coatings on Aluminium and Magnesium. *Surf. Coatings Technol.* **2005**, *199* (2-3 SPEC. ISS.), 177–183. <https://doi.org/10.1016/j.surfcoat.2004.11.045>.
- (39) Shen, X.; Nie, X.; Hu, H.; Tjong, J. Effects of Coating Thickness on Thermal Conductivities of Alumina Coatings and Alumina/Aluminum Hybrid Materials Prepared Using Plasma Electrolytic Oxidation. *Surf. Coatings Technol.* **2012**, *207*, 96–101. <https://doi.org/10.1016/j.surfcoat.2012.06.009>.
- (40) Apelfeld, A. V.; Borisov, A. M.; Krit, B. L.; Ludin, V. B.; Polyansky, M. N.; Romanovsky, E. A.; Savushkina, S. V.; Suminov, I. V.; Tkachenko, N. V.; Vinogradov, A. V.; Vostrikov, V. G. The Study of Plasma Electrolytic Oxidation Coatings on Zr and Zr-1% Nb Alloy at Thermal Cycling. *Surf. Coatings Technol.* **2015**, *269* (1), 279–285. <https://doi.org/10.1016/j.surfcoat.2015.02.039>.
- (41) Curran, J. A.; Kalkanci, H.; Magurova, Y.; Clyne, T. W. Mullite-Rich Plasma Electrolytic Oxide Coatings for Thermal Barrier Applications. *Surf. Coatings Technol.* **2007**, *201* (21), 8683–8687. <https://doi.org/10.1016/j.surfcoat.2006.06.050>.
- (42) Wang, L.; Zhou, J.; Liang, J.; Chen, J. Thermal Control Coatings on Magnesium Alloys Prepared by Plasma Electrolytic Oxidation. *Appl. Surf. Sci.* **2013**, *280*, 151–155. <https://doi.org/10.1016/j.apsusc.2013.04.115>.

- (43) Yao, Z.; Hu, B.; Shen, Q.; Niu, A.; Jiang, Z.; Su, P.; Ju, P. Preparation of Black High Absorbance and High Emissivity Thermal Control Coating on Ti Alloy by Plasma Electrolytic Oxidation. *Surf. Coatings Technol.* **2014**, *253*, 166–170. <https://doi.org/10.1016/j.surfcoat.2014.05.032>.
- (44) Ikonopisov, S. Theory of Electrical Breakdown during Formation of Barrier Anodic Films. *Electrochim. Acta* **1977**, *22* (10), 1077–1082. [https://doi.org/10.1016/0013-4686\(77\)80042-X](https://doi.org/10.1016/0013-4686(77)80042-X).
- (45) Montero, I.; Fernández, M.; Albella, J. M. Pore Formation during the Breakdown Process in Anodic Ta₂O₅ Films. *Electrochim. Acta* **1987**, *32* (1), 171–174. [https://doi.org/10.1016/0013-4686\(87\)87028-7](https://doi.org/10.1016/0013-4686(87)87028-7).
- (46) Hussein, R. O.; Northwood, D. O.; Nie, X. The Influence of Pulse Timing and Current Mode on the Microstructure and Corrosion Behaviour of a Plasma Electrolytic Oxidation (PEO) Coated AM60B Magnesium Alloy. *J. Alloys Compd.* **2012**, *541*, 41–48. <https://doi.org/10.1016/j.jallcom.2012.07.003>.
- (47) Cheng, Y.; Matykina, E.; Arrabal, R.; Skeldon, P.; Thompson, G. E. Plasma Electrolytic Oxidation and Corrosion Protection of Zircaloy-4. *Surf. Coatings Technol.* **2012**, *206* (14), 3230–3239. <https://doi.org/10.1016/j.surfcoat.2012.01.011>.
- (48) Zhu, W.; Fang, Y. J.; Zheng, H.; Tan, G.; Cheng, H.; Ning, C. Effect of Applied Voltage on Phase Components of Composite Coatings Prepared by Micro-Arc Oxidation. *Thin Solid Films* **2013**, *544*, 79–82. <https://doi.org/10.1016/j.tsf.2013.04.121>.
- (49) Wheeler, J. M.; Curran, J. A.; Shrestha, S. Microstructure and Multi-Scale Mechanical Behavior of Hard Anodized and Plasma Electrolytic Oxidation (PEO)

Coatings on Aluminum Alloy 5052. *Surf. Coatings Technol.* **2012**, *207*, 480–488.
<https://doi.org/10.1016/j.surfcoat.2012.07.056>.

(50) Kasalica, B.; Petkovic, M.; Belca, I.; Stojadinovic, S.; Zekovic, L. Electronic Transitions during Plasma Electrolytic Oxidation of Aluminum. *Surf. Coatings Technol.* **2009**, *203* (20–21), 3000–3004. <https://doi.org/10.1016/j.surfcoat.2009.03.038>.

(51) Chen, Y.; Cheng, T.; Nie, X. Wear Failure Behaviour of Titanium-Based Oxide Coatings on a Titanium Alloy under Impact and Sliding Forces. *J. Alloys Compd.* **2013**, *578*, 336–344. <https://doi.org/10.1016/j.jallcom.2013.05.199>.

(52) Cheng, Y.; Cao, J.; Peng, Z.; Wang, Q.; Matykina, E.; Skeldon, P.; Thompson, G. E. Wear-Resistant Coatings Formed on Zircaloy-2 by Plasma Electrolytic Oxidation in Sodium Aluminate Electrolytes. *Electrochim. Acta* **2014**, *116*, 453–466. <https://doi.org/10.1016/j.electacta.2013.11.079>.

(53) Cheng, Y. L.; Xue, Z. G.; Wang, Q.; Wu, X. Q.; Matykina, E.; Skeldon, P.; Thompson, G. E. New Findings on Properties of Plasma Electrolytic Oxidation Coatings from Study of an Al-Cu-Li Alloy. *Electrochim. Acta* **2013**, *107*, 358–378. <https://doi.org/10.1016/j.electacta.2013.06.022>.

(54) Hussein, R. O.; Nie, X.; Northwood, D. O.; Yerokhin, A.; Matthews, A. Spectroscopic Study of Electrolytic Plasma and Discharging Behaviour during the Plasma Electrolytic Oxidation (PEO) Process. *J. Phys. D. Appl. Phys.* **2010**, *43* (10), 13. <https://doi.org/10.1088/0022-3727/43/10/105203>.

(55) Guo, H.; An, M.; Xu, S.; Huo, H. Formation of Oxygen Bubbles and Its Influence on Current Efficiency in Micro-Arc Oxidation Process of AZ91D Magnesium Alloy. *Thin Solid Films* **2005**, *485* (1–2), 53–58. <https://doi.org/10.1016/j.tsf.2005.03.050>.

- (56) Xue, W.; Deng, Z.; Lai, Y.; Chen, R. Analysis of Phase Distribution for Ceramic Coatings Formed by Microarc Oxidation on Aluminum Alloy. *J. Am. Ceram. Soc.* **2005**, *81* (5), 1365–1368. <https://doi.org/10.1111/j.1151-2916.1998.tb02493.x>.
- (57) Sundararajan, G.; Rama Krishna, L. Mechanisms Underlying the Formation of Thick Alumina Coatings through the MAO Coating Technology. *Surf. Coatings Technol.* **2003**, *167* (2–3), 269–277. [https://doi.org/10.1016/S0257-8972\(02\)00918-0](https://doi.org/10.1016/S0257-8972(02)00918-0).
- (58) Yerokhin, A. L.; Snizhko, L. O.; Gurevina, N. L.; Leyland, A.; Pilkington, A.; Matthews, A. Discharge Characterization in Plasma Electrolytic Oxidation of Aluminium. *J. Phys. D. Appl. Phys.* **2003**, *36* (17), 2110–2120. <https://doi.org/10.1088/0022-3727/36/17/314>.
- (59) Hussein, R. O.; Nie, X.; Northwood, D. O. An Investigation of Ceramic Coating Growth Mechanisms in Plasma Electrolytic Oxidation (PEO) Processing. *Electrochim. Acta* **2013**, *112*, 111–119. <https://doi.org/10.1016/j.electacta.2013.08.137>.
- (60) Treviño, M.; Mercado-Solis, R. D.; Colás, R.; Pérez, A.; Talamantes, J.; Velasco, A. Erosive Wear of Plasma Electrolytic Oxidation Layers on Aluminium Alloy 6061. *Wear* **2013**, *301* (1–2), 434–441. <https://doi.org/10.1016/j.wear.2012.12.011>.
- (61) WANG, K.; KOO, B. H.; LEE, C. G.; KIM, Y. J.; LEE, S. H.; BYON, E. Effects of Electrolytes Variation on Formation of Oxide Layers of 6061 Al Alloys by Plasma Electrolytic Oxidation. *Trans. Nonferrous Met. Soc. China (English Ed.)* **2009**, *19* (4), 866–870. [https://doi.org/10.1016/S1003-6326\(08\)60366-0](https://doi.org/10.1016/S1003-6326(08)60366-0).
- (62) Cheng, Y.; Wu, F.; Matykina, E.; Skeldon, P.; Thompson, G. E. The Influences of Microdischarge Types and Silicate on the Morphologies and Phase Compositions of

Plasma Electrolytic Oxidation Coatings on Zircaloy-2. *Corros. Sci.* **2012**, *59*, 307–315.
<https://doi.org/10.1016/j.corsci.2012.03.017>.

(63) Mohedano, M.; Blawert, C.; Zheludkevich, M. L. Silicate-Based Plasma Electrolytic Oxidation (PEO) Coatings with Incorporated CeO₂ Particles on AM50 Magnesium Alloy. *Mater. Des.* **2015**, *86*, 735–744.
<https://doi.org/10.1016/j.matdes.2015.07.132>.

(64) Lv, G.; Gu, W.; Chen, H.; Feng, W.; Khosa, M. L.; Li, L.; Niu, E.; Zhang, G.; Yang, S. Z. Characteristic of Ceramic Coatings on Aluminum by Plasma Electrolytic Oxidation in Silicate and Phosphate Electrolyte. *Appl. Surf. Sci.* **2006**, *253* (5), 2947–2952.
<https://doi.org/10.1016/j.apsusc.2006.06.036>.

(65) Khan, R. H. U.; Yerokhin, A. L.; Pilkington, T.; Leyland, A.; Matthews, A. Residual Stresses in Plasma Electrolytic Oxidation Coatings on Al Alloy Produced by Pulsed Unipolar Current. *Surf. Coatings Technol.* **2005**, *200* (5–6), 1580–1586.
<https://doi.org/10.1016/j.surfcoat.2005.08.092>.

(66) Guo, P.; Shao, Y.; Ji, Y.; Zhu, W.; Yan, H. Growth Mechanism and Corrosion Behavior of Ceramic Coatings on CP-Ti Produced by Plasma Electrolytic Oxidation. *Adv. Mater. Res.* **2011**, *154–155*, 896–901.
<https://doi.org/10.4028/www.scientific.net/AMR.154-155.896>.

(67) Polat, A.; Makaraci, M.; Usta, M. Influence of Sodium Silicate Concentration on Structural and Tribological Properties of Microarc Oxidation Coatings on 2017A Aluminum Alloy Substrate. *J. Alloys Compd.* **2010**, *504* (2), 519–526.
<https://doi.org/10.1016/j.jallcom.2010.06.008>.

- (68) Salehi Doolabi, D.; Ehteshamzadeh, M.; Mirhosseini, S. M. M. Effect of NaOH on the Structure and Corrosion Performance of Alumina and Silica PEO Coatings on Aluminum. *J. Mater. Eng. Perform.* **2012**, *21* (10), 2195–2202. <https://doi.org/10.1007/s11665-012-0151-1>.
- (69) Liu, Y.; Xu, J.; Gao, Y.; Yuan, Y.; Gao, C. Influences of Additive on the Formation and Corrosion Resistance of Micro-Arc Oxidation Ceramic Coatings on Aluminum Alloy. *Phys. Procedia* **2012**, *32*, 107–112. <https://doi.org/10.1016/j.phpro.2012.03.526>.
- (70) Hakimzad, A.; Raeissi, K.; Santamaria, M.; Asghari, M. Effects of Pulse Current Mode on Plasma Electrolytic Oxidation of 7075 Al in Na₂WO₄ Containing Solution: From Unipolar to Soft-Sparking Regime. *Electrochim. Acta* **2018**, *284*, 618–629. <https://doi.org/10.1016/j.electacta.2018.07.200>.
- (71) Chen, X.; Cai, Q.; Yin, L. Effects of Na₂WO₄ Additive on Properties of Plasma Electrolytic Oxidation Coatings on 6061 Al Alloy. *Adv. Mater. Res.* **2012**, *550–553*, 1969–1975. <https://doi.org/10.4028/www.scientific.net/AMR.550-553.1969>.
- (72) Hwang, I. J.; Shin, K. R.; Lee, J. S.; Ko, Y. G.; Shin, D. H. Formation of Black Ceramic Layer on Aluminum Alloy by Plasma Electrolytic Oxidation in Electrolyte Containing Na₂WO₄. *Mater. Trans.* **2012**, *53* (3), 559–564. <https://doi.org/10.2320/matertrans.M2011263>.
- (73) Ma, C.; Lu, Y.; Sun, P.; Yuan, Y.; Jing, X.; Zhang, M. Characterization of Plasma Electrolytic Oxidation Coatings Formed on Mg-Li Alloy in an Alkaline Polyphosphate Electrolyte. *Surf. Coatings Technol.* **2011**, *206* (2–3), 287–294. <https://doi.org/10.1016/j.surfcoat.2011.07.019>.

- (74) Tang, M.; Li, W.; Liu, H.; Zhu, L. Influence of K₂TiF₆ in Electrolyte on Characteristics of the Microarc Oxidation Coating on Aluminum Alloy. *Curr. Appl. Phys.* **2012**, *12* (5), 1259–1265. <https://doi.org/10.1016/j.cap.2012.03.003>.
- (75) Matykina, E.; Arrabal, R.; Skeldon, P.; Thompson, G. E. Incorporation of Zirconia Nanoparticles into Coatings Formed on Aluminium by AC Plasma Electrolytic Oxidation. *J. Appl. Electrochem.* **2008**, *38* (10), 1375–1383. <https://doi.org/10.1007/s10800-008-9575-6>.
- (76) Toorani, M.; Aliofkhazraei, M.; Sabour Rouhaghdam, A. Microstructural, Protective, Inhibitory and Semiconducting Properties of PEO Coatings Containing CeO₂ Nanoparticles Formed on AZ31 Mg Alloy. *Surf. Coatings Technol.* **2018**, *352*, 561–580. <https://doi.org/10.1016/j.surfcoat.2018.08.053>.
- (77) Aliofkhazraei, M.; Gharabagh, R. S.; Teimouri, M.; Ahmadzadeh, M.; Darband, G. B.; Hasannejad, H. Ceria Embedded Nanocomposite Coating Fabricated by Plasma Electrolytic Oxidation on Titanium. *J. Alloys Compd.* **2016**, *685*, 376–383. <https://doi.org/10.1016/j.jallcom.2016.05.315>.
- (78) Arunnellaiappan, T.; Ashfaq, M.; Rama Krishna, L.; Rameshbabu, N. Fabrication of Corrosion-Resistant Al₂O₃-CeO₂ Composite Coating on AA7075 via Plasma Electrolytic Oxidation Coupled with Electrophoretic Deposition. *Ceram. Int.* **2016**, *42* (5), 5897–5905. <https://doi.org/10.1016/j.ceramint.2015.12.136>.
- (79) Fatimah, S.; Kamil, M. P.; Kwon, J. H.; Kaseem, M.; Ko, Y. G. Dual Incorporation of SiO₂ and ZrO₂ Nanoparticles into the Oxide Layer on 6061 Al Alloy via Plasma Electrolytic Oxidation: Coating Structure and Corrosion Properties. *J. Alloys Compd.* **2017**, *707*, 358–364. <https://doi.org/10.1016/j.jallcom.2016.11.098>.

- (80) Lee, K. M.; Shin, K. R.; Namgung, S.; Yoo, B.; Shin, D. H. Electrochemical Response of ZrO₂-Incorporated Oxide Layer on AZ91 Mg Alloy Processed by Plasma Electrolytic Oxidation. *Surf. Coatings Technol.* **2011**, *205* (13–14), 3779–3784. <https://doi.org/10.1016/j.surfcoat.2011.01.033>.
- (81) Matykina, E.; Arrabal, R.; Monfort, F.; Skeldon, P.; Thompson, G. E. Incorporation of Zirconia into Coatings Formed by DC Plasma Electrolytic Oxidation of Aluminium in Nanoparticle Suspensions. *Appl. Surf. Sci.* **2008**, *255* (5 PART 2), 2830–2839. <https://doi.org/10.1016/j.apsusc.2008.08.036>.
- (82) Arrabal, R.; Matykina, E.; Viejo, F.; Skeldon, P.; Thompson, G. E.; Merino, M. C. AC Plasma Electrolytic Oxidation of Magnesium with Zirconia Nanoparticles. *Appl. Surf. Sci.* **2008**, *254* (21), 6937–6942. <https://doi.org/10.1016/j.apsusc.2008.04.100>.
- (83) Lee, K. M.; Ko, Y. G.; Shin, D. H. Incorporation of Multi-Walled Carbon Nanotubes into the Oxide Layer on a 7075 Al Alloy Coated by Plasma Electrolytic Oxidation: Coating Structure and Corrosion Properties. *Curr. Appl. Phys.* **2011**, *11* (4 SUPPL.). <https://doi.org/10.1016/j.cap.2011.07.009>.
- (84) Lee, K. M.; Ko, Y. G.; Shin, D. H. Incorporation of Carbon Nanotubes into Micro-Coatings Film Formed on Aluminum Alloy via Plasma Electrolytic Oxidation. *Mater. Lett.* **2011**, *65* (14), 2269–2273. <https://doi.org/10.1016/j.matlet.2011.04.001>.
- (85) Lee, K. M.; Jo, J. O.; Lee, E. S.; Yoo, B.; Shin, D. H. Incorporation of Carbon Nanotubes into Oxide Layer on 7075 Al Alloy by Plasma Electrolytic Oxidation. *J. Electrochem. Soc.* **2011**, *158* (10), C325. <https://doi.org/10.1149/1.3617754>.
- (86) Sabouri, M.; Mousavi Khoei, S. M. Plasma Electrolytic Oxidation in the Presence of Multiwall Carbon Nanotubes on Aluminum Substrate: Morphological and Corrosion

- Studies. *Surf. Coatings Technol.* **2018**, *334*, 543–555.
<https://doi.org/10.1016/j.surfcoat.2017.10.045>.
- (87) Zhao, J.; Xie, X.; Zhang, C. Effect of the Graphene Oxide Additive on the Corrosion Resistance of the Plasma Electrolytic Oxidation Coating of the AZ31 Magnesium Alloy. *Corros. Sci.* **2017**, *114*, 146–155.
<https://doi.org/10.1016/j.corsci.2016.11.007>.
- (88) Bordbar Khiabani, A.; Rahimi, S.; Yarmand, B.; Mozafari, M. Electrophoretic Deposition of Graphene Oxide on Plasma Electrolytic Oxidized-Magnesium Implants for Bone Tissue Engineering Applications. *Mater. Today Proc.* **2018**, *5* (7), 15603–15612.
<https://doi.org/10.1016/j.matpr.2018.04.169>.
- (89) Liu, W.; Liu, Y.; Lin, Y.; Zhang, Z.; Feng, S.; Talha, M.; Shi, Y.; Shi, T. Effects of Graphene on Structure and Corrosion Resistance of Plasma Electrolytic Oxidation Coatings Formed on D16T Al Alloy. *Appl. Surf. Sci.* **2019**, *475*, 645–659.
<https://doi.org/10.1016/j.apsusc.2018.12.233>.
- (90) Nasiri Vatan, H.; Adabi, M. Investigation of Tribological Behavior of Ceramic–Graphene Composite Coating Produced by Plasma Electrolytic Oxidation. *Trans. Indian Inst. Met.* **2018**, *71* (7), 1643–1652. <https://doi.org/10.1007/s12666-018-1300-5>.
- (91) Han, B.; Yang, Y.; Li, J.; Deng, H.; Yang, C. Effects of the Graphene Additive on the Corrosion Resistance of the Plasma Electrolytic Oxidation (PEO) Coating on the AZ91 Magnesium Alloy. *Int. J. Electrochem. Sci.* **2018**, *13* (9), 9166–9182.
<https://doi.org/10.20964/2018.09.06>.
- (92) Petrović, S.; Stojadinović, S.; Rožić, L.; Radić, N.; Grbić, B.; Vasilić, R. Process Modelling and Analysis of Plasma Electrolytic Oxidation of Titanium for TiO₂/WO₃ Thin

- Film Photocatalysts by Response Surface Methodology. *Surf. Coatings Technol.* **2015**, 269 (1), 250–257. <https://doi.org/10.1016/j.surfcoat.2014.12.026>.
- (93) Kim, Y. S.; Shin, K. R.; Kim, G. W.; Ko, Y. G.; Shin, D. H. Photocatalytic Activity of TiO₂ Film Containing Fe₂O₃ via Plasma Electrolytic Oxidation. *Surf. Eng.* **2016**, 32 (6), 443–447. <https://doi.org/10.1179/1743294415Y.0000000077>.
- (94) Tadić, N.; Stojadinović, S.; Radić, N.; Grbić, B.; Vasilić, R. Characterization and Photocatalytic Properties of Tungsten Doped TiO₂ Coatings on Aluminum Obtained by Plasma Electrolytic Oxidation. *Surf. Coatings Technol.* **2016**, 305, 192–199. <https://doi.org/10.1016/j.surfcoat.2016.08.045>.
- (95) Franz, S.; Perego, D.; Marchese, O.; Lucotti, A.; Bestetti, M. Photoactive TiO₂ Coatings Obtained by Plasma Electrolytic Oxidation in Refrigerated Electrolytes. *Appl. Surf. Sci.* **2016**, 385, 498–505. <https://doi.org/10.1016/j.apsusc.2016.05.032>.
- (96) Stojadinović, S.; Tadić, N.; Radić, N.; Grbić, B.; Vasilić, R. TiO₂/SnO₂ Photocatalyst Formed by Plasma Electrolytic Oxidation. *Mater. Lett.* **2017**, 196, 292–295. <https://doi.org/10.1016/j.matlet.2017.03.115>.
- (97) Soejima, T.; Yagyu, H.; Ito, S. One-Pot Synthesis and Photocatalytic Activity of Fe-Doped TiO₂ Films with Anatase-Rutile Nanojunction Prepared by Plasma Electrolytic Oxidation. *J. Mater. Sci.* **2011**, 46 (16), 5378–5384. <https://doi.org/10.1007/s10853-011-5476-x>.
- (98) Stojadinović, S.; Tadić, N.; Radić, N.; Grbić, B.; Vasilić, R. CdS Particles Modified TiO₂ Coatings Formed by Plasma Electrolytic Oxidation with Enhanced Photocatalytic Activity. *Surf. Coatings Technol.* **2018**, 344, 528–533. <https://doi.org/10.1016/j.surfcoat.2018.03.080>.

- (99) Yao, Z.; Jia, F.; Jiang, Y.; Li, C. X.; Jiang, Z.; Bai, X. Photocatalytic Reduction of Potassium Chromate by Zn-Doped TiO₂/Ti Film Catalyst. *Appl. Surf. Sci.* **2010**, *256* (6), 1793–1797. <https://doi.org/10.1016/j.apsusc.2009.10.005>.
- (100) Khan, R. H. U.; Yerokhin, A.; Li, X.; Dong, H.; Matthews, A. Surface Characterisation of DC Plasma Electrolytic Oxidation Treated 6082 Aluminium Alloy: Effect of Current Density and Electrolyte Concentration. *Surf. Coatings Technol.* **2010**, *205* (6), 1679–1688. <https://doi.org/10.1016/j.surfcoat.2010.04.052>.
- (101) Gu, Y.; Xiong, W.; Ning, C.; Zhang, J. Residual Stresses in Microarc Oxidation Ceramic Coatings on Biocompatible AZ31 Magnesium Alloys. *J. Mater. Eng. Perform.* **2012**, *21* (6), 1085–1090. <https://doi.org/10.1007/s11665-011-9980-6>.
- (102) Matykina, E.; Arrabal, R.; Skeldon, P.; Thompson, G. E. Investigation of the Growth Processes of Coatings Formed by AC Plasma Electrolytic Oxidation of Aluminium. *Electrochim. Acta* **2009**, *54* (27), 6767–6778. <https://doi.org/10.1016/j.electacta.2009.06.088>.
- (103) Moon, S.; Jeong, Y. Generation Mechanism of Microdischarges during Plasma Electrolytic Oxidation of Al in Aqueous Solutions. *Corros. Sci.* **2009**, *51* (7), 1506–1512. <https://doi.org/10.1016/j.corsci.2008.10.039>.
- (104) Jin, F.; Chu, P. K.; Xu, G.; Zhao, J.; Tang, D.; Tong, H. Structure and Mechanical Properties of Magnesium Alloy Treated by Micro-Arc Discharge Oxidation Using Direct Current and High-Frequency Bipolar Pulsing Modes. *Mater. Sci. Eng. A* **2006**, *435–436*, 123–126. <https://doi.org/10.1016/j.msea.2006.07.059>.
- (105) Xin, S.; Song, L.; Zhao, R.; Hu, X. Influence of Cathodic Current on Composition, Structure and Properties of Al₂O₃ Coatings on Aluminum Alloy Prepared by Micro-Arc

- Oxidation Process. *Thin Solid Films* **2006**, 515 (1), 326–332.
<https://doi.org/10.1016/j.tsf.2005.12.087>.
- (106) Gnedenkov, S. V.; Khrisanfova, O. A.; Zavidnaya, A. G.; Sinebryukhov, S. L.; Egorkin, V. S.; Nistratova, M. V.; Yerokhin, A.; Matthews, A. PEO Coatings Obtained on an Mg-Mn Type Alloy under Unipolar and Bipolar Modes in Silicate-Containing Electrolytes. *Surf. Coatings Technol.* **2010**, 204 (14), 2316–2322.
<https://doi.org/10.1016/j.surfcoat.2009.12.024>.
- (107) Guo, X.; Du, K.; Guo, Q.; Wang, Y.; Wang, F. Effect of Carrierwaveform Frequency on the Microstructure of Al₂O₃ Plasma Electrolytic Oxidation Films. *ECS Electrochem. Lett.* **2013**, 2 (4). <https://doi.org/10.1149/2.001304eel>.
- (108) Su, P.; Wu, X.; Jiang, Z.; Guo, Y. Effects of Working Frequency on the Structure and Corrosion Resistance of Plasma Electrolytic Oxidation Coatings Formed on a ZK60 Mg Alloy. *Int. J. Appl. Ceram. Technol.* **2011**, 8 (1), 112–119.
<https://doi.org/10.1111/j.1744-7402.2009.02411.x>.
- (109) Dehnavi, V.; Liu, X. Y.; Luan, B. L.; Shoesmith, D. W.; Rohani, S. Phase Transformation in Plasma Electrolytic Oxidation Coatings on 6061 Aluminum Alloy. *Surf. Coatings Technol.* **2014**, 251, 106–114. <https://doi.org/10.1016/j.surfcoat.2014.04.010>.
- (110) Dehnavi, V.; Luan, B. L.; Shoesmith, D. W.; Liu, X. Y.; Rohani, S. Effect of Duty Cycle and Applied Current Frequency on Plasma Electrolytic Oxidation (PEO) Coating Growth Behavior. *Surf. Coatings Technol.* **2013**, 226, 100–107.
<https://doi.org/10.1016/j.surfcoat.2013.03.041>.
- (111) Su, P.; Wu, X.; Jiang, Z.; Guo, Y. Effects of Working Frequency on the Structure and Corrosion Resistance of Plasma Electrolytic Oxidation Coatings Formed on a ZK60

Mg Alloy. *Int. J. Appl. Ceram. Technol.* **2011**, 8 (1), 112–119.
<https://doi.org/10.1111/j.1744-7402.2009.02411.x>.

(112) Yao, Z.; Liu, Y.; Xu, Y.; Jiang, Z.; Wang, F. Effects of Cathode Pulse at High Frequency on Structure and Composition of Al₂TiO₅ Ceramic Coatings on Ti Alloy by Plasma Electrolytic Oxidation. *Mater. Chem. Phys.* **2011**, 126 (1–2), 227–231.
<https://doi.org/10.1016/j.matchemphys.2010.11.035>.

(113) Stojadinović, S.; Vasilić, R.; Perić, M. Investigation of Plasma Electrolytic Oxidation on Valve Metals by Means of Molecular Spectroscopy—a Review. *RSC Advances*. Royal Society of Chemistry 2014, pp 25759–25789. <https://doi.org/10.1039/c4ra03873h>.

(114) Michaelis, A. Valve Metal, Si and Ceramic Oxides as Dielectric Films for Passive and Active Electronic Devices. In *Electrochemical Surface Modification Thin Films, Functionalization and Characterization*; 2008; Vol. 10, pp 1–106.
<https://doi.org/10.1002/9783527625307.ch1>.

(115) Strehlow, W. H.; Cook, E. L. Compilation of Energy Band Gaps in Elemental and Binary Compound Semiconductors and Insulators. *J. Phys. Chem. Ref. Data* **1973**, 2 (1), 163–200. <https://doi.org/10.1063/1.3253115>.

(116) Wang, Y.; Lei, T.; Jiang, B.; Guo, L. Growth, Microstructure and Mechanical Properties of Microarc Oxidation Coatings on Titanium Alloy in Phosphate-Containing Solution. *Appl. Surf. Sci.* **2004**, 233 (1–4), 258–267.
<https://doi.org/10.1016/j.apsusc.2004.03.231>.

(117) Duan, H.; Li, Y.; Xia, Y.; Chen, S. Transient Voltage-Current Characteristics: New Insights into Plasma Electrolytic Oxidation Process of Aluminium Alloy. *Int. J. Electrochem. Sci.* **2012**, 7 (8), 7619–7630.

- (118) Tian, J.; Luo, Z.; Qi, S.; Sun, X. Structure and Antiwear Behavior of Micro-Arc Oxidized Coatings on Aluminum Alloy. *Surf. Coatings Technol.* **2002**, *154* (1), 1–7. [https://doi.org/10.1016/S0257-8972\(01\)01671-1](https://doi.org/10.1016/S0257-8972(01)01671-1).
- (119) Krishna, L. R.; Purnima, A. S.; Sundararajan, G. A Comparative Study of Tribological Behavior of Microarc Oxidation and Hard-Anodized Coatings. *Wear* **2006**, *261* (10), 1095–1101. <https://doi.org/10.1016/j.wear.2006.02.002>.
- (120) Bajat, J. B.; Vasilić, R.; Stojadinović, S.; Mišković-Stankovic, V. Corrosion Stability of Oxide Coatings Formed by Plasma Electrolytic Oxidation of Aluminum: Optimization of Process Time. *Corrosion* **2013**, *69* (7), 693–702. <https://doi.org/10.5006/0859>.
- (121) Hussein, R. O.; Northwood, D. O.; Nie, X. The Effect of Processing Parameters and Substrate Composition on the Corrosion Resistance of Plasma Electrolytic Oxidation (PEO) Coated Magnesium Alloys. *Surf. Coatings Technol.* **2013**, *237*, 357–368. <https://doi.org/10.1016/j.surfcoat.2013.09.021>.
- (122) Venugopal, A.; Ramesh Narayanan, P.; Sharma, S. C.; George, K. M. Effect of Micro Arc Oxidation Treatment on the Corrosion and Stress Corrosion Cracking (SCC) Behaviours of AA7020-T6 Aluminum Alloy in 3.5% NaCl Solution. *Mater. Sci. Forum* **2015**, *830–831*, 639–642. <https://doi.org/10.4028/www.scientific.net/MSF.830-831.639>.
- (123) Krupa, D.; Baszkiewicz, J.; Zdunek, J.; Sobczak, J. W.; Lisowski, W.; Smolik, J.; Słomka, Z. Effect of Plasma Electrolytic Oxidation in the Solutions Containing Ca, P, Si, Na on the Properties of Titanium. *J. Biomed. Mater. Res. Part B Appl. Biomater.* **2012**, *100B* (8), 2156–2166. <https://doi.org/10.1002/jbm.b.32781>.

- (124) Chen, M.; Liu, S.; Li, J.; Cheng, N.; Zhang, X. Improvement to Corrosion Resistance of MAO Coated 2519 Aluminum Alloy by Formation of Polypropylene Film on Its Surface. *Surf. Coatings Technol.* **2013**, *232*, 674–679. <https://doi.org/10.1016/j.surfcoat.2013.06.073>.
- (125) Pezzato, L.; Rigon, M.; Martucci, A.; Brunelli, K.; Dabalà, M. Plasma Electrolytic Oxidation (PEO) as Pre-Treatment for Sol-Gel Coating on Aluminum and Magnesium Alloys. *Surf. Coatings Technol.* **2019**, *366*, 114–123. <https://doi.org/10.1016/j.surfcoat.2019.03.023>.
- (126) Ivanou, D. K.; Starykevich, M.; Lisenkov, A. D.; Zheludkevich, M. L.; Xue, H. B.; Lamaka, S. V.; Ferreira, M. G. S. Plasma Anodized ZE41 Magnesium Alloy Sealed with Hybrid Epoxy-Silane Coating. *Corros. Sci.* **2013**, *73*, 300–308. <https://doi.org/10.1016/j.corsci.2013.04.019>.
- (127) Li, Z.; Jing, X.; Yuan, Y.; Zhang, M. Composite Coatings on a Mg-Li Alloy Prepared by Combined Plasma Electrolytic Oxidation and Sol-Gel Techniques. *Corros. Sci.* **2012**, *63*, 358–366. <https://doi.org/10.1016/j.corsci.2012.06.018>.
- (128) Li, H. X.; Song, R. G.; Zhao, J. Structure and Mechanical Properties of Ceramic Coatings Fabricated by Micro-Arc Oxidation. *Adv. Mater. Res.* **2008**, *47-50 PART*, 554–557. <https://doi.org/10.4028/www.scientific.net/amr.47-50.554>.
- (129) Gu, W.; Shen, D.; Wang, Y.; Chen, G.; Feng, W.; Zhang, G.; Fan, S.; Liu, C.; Yang, S. Deposition of Duplex Al₂O₃/Aluminum Coatings on Steel Using a Combined Technique of Arc Spraying and Plasma Electrolytic Oxidation. *Appl. Surf. Sci.* **2006**, *252* (8), 2927–2932. <https://doi.org/10.1016/j.apsusc.2005.04.036>.

- (130) Wang, Y.; Jiang, Z.; Yao, Z.; Tang, H. Microstructure and Corrosion Resistance of Ceramic Coating on Carbon Steel Prepared by Plasma Electrolytic Oxidation. *Surf. Coatings Technol.* **2010**, *204* (11), 1685–1688. <https://doi.org/10.1016/j.surfcoat.2009.10.023>.
- (131) Wang, Y.; Jiang, Z.; Yao, Z. Preparation and Properties of Ceramic Coating on Q235 Carbon Steel by Plasma Electrolytic Oxidation. *Curr. Appl. Phys.* **2009**, *9* (5), 1067–1071. <https://doi.org/10.1016/j.cap.2008.12.004>.
- (132) Li, Z.; Cheng, Y.; Kang, S. hang; Tu, W.; Cheng, Y. A Re-Understanding of the Breakdown Theory from the Study of the Plasma Electrolytic Oxidation of a Carbon Steel — A Non-Valve Metal. *Electrochim. Acta* **2018**, *284*, 681–695. <https://doi.org/10.1016/j.electacta.2018.07.201>.
- (133) Stauffer, J. *Finishing Systems Design and Implementation: A Guide for Product Parameters, Coatings, Process, and Equipment*; 1993.
- (134) Conley, D. J.; Paerl, H. W.; Howarth, R. W.; Boesch, D. F.; Seitzinger, S. P.; Havens, K. E.; Lancelot, C.; Likens, G. E. Controlling Eutrophication: Nitrogen and Phosphorus. *Science* **2009**, *323* (5917), 1014–1015. <https://doi.org/10.1126/science.1167755>.
- (135) Sprague, J. B.; Elson, P. F.; Saunders, R. L. Sublethal Copper-Zinc Pollution in a Salmon River—a Field and Laboratory Study. *Adv. Water Pollut. Res.* **1965**, 61–82. <https://doi.org/10.1016/b978-0-08-011438-5.50012-x>.

3. CHAPTER 3 Study of Plasma Electrolytic Aluminating Process Using the Taguchi Experimental Design and ANOVA analysis

3.1 Introduction

Because of the cost-effectiveness, environmentally friendliness and superior surface properties, anodic plasma electrolysis has attracted tremendous attention for the surface engineering of metals. Anodic plasma electrolysis could be divided into two main categories: plasma electrolytic oxidation (PEO) and non-oxidizing treatments with vapor-gaseous envelope¹, based on the conductive properties of the oxides that are formed on the surface of the substrate. PEO is thought to be suitable for the “valve metals”, which form n-type oxides or insulators (Al_2O_3 , TiO_2 , MgO , ZrO_2 , ZnO). On the other hand, anodic dissolution, known as plasma electrolytic polishing (PEP)^{2,3}, dominates for the non-valve metals which form oxides of p-type semiconductors. A well-accepted definition of “valve metals” is that the current cannot flow through the oxide layer when the metal is anode^{3,4}. PEO has been successfully applied on Al⁵⁻⁸, Mg⁹⁻¹², Ti¹³⁻¹⁶, Zr¹⁷⁻²⁰, Ta²¹⁻²⁴ and their alloys for deposition of multi-functional coatings.

As for the non-valve metals, PEO is normally considered not applicable since stable plasma discharges cannot be easily established in this case⁴. The unsuitability for non-valve metals is one of the major obstacles to wide application of PEO. In recent years, several papers have been published on the PEO of carbon steel and cast iron in the electrolyte contains sodium aluminate and sodium phosphate²⁵⁻²⁷. Recent studies demonstrate that the electrolyte species contribute to build the passive layer on the iron surface²⁸, thus this process could also be termed as plasma electrolytic aluminating (PEA). However, the reported study²⁸ have revealed that extremely high voltage (> 700 V) is required to realize

the PEO process on carbon steels in the dilute solution of sodium aluminate and sodium phosphate. To be practically used for industry application, the applied voltage needs to be lowered (< 600 V). In our primary experiments, we have found that the most effective way to lower the voltage required for initiation of plasma discharge is to increase the concentration of sodium aluminate. Therefore, we mainly focused on the influence of the composition of electrolyte on the coating's properties in this work to develop a medium-voltage-plasma-electrolysis process, which is aiming for practical industry applications. The applied voltage and processing time were fixed at 500 V and 600 s, respectively. The influence of applied voltage and processing time would be part of future works.

In this work, the Taguchi design of experiment and ANOVA analysis were used to investigate the PEA process. The parameter factors chosen for this study include the concentration of NaAlO_2 ($C = 10$ g/L, 20g/L and 30 g/L while the concentration of Na_3PO_4 was kept being 5 g/L), the frequency (f : 500 Hz, 750 Hz, 1000 Hz) and duty cycle (δ : 0.2, 0.3, 0.4) of the unipolar pulsed power supply. Properties such as hardness, corrosion resistance and thickness were selected as three individual responses. The contribution of each factor was determined by the ANOVA analysis.

3.2 Experimental details

3.2.1 Taguchi design of experiment

For experimental design of process parameters, three parameters, including the concentration of NaAlO_2 (C), the frequency (f) and duty cycle (δ) of the unipolar pulsed power supply, were chosen.

The three factors with three levels are listed in Table 3-1. The experimental layout using L9 orthogonal array is given in Table 3-2. Two sets of the Taguchi experiments were conducted to ensure the reliability of experimental data for signal-to-noise analysis.

Table 3-1 Design factors and levels.

Level	Factor		
	C (g/L)	f (Hz)	δ
1	10	500	0.2
2	20	750	0.3
3	30	1000	0.4

Table 3-2 Designed L9 orthogonal array of experiment plans.

Experiment NO.	C (g/L)	f (Hz)	δ
1	10 (A1)	500 (B1)	0.2 (C1)
2	10 (A1)	750 (B2)	0.3 (C2)
3	10 (A1)	1000 (B3)	0.4 (C3)
4	20 (A2)	500 (B1)	0.3 (C2)
5	20 (A2)	750 (B2)	0.4 (C3)
6	20 (A2)	1000 (B3)	0.2 (C1)
7	30 (A3)	500 (B1)	0.4 (C3)
8	30 (A3)	750 (B2)	0.2 (C1)
9	30 (A3)	1000 (B3)	0.3 (C2)

To minimize the influence of the variation of characteristics, the Taguchi method²⁹⁻³² uses signal-to-noise (S/N) ratio instead of the average value to interpret the data of trial experiments. The signal-to-noise(S/N) ratio is converted from the data of trial experiments, which consolidated several repetitions into one value and reflected the degree of variation. In other words, the S/N ratio represents both the average and the variation of the selected responses. Therefore, the S/N ratio is suitable for the optimization analysis. Based on the desired responses, several S/N ratio definitions are available²⁹: lowest is best (LB, seeking

for lowest response), nominal is best (NB, looking for response close to specific value), and highest is best (HB, looking for highest response). In the present study, the hardness, corrosion resistance and thickness of the coatings were intended to be maximized, the S/N ratio for HB characteristics was selected, which was be calculated as follows:

$$S/N_{HB} = -10 \log \left(\frac{1}{n} \sum_{i=1}^n \frac{1}{T_i^2} \right) \quad (1)$$

where n is the repetition number of trials; T_i is the value of response of the i_{th} trial. For the optimal setting of each factor, the level with the largest S/N ratio was chosen.

The optimization of PEA process with multiple responses could be carried out with a weighting method:

$$X = Y \times Z \quad (2)$$

where

$$X = \begin{bmatrix} \eta_{1c} \\ \eta_{2c} \\ \vdots \\ \eta_{9c} \end{bmatrix}, Y = \begin{bmatrix} \eta_{11} & \eta_{12} & \eta_{13} \\ \eta_{21} & \eta_{22} & \eta_{23} \\ \vdots & \vdots & \vdots \\ \eta_{91} & \eta_{92} & \eta_{93} \end{bmatrix}, w = \begin{bmatrix} w_1 \\ w_2 \\ w_3 \end{bmatrix} \quad (3)$$

and

$$\sum_{i=1}^3 w_i = 1 \quad (4)$$

where w_1 , w_2 and w_3 are the weighting factors of hardness, corrosion resistance and thickness of the coatings, respectively; η_{jc} is the multi-response S/N ratio of the j_{th} experiment; η_{ji} is the i_{th} single response S/N ratio of the j_{th} experiment; w_i is the weighting factor in the i_{th} response.

The objective function was formulated as following:

$$\text{Maximize } f(X) = w_1 \eta_{hardness} + w_2 \eta_{corrosion\ resistance} + w_3 \eta_{thickness} \quad (5)$$

The above objective function summarizes the hardness, corrosion resistance and thickness of the coatings. Generally, all these three characteristics are desired to be high. However, in actual manufacturing process, for different engineering applications, the three characteristics should be considered as different critical roles by weighting factors. When wear resistance becomes critical, a high weighting factor of hardness needs to be considered. When corrosion is the major concern, corrosion resistance should have a higher weighting factor. A high weighting factor should be assigned to thickness when high productivity is required to reduce the cost. As an example, the case with weighting factors as 0.5:0.5:0 is selected to demonstrate the optimization of coating's mechanical and electrochemical properties. Another case of 0.4:0.4:0.2 is also discussed to demonstrate the process with moderate mechanical and electrochemical properties and high productivity.

3.2.2 Analysis of variance (ANOVA)

The purpose of the analysis of variance is to investigate the contribution of each factor to every single response as well as the multi-response. The ANOVA was established based on the sum of the square (SS), the degree of freedom (D), the variance (V), and the percentage of the contribution to the total variation (P).

Sum of squares (SS): the sum of square SS could be calculated from S/N ratio values for a specific response:

$$SS_T = \sum_{i=1}^m \eta_i^2 - \frac{1}{m} \left[\sum_{i=1}^m \eta_i \right]^2 \quad (6)$$

$$SS_P = \sum_{i=1}^m \frac{(S_{\eta_j})^2}{t} - \frac{1}{m} \left[\sum_{i=1}^m \eta_i \right]^2 \quad (7)$$

where m is the number of the tests ($m=9$); t is the repetition times of j^{th} level of the factor p ; S_{η_j} is the sum of the S/N ratios of factor p at level j .

Degree of freedom (D): D denotes the number of independent variables. The degree of freedom for each factor (D_p) is the number of its levels minus one. The total degrees of freedom (D_T) are the number of total numbers of the result data points minus one.

Variance (V): Variance is defined as the sum of squares of each trial sum result involved the factor, divided by the degrees of freedom of the factor:

$$V_p (\%) = \frac{SS_p}{D_p} \times 100 \quad (8)$$

The corrected sum of squares (SS'_p): SS'_p is defined as the sum of squares of factors minus the error variance times the degree of freedom of each factor:

$$SS'_p = SS_p - D_p V_e \quad (9)$$

V_e is the error of variance and can be calculated as:

$$V_e = \frac{SS_T - \sum_p SS_p}{SS_T} \quad (10)$$

Percentage of the contribution to the total variation (P): P_p denotes the percentage of the total variance of factor p , i.e., the contribution of factor p to the specific response:

$$P_p (\%) = \frac{SS'_p}{SS_T} \times 100 \quad (11)$$

By replacing the S/N ratio of the specific response (η_i) with the multi-response S/N ratio (η_{ic}), the contribution of each factor to the multiple characteristics could be evaluated.

3.2.3 Experimental procedures

Plasma electrolytic oxidation on grey cast iron: Set of compacted graphite iron samples (0.2-1% Mn, 2.5-4% C, 1-3% Si, <0.25% S, <0.1% P, and Fe balance) with dimension

20*20*5 mm³ were polished with #1200 abrasive paper. Then the polished samples were ultrasonically cleaned in ethanol and rinsed with distilled water. The sample (anode) was immersed in electrolyte (< 25 °C) in stainless steel vessel (cathode). A unipolar pulsed DC power supply was used. After 12 s of ramping, the voltage was kept at 500 V for 600 s. After taking out from the electrolyte, all samples were dried at 60 °C. The composition of electrolyte, frequency and duty cycle of the DC power supply follow the parameters listed in Table 3-2. For each set of parameters, two samples were prepared.

Characterization of coatings: The hardness of the coating was measured by Vickers hardness tester (Wilson VH1102) on the cross-sections with an applied load of 0.5 N and a holding time of 12 s. For each sample, 10 measurements were conducted, and the average hardness was calculated. The thickness of the coating was measured on the cross-sections by the optical microscope. For each sample, 10 measurements were conducted, and the average thickness was calculated. Potentiodynamic polarization tests were carried out from -0.5 V to 0.5 V with respect to the open circuit potential (E_{oc}) at a scan rate of 1 mV/s (BioLogic SP-150). All electrochemical tests were carried out in 3.5% NaCl solution at room temperature. Ag/AgCl (KCl saturated) and Pt wire were selected as reference electrode and counter electrode, respectively. The working surface area for each specimen was chosen to be 0.5 cm². Polarization resistances (R_p) were determined with Stern-Geary equation:³²

$$R_p = \frac{\beta_a \times \beta_c}{2.303 \times (\beta_a + \beta_c) \times i_{corr}} \quad (12)$$

The corrosion current density (i_{corr}), cathodic and anodic Tafel constants (β_c and β_a) could be obtained from Tafel-fitting of the polarization curves.

3.3 Results and discussion

Coating properties and multi-response S/N ratios

The coating's properties, including hardness, polarization resistance and thickness, are listed in Table 3-3. The S/N ratio for HB characteristics was used. The S/N ratios of these properties were given in Table 3-4. The response of each factor to its individual level was calculated by averaging the S/N ratios of all experiments at each level for each factor.

Table 3-3 Properties of deposited coatings.

Experiment NO.	Average hardness (HV)		Polarization resistance ($k\Omega \cdot cm^2$)		Average thickness (μm)	
	Sample 1	Sample 2	Sample 1	Sample 2	Sample 1	Sample 2
1	385.0	385.7	119.1	133.9	22	24
2	484.7	507.3	172.5	179.2	29	28
3	448.4	519.5	159.2	180.6	35	37
4	525.5	583.6	182.9	205.2	46	48
5	700.6	650.4	254.6	219.4	40	41
6	810.9	832.9	291.6	300.4	34	36
7	291.8	300	104	99.1	31	30
8	319.1	308.2	114.3	109.9	22	20
9	335.6	321.3	119.8	106.3	26	24

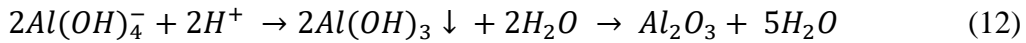
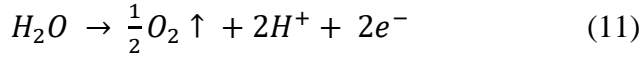
Table 3-4 The S/N ratio of objectives and Multi-response S/N ratio.

Experiment NO.	S/N ratio (average hardness)	S/N ratio (polarization resistance)	S/N ratio (average thickness)	Multi-response S/N ratio ($w_1=0.5, w_2=0.5, w_3=0$)
1	51.72	42.00	27.21	46.86
2	53.90	44.90	29.09	49.40
3	53.63	44.55	32.12	49.09
4	54.84	45.72	33.44	50.28
5	56.57	47.42	32.15	52.00
6	58.29	49.42	30.87	53.86
7	49.42	40.13	29.68	44.77
8	49.92	40.99	26.41	45.46
9	50.32	41.02	27.94	45.67

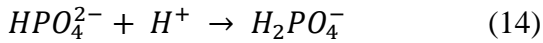
In order to figure out the influence of each factor on each response, Figure 3-1 depicts the S/N ratios for average hardness, polarization resistance and average thickness. It is noted that the S/N ratios for average hardness and polarization resistance had similar trends, because both properties closely related to the porosity of the coating. The lower the porosity, the higher the average hardness and polarization resistance. As show in Figure 3-1, the mean S/N ratio for factor A (C , concentration of NaAlO_2) increased with the C from 10 g/L (level 1) to 20 g/L (level 2) and decreased with further increasing of C up to 30 g/L (level 3).

We have done several trials with various concentrations of NaAlO_2 . When the concentration of NaAlO_2 is 5 g/L (dilute solution), there was no plasma discharge occurred. This observation was consistent with the Li's work in dilute electrolyte ²⁸. They have reported that the plasma discharges initiated at $\sim 700 \text{ V}$ ²⁸, which is far beyond the capability of our power supply (Max. 600 V). Therefore, dilute solutions cannot be used for the PEO/PEA process on ferrous alloys with medium applied voltages ($< 600 \text{ V}$). On the other hand, severe bumps and pillar-like structure could be observed when the concentration of NaAlO_2 is 40 g/L. The coating's surface was very rough and inhomogeneous. Two more trials were carried with the solution solely containing NaAlO_2 and solution solely containing Na_3PO_4 , respectively. It turns out that ceramic coatings could be obtained in the electrolyte only containing NaAlO_2 , but the coating surface was very rough and inhomogeneous. Meanwhile, no plasma discharge was observed in the electrolyte only containing Na_3PO_4 , no coating was formed either. Therefore, NaAlO_2 is indispensable for the deposition of the ceramic coating while Na_3PO_4 could improve the quality of the coating.

Based on the existed literatures³³ and our experimental results, the procedure of formation of the ceramic coating and the potential function of the Na₃PO₄ during this procedure are discussed. During the coating deposition process, following indirect deposition reaction should dominates since the concentration of water molecules is much higher than that of aluminate ions:



It is well known that the hydrolysis products of aluminate ions strongly rely on the pH values³³: the monomer aluminate ions prevail when pH > 13; at pH 9.3-12.8 the polymers with the composition $[Al(OH)_4]_n(OH)_2^{(n+2)-}$ are formed. When pH < 9.3, rapid precipitation of aluminum hydroxide would dominate. It needs to point out there is another pH-related balance reaction for phosphate ions in the electrolyte:

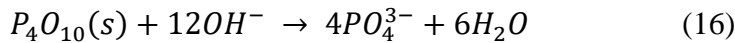
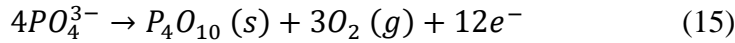


The pK_a values for reactions (13) and (14) are 12.37 and 7.20, respectively. Therefore, the effect of phosphate ions is to stabilize the localized pH value near the anode surface and control the rate of precipitation of aluminum hydroxide.

In addition, Na₃PO₄ might be beneficial for uniformly depositing of passive layer and coating by forming the phosphate-aluminate complexes. The optimal composition of the electrolyte is 20 g/L of NaAlO₂ and 5 g/L of Na₃PO₄, which could realize the balance between reactions (12) - (14). The passive layer and coating formed in this optimal solution were uniform and smooth, as shown in Figures 3-2a and 3-3a. The passive layer formed under this condition contains high amount of Fe (10~15 at. %), Al (20~25 at. %) and O

(50~60 at. %) with minor amount of P (2~3 at. %). Therefore, the passive layer should be mainly FeAl_2O_4 with a little phosphate-aluminate complexes. After the plasma sintering reaction, the amount of P is negligible in the ceramic coating (< 1 at. %), which means the P was removed during the phosphate-aluminate complexes were transformed into alumina.

The possible reactions might involve the plasma sintering and dissolution into basic water:



When the concentration of NaAlO_2 is too high (40 g/L), the amount of phosphate ions (5 g/L) in the electrolyte is not sufficient to stabilize the localized pH value near the anode surface or form the phosphate-aluminate complexes. The uncontrolled rapid precipitation of aluminum hydroxide could lead to loosely stacked particles with gas bubbles trapped inside the coating. The passive film formed under this condition is rough and inhomogeneous, as shown in Figure 3-2b. Bumps and pillar-like structures could be observed for the coating, as shown in Figure 3-3b.

The effect of factor B (f , i.e., the frequency of the power supply) on the mean S/N ratio of the mechanical properties was also plotted in Figure 3-1. The mean S/N ratio rose when frequency increased. As f increased from the 500 Hz (level 1) to 1000 Hz (level 3), the S/N ratio increased from 51.99 to 54.08 for mechanical property (average hardness) and from 42.61 to 45.00 for electrochemical property (polarization resistance), respectively. This might be due to the lower porosity, which could be generated from shorter pulse duration. For factor C (δ , i.e., the duty cycle of the power supply), as δ increased from level 1 to level 2, the S/N ratio decreased slightly. Further increasing the duty cycle led to negligible

increase in the S/N ratio, which suggested that the influence of δ on the coating's mechanical and electrochemical properties is insignificant.

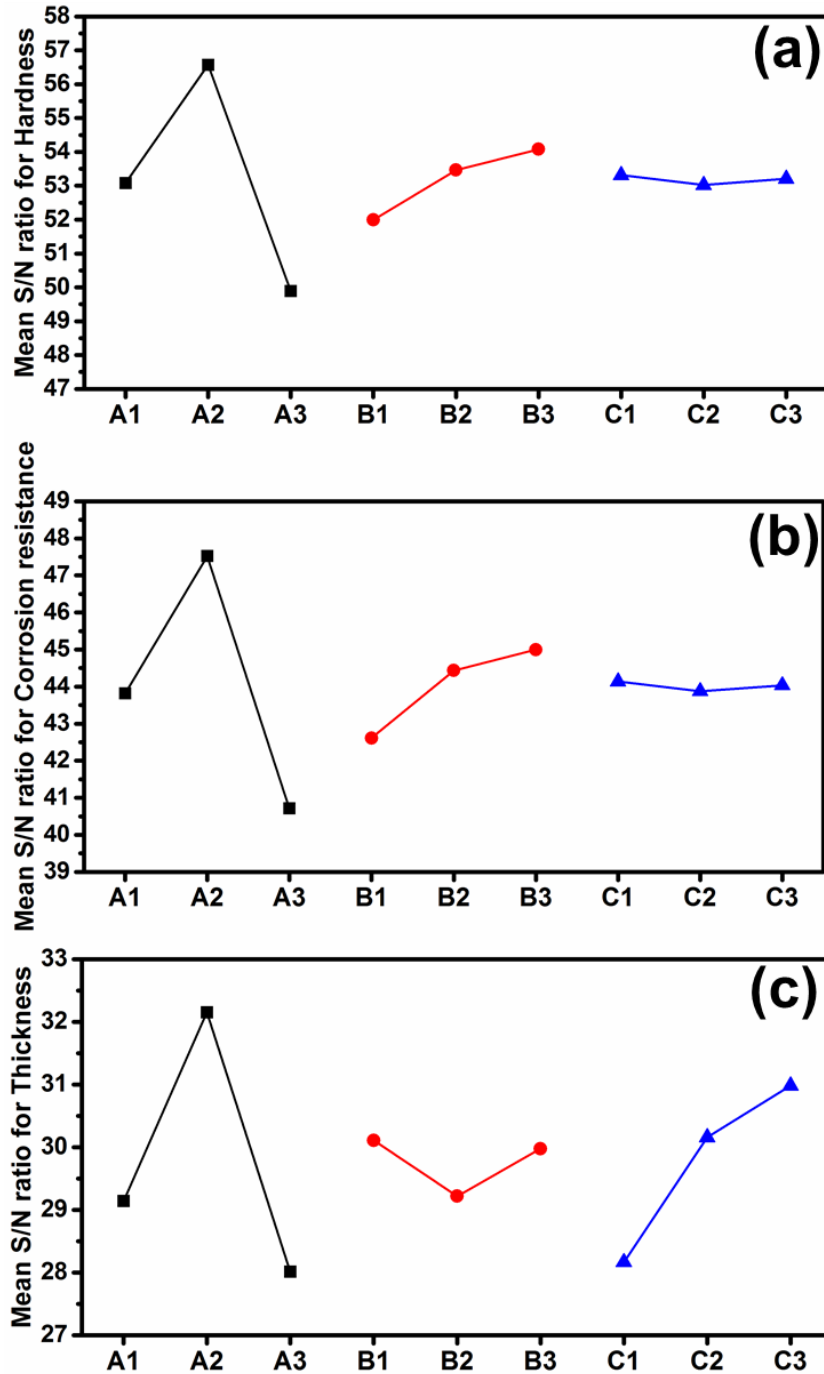


Figure 3-1 S/N ratio graphs for (a) average hardness, (b) polarization resistance, and (c) average thickness.

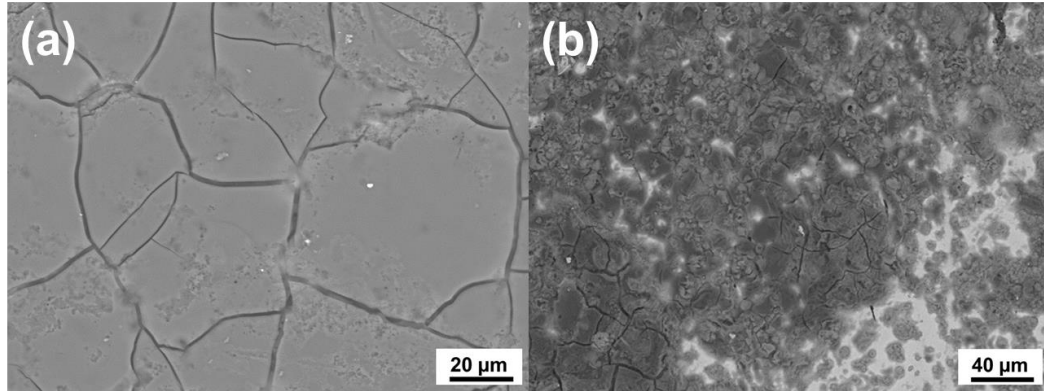


Figure 3-2 Surface morphology of the passive layer formed in electrolyte containing (a) 20 g/L, (b) 40 g/L NaAlO_2 . The concentration of Na_3PO_4 was fixed at 5 g/L.

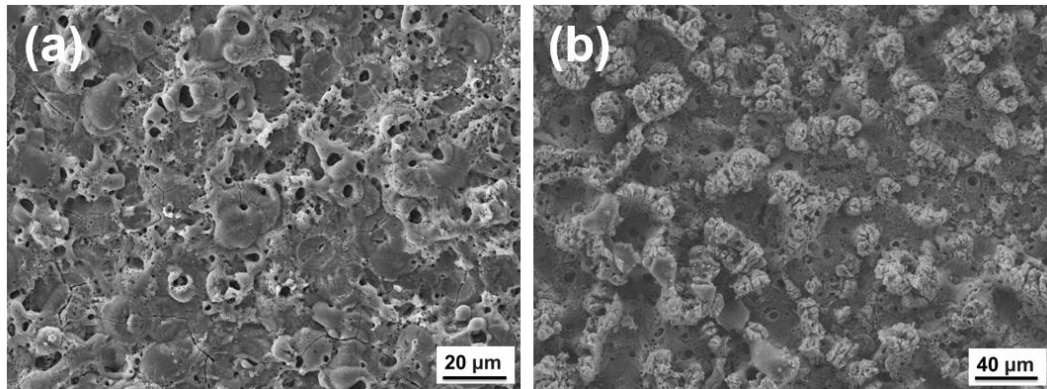


Figure 3-3 Surface morphology of the coatings formed in electrolyte containing (a) 20 g/L, (b) 40 g/L NaAlO_2 . The concentration of Na_3PO_4 was fixed at 5 g/L.

The contribution of each factor to the coating's properties was determined by performing analysis of variance based on Eqs. (6) - (10). The results of analysis of variance (ANOVA) for each response are summarized in Tables 3-5, 3-6 and 3-7.

Table 3-5 Results of the ANOVA for average hardness.

Factors	Degree of freedom (D)	Sum of squares (SS _p)	Variance (V)	Corrected sums of squares (SS _p ')	Contribution	Rank
<i>C</i> (g/L)	2	67.00	33.50	67.00	87.93%	1
<i>f</i> (Hz)	2	8.91	4.46	8.91	11.69%	2
<i>δ</i>	2	0.29	0.15	0.29	0.38%	3
error		0.00	0.00		0	
Total		76.20			100%	

Table 3-6 Results of the ANOVA for polarization resistance.

Factors	Degree of freedom (D)	Sum of squares (SS _p)	Variance (V)	Corrected sums of squares (SS _p ')	Contribution	Rank
<i>C</i> (g/L)	2	69.74	34.87	69.74	84.88%	1
<i>f</i> (Hz)	2	11.33	5.67	11.33	13.79%	2
<i>δ</i>	2	1.09	0.55	1.09	1.33%	3
error		0.00	0.00		0	
Total		82.16			100%	

Table 3-7 Results of the ANOVA for average thickness.

Factors	Degree of freedom (D)	Sum of squares (SS _p)	Variance (V)	Corrected sums of squares (SS _p ')	Contribution	Rank
<i>C</i> (g/L)	2	27.48	13.74	27.48	62.81%	1
<i>f</i> (Hz)	2	1.69	0.85	1.69	3.86%	3
<i>δ</i>	2	14.58	7.29	14.58	33.33%	2
error		0.00	0.00		0	
Total		43.75			100%	

Tables 3-5 and 3-6 list the contribution of the three factors on the average hardness and polarization resistance, respectively. It is clear that the concentration of NaAlO₂ has the

most significant contribution (87.93% for hardness and 84.88% for polarization resistance). The frequency also has some contribution (11.69% for hardness and 13.79% for polarization resistance). However, the duty cycle only has negligible contribution of less than 1%. Table 3-7 lists the contribution of the three factors on the average thickness. The contribution of the concentration of NaAlO_2 and the frequency decreased to 62.81% and 3.86%, respectively. On the other hand, the contribution of duty cycle increased to 33.33%. For pulsed DC power supply, while the frequency mainly controls the duration of a single pulse, the duty cycle mainly controls the total power input. The higher duty cycle, the higher power input. Therefore, the average thickness should strongly rely on the duty cycle and increase with increasing duty cycle.

Optimal parameters for mechanical and electrochemical properties

In order to optimize mechanical and electrochemical properties of the coating, the order of the performance characteristics is given as hardness ($w_1 = 0.5$) and polarization resistance ($w_2 = 0.5$), and thickness ($w_3 = 0$). With three combinations of weighting factors, the factor's mean multi-response S/N ratios for each level were summarized in Table 3-8, respectively. For instance, the mean S/N ratio (52.05) for C at level 2 in Table 3-8 with the weighting factors of $w_1 = 0.5$, $w_2 = 0.5$ and $w_3 = 0$ was the average value of the S/N ratios of experiment No.4 (50.28), No.5 (52.00) and No.6 (53.86) which were listed in Table 3-4. Figure 3-4 depicts the multi-response S/N ratios for the certain case of mechanical and electrochemical properties optimization. By selecting the highest value of the mean S/N ratio for each factor, the optimal levels were determined, which were A2B3C1, i.e. $C = 20$ g/L, $f = 1000$ Hz and $\delta = 0.2$.

Table 3-8 The Factor's Mean multi-response S/N ratio for each level.

Level	Mean S/N ratio for case: $w_1=0.5, w_2=0.5, w_3=0$		
	A (C)	B (f)	C (δ)
1	48.45	47.30	48.72
2	52.05	48.95	48.45
3	45.30	49.54	48.62

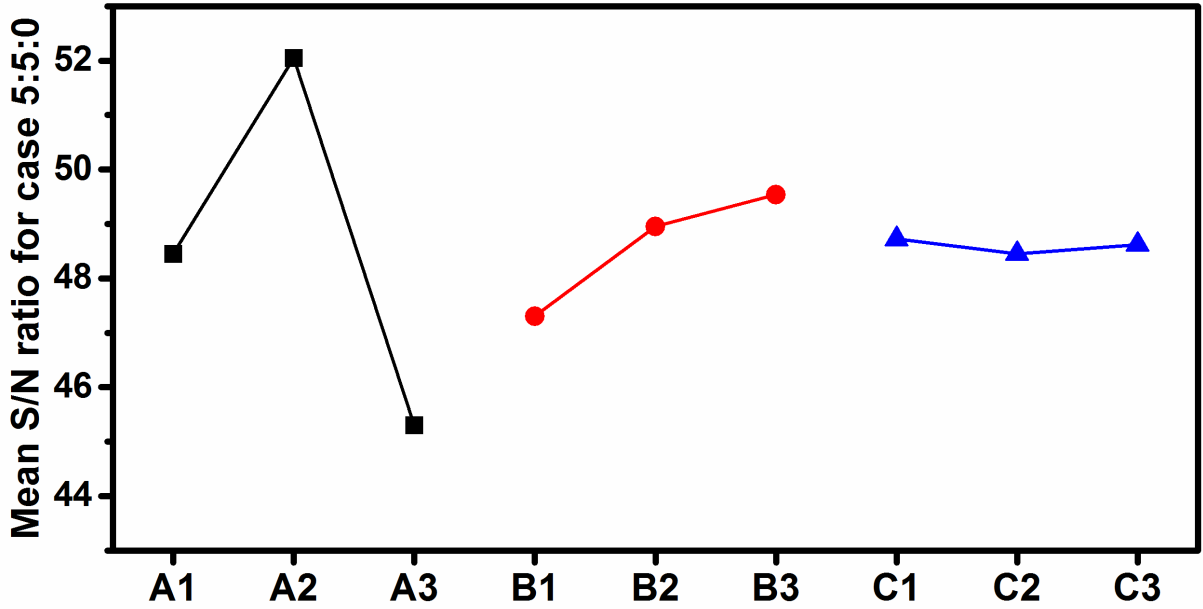


Figure 3-4 Multi-response S/N ratio graph for case: $w_1=0.5, w_2=0.5, w_3=0$.

Table 3-9 Results of ANOVA for the specific multi-response case: $w_1=0.5, w_2=0.5, w_3=0$.

Factors	Degree of freedom (D)	Sum of squares (SS_p)	Variance (V)	Corrected sums of squares (SS_p')	Contribution	Rank
C (g/L)	2	68.35	34.18	68.35	86.46%	1
f (Hz)	2	9.56	4.78	9.56	12.09%	2
δ	2	1.13	0.57	1.13	1.43%	3
error		0.00	0.00		0	
Total		79.05			100%	

The contribution of each factor to multiple response was determined by performing analysis of variance based on Eqs. (6) - (10). The results of analysis of variance (ANOVA) for this specific multi-response case ($w_1=0.5$, $w_2=0.5$, $w_3=0$) are summarized in Tables 3-9. Since we do not consider the average thickness, the results are similar with the results in Tables 3-5 and 3-6. The most influential factor is the concentration of NaAlO_2 , followed by the frequency. The duty cycle only has negligible contribution to the mechanical and electrochemical properties of the coating.

Confirmation experiment

To confirm the optimal parameter obtained from the DOE based on the Taguchi method, two individual experiments were conducted. As discussed above, the designed factors A2B3C1 were selected as the optimal combination for mechanical and electrochemical properties ($w_1=0.5$, $w_2=0.5$, $w_3=0$). The results from the confirmation experiment showed that the coating deposited under optimal parameters had an average hardness of 822 HV, polarization resistance of $296 \text{ k}\Omega\cdot\text{cm}^2$ and thickness of $35 \mu\text{m}$. Using Eqs. (1) to (5), the S/N ratio of multi-response of the optimized coating was calculated as 53.86 and listed in Table 3-10.

Table 3-10 The S/N ratio of objectives and multi-response S/N ratio of confirmation experiments.

Experiment	S/N ratio (average hardness)	S/N ratio (polarization resistance)	S/N ratio (average thickness)	Multi-response S/N ratio ($w_1=0.5$, $w_2=0.5$, $w_3=0$)
Confirmation	58.29	49.42	30.87	53.86

3.4 Conclusions

Plasma electrolytic aluminating (PEA) process was successfully applied on the cast iron with a medium voltage (500 V) in solution containing concentrated NaAlO_2 and Na_3PO_4 . The NaAlO_2 is the precursor of the passive layer and the coating, which is indispensable. Na_3PO_4 could help to improve the coating's quality by acting as the buffer and complexing agent during the PEA process. Taguchi design of experiment was performed to study the influence of the concentration of NaAlO_2 in the electrolyte (C), the frequency (f) and duty cycle (δ) of the power supply, on the hardness, polarization resistance and thickness of the coating. If the concentration of NaAlO_2 is too high, the amount of phosphate ions in the electrolyte is not sufficient to stabilize the localized pH value near the anode surface or form the phosphate-aluminate complexes. The uncontrolled rapid precipitation of aluminum hydroxide could lead to loosely stacked particles with gas bubbles trapped inside the coating. If the concentration of NaAlO_2 is too low, no plasma discharge was observed. For pulsed DC power supply, while the frequency mainly controls the duration of a single pulse, the duty cycle mainly controls the total power input. The shorter single duration, the lower porosity. The higher duty cycle, the higher power input. Therefore, the average thickness strongly relies on the duty cycle and increase with increasing duty cycle, while the frequency has more significant influence on the coating's hardness and polarization resistance and the higher frequency led to the higher hardness and polarization resistance. The maximum multi-response S/N ratio (53.86) was achieved by confirm experiment with optimum level of A2B3C1 ($C = 20 \text{ g/L}$, $f = 1000 \text{ Hz}$ and $\delta = 0.2$), which had an average hardness of 822 HV, polarization resistance of $296 \text{ k}\Omega\cdot\text{cm}^2$ and thickness of $35 \text{ }\mu\text{m}$.

REFERENCES

- (1) Parfenov, E. V.; Mukaeva, V. R.; Farrakhov, R. G. Plasma Electrolytic Treatments for Advanced Surface Finishing Technologies. *Mater. Technol. Des.* **2019**, *1* (1), 34–41.
- (2) Belkin, P. N.; Kusmanov, S. A.; Parfenov, E. V. Mechanism and Technological Opportunity of Plasma Electrolytic Polishing of Metals and Alloys Surfaces. *Appl. Surf. Sci. Adv.* **2020**, *1*, 100016. <https://doi.org/10.1016/j.apsadv.2020.100016>.
- (3) Yerokhin, A. L.; Nie, X.; Leyland, A.; Matthews, A.; Dowey, S. J. Plasma Electrolysis for Surface Engineering. *Surf. Coatings Technol.* **1999**, *122* (2–3), 73–93. [https://doi.org/10.1016/S0257-8972\(99\)00441-7](https://doi.org/10.1016/S0257-8972(99)00441-7).
- (4) Clyne, T. W.; Troughton, S. C. A Review of Recent Work on Discharge Characteristics during Plasma Electrolytic Oxidation of Various Metals. *Int. Mater. Rev.* **2019**, *64* (3), 127–162. <https://doi.org/10.1080/09506608.2018.1466492>.
- (5) Yerokhin, A. L.; Shatrov, A.; Samsonov, V.; Shashkov, P.; Pilkington, A.; Leyland, A.; Matthews, A. Oxide Ceramic Coatings on Aluminium Alloys Produced by a Pulsed Bipolar Plasma Electrolytic Oxidation Process. *Surf. Coatings Technol.* **2005**, *199* (2-3), 150–157. <https://doi.org/10.1016/j.surfcoat.2004.10.147>.
- (6) Matykina, E.; Arrabal, R.; Skeldon, P.; Thompson, G. E. Investigation of the Growth Processes of Coatings Formed by AC Plasma Electrolytic Oxidation of Aluminium. *Electrochim. Acta* **2009**, *54* (27), 6767–6778. <https://doi.org/10.1016/j.electacta.2009.06.088>.
- (7) Yerokhin, A. L.; Snizhko, L. O.; Gurevina, N. L.; Leyland, A.; Pilkington, A.; Matthews, A. Discharge Characterization in Plasma Electrolytic Oxidation of Aluminium.

- J. Phys. D. Appl. Phys.* **2003**, *36* (17), 2110–2120. <https://doi.org/10.1088/0022-3727/36/17/314>.
- (8) Yerokhin, A. L.; Lyubimov, V. V.; Ashitkov, R. V. Phase Formation in Ceramic Coatings during Plasma Electrolytic Oxidation of Aluminium Alloys. *Ceram. Int.* **1998**, *24* (1), 1–6. [https://doi.org/10.1016/S0272-8842\(96\)00067-3](https://doi.org/10.1016/S0272-8842(96)00067-3).
- (9) Arrabal, R.; Matykina, E.; Viejo, F.; Skeldon, P.; Thompson, G. E.; Merino, M. C. AC Plasma Electrolytic Oxidation of Magnesium with Zirconia Nanoparticles. *Appl. Surf. Sci.* **2008**, *254* (21), 6937–6942. <https://doi.org/10.1016/j.apsusc.2008.04.100>.
- (10) Bala Srinivasan, P.; Liang, J.; Blawert, C.; Störmer, M.; Dietzel, W. Effect of Current Density on the Microstructure and Corrosion Behaviour of Plasma Electrolytic Oxidation Treated AM50 Magnesium Alloy. *Appl. Surf. Sci.* **2009**, *255* (7), 4212–4218. <https://doi.org/10.1016/j.apsusc.2008.11.008>.
- (11) Liang, J.; Srinivasan, P. B.; Blawert, C.; Störmer, M.; Dietzel, W. Electrochemical Corrosion Behaviour of Plasma Electrolytic Oxidation Coatings on AM50 Magnesium Alloy Formed in Silicate and Phosphate Based Electrolytes. *Electrochim. Acta* **2009**, *54* (14), 3842–3850. <https://doi.org/10.1016/j.electacta.2009.02.004>.
- (12) Duan, H.; Yan, C.; Wang, F. Growth Process of Plasma Electrolytic Oxidation Films Formed on Magnesium Alloy AZ91D in Silicate Solution. *Electrochim. Acta* **2007**, *52* (15), 5002–5009. <https://doi.org/10.1016/j.electacta.2007.02.021>.
- (13) Yerokhin, A. L.; Nie, X.; Leyland, A.; Matthews, A. Characterisation of Oxide Films Produced by Plasma Electrolytic Oxidation of a Ti-6Al-4V Alloy. *Surf. Coatings Technol.* **2000**, *130* (2–3), 195–206. [https://doi.org/10.1016/S0257-8972\(00\)00719-2](https://doi.org/10.1016/S0257-8972(00)00719-2).

- (14) Shokouhfar, M.; Dehghanian, C.; Montazeri, M.; Baradaran, A. Preparation of Ceramic Coating on Ti Substrate by Plasma Electrolytic Oxidation in Different Electrolytes and Evaluation of Its Corrosion Resistance: Part II. *Appl. Surf. Sci.* **2012**, *258* (7), 2416–2423. <https://doi.org/10.1016/j.apsusc.2011.10.064>.
- (15) Teh, T. H.; Berkani, A.; Mato, S.; Skeldon, P.; Thompson, G. E.; Habazaki, H.; Shimizu, K. Initial Stages of Plasma Electrolytic Oxidation of Titanium. *Corros. Sci.* **2003**, *45* (12), 2757–2768. [https://doi.org/10.1016/S0010-938X\(03\)00101-X](https://doi.org/10.1016/S0010-938X(03)00101-X).
- (16) Matykina, E.; Berkani, A.; Skeldon, P.; Thompson, G. E. Real-Time Imaging of Coating Growth during Plasma Electrolytic Oxidation of Titanium. *Electrochim. Acta* **2007**, *53* (4), 1987–1994. <https://doi.org/10.1016/j.electacta.2007.08.074>.
- (17) Xue, W.; Zhu, Q.; Jin, Q.; Hua, M. Characterization of Ceramic Coatings Fabricated on Zirconium Alloy by Plasma Electrolytic Oxidation in Silicate Electrolyte. *Mater. Chem. Phys.* **2010**, *120* (2–3), 656–660. <https://doi.org/10.1016/j.matchemphys.2009.12.012>.
- (18) Matykina, E.; Arrabal, R.; Skeldon, P.; Thompson, G. E.; Wang, P.; Wood, P. Plasma Electrolytic Oxidation of a Zirconium Alloy under AC Conditions. *Surf. Coatings Technol.* **2010**, *204* (14), 2142–2151. <https://doi.org/10.1016/j.surfcoat.2009.11.042>.
- (19) Aktuğ, S. L.; Durdu, S.; Yalçın, E.; Çavuşoğlu, K.; Usta, M. Bioactivity and Biocompatibility of Hydroxyapatite-Based Bioceramic Coatings on Zirconium by Plasma Electrolytic Oxidation. *Mater. Sci. Eng. C* **2017**, *71*, 1020–1027. <https://doi.org/10.1016/j.msec.2016.11.012>.

- (20) Wang, L.; Hu, X.; Nie, X. Deposition and Properties of Zirconia Coatings on a Zirconium Alloy Produced by Pulsed DC Plasma Electrolytic Oxidation. *Surf. Coatings Technol.* **2013**, *221*, 150–157. <https://doi.org/10.1016/j.surfcoat.2013.01.040>.
- (21) Sowa, M.; Kazek-Kęsik, A.; Socha, R. P.; Dercz, G.; Michalska, J.; Simka, W. Modification of Tantalum Surface via Plasma Electrolytic Oxidation in Silicate Solutions. *Electrochim. Acta* **2013**, *114*, 627–636. <https://doi.org/10.1016/j.electacta.2013.10.047>.
- (22) Petković, M.; Stojadinović, S.; Vasilić, R.; Zeković, L. Characterization of Oxide Coatings Formed on Tantalum by Plasma Electrolytic Oxidation in 12-Tungstosilicic Acid. *Appl. Surf. Sci.* **2011**, *257* (24), 10590–10594. <https://doi.org/10.1016/j.apsusc.2011.07.055>.
- (23) Stojadinović, S.; Jovović, J.; Petković, M.; Vasilić, R.; Konjević, N. Spectroscopic and Real-Time Imaging Investigation of Tantalum Plasma Electrolytic Oxidation (PEO). *Surf. Coatings Technol.* **2011**, *205* (23–24), 5406–5413. <https://doi.org/10.1016/j.surfcoat.2011.06.013>.
- (24) Huang, H. L.; Tsai, M. T.; Lin, Y. J.; Chang, Y. Y. Antibacterial and Biological Characteristics of Tantalum Oxide Coated Titanium Pretreated by Plasma Electrolytic Oxidation. *Thin Solid Films* **2019**, *688*. <https://doi.org/10.1016/j.tsf.2019.04.043>.
- (25) Wang, Y.; Jiang, Z.; Yao, Z.; Tang, H. Microstructure and Corrosion Resistance of Ceramic Coating on Carbon Steel Prepared by Plasma Electrolytic Oxidation. *Surf. Coatings Technol.* **2010**, *204* (11), 1685–1688. <https://doi.org/10.1016/j.surfcoat.2009.10.023>.

- (26) Wang, Y.; Jiang, Z.; Yao, Z. Preparation and Properties of Ceramic Coating on Q235 Carbon Steel by Plasma Electrolytic Oxidation. *Curr. Appl. Phys.* **2009**, *9* (5), 1067–1071. <https://doi.org/10.1016/j.cap.2008.12.004>.
- (27) Yang, W.; Li, Q.; Liu, W.; Liang, J.; Peng, Z.; Liu, B. Characterization and Properties of Plasma Electrolytic Oxidation Coating on Low Carbon Steel Fabricated from Aluminate Electrolyte. *Vacuum* **2017**, *144*, 207–216. <https://doi.org/10.1016/j.vacuum.2017.08.003>.
- (28) Li, Z.; Cheng, Y.; Kang, S. hang; Tu, W.; Cheng, Y. A Re-Understanding of the Breakdown Theory from the Study of the Plasma Electrolytic Oxidation of a Carbon Steel — A Non-Valve Metal. *Electrochim. Acta* **2018**, *284*, 681–695. <https://doi.org/10.1016/j.electacta.2018.07.201>.
- (29) Taguchi, G.; Phadke, M. S. Quality Engineering Through Design Optimization. In *Quality Control, Robust Design, and the Taguchi Method*; Springer US: Boston, MA, 1984; pp 1106–1113. https://doi.org/10.1007/978-1-4684-1472-1_5.
- (30) Sun, Z.; Hu, H.; Chen, X. Numerical Optimization of Gating System Parameters for a Magnesium Alloy Casting with Multiple Performance Characteristics. *J. Mater. Process. Technol.* **2008**, *199* (1), 256–264. <https://doi.org/10.1016/j.jmatprotec.2007.08.036>.
- (31) Souissi, N.; Souissi, S.; Lecompte, J. P.; Amar, M. Ben; Bradai, C.; Halouani, F. Improvement of Ductility for Squeeze Cast 2017 A Wrought Aluminum Alloy Using the Taguchi Method. *Int. J. Adv. Manuf. Technol.* **2015**, *78* (9–12), 2069–2077. <https://doi.org/10.1007/s00170-015-6792-0>.

- (32) Balaram Naik, A.; Chennakeshava Reddy, A. Optimization of Tensile Strength in TIG Welding Using the Taguchi Method and Analysis of Variance (ANOVA). *Therm. Sci. Eng. Prog.* **2018**, *8*, 327–339. <https://doi.org/10.1016/j.tsep.2018.08.005>.
- (33) Karpushenkov, S.A.; Shchukin, G.L.; Belanovich, A.L., Savenko, V.P.; and Kulak, A.I. Plasma Electrolytic Ceramic-like Aluminum Oxide Coatings on Iron. *J. Appl. Electrochem.* **2010**, *40*, 365-374. <https://doi.org/10.1007/s10800-009-0005-1>.

4. CHAPTER 4 A New Eco-friendly Anti-Corrosion Strategy for Ferrous Metals: Plasma Electrolytic Aluminating

4.1 Introduction

Ferrous metals, including cast irons, mild steels and other iron-based alloys, have been widely used nowadays. However, ferrous metals are vulnerable to corrosion. The global cost of corrosion was reported to be \$2.5 trillion in 2013, which accounted for 3.4% of the global GDP.¹ The fact that corrosion control can be profitable has been realized repeatedly by industry where severe business interruption always happens due to failures of equipment and assets. Traditional anti-corrosion strategies for ferrous metals include the phosphating and zinc plating. The phosphating serves as a conversion coating process in which a dilute solution of phosphoric acid and phosphate salts chemically react with the surface of the part being coated to form a layer of insoluble, crystalline phosphates.² There are several drawbacks of the phosphating process. On one hand, the reaction generates tiny hydrogen gas bubbles, which adhere to the surface of the metal. These bubbles prevent the acid from reaching the metal surface and slow down the reaction. Therefore, sodium nitrite, which is toxic for humans, is frequently added to act as an oxidizing agent that reacts with the hydrogen.^{3,4} On the other hand, the wastewater with high concentration of PO_4^{3-} and NO_3^- could lead to harmful algal blooms, like the green or red tides, in eco-systems.⁵ The post-treatment of the phosphating process like organic painting is desired to enhance the corrosion resistance.^{6,7} However, it sacrifices the surface hardness and wear resistance. Thus, the lifespan of the protective layer decreases while the cost of maintenance during the service increases. Zinc plating, also known as galvanization, is the process of applying a protective zinc coating to steel or iron.^{8,9} However, corrosion will be inevitable after the

steel is longtime exposed to the surrounding, especially to acidic environments.¹⁰ Marine and salty environments can also cause the increased degradation since the highly conductive sea water could accelerate the dissolution of zinc into soluble zinc chloride.¹¹ For instance, galvanized car frames corrode much faster in the regions where road deicing salt is used. Degradation of galvanized steel will release a large amount of zinc ions, which could be the source of zinc pollution.¹² The emission of zinc is now controlled through the Pollution Prevention and Control regulations (PPC) in UK and Council Directive 76/464/EEC in Europe. At an international level, release of zinc is controlled through the OSPAR convention on protection of the marine environment of the north-east Atlantic. Therefore, an eco-friendly anti-corrosion strategy for ferrous metals is desired to achieve sustainable development of the whole society. Plasma electrolytic oxidation (PEO) is considered as a green coating process and has been used for corrosion protection of aluminum (Al) and magnesium (Mg) alloys.¹³ However, PEO cannot be readily applied on the ferrous metals because the ferrous metals hardly form a good isolating passive film on their surfaces to provide a prerequisite condition for the dielectric plasma discharging mechanism of the PEO process, unlike the Al case.¹⁴ Hercynite (FeAl_2O_4) and alumina (Al_2O_3) are known to be chemically stable to both acids and bases, and nontoxic to humans or environments. If a hercynite-alumina composite coating can be prepared on ferrous metals, it would be much eco-friendlier than the Zn coating. Inspired by both the phosphating and PEO processes, we developed a plasma electrolytic aluminating (PEA) process to deposit a hercynite-alumina composite coating for anti-corrosion of ferrous metals. PEA is a coating process during which a composite ceramic coating (hercynite-alumina) is deposited on the surfaces of cast irons or steels with assistance of plasma

discharging in the aluminate-based solutions. It could be considered as a new route of plasma chemical reactions.¹³ This work also demonstrated that the hercynite-alumina composite coating would have high surface hardness, superior wear resistance and excellent corrosion resistance.

4.2 Experimental setup

Plasma electrolytic aluminating on grey cast iron: Set of grey cast iron samples (as examples of ferrous metals) with dimension 20*20*5 mm³ were polished with #1200 abrasive paper, rinsed with distilled water and ultrasonically cleaned in ethanol. The sample (anode) was immersed in electrolyte (15-20 g/L NaAlO₂ as a precursor and 1-5 g/L Na₃PO₄ as a buffer dissolved in deionized water, pH=12, Sigma Aldrich) in stainless steel vessel (cathode). A unipolar pulsed ($f = 1$ KHz) DC power supply was used. After 12 s of ramping, the voltage was kept at 480 V. After taking out from the electrolyte, all samples were dried at 60 °C.

Materials characterization: Phases and compositions of the coatings were determined by X-ray diffraction (XRD, PROTO AXRD) and X-ray photoelectron spectroscopy (XPS, Kratos Axis Nova). The microstructures of coatings were observed by scanning electron microscopy (SEM, FEI Quanta 200 FEG). The hardness of the coating and substrate was measured by Vickers hardness tester (Wilson VH1102).

Pin-on-disk sliding wear test: Regarding the wear performance, pin-on-disk sliding wear tests were conducted on the blank and PEA coated samples, respectively. Before the sliding tests, all samples were polished to $R_{pk}=0.22$ μm . The testing conditions were dry sliding; $F_n = 10$ N; sliding velocity = 0.05 m/s and sliding distance = 120 m. SAE 52100 hardened steel balls (5.5 mm diameter, HRC 62) were used as the counterpart pins.

Corrosion test: Potentiodynamic polarization tests were carried out from -1 V to 0.5 V with respect to the corrosion potential (E_{corr}) at a scan rate of 1 mV/s (BioLogic SP-150). Electrochemical impedance spectroscopy (EIS) in the frequency range between 10^5 and 10^3 Hz with ± 10 mV amplitude was also employed. All electrochemical tests were carried out in 3.5% NaCl solution, at room temperature. Ag/AgCl (KCl saturated) and Pt wire were selected as reference electrode and counter electrode, respectively. The working surface area for each specimen was chosen to be 0.5 cm^2 . All EIS data were analyzed using EC-Lab software.

4.3 Results and discussion

Figure 4-1 shows changes of the voltage and current density vs. time during the PEA process, from which the process could be divided into four stages: stage I (0-6 s), stage II (6-12 s), stage III (12-100 s) and stage IV (100-300 s). As mentioned before, the first two stages correspond to the ramping period of the DC power supplier. As illustrated in the inset of Figure 1b, the current density increased linearly during stage I, which implies the system obeyed the Ohm's law and Faraday's law of electrolysis. Then, the current density increased nonlinearly and slower during stage II, which implies the formation of isolating film and increasing of impedance. After the ramping period of the power supplier, the current density decreased quickly because the growth of the coating significantly increased the impedance during stage III.^{13, 15, 16} Finally, the current density reached to a plateau of 0.05 A/cm^2 during stage IV.

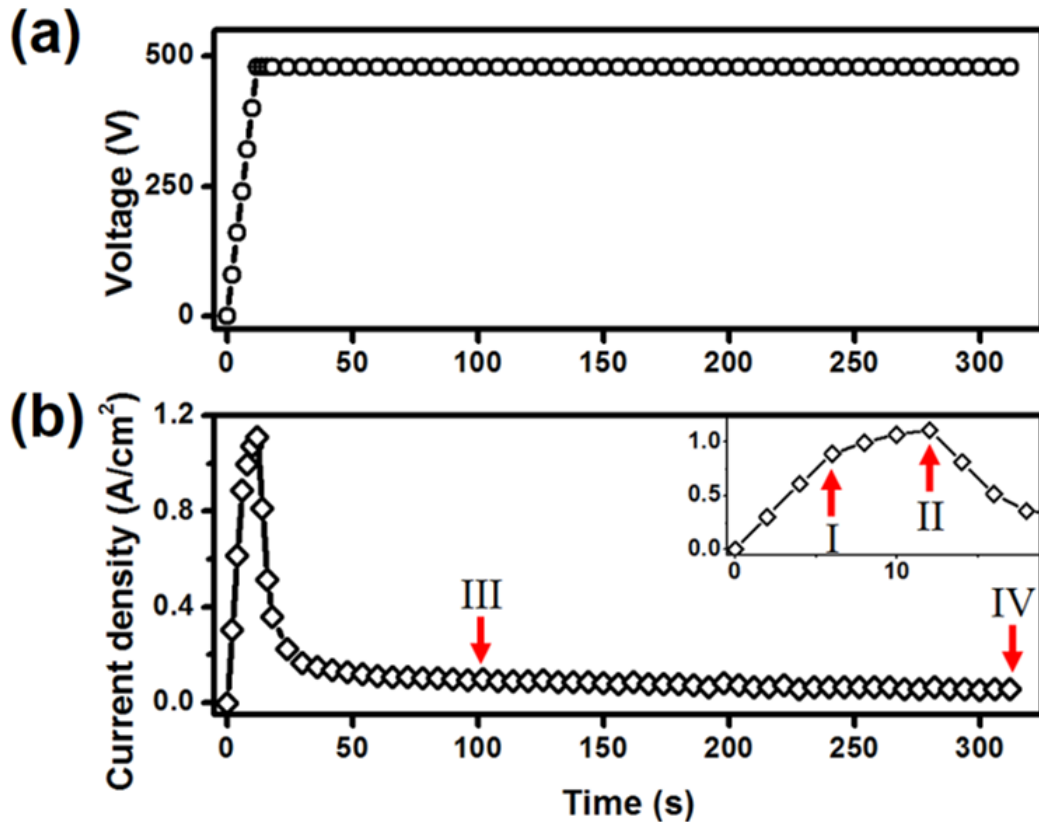


Figure 4-1 (a) Voltage and (b) current density vs. time curves during the PEA process.

Figure 4-2 presents SEM images of the samples treated for 6 s, 12 s, and 100 s, respectively. As shown in Figure 4-2a, the sample surface consists of numerous platelets of deposited materials at the end of stage I. EDS point analysis on these platelets demonstrates high contents of Fe, Al and O (Figure 4-2g), which indicates possible formation of hercynite ($FeAl_2O_4$). A few tiny pores could be observed on the sample (Figure 4-2d), which were footprints of the initiation of plasma discharge. However, the plasma discharge was too weak to be seen by naked eyes at this point. Then, numerous small plasma discharges started to spread out on the sample surface during stage II. These plasma discharges converted some platelets into coatings with dimpled structure (Figures 4-2b and 4-2e). EDS point analysis on the dimpled coatings illustrates reduced content of Fe (Figure 4-2h),

which might be due to the formation of alumina (Al_2O_3). A lot of gas bubbles were also generated on the surface. During stage III, the plasma discharges homogeneously distributed and the composite coating with dimples was deposited (Figures 4-2c and 4-2f).

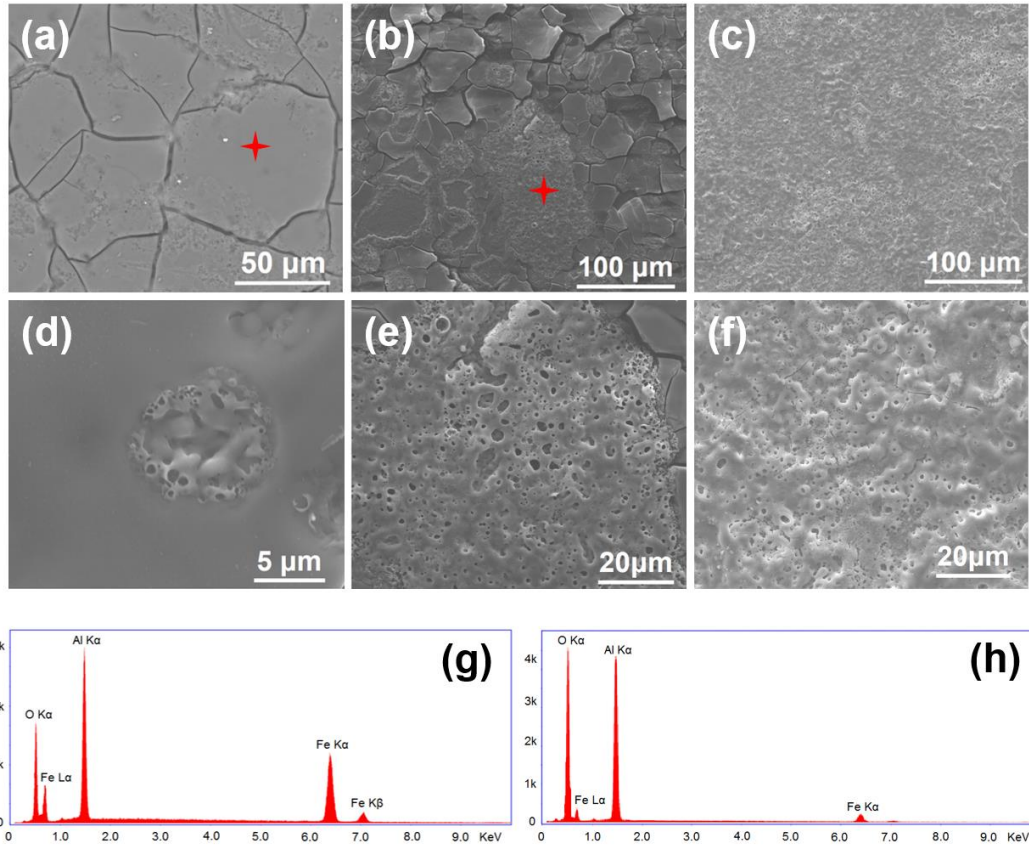


Figure 4-2 SEM images of the samples treated for (a, d) 6s, (b, e) 12s, (c, f) 100s, respectively; (g) and (h) EDS spectra from marked areas in (a) and (b), respectively.

The formation of FeAl_2O_4 during stage I was confirmed by XPS (Figure 4-3) and XRD (Figure 4-4). Fe 2p core level spectra could be deconvoluted into three peaks with the positions at 710.1, 713.8 and 723.7 eV. The first two peaks are corresponding to $\text{Fe}^{2+} 2p_{3/2}$ in FeAl_2O_4 ,^{17, 18} while the last peak is corresponding to $\text{Fe}^{2+} 2p_{1/2}$ in FeAl_2O_4 .¹⁹⁻²² Al 2p core level spectra only has one peak at 74.5 eV, which is consistent with the Al^{3+} in FeAl_2O_4 .^{17, 19} O 1s level spectra could be deconvoluted into three peaks with the positions

at 530.5, 531.9 and 532.8 eV, which represent the oxygen in Al_2O_3 , AlO_2^- and water, respectively.^{17, 23, 24} The small peak for Al_2O_3 indicates that the plasma ignited, and a small amount of alumina formed due to the high-temperature plasma discharge. As shown in Figure 4-4b, the XRD pattern of the 6s-treated sample has four peaks at 29.3° , 43.6° , 50.5° and 62.3° , which could be attributed to (220), (400), (331) and (440) planes of FeAl_2O_4 (JCPDS # 3-0894), respectively.^{25, 26} Three peaks at 44.8° , 65.2° and 82.5° are corresponding to the (110), (200) and (211) planes of iron (JCPDS # 65-4899), respectively.²⁷ The peaks of iron come from the substrate since the film was still very thin. It is noted that two small peaks of Al_2O_3 could also be found, which is consistent with the XPS study. Therefore, a thin film of FeAl_2O_4 was formed on the iron surface before the initiation of plasma. We have done several trials in electrolyte only containing NaAlO_2 and electrolyte only containing Na_3PO_4 , respectively. It turns out that ceramic coatings could be obtained in the electrolyte only containing NaAlO_2 , while no plasma discharge was observed in the electrolyte only containing Na_3PO_4 . We also tried to do PEA on the stainless steel. It turns out that FeAl_2O_4 did not form on the stainless-steel surface. It is well known that a compact and chemically stable Cr_2O_3 film existed on the surface of stainless steel, which prohibits the diffusion of oxygen. This Cr_2O_3 layer might also prohibit the dissolution of iron into the electrolyte and thus inhibits the formation of FeAl_2O_4 . The current density increased linearly during the 12 s of ramping and kept at 1.8 A/cm^2 constantly for stainless steel sample. No plasma discharging was observed, which means thin FeAl_2O_4 film was indispensable for ignition of dielectric plasma discharge and subsequent growth of hercynite-alumina composite coating.

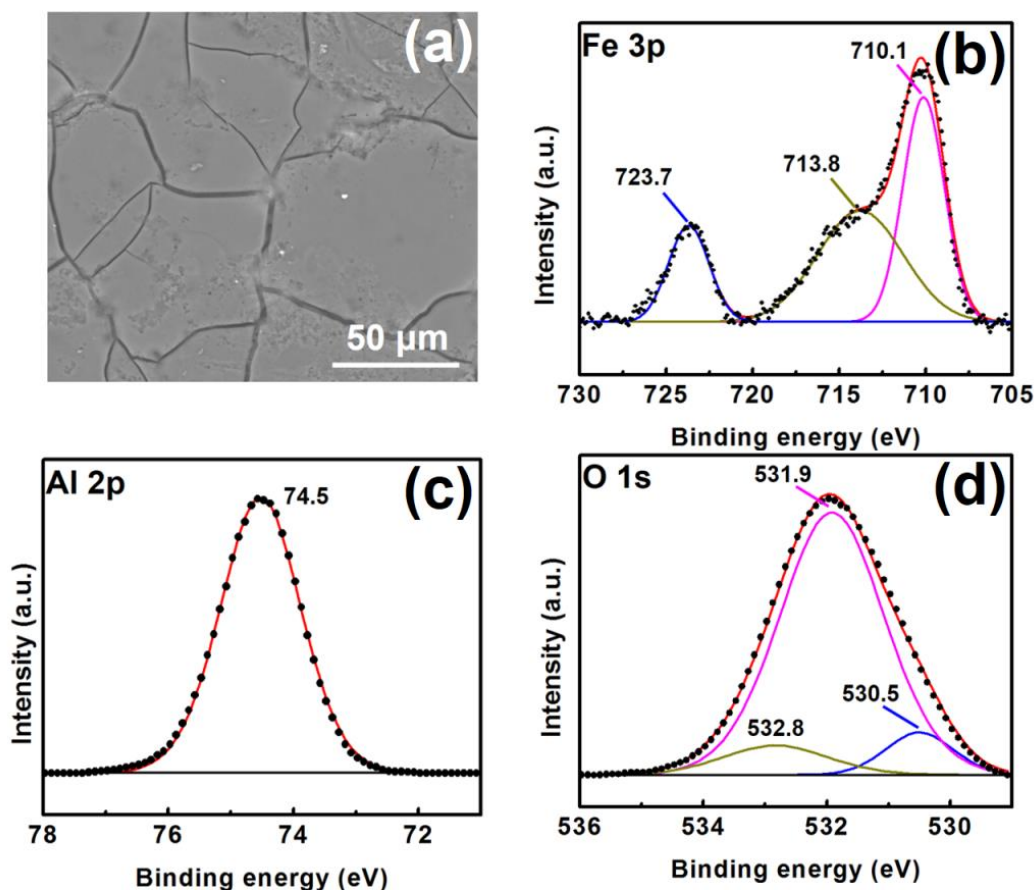
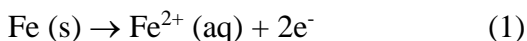


Figure 4-3 (a) SEM image of the sample treated for 6s; (b-d) high resolution spectra of Fe 2p, Al 2p and O 1s, respectively.

During stage I, the dissolution of iron into the electrolyte occurred:



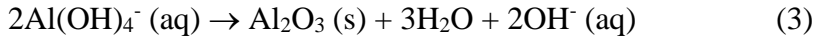
Meanwhile, the Al(OH)_4^- anions (AlO_2^- would exist as Al(OH)_4^- in basic aqueous solution) migrated towards the iron anode and combined with the Fe^{2+} cations to form FeAl_2O_4 :



When the sample was taken out from the electrolyte and dried in vacuum at 60 °C, the water in crystal structure evaporated and caused volume shrinkage of the film. Therefore, cracks formed as observed in Figure 4-2a. It is worthy to point out that the $\text{FeAl}_2\text{O}_4 \cdot 4\text{H}_2\text{O}$

film should be homogeneous when the sample was immersed in the electrolyte, otherwise the insulating property of the deposited layer will be hampered, and plasma discharge will not be built due to the leakage of current at the site of these cracks.²⁸

During stages II-IV, the Al(OH)_4^- anions absorbed on the surface were transformed into Al_2O_3 with the help of plasma discharge:



And the oxygen was released in the form of gas bubbles:

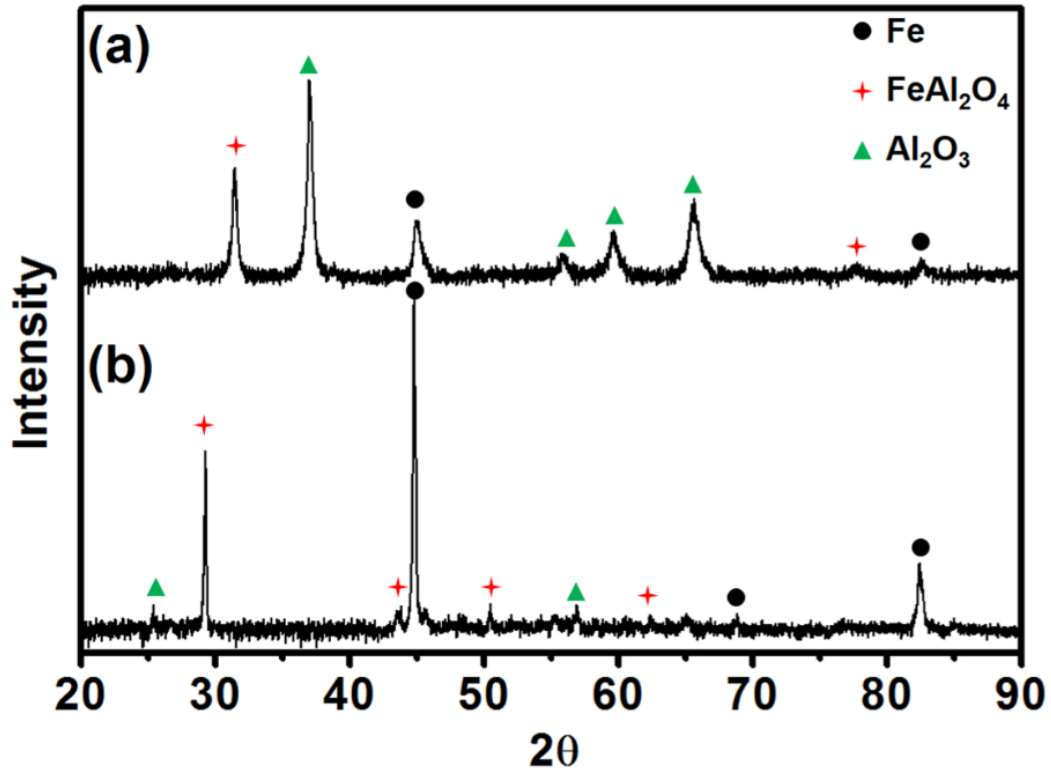
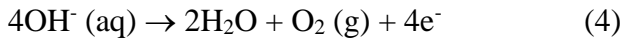


Figure 4-4 XRD patterns of samples treated with (a) 10 mins and (b) 6 s.

Meanwhile, iron from the substrate might be melted by the occasional strong plasma discharges (stages III and IV) and spitted out to the surface along the discharge channel,¹⁶ which could be the iron source of FeAl_2O_4 . Sintered by high-temperature plasma discharge,

the hercynite-alumina composite coating formed, as confirmed by the XRD (Figure 4-4a). The peaks at 31.3° and 77.8° represent the (220) and (533) planes of FeAl_2O_4 (JCPDS # 3-0894).^{25,26} Compared to standard pattern, these peaks shift rightwards by 2° , which implies smaller crystalline lattice constant. The smaller lattice constant might be explained by the compressive residual stress in the composite coating.²⁹

Based on above analysis, the mechanism of PEA was proposed. As shown in Figure 4-5a, $\text{Al}(\text{OH})_4^-$ anions homogeneously distributed in the electrolyte before applying current. When the anodic current was applied, the iron dissolved into the electrolyte as Fe^{2+} cations. Meanwhile, the $\text{Al}(\text{OH})_4^-$ anions migrated towards the anode surface and combined with Fe^{2+} cations to form the hercynite (FeAl_2O_4) film on the iron surface, as demonstrated in Figure 4-5b. When a continuous hercynite film fully covered the surface, initiation of plasma occurred (Figure 4-5c). The $\text{Al}(\text{OH})_4^-$ anions continuously migrated towards the anode and absorbed on the hercynite film. These $\text{Al}(\text{OH})_4^-$ anions were transformed into Al_2O_3 and then sintered with FeAl_2O_4 by the high-temperature plasma.³⁰ Oxygen was also released in the form of gas bubbles during this process. As illustrated in Figure 4-5d, iron from the substrate might be melted by the strong plasma discharging and spitted out to the surface along the discharge channel. These melted irons could be the iron source for the growth of hercynite-alumina composite ceramic coating.

Two more trials were carried with the solution solely containing NaAlO_2 and solution solely containing Na_3PO_4 , respectively. It turns out that ceramic coatings could be obtained in the electrolyte only containing NaAlO_2 , but the coating surface was very rough and inhomogeneous. Meanwhile, no plasma discharge was observed in the electrolyte only containing Na_3PO_4 , no coating was formed either. Therefore, NaAlO_2 is indispensable for

the deposition of the ceramic coating while Na_3PO_4 could improve the quality of the coating. As discussed on Chapter 3, the Na_3PO_4 might act as the buffer and the complexing agent during the PEA process, which prompt the uniform deposition of the passive layer and the coating.

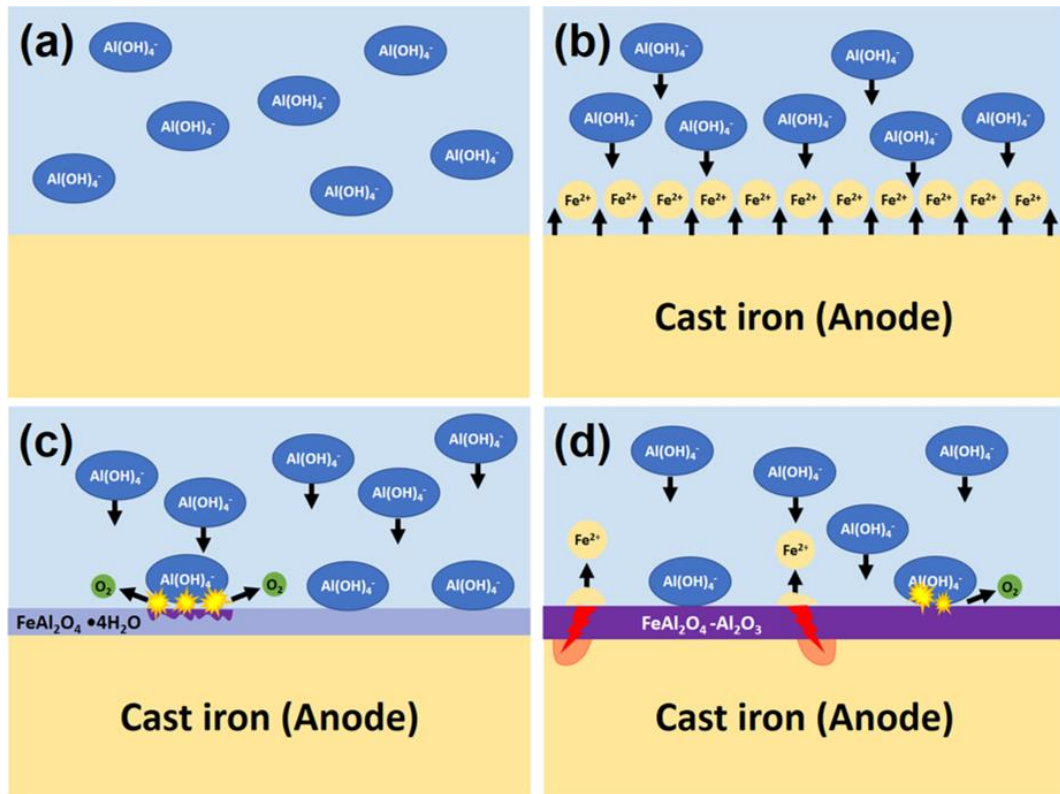


Figure 4-5 Schematic illustration of the PEA of cast iron. (a) The system before applying current, (b) dissolution of iron into the electrolyte and migration of Al(OH)_4^- anions towards the anode after applying current, (c) formation of hercynite film on the iron surface and the initiation of plasma discharge sparks, (d) growth of the hercynite-alumina composite ceramic coating via strong plasma discharge.

The SEM image and hardness profile of the sample treated by PEA for 10 minutes are shown in Figures 4-6a and 4-6b. The hardness of the composite coating was 2-3 times higher than that of the substrate, which should provide better surface protection from wear

damage. The surface morphologies of the blank sample and the PEA coated sample after the sliding wear tests are demonstrated in Figures 4-6c and 4-6d. The blank sample exhibited severe plastic deformation. In addition, deep ploughing and scratch tracks could be found as well. On the contrary, although materials transfer occurred, the PEA composite coating did not show any obvious wear scars or any chipping or peeling. The composite coating demonstrated superior wear resistance compared with cast iron.

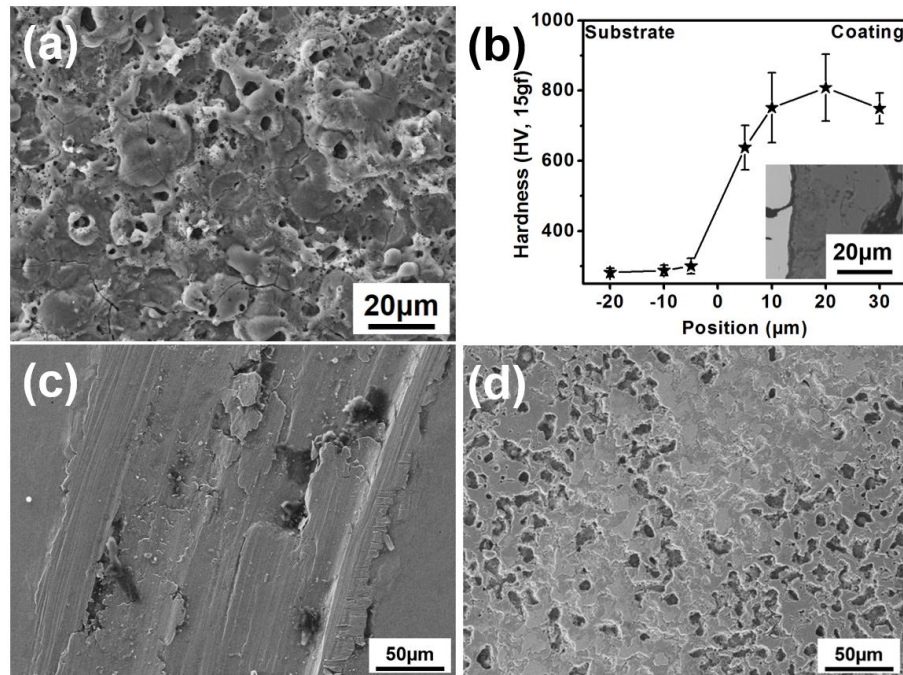


Figure 4-6 (a) SEM image and (b) hardness profile of the sample after 10 mins of PEA treatment, inset is the cross-sectional SEM image; SEM images showing wear tracks of (c) the uncoated blank sample and (d) PEA coated sample after the sliding tests.

The surface profiles of the as polished (before the sliding test) PEA coated sample and PEA coated sample after the sliding test are shown in Figure 4-7, as well as the blank sample after the sliding test. These surface profiles further verified that although materials transfer occurred on the coating surface during the sliding test, the coating itself was barely worn.

The pin-on-disk wear tests demonstrated the hercynite-alumina composite coating formed during the PEA process has a superior wear resistance.

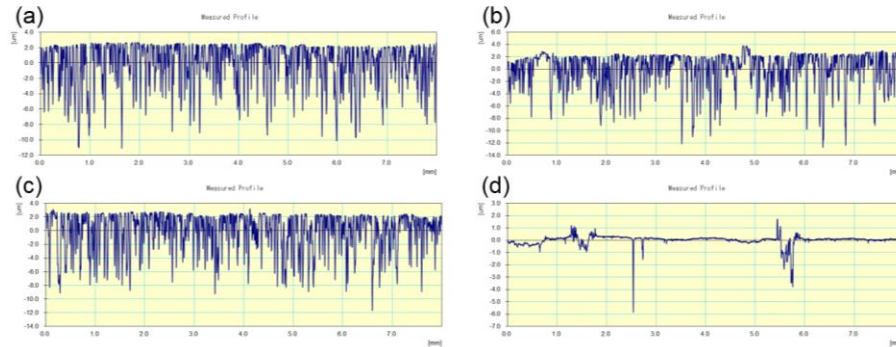


Figure 4-7 (a) PEA coated sample after polishing to $R_{pk}=0.22\mu\text{m}$; (b) PEA coated sample after the sliding test; (c) ultra-sonic cleaning to remove wear debris/materials transfer in (b); (d) uncoated blank sample after the sliding test.

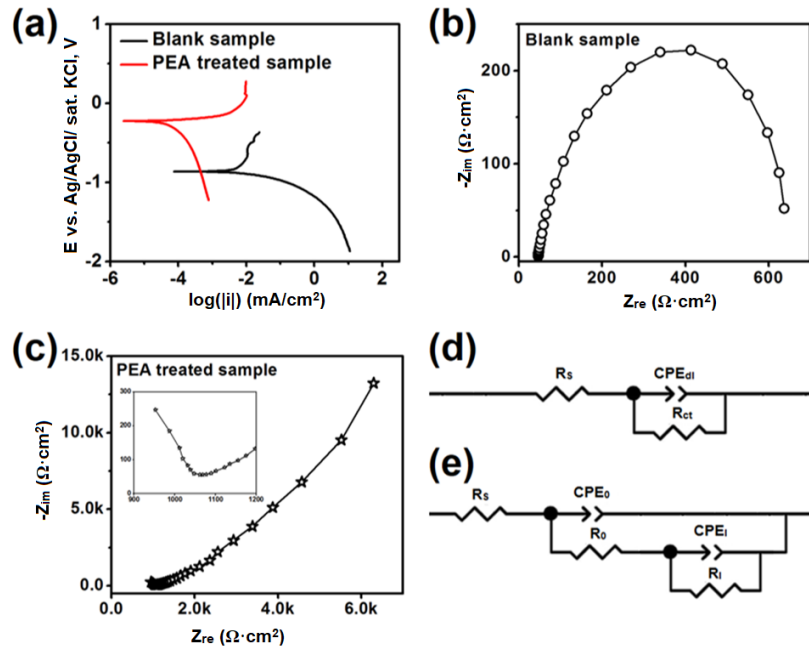


Figure 4-8 (a) Tafel curves of the PEA treated and blank samples; (b-c) Nyquist impedance plots, (d-e) and corresponding equivalent circuits of the blank and PEA treated samples, respectively.

The results of electrochemical corrosion tests on both the PEA treated and blank samples are presented in Figure 4-8. As shown in Figure 4-8a, the hercynite-alumina composite coating shifts the surface potential and reduces the charge-carrier mobility at the metal-electrolyte interface which in turn protects substrate from corrosion damage.³¹ From the Tafel curves, the corrosion potential (E_{corr}), corrosion current density (i_{corr}), cathodic and anodic Tafel constants (β_c and β_a) could be obtained. The results are summarized in Table 4-1. Polarization resistances (R_p) were determined with Stern-Geary equation:³²

$$R_p = \frac{\beta_a \times \beta_c}{2.303 \times (\beta_a + \beta_c) \times i_{corr}} \quad (\text{Eq. 1})$$

We might get two obvious information. Firstly, the corrosion potential of the PEA treated sample was higher than the blank sample, indicating a decrease in thermodynamic tendency for corrosion to take place.³¹ Secondly, the corrosion current density decreased after the PEA treatment. This indicates that the corrosion was restrained by hercynite-alumina composite coating. The corrosion current density tested by the Tafel method is 3×10^{-6} A/cm² for zinc coating³³ and $\sim 10^{-6}$ A/cm² for Zn alloy coating (Figure 4-9), which is two orders higher than the corrosion current of the PEA composite coating. The polarization tests on the PEA treated samples were carried out at 25°C, 40°C, 55°C and 70°C, respectively. There was no significant difference found, as demonstrated in Figure 4-10. These results indicate that the PEA composite could functionalize well under the tested elevated temperatures.

Table 4-1 Kinetic parameters obtained from the polarization curves.

Sample	E_{corr} (V)	i_{corr} (A/cm ²)	β_c (V/dec)	β_a (V/dec)	R_p ($\Omega \cdot \text{cm}^2$)
PEA treated	-0.22	3.5E-8	0.290	0.026	3.0E5
Blank	-0.88	4.5E-6	0.037	0.527	3.3E3

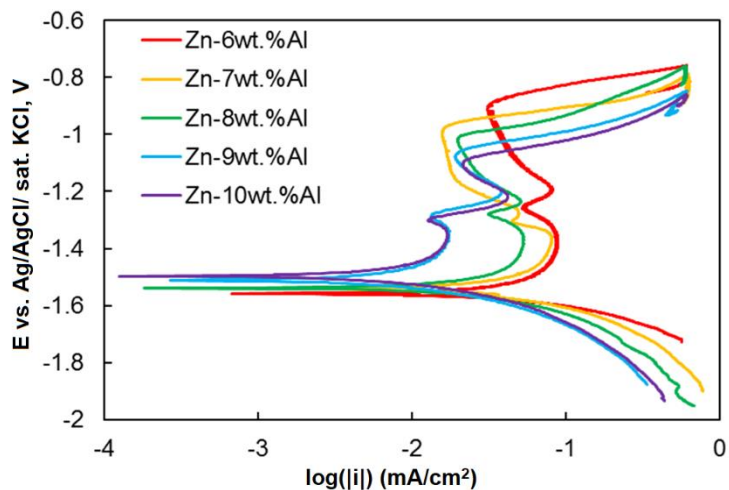


Figure 4-9 Tafel plots of various Zn alloy coated samples in a 3.5% NaCl solution at a room temperature.

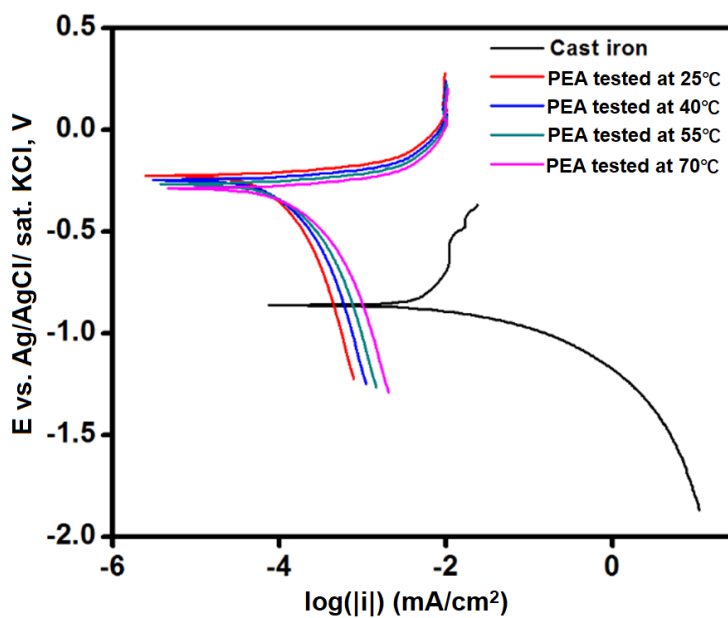


Figure 4-10 Tafel plots of the PEA coated samples test at 25°C, 40°C, 55°C and 70°C, respectively.

The impedance plot of blank sample (Figure 4-8b) shows a single loop attributed to electrical double layer of the grey cast iron surface. Therefore, the equivalent circuit

(Figure 4-8d) shows a double-layer capacitance in parallel to the charge transfer resistance and in series with the solution resistance.³¹ EIS Nyquist plot of the PEA treated sample has two loops, one at high frequency domain and one at low frequency domain (Figure 4-8c). Noticing the surface inhomogeneity factor, the constant phase element (CPE), instead of pure capacitive elements, was employed to simulate the low frequency tail of the diffusive response. The impedance is expressed by the following equation:

$$Z_{CPE} = 1/[T(j\omega)^P] \quad (\text{Eq. 2})$$

where j is the imaginary unit, ω is the angular frequency defined as $\omega = 2\pi f$, f is the frequency in Hz, T is CPE constant; the value of P varies between 0 and 1. The values 0 and 1 of P imply the CPE of the circuit to be pure resistor and ideal capacitor, respectively.³⁴ The proposed electrical equivalent circuit (Figure 4-8e) with two constant phase elements achieved acceptable fitness of the data. These constant phase elements represented in the equivalent circuit correspond to the composite coating with an outer porous layer and an inner compact layer.^{13, 15, 16, 31} The porous layer was formed due to the plasma discharge and gas mass spitting out.^{13, 16}

The parameters of the equivalent circuits fitted from the EIS spectra were summarized in Table 4-2. R_s represents the resistance of the solution. C_{dl} and R_{ct} represent the double layer capacitor and charge transfer resistance at the iron-electrolyte interface, respectively. R_0 and CPE_0 are the charge transfer resistance and double layer constant phase element at the coating-electrolyte interface, respectively. R_1 and CPE_1 are the resistance and the constant phase element of the ceramic coating, respectively. As shown in the Table, the charge transfer resistance at the coating-electrolyte interface (R_0) is much smaller than the

resistance of the ceramic coating (R_1). Therefore, the overall corrosion resistance of the composite coating depends on R_1 .

Table 4-2 Fitted data from the equivalent circuits.

Sample	R_s $\Omega \cdot \text{cm}^2$	C_{dl} mF	R_{ct} $\Omega \cdot \text{cm}^2$	R_0 $\Omega \cdot \text{cm}^2$	CPE_{0-P}	CPE_{0-T}	R_1 $\Omega \cdot \text{cm}^2$	CPE_{1-P}	CPE_{1-T}
PEA	62.8	-	-	978.3	0.71	2.0E-4	1.0E6	0.64	6.2E-5
Blank	60.7	0.24	543.2	-	-	-	-	-	-

To show applicability of PEA on steels, PEA treatments were conducted on low-carbon steel foils (25 μm in thickness) and 1095 spring steel foils (50 μm in thickness). The coated areas on the steel foils were also 20*20mm² to fit the size of a mask which allowed only one side of the foil to be exposed to the electrolyte. As demonstrated in Figure 4-11, uniform hercynite-alumina composite coatings with high flexibility and excellent adhesion were successfully deposited on the steel foils by the PEA process. It has been proved that the PEA process is widely applicable on ferrous metals.

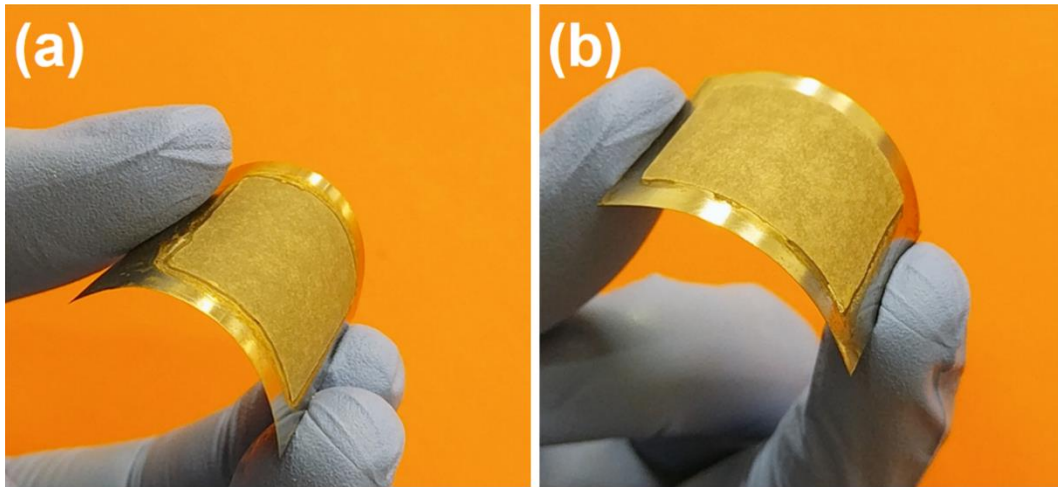


Figure 4-11 Flexible hercynite-alumina composite coating deposited on (a) low-carbon-steel foil and (b) 1095 spring steel (high-carbon-steel) foil.

Traditional phosphating and zinc plating processes require complex pre-treatments like the rising and surface activation. On the contrary, the PEA process could get rid of such pre-treatments because the high energy plasma discharge could spontaneously clean and activate the surface during the process. Moreover, the solution used for PEA process only contains 15-20 g/l sodium aluminate and 0-5 g/l sodium phosphate as a buffer. The solution used for the PEA process is free of additives (PO_4^{3-} , NO_2^- , NO_3^- , Zn^{2+} , Cr^{6+} , etc.). Therefore, the PEA process is simpler and eco-friendlier in terms of both sample and solution preparations. Furthermore, the high hardness and excellent corrosion resistance of the hercynite-alumina composite coating could provide the ferrous metals with long-term protection against wear-corrosion damage. Thus, the cost of maintenance and replacement of equipment or structures made of ferrous metals could be significantly reduced.

4.4 Conclusions

In this research, a new method named as plasma electrolytic aluminating (PEA) was developed and applied on grey cast iron as an example for ferrous metals. The XPS and XRD study show that the hercynite film formed on the sample surface was indispensable for the plasma ignition and subsequent coating growth. Only when a continuous hercynite film formed on the iron surface, acting as an isolating passive layer, could the stable plasma discharge build around the sample. During the PEA process, both the hercynite and alumina were synthesized and sintered together by the plasma discharge. Therefore, a hercynite-alumina composite coating with high hardness was deposited on the grey cast iron samples after PEA treatment. The coating could sufficiently protect the sample from wear damage. Potentiodynamic polarization tests show that the PEA treated sample had a more noble corrosion potential with a lower corrosion current density than the blank sample. The

polarization resistance of the PEA treated sample was 2 orders higher than that of the blank sample. EIS study indicates the overall corrosion resistance of the composite coating depended on the inner compact layer, and a resistance of $10^6 \Omega \cdot \text{cm}^2$ was obtained. The electrochemical study demonstrates that the coating was excellent for corrosion prevention. The present work has shown a new perspective for the corrosion prevention of ferrous metals with minimum impact on environment and eco-system.

REFERENCES

- (1) Koch, G.; Varney, J.; Thompson, N.; Moghissi, O.; Gould, M.; Payer, J. International Measures of Prevention, Application, and Economics of Corrosion Technologies Study. *NACE International IMPACT Report*, **2016**.
- (2) Rausch, W. *The Phosphating of Metals*. Finishing Publications Ltd. (UK), **1990**.
- (3) Helliwell, N.; Gabe, D.R.; Richardson, M.O.W. Potential Measurements during Phosphating. *Trans. Inst. Met. Finish.* **1976**, *54*, 185-190. <https://doi.org/10.1080/00202967.1976.11870397>.
- (4) Stauffer, J. L. Finishing Systems Design and Implementation: A Guide for Product Parameters, Coatings, Process, and Equipment. *Society of Manufacturing Engineers*, **1993**.
- (5) Conley, D.J.; Paerl, H.W.; Howarth, R.W.; Boesch, D.F.; Seitzinger, S.P.; Havens, K.E.; Lancelot, C.; Likens, G.E. Controlling Eutrophication: Nitrogen and Phosphorus. *Science* **2009**, *323*, 1014-1015. <https://doi.org/10.1126/science.1167755>.
- (6) Maeda, S.; Yamamoto, M. The Role of Chromate Treatment after Phosphating in Paint Adhesion. *Prog. Org. Coat.* **1998**, *33*, 83-89. [https://doi.org/10.1016/S0300-9440\(98\)00014-9](https://doi.org/10.1016/S0300-9440(98)00014-9).

- (7) Claffey, W.J.; Reid, A.J. Post Treatment of Phosphated Metal Surfaces by Organic Titanates. U.S. Patent 4656097, **1987**.
- (8) Geduld, H. *Zinc Plating*. Finishing Publications Ltd. (UK), **1988**.
- (9) Lowery, R.K.; Willis, W.J. Acid Zinc Plating Baths, Compositions Useful Therein, and Methods for Electrodepositing Bright Zinc Deposits. U.S. Patent 4169772, **1979**.
- (10) Graedel, T.E. Corrosion Mechanisms for Zinc Exposed to the Atmosphere. *J. Electrochem. Soc.* **1989**, *136*, 193C-203C. <https://doi.org/10.1149/1.2096868>.
- (11) Yadav, A.P.; Nishikata, A.; Tsuru, T. Degradation Mechanism of Galvanized Steel in Wet-dry Cyclic Environment Containing Chloride Ions. *Corros. Sci.* **2004**, *46*, 361-376. [https://doi.org/10.1016/S0010-938X\(03\)00153-7](https://doi.org/10.1016/S0010-938X(03)00153-7).
- (12) Sprague, J.B.; Elson, P.F.; Saunders, R.L. Sublethal Copper-zinc Pollution in a Salmon River- a Field and Laboratory Study. *Adv. Water Pollut. Res.* **1965**, 61-82. <https://doi.org/10.1016/B978-0-08-011438-5.50012-X>.
- (13) Yerokhin, A.L.; Nie, X.; Leyland, A.; Matthews, A.; Dowey, S.J. Plasma Electrolysis for Surface Engineering. *Surf. Coatings Technol.* **1999**, *122*, 73-93. [https://doi.org/10.1016/S0257-8972\(99\)00441-7](https://doi.org/10.1016/S0257-8972(99)00441-7).
- (14) Clyne, T.W.; Troughton, S.C. A Review of Recent Work on Discharge Characteristics during Plasma Electrolytic Oxidation of Various Metals. *Int. Mater. Rev.* **2019**, *64*, 127-162. <https://doi.org/10.1080/09506608.2018.1466492>.
- (15) Teh, T.H.; Berkani, A.; Mato, S.; Skeldon, P.; Thompson, G.E.; Habazaki, H.; Shimizu, K. Initial Stages of Plasma Electrolytic Oxidation of Titanium. *Corros. Sci.* **2003**, *45*, 2757-2768. [https://doi.org/10.1016/S0010-938X\(03\)00101-X](https://doi.org/10.1016/S0010-938X(03)00101-X).

- (16) Hussein, R.O.; Nie, X.; Northwood, D.O. An Investigation of Ceramic Coating Growth Mechanisms in Plasma Electrolytic Oxidation (PEO) Processing. *Electrochim. Acta* **2013**, *112*, 111-119. <https://doi.org/10.1016/j.electacta.2013.08.137>.
- (17) Velon, A.; Olefjord, I. Oxidation Behavior of Ni₃Al and Fe₃Al: I. XPS Calibrations of Pure Compounds and Quantification of the Results. *Oxid. Met.* **2001**, *56*, 415-424. <https://doi.org/10.1023/A:1012589315800>.
- (18) Wang, J.; Yao, Z.; Yang, M.; Wang, Y.; Xia, Q.; Jiang, Z. A Fe₃O₄/FeAl₂O₄ Composite Coating via Plasma Electrolytic Oxidation on Q235 Carbon Steel for Fenton-like Degradation of Phenol. *Environ. Sci. Pollut. Res.* **2016**, *23*, 14927-14936. <https://doi.org/10.1007/s11356-016-6613-5>.
- (19) Maiti, S.; Kundu, A.K.; Lebedev, O.I.; Bera, P.; Anandan, C.; Gayen, A.; Seikh, M.M. Synthesis and Magnetic Properties of Nano-dimensional Fe_{1-x}Cu_xAl₂O₄ (0.3 ≤ x ≤ 0.8). *RSC Adv.* **2015**, *5*, 83809-83817. <https://doi.org/10.1039/C5RA14623B>.
- (20) Castillo Rodriguez, G.A.; Guillen, G.G.; Mendivil Palma, M.I.; Das Roy, T.K.; Guzman Hernandez, A.M.; Krishnan, B.; Shaji, S. Synthesis and Characterization of Hercynite Nanoparticles by Pulsed Laser Ablation in Liquid Technique. *Int. J. Appl. Ceram. Technol.* **2015**, *12*, E34-E43. <https://doi.org/10.1111/ijac.12212>.
- (21) Biesinger, M.C.; Payne, B.P.; Grosvenor, A.P.; Lau, L.W.; Gerson, A.R.; Smart, R.S.C.; Resolving Surface Chemical States in XPS Analysis of First Row Transition Metals, Oxides and Hydroxides: Cr, Mn, Fe, Co and Ni. *Appl. Surf. Sci.* **2011**, *257*, 2717-2730. <https://doi.org/10.1016/j.apsusc.2010.10.051>.

- (22) Grosvenor, A.P.; Kobe, B.A.; Biesinger, M.C.; McIntyre, N.S.; Investigation of Multiplet Splitting of Fe 2p XPS Spectra and Bonding in Iron Compounds. *Surf. Interface Anal.* **2004**, *36*, 1564-1574. <https://doi.org/10.1002/sia.1984>
- (23) Sayeed, M. A.; Herd, T.; O'Mullane, A. P.; Direct Electrochemical Formation of Nanostructured Amorphous Co(OH)₂ on Gold Electrodes with Enhanced Activity for the Oxygen Evolution Reaction. *J. Mater. Chem. A* **2016**, *4*, 991-999. <https://doi.org/10.1039/C5TA09125J>.
- (24) Li, T.; Nie, X. One Step Fast Synthesized Foam-like Amorphous Co(OH)₂ Flexible Film on Ti Foil by Plasma Assisted Electrolytic Deposition as a Binder-free Anode of High Capacity Lithium Ion Battery. *ACS Appl. Mater. Interfaces* **2018**, *10*, 16943-16946. <https://doi.org/10.1021/acsami.8b05482>.
- (25) Dutta, D.P.; Sharma, G. Synthesis and Magnetic Behavior of Spinel FeAl₂O₄ Nanoparticles. *Mater. Sci. Eng., B* **2011**, *176*, 177-180. <https://doi.org/10.1016/j.mseb.2010.10.018>.
- (26) Mukhtar, F.; Kayani, Z.N.; Riaz, S.; Naseem, S. Effect of In-situ Oxidation on Structure and Ferromagnetic Properties of Fe₃Al and FeAl₂O₄ Thin Films Prepared by Electrodeposition. *Ceram. Int.* **2018**, *44*, 9550-9560. <https://doi.org/10.1016/j.ceramint.2018.02.176>.
- (27) Zhu, K.; Li, M.; Li, X.; Zhu, X.; Wang, J.; Yang, W. Enhancement of Oxygen Evolution Performance through Synergetic Action between NiFe Metal Core and NiFeO_x Shell. *Chem. Commun.* **2016**, *52*, 11803-11806. <https://doi.org/10.1039/C6CC04951F>.
- (28) Li, Z.; Cheng, Y.; Kang, S.H.; Tu, W.; Cheng, Y. A Re-understanding of the Breakdown Theory from the Study of the Plasma Electrolytic Oxidation of a Carbon Steel-

A Non-valve Metal. *Electrochim. Acta* **2018**, *284*, 681-695.
<https://doi.org/10.1016/j.electacta.2018.07.201>.

(29) Khan, R.H.U.; Yerokhin, A.L.; Pilkington, T.; Leyland, A.; Matthews, A. Residual Stresses in Plasma Electrolytic Oxidation Coatings on Al Alloy Produced by Pulsed Unipolar Current. *Surf. Coatings Technol.* **2005**, *200*, 1580-1586.
<https://doi.org/10.1016/j.surfcoat.2005.08.092>.

(30) Hussein, R.O.; Nie, X.; Northwood, D.O.; Yerokhin, A.; Matthews, A. Spectroscopic Study of Electrolytic Plasma and Discharging Behaviour during the Plasma Electrolytic Oxidation (PEO) Process. *J. Phys. D: Appl. Phys.* **2010**, *43*, 105203-105216.
<https://doi.org/10.1088/0022-3727/43/10/105203>.

(31) Shokouhfar, M.; Dehghanian, C.; Montazeri, M.; Baradaran, A. Preparation of Ceramic Coating on Ti Substrate by Plasma Electrolytic Oxidation in Different Electrolytes and Evaluation of its Corrosion Resistance: Part II. *Appl. Surf. Sci.* **2012**, *258*, 2416-2423.
<https://doi.org/10.1016/j.apsusc.2011.10.064>.

(32) Stern, M.; Geary, A.L. Electrochemical Polarization I. A Theoretical Analysis of the Shape of Polarization Curves. *J. Electrochem. Soc.* **1957**, *104*, 56-63.
<https://doi.org/10.1149/1.2428496>.

(33) Hosking, N.C.; Ström, M.A.; Shipway, P.H.; Rudd, C.D. Corrosion Resistance of Zinc–magnesium Coated Steel. *Corros. Sci.* **2007**, *49*, 3669-3695.
<https://doi.org/10.1016/j.corsci.2007.03.032>.

(34) Bisquert, J.; Garcia-Belmonte, G.; Bueno, P.; Longo, E.; Bulhoes, L.O.S. Impedance of Constant Phase Element (CPE)- Blocked Diffusion in Film Electrodes. *J. Electroanal. Chem.* **1998**, *452*, 229-234. [https://doi.org/10.1016/S0022-0728\(98\)00115-6](https://doi.org/10.1016/S0022-0728(98)00115-6).

5. CHAPTER 5 Anodic Plasma Electrolytic Deposition of Composite Coating on Ferrous Alloys with Low Thermal Conductivity and High Adhesion Strength

5.1 Introduction

Thermal barrier coatings (TBCs) are used to insulate turbine and combustor engine components from the hot gas stream, thereby improving the durability and energy efficiency of the engine ¹. For TBCs applied on aero turbines, stresses due to thermal expansion mismatch upon cooling, plastic deformation of the bond coat and oxidation of the irregular bond coat have been cited as coating lifetime-limiting factors ². Numerous researches have thus been carried to address these problems ^{1,3-5}. TBCs are also extremely attractive for applications in automotive engines to improve thermal efficiency. However, the operational conditions of pistons in automotive engines are markedly different as compared to the aero turbines. The requirements for TBCs in automotive engines are outlined elsewhere but include having insulative properties, high thermal-shock resistance and low cost ⁶. During engine operation, a piston is first heated by forced convection with the combustion flux and then cooled by forced convection with engine oil and intake air and by conduction with the rings and the cylinder block. These heat exchanges generate transient thermal-mechanical loading cycles during operation ^{7,8}. However, a major weakness of TBCs in automotive engines is the interface between the bond-coat and the substrate as well as the interface between the bond-coat and the top ceramic coat ^{9,10}. It is also desirable to generate coating solutions without the need for a bond-coat in order to have a relatively thin coating thickness for achievement of a “Temperature Swing” or “Temperature Oscillation” behavior for internal combustion engines. Recently, the concept of heat insulation by using “Temperature Swing” has been investigated ¹¹⁻¹⁵. In this case,

a thin coating having a low-heat-conductivity and low-heat-capacity is deposited on the combustion chamber wall, resulting in a large change in surface temperature. Specifically, it is shown that the surface temperature with such an insulation coating follows the transient gas temperature, decreasing the heat loss while preventing the heating of intake air. A good example of such a coating is silica-reinforced anodized aluminum ¹².

In recent years, plasma electrolytic oxidation (PEO) coatings ¹⁶ have attracted researchers' attention. Unlike conventional processes, the substrate is directly involved in the plasma chemical reaction during PEO processing. For this reason, PEO coatings do not need a bond coat to achieve a good bonding strength. Meanwhile, PEO coatings also exhibit high strain tolerance and relatively low stiffness ¹⁷. Therefore, PEO coatings could have a high thermal shock resistance. Although the thermal conductivity of bulk alumina (32-34 W/m·K) is not as low as that of zirconia (1.7 W/m·K), PEO coatings still demonstrate a low thermal conductivity (~1 W/m·K), which has been attributed to the presence of amorphous phases, together with nanograins ^{18,19}. Such properties enable the generation of "Temperature Swing" through PEO coating as reported in the references ^{20,21}. However, PEO cannot be readily applied on the ferrous metals. Most investigators agree that the formation of a dense passive layer on the metal surface is critical for the PEO process ¹⁶. Hercynite (FeAl₂O₄) is a good electrical isolator and is chemically stable in acidic/basic aqueous environments. Thus, we have developed a plasma electrolytic aluminating process ²² in an aluminate-contained electrolyte where the first step is to form hercynite as a passive layer. AlO₂⁻ anions are continuously absorbed on the hercynite film and then sintered into Al₂O₃ by the high-temperature plasma, forming a hercynite-alumina composite coating. The plasma chemical reaction of the substrate can provide good adhesive properties and

high thermal shock resistance. Meanwhile, nanograins and amorphous phase could form due to rapid localized quenching around each individual discharge during PEO processing^{17,18,23}, which might result in low thermal conductivity of the coating^{18,19}. The main objectives of the present study are to prepare and characterize hercynite-alumina composite coatings on ferrous alloys and to study both thermal and adhesion properties of the coatings.

5.2 Experimental details

5.2.1 Plasma electrolytic aluminating (PEA) and materials characterization

AISI 4140 alloy steel (0.8-1.1% Cr, 0.75-1% Mn, 0.38-0.43% C, 0.15-0.3% Si, 0.15-0.25% Mo, <0.04% S, <0.035% P, and Fe balance) and compacted graphite iron (0.2-1% Mn, 2.5-4% C, 1-3% Si, <0.25% S, <0.1% P, and Fe balance) samples ($\Phi 25.4$ mm \times 3 mm) were polished with #1200 abrasive paper, rinsed with distilled water and ultrasonically cleaned in ethanol. The sample (anode) was immersed in the electrolyte (15-20 g/L NaAlO₂ as a precursor and 1-5 g/L Na₃PO₄ as a buffer dissolved in deionized water, pH=12, Sigma Aldrich) within a stainless-steel vessel (cathode). A pulsed ($f = 1$ kHz, duty cycle = 20%) DC power supply was used. After successful initiation of sparks, the current density was kept at 0.15 A/cm² for 20 and 40 mins to produce coatings with different thicknesses. After removal from the electrolyte, all samples were dried at 60 °C. For simplicity, the 20-min-treated cast iron samples are named as C1-C3, the 20-min-treated steel samples are named as S1-S3, the 40-min-treated iron samples are named as C4-C6 and the 40-min-treated steel samples are named as S4-S6.

The coating deposition process is illustrated schematically in Figure 5-1. At the beginning, active iron ions (Fe²⁺ cations) were released into the electrolyte and combined with aluminate ions (AlO₂⁻ anions) in the electrolyte to form hercynite nanoparticles (FeAl₂O₄)

with negative charges. These negatively charged nanoparticles $(\text{FeAl}_2\text{O}_4)\cdot(\text{OH})^-$ were deposited back to sample surface and form the passive layer. Charge build-up causes the voltage to increase. After the voltage reaches the dielectric breakdown point, plasma discharges initiate. The plasma sinters the hercynite and aluminate into a hard-composite coating. Occasionally, strong discharges penetrate the coating and reach the substrate, releasing the iron ions. These iron ions released from the discharge channels are the source of the hercynite phase. A more detailed analysis of the coating deposition mechanism can be found in our previous publication ²².

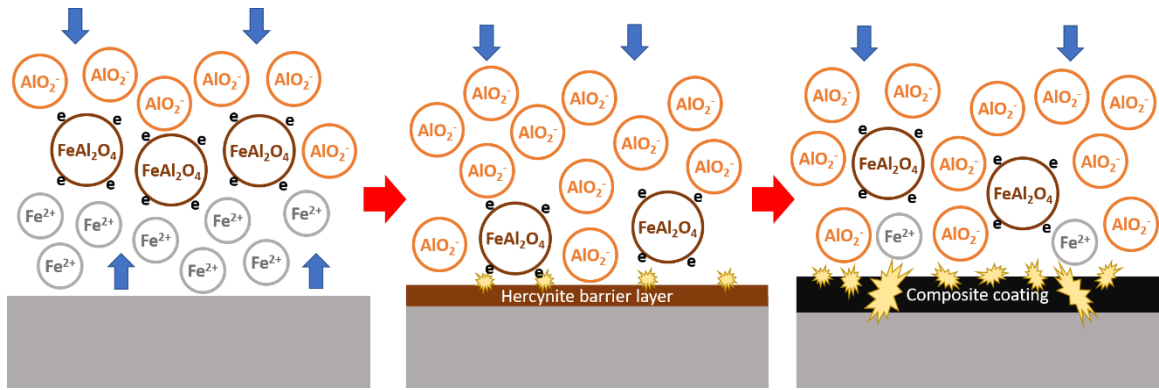


Figure 5-1 Illustration of the coating deposition process.

Phase structures of the coatings were determined by X-ray diffraction (XRD, PROTO AXRD), using Cu $K\alpha$ radiation in scans from 20° to 90° . Phase proportions were determined by profile fitting of low-angle amorphous peaks ²⁴. Estimates of crystallite size were made from peak broadening. During calculation of the average grain size, the effect of microstrain on the peak broadening must be subtracted by the Williamson–Hall methods ^{25–27}. The microstructures of the coatings were observed by scanning electron microscopy (SEM, FEI Quanta 200 FEG). The adhesive strength of the coatings was evaluated by adhesive tensile testing (MTS Criterion Model 430) in which a test sample was sandwiched

and adhered to a pair of holding tools with epoxy elastomeric wafers (FM-1000, Sturbridge Metallurgical Service Inc.).

5.2.2 Thermal conductivity measurement

The thermal conductivities were measured using the experimental setup shown in Figure 5-2. A test sample was aligned between a pair of stainless steel 304 bars (16.2 W/m·K at 100 °C, National Physical Laboratory, UK). The metallic bars and the sample were surrounded by insulation material which was encased in a longitudinal aluminum guard shell. The purpose of this design was to minimize the radial heat exchange. In addition, a hot plate (Scholar 170, Corning Inc., USA) as the heat provider and a water-cooled heat sink were placed at the bottom and the top of the test stack, respectively. In order to achieve excellent interfacial contact, the mating faces of the meter bars were polished to a 0.03 μm finish and with a small amount (about 0.1 mL) of high conductivity silicone-based thermal grease (3.1 W/m·K, Tgrease 880, Laird Technologies, USA) was applied to the sample. In this setup, standard grade K-type thermocouples (KTSS-062G-06, Omega Engineering Inc., USA) were inserted radially into the meter bars. The output from these thermocouples was recorded by a 16-channel data acquisition system (OM-DAQ-USB-2401, Omega Engineering Inc., USA). The thermal resistance associated with the interface and its filling paste was measured by using uncoated samples in the same set-up and was found to be repeatable and equivalent to a 10 ± 1 μm thickness of paste. The paste layer therefore contributes a predictable and repeatable thermal resistance, which was subtracted from the apparent thermal resistance of the coated samples to obtain the effective thermal conductivities of the coated samples.

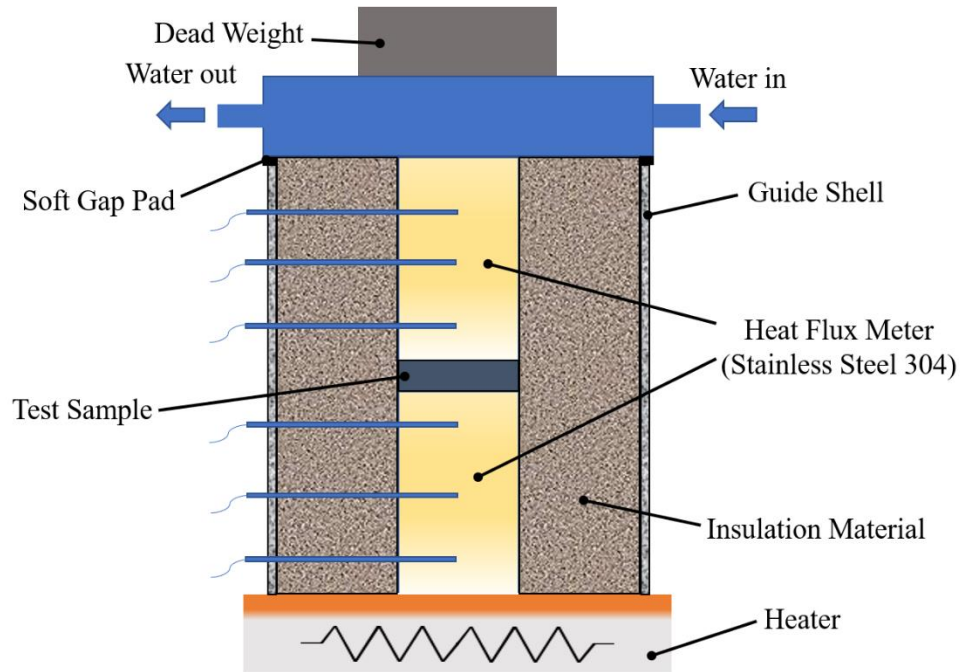


Figure 5-2 Experimental setup for thermal conductivity measurement.

5.2.3 Thermal shock tests

Studies on the working conditions of internal combustion engines have shown that the maximum temperature of the pistons would not exceed 370 °C²⁸. For thermal shock tests in this work, the samples were heated up to 425 °C in a muffle furnace and then quenched to 20 °C in distilled water. 425°C was chosen to ensure the given coating's success in the potential application as TBC for pistons. Quenching in water increases the cyclic thermal stress for accelerated testing. Similar tests have been carried by other researchers²⁹. After each cycle of thermal shock, the samples were examined by optical microscopy to determine if interfacial spallation had occurred. The total number of thermal shock cycles is 100.

5.3 Results and discussion

The coating thickness was measured using a scanning electron microscopy (SEM) on polished cross-sections and the results are summarized in Table 5-1. With treatment times of 20 and 40 mins, coatings were produced with the PEA process having thicknesses around 40 and 70 μm , respectively (see also Figures 5-3g and 5-3h). Figure 5-3 also shows the surface morphologies of selected samples (i.e., samples S1, S4, C1 and C4). As like a typical PEO coating¹⁶, the PEA composite coatings have a porous structure. Some large pores could be found on the surface, which were caused by the intermittent strong discharge events. The average pore size and porosity were measured from the SEM images of both the plane surface and cross-sections. The results are summarized in Table 5-2. As the processing time and thus coating thickness increased, the porosity and average pore size increased. It is also noted that the coating produced on steel substrates have higher porosity and average pore size than those grown on iron substrates. This can be explained by more intensive discharge events on the steel samples, which was verified by higher voltages reached during the coating process. It is noteworthy that numerous mesopores (100-500 nm) could be found in the coatings produced on both substrates, as shown in Figures 5-3e and 5-3f. When the pore sizes are comparative to the phonon free mean path, increased phonon scattering could occur at the pore surfaces³⁰. Therefore, these mesopores are also beneficial for reducing the thermal conductivities of the coatings.

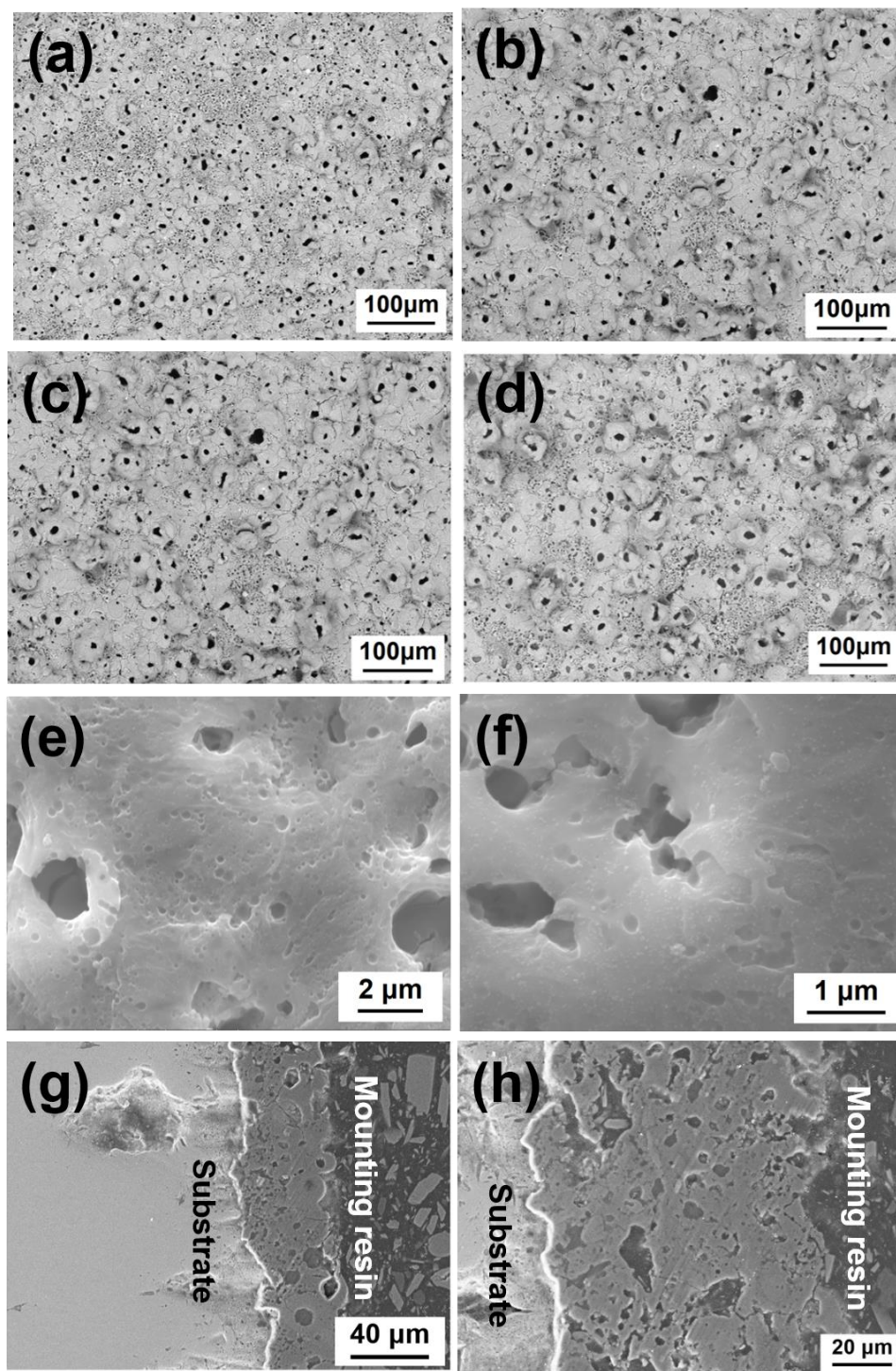


Figure 5-3 SEM plain view of selected samples (a) S1, (b) S4, (c) C1, and (d) C4. High magnification SEM images of selected samples (e) S1 and (f) C1 showing the existence of mesopores. Cross-sectional SEM images of selected samples (g) S1 and (h) S4.

Table 5-1 Sample number, corresponding to PEA treatment time and substrate type (see also section 5.2.1) and the average (\pm standard deviation) of the resulting coating thicknesses and thermal conductivities.

Sample NO.	Thickness (μm)	Thermal conductivity ($\text{W/m}\cdot\text{K}$)
S1	39 \pm 2.6	0.50 \pm 0.01
S2	41 \pm 2.1	0.48 \pm 0.02
S3	40 \pm 1.9	0.50 \pm 0.01
S4	72 \pm 5.2	0.46 \pm 0.02
S5	76 \pm 4.8	0.51 \pm 0.02
S6	73 \pm 3.6	0.48 \pm 0.01
C1	40 \pm 3.5	0.54 \pm 0.02
C2	39 \pm 3.1	0.54 \pm 0.01
C3	42 \pm 2.7	0.55 \pm 0.02
C4	70 \pm 5.8	0.52 \pm 0.01
C5	68 \pm 5.5	0.53 \pm 0.01
C6	71 \pm 4.9	0.53 \pm 0.02

Figure 5-4 demonstrates the XRD patterns of the coated samples. The peaks at 31.4° and 77.8° represent the (220) and (533) planes of FeAl_2O_4 (JCPDS # 3-0894), while the peaks at 37.0°, 55.9°, 59.7° and 65.7° confirm the existence of Al_2O_3 (JCPDS # 46-1212). Therefore, these deposited coatings are composites of hercynite and alumina. As demonstrated in the XRD pattern, the relative peak intensities between FeAl_2O_4 and Al_2O_3 were 0.59:1, 0.74:1, 0.42:1 and 0.32:1 for samples S1, C1, S4 and C4 respectively. Compared with 40-min-treated samples (S4 and C4), 20-min-treated samples (S1 and C1) have a higher amount of FeAl_2O_4 phase. This observation can be explained by the reduced contribution of the iron substrate to the plasma chemical reaction as the coatings' thicknesses increase. There is approximately 35% of amorphous material in these coatings as suggested by profile fitting of the low-angle amorphous peak (see example in Figure 5-4e)²⁴:

$$v = I_a / (I_a + I_c) \quad (\text{Eq. 1})$$

where v is the amorphous phase portion, I_a the total area of amorphous peaks, I_c the total area of crystalline phase peaks. Estimates of grain size were made from peak broadening by Williamson–Hall methods^{25–27}:

$$\beta \cos \theta = \frac{K\lambda}{D} + 4\varepsilon \sin \theta \quad (\text{Eq. 2})$$

where D is the average grain size, K the dimensionless shape factor with a typical value of about 0.9, λ the X-ray wavelength, β the line broadening at half the maximum intensity (FWHM), θ the Bragg angle, ε the microstrain. By plotting $\beta \cos \theta$ vs. $4 \sin \theta$, the average grain size could be calculated from the intercept. It is noted that only two distinct peaks could be attributed to FeAl_2O_4 and the peak at 77.8° is too weak to be analyzed, which means the Williamson–Hall method is not applicable for FeAl_2O_4 in this study. Therefore, we only calculated the grain sizes for Al_2O_3 . However, it is reasonable to assume that FeAl_2O_4 should have similar grain size with Al_2O_3 since they experience similar heating and cooling conditions.

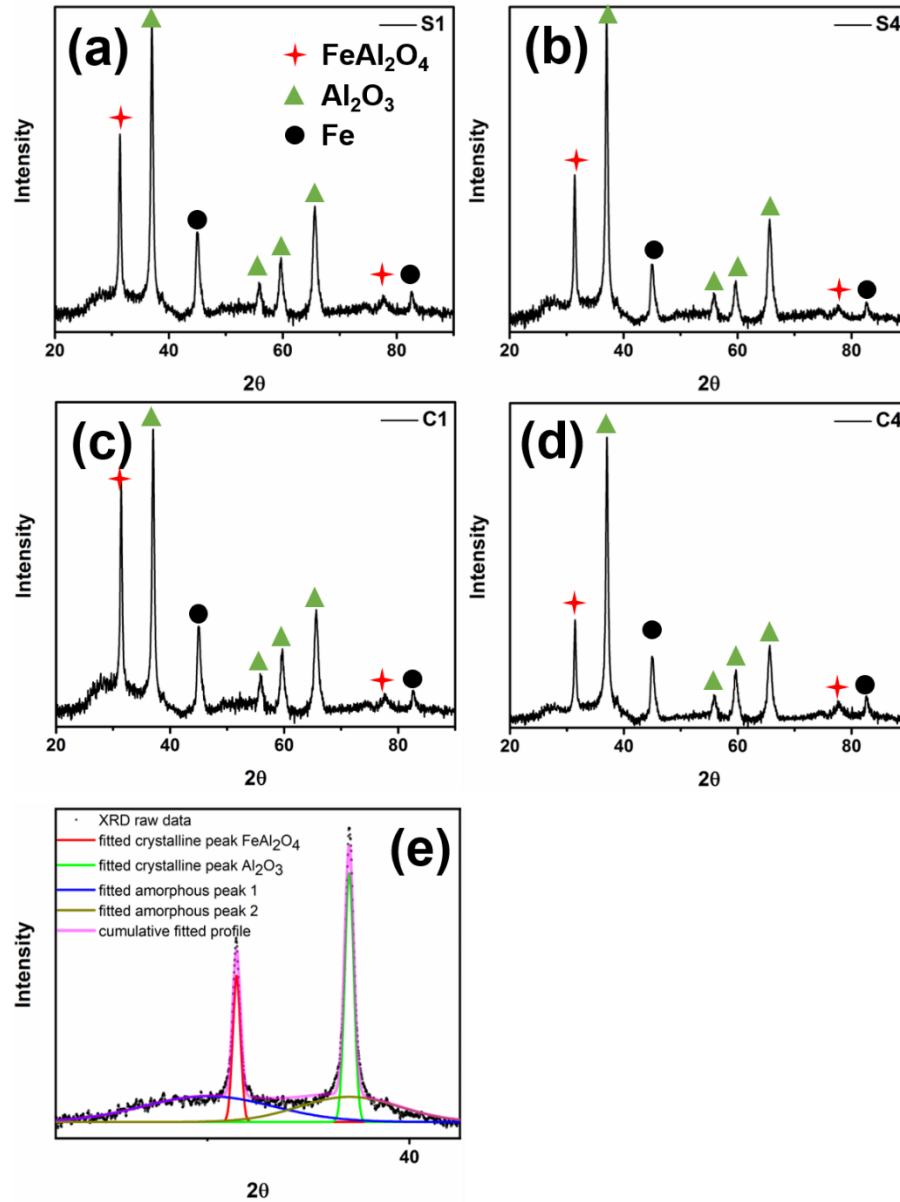


Figure 5-4 XRD patterns of selected samples(a) S1, (b) S4, (c) C1 and (d) C4. (e) Illustration of peak fitting at low angle for estimation of amorphous materials and grain size.

The results are summarized in Table 5-2. It is noticed that as treatment time increased, the average grain size decreased, which is not consistent with other reports ²³. This contradiction can be explained by the peak broadening due to the presence of an amorphous

phase ³¹. For 20-min-treated samples, the amorphous phase percentages are estimated to be 31.6% for the iron-based substrate C1 and 32.1% for the steel-based substrate S1. On the other hand, the amorphous phase percentages are estimated to be 36.5% and 37.3% for the equivalent 40-min-treated samples (C4 and S4 respectively). The higher amount of amorphous phase could contribute more to the peak broadening. Therefore, the calculated average grain sizes of 40-min-treated samples are slightly lower than those of 20-min-treated samples. Nevertheless, the Williamson–Hall method provided a good approximation of the average grain size in our coatings.

Table 5-2 Surface Porosity, cross-sectional porosity, average pore size and average grain sizes for samples S1, S4, C1 and C4.

Sample NO.	Surface porosity (%)	Sectional porosity (%)	Average pore size (μm)	Average grain size (nm)
S1	9.5	9.8	9.23	42.6
S4	11.8	12.5	13.85	41.3
C1	7.3	7.4	5.8	43.2
C4	8.7	8.9	12.7	40.9

Figure 5-5a illustrates temperature-time profiles for measurement of a given sample's thermal conductivity. T1-T6 represent the measured temperatures at different locations (from bottom to top) of the two stainless steel bars when a steady-state was reached.

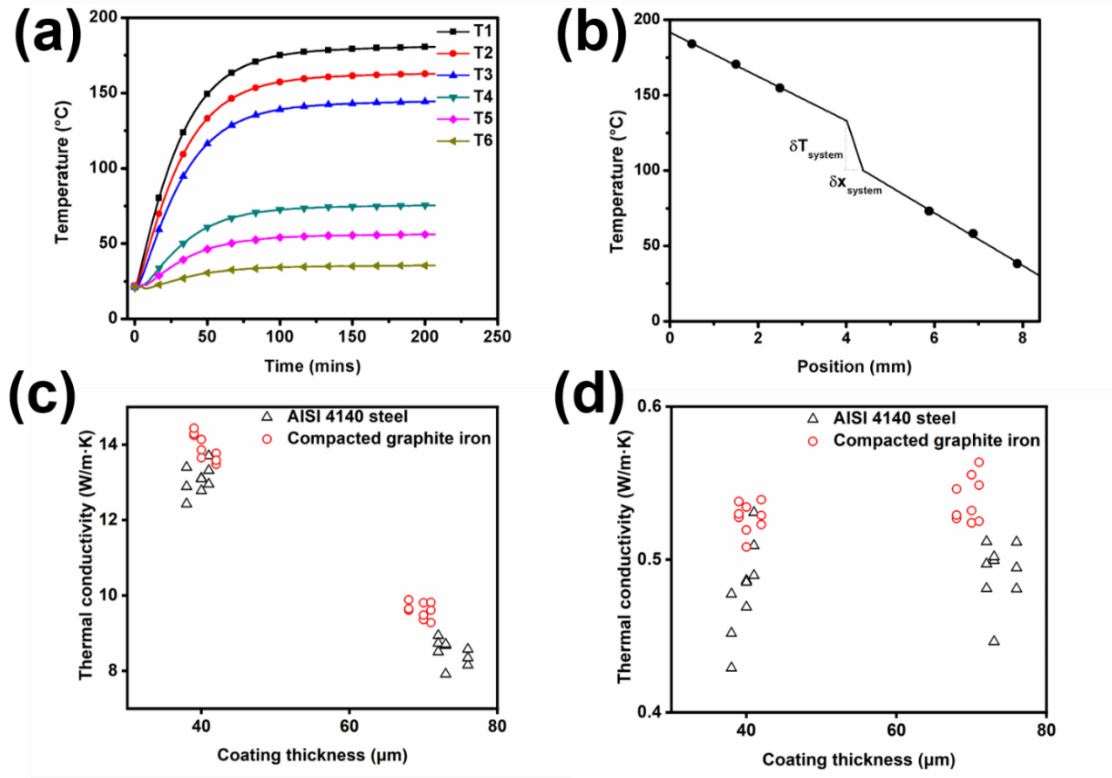


Figure 5-5 (a) Temperature-time profile for a thermal conductivity measurement; (b) A typical steady-state thermal profile for coated ferrous metals; (c) Measured effective thermal conductivities of the coated ferrous metal samples; (d) Calculated thermal conductivities of the composite coatings.

Linear fitting was conducted based on T1-T3 and T4-T6 to calculate the steady-state heat flux \dot{q} with:

$$\dot{q} = 0.5(\dot{q}_B + \dot{q}_T) = 0.5k_r(g_B + g_T) \quad (\text{Eq. 3})$$

where k_r is the thermal conductivity of the stainless-steel bars (16.2 W/m·K, stainless steel 304), g_B and g_T the temperature gradients of the bottom and top bars, respectively. For all thermal conductivity measurements, the difference between g_B and g_T was smaller than 8%, which indicates the unidirectional heat transfer condition was well satisfied.

After linear extrapolation to the sample surfaces and subtracting the temperature difference across the filling paste layers, the temperature difference across the sample could be obtained, as shown in Figure 5-5b. Then the effective thermal conductivity of the sample K_{eff} could be calculated as:

$$K_{eff} = \dot{q} \delta x / \delta T \quad (\text{Eq. 4})$$

where δx and δT are thickness of the sample and temperature difference across the sample, respectively.

Then the thermal conductivity of the composite coating K_c could be calculated by:

$$\delta x / K_{eff} = t_s / K_s + t_c / K_c \quad (\text{Eq. 5})$$

where t_s and t_c are the thickness of substrate and coating, respectively; K_s the thermal conductivity of a given substrate, which was pre-measured, using the same method above, as 44 W/m·K and 46 W/m·K for AISI 4140 alloy steel and compacted graphite iron, respectively. These values are in good agreement with reported data^{32,33}. It is worth pointing out that the uncertainty of the system was estimated to be 9%, which mainly arose from possible cross-sectional area mismatching or misalignment between the stainless-steel bars and test sample, non-uniformity of coating thickness, reliability of temperature measurement, and non-uniform heat flux.

The effective thermal conductivities of the coated samples and the calculated thermal conductivities of the coatings were plotted in Figure 5-5c and 5-5d. It has been demonstrated that the effective thermal conductivities of the coated samples were reduced to 12-14 W/m·K with a 40 μm coating and 8-10 W/m·K with a 70 μm coating. The thermal conductivities were 0.486 ± 0.025 W/m·K for coatings on steels and 0.533 ± 0.013 W/m·K

for coatings on irons, which both are considerably lower than the thermal conductivities of dense alumina and dense hercynite.

In the simplest theoretical models, the thermal conductivity could be predicted as ³⁴:

$$\lambda_{eff} = (1 - \varphi)^3 \lambda_0 \quad (\text{Eq. 6})$$

where λ_{eff} is the effective thermal conductivity, φ the porosity and λ_0 the thermal conductivity of dense material. Therefore, the thermal conductivity would decrease as the porosity increases. Meanwhile, higher amount of FeAl_2O_4 content would also reduce the thermal conductivity since hercynite has a lower thermal conductivity than alumina. However, the composition of FeAl_2O_4 crystalline phase and the porosity cannot account for such low thermal conductivities measured, which are almost two orders of magnitude lower than the bulk values. Therefore, other factors might play more significant roles in reducing the thermal conductivities.

Curran and co-workers ¹⁹ have reported a low value ($\sim 0.5 \text{ W/m}\cdot\text{K}$) for mullite-rich PEO coatings on aluminum alloys and attributed this low value to the presence of amorphous phases together with nanograins. Amorphous materials also significantly reduce the thermal conductivity. It follows that the thermal conductivity of amorphous alumina can be $\sim 0.1 \text{ W/m}\cdot\text{K}$ ¹⁸. The combination of amorphous phases (approximately 35%) and nanocrystalline grains (average size around 40 nm) have been reported to result in thermal conductivity values as low as $0.2\text{-}0.8 \text{ W/m}\cdot\text{K}$ ¹⁸, which are broadly consistent with the measured values presented here. Another possible contribution comes from the strong phonon scattering at the surface of mesopores ³⁰. As shown in Figures 5-3e and 5-3f, numerous mesopores could be found in the coatings, which can also contribute to the low thermal conductivities. However, it is very difficult to distinguish the relative contribution

of mesopores from the contribution of the amorphous phase and nanocrystalline grains on the low thermal conductivity values. Transmission Electron Microscopy (TEM) characterization on the shape and distribution of each component (amorphous phase, nanocrystalline grains and mesopores) might help to quantify the influence of each individual component. Nevertheless, it is evident from the results presented here that the amorphous phase, nanocrystalline grains and mesopores together contribute to the measured low thermal conductivities.

It is worth noting that all these micro-structural features (amorphous phase, nanocrystalline grains and mesopores) come from the plasma electrolysis process. Nie and co-workers²³ used TEM to investigate Al₂O₃ coatings fabricated using plasma electrolysis. They have found an amorphous plus nanocrystalline inner layer and a nanocrystalline intermediate layer in the coating. During the process, the coating materials were continuously melted by the hot plasma core and then quenched by adjacent cold electrolyte, leading to grain refinement and formation of amorphous materials.

To be useful as thermal barrier coatings for automotive engines, the coatings must have good adhesive strength to the substrates and high resistance to thermal shock induced spallation. Figure 5-6a demonstrates the setup of adhesive tensile test. A single-side coated sample was sandwiched and adhered with a pair of holding tools with epoxy elastomeric wafers (FM-1000, Sturbridge Metallurgical Service Inc.). After the tensile test, adhesive failure occurred at the interface between the cast iron and glue film on the uncoated backside, with the coated side still well attached with the holding tool, as illustrated in Figure 5-6c. Previous research highlights the strong influence of the surface morphology on the bonding behavior between the coating and the glue film. The works show that this

is due to mechanical interlocking by flow of molten polymers into open pores, cracks and cavities^{35,36}. The bonding between the coating and the glue film is increased due to mechanical interlocking. Depending on bonding at the coating interface or binding strength within the coating, the failure locations can be at the coating/substrate interface (adhesion strength) or inside the coating (cohesion strength). We have also observed this glue-filling process during our experiments. Since no adhesive or cohesive failure for the coating was observed during the test, we are thus able to say that the coating has a good bonding strength and cohesion strength due to the topologies of the developed coatings.

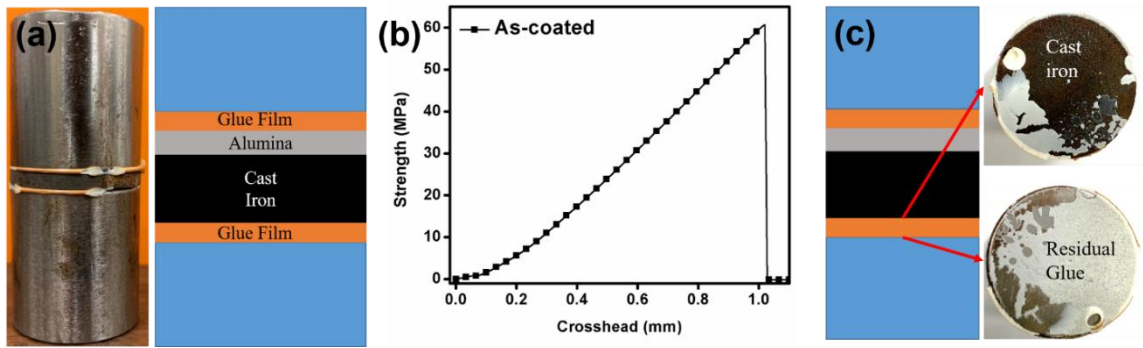


Figure 5-6 (a) Illustration of the adhesive tensile test; (b) A typical tensile curves of single-side coated cast iron sample; (c) Fracture surfaces after tensile test showing adhesive failure on the uncoated side.

Figures 5-7a, 5-7b, 5-7c and 5-7d demonstrate the optical images of samples S3, S6, C3 and C6 during and after the thermal shock tests. For all four samples, no interfacial spallation was found after 100 cycles of thermal shock testing. The SEM images of sample C6 (Figures 5-7e, 5-7f and 5-7g) demonstrate that the porous structure was retained after the thermal shock tests. Although some small surface cracks were formed (red arrows in Figure 5-7f and 5-7g), no crack was observed at the interface between the coating and

substrate. This supports the observation that spallation was not observed after the thermal shock testing.

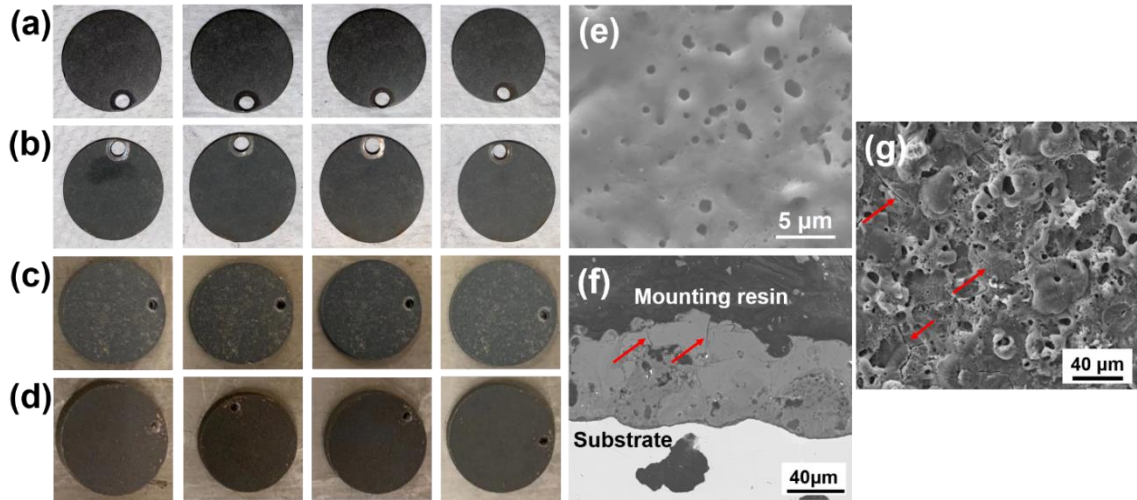


Figure 5-7 Optical images of selected samples (a) C3, (b) C6, (c) S3 and (d) S6 after 1, 25, 50 and 100 cycles (left to right) of thermal shock tests. (e) and (g) (plain views) and (f) (cross-section) are SEM images of selected sample C6 after 100 cycles of thermal shock test. Red arrows in (f) and (g) indicate the formation of small cracks after thermal shock test in the coating. The coupons in figure a-d have diameters of 25.4 mm.

Traditional TBCs deposition technologies, like PVD and thermal spray, are usually “line-of-sight” processes, which means it is difficult to deal with parts with complex shapes. The high cost of facilities and process control may be another obstacle for mass production in the automotive sector. On the contrary, the PEA is a non-line-of-sight process with relatively low cost³⁷. Considering the coatings’ thermal barrier behavior is comparative with traditional TBCs, it can be concluded that this PEA technology might be useful for TBC applications in the automotive industry.

5.4 Conclusions

In this work, a $\text{FeAl}_2\text{O}_4\text{-Al}_2\text{O}_3$ composite coating was successfully prepared on AISI 4140 alloy steel and compacted graphite iron by the plasma electrolytic aluminating process. The coatings have good adhesion strength (>60 MPa) and low thermal conductivity (~ 0.5 W/m·K). Scanning electron microscope (SEM) observations reveal that the coating has numerous mesopores. X-ray diffraction (XRD) analysis shows that the coating mainly consists of nanocrystalline (~ 40 nm) Al_2O_3 and FeAl_2O_4 , and amorphous materials ($\sim 35\%$). These amorphous phases, nanocrystalline grains and mesopores significantly decreased the thermal conductivities. The hercynite phase indicated that the substrate is directly involved in the PEA reaction and thus the coating had a metallurgical bonding to the substrate, which could account for high adhesive strength of the coating. No interfacial spallation was observed in the coatings after 100 cycles of thermal shock testing, indicating that these coatings have excellent thermal shock resistance. Therefore, PEA process might be a promising method for mass production of thermal barrier coatings for automotive applications.

REFERENCES

- (1) Padture, N. P.; Gell, M.; Jordan, E. H. Thermal Barrier Coatings for Gas-Turbine Engine Applications. *Science* **2002**, *296* (5566), 280–284. <https://doi.org/10.1126/science.1068609>.
- (2) Miller, R. A.; Lowell, C. E. Failure Mechanisms of Thermal Barrier Coatings Exposed to Elevated Temperatures. *Thin Solid Films* **1982**, *95* (3), 265–273. [https://doi.org/10.1016/0040-6090\(82\)90019-0](https://doi.org/10.1016/0040-6090(82)90019-0).

- (3) Darolia, R. Thermal Barrier Coatings Technology: Critical Review, Progress Update, Remaining Challenges and Prospects. *Int. Mater. Rev.* **2013**, 58 (6), 315–348. <https://doi.org/10.1179/1743280413Y.0000000019>.
- (4) Clarke, D. R.; Levi, C. G. Materials Design for the next Generation Thermal Barrier Coatings. *Annu. Rev. Mater. Res.* **2003**, 33 (1), 383–417. <https://doi.org/10.1146/annurev.matsci.33.011403.113718>.
- (5) Feuerstein, A.; Knapp, J.; Taylor, T.; Ashary, A.; Bolcavage, A.; Hitchman, N. Technical and Economical Aspects of Current Thermal Barrier Coating Systems for Gas Turbine Engines by Thermal Spray and EBPVD: A Review. *J. Therm. Spray Technol.* **2008**, 17 (2), 199–213. <https://doi.org/10.1007/s11666-007-9148-y>.
- (6) Uzun, A.; Çevik, I.; Akçil, M. Effects of Thermal Barrier Coating on a Turbocharged Diesel Engine Performance. *Surf. Coatings Technol.* **1999**, 116–119, 505–507. [https://doi.org/10.1016/S0257-8972\(99\)00099-7](https://doi.org/10.1016/S0257-8972(99)00099-7).
- (7) Szymtka, F.; Salem, M.; Rézai-Aria, F.; Oudin, A. Thermal Fatigue Analysis of Automotive Diesel Piston: Experimental Procedure and Numerical Protocol. *Int. J. Fatigue* **2015**, 73, 48–57. <https://doi.org/10.1016/j.ijfatigue.2014.11.011>.
- (8) Silva, F. S. Fatigue on Engine Pistons - A Compendium of Case Studies. *Eng. Fail. Anal.* **2006**, 13 (3), 480–492. <https://doi.org/10.1016/j.engfailanal.2004.12.023>.
- (9) Białas, M. Finite Element Analysis of Stress Distribution in Thermal Barrier Coatings. *Surf. Coatings Technol.* **2008**, 202 (24), 6002–6010. <https://doi.org/10.1016/j.surfcoat.2008.06.178>.

- (10) Moridi, A.; Azadi, M.; Farrahi, G. H. Thermo-Mechanical Stress Analysis of Thermal Barrier Coating System Considering Thickness and Roughness Effects. *Surf. Coatings Technol.* **2014**, *243*, 91–99. <https://doi.org/10.1016/j.surfcoat.2012.02.019>.
- (11) Kosaka, H.; Wakisaka, Y.; Nomura, Y.; Hotta, Y.; Koike, M.; Nakakita, K.; Kawaguchi, A. Concept of “Temperature Swing Heat Insulation” in Combustion Chamber Walls, and Appropriate Thermo- Physical Properties for Heat Insulation Coat. *SAE Int. J. Engines* **2013**, *6* (1), 142–149. <https://doi.org/10.4271/2013-01-0274>.
- (12) Wakisaka, Y.; Inayoshi, M.; Fukui, K.; Kosaka, H.; Hotta, Y.; Kawaguchi, A.; Takada, N. Reduction of Heat Loss and Improvement of Thermal Efficiency by Application of “Temperature Swing” Insulation to Direct-Injection Diesel Engines. *SAE Int. J. Engines* **2016**, *9* (3). <https://doi.org/10.4271/2016-01-0661>.
- (13) Powell, T.; O’Donnell, R.; Hoffman, M.; Filipi, Z.; Jordan, E. H.; Kumar, R.; Killingsworth, N. J. Experimental Investigation of the Relationship between Thermal Barrier Coating Structured Porosity and Homogeneous Charge Compression Ignition Engine Combustion. *Int. J. Engine Res.* **2019**, 146808741984375. <https://doi.org/10.1177/1468087419843752>.
- (14) Rakopoulos, C. D.; Giakoumis, E. G. Study of the Transient Operation of Low Heat Rejection Turbocharged Diesel Engine Including Wall Temperature Oscillations. In *SAE Technical Papers*; 2007. <https://doi.org/10.4271/2007-01-1091>.
- (15) Caputo, S.; Millo, F.; Boccardo, G.; Piano, A.; Cifali, G.; Pesce, F. C. Numerical and Experimental Investigation of a Piston Thermal Barrier Coating for an Automotive Diesel Engine Application. *Appl. Therm. Eng.* **2019**, 162. <https://doi.org/10.1016/j.applthermaleng.2019.114233>.

- (16) Yerokhin, A. L.; Nie, X.; Leyland, A.; Matthews, A.; Dowey, S. J. Plasma Electrolysis for Surface Engineering. *Surf. Coatings Technol.* **1999**, *122* (2–3), 73–93. [https://doi.org/10.1016/S0257-8972\(99\)00441-7](https://doi.org/10.1016/S0257-8972(99)00441-7).
- (17) Curran, J. A.; Clyne, T. W. Thermo-Physical Properties of Plasma Electrolytic Oxide Coatings on Aluminium. *Surf. Coatings Technol.* **2005**, *199* (2-3), 168–176. <https://doi.org/10.1016/j.surfcoat.2004.09.037>.
- (18) Curran, J. A.; Clyne, T. W. The Thermal Conductivity of Plasma Electrolytic Oxide Coatings on Aluminium and Magnesium. *Surf. Coatings Technol.* **2005**, *199* (2-3), 177–183. <https://doi.org/10.1016/j.surfcoat.2004.11.045>.
- (19) Curran, J. A.; Kalkanci, H.; Magurova, Y.; Clyne, T. W. Mullite-Rich Plasma Electrolytic Oxide Coatings for Thermal Barrier Applications. *Surf. Coatings Technol.* **2007**, *201* (21), 8683–8687. <https://doi.org/10.1016/j.surfcoat.2006.06.050>.
- (20) Shen, X.; Nie, X.; Tjong, J. Effects of Electrolytic Jet Plasma Oxidation (EJPO) Coatings on Thermal Behavior of Engine Cylinders. *Heat Mass Transf. und Stoffuebertragung* **2019**, *55* (9), 2503–2515. <https://doi.org/10.1007/s00231-019-02600-6>.
- (21) Shen, X.; Nie, X.; Hu, H. Numerical Analysis of Thermal Distributions in Aluminum Engine Cylinders Influenced by Alumina Ceramic Coatings. *Numer. Heat Transf. Part A Appl.* **2012**, *62* (6), 463–478. <https://doi.org/10.1080/10407782.2012.703095>.
- (22) Zhao, C.; Zha, W.; Cai, R.; Nie, X.; Tjong, J. A New Eco-Friendly Anticorrosion Strategy for Ferrous Metals: Plasma Electrolytic Aluminating. *ACS Sustain. Chem. Eng.* **2019**, *7* (5), 5524–5531. <https://doi.org/10.1021/acssuschemeng.8b06839>.

- (23) Nie, X.; Meletis, E. I.; Jiang, J. C.; Leyland, A.; Yerokhin, A. L.; Matthews, A. Abrasive Wear/Corrosion Properties and TEM Analysis of Al₂O₃ Coatings Fabricated Using Plasma Electrolysis. *Surf. Coatings Technol.* **2002**, *149* (2–3), 245–251. [https://doi.org/10.1016/S0257-8972\(01\)01453-0](https://doi.org/10.1016/S0257-8972(01)01453-0).
- (24) Murthy, N. S.; Minor, H. General Procedure for Evaluating Amorphous Scattering and Crystallinity from X-Ray Diffraction Scans of Semicrystalline Polymers. *Polymer (Guildf)*. **1990**, *31* (6), 996–1002. [https://doi.org/10.1016/0032-3861\(90\)90243-R](https://doi.org/10.1016/0032-3861(90)90243-R).
- (25) Khorsand Zak, A.; Abd. Majid, W. H.; Abrishami, M. E.; Yousefi, R. X-Ray Analysis of ZnO Nanoparticles by Williamson-Hall and Size-Strain Plot Methods. *Solid State Sci.* **2011**, *13* (1), 251–256. <https://doi.org/10.1016/j.solidstatesciences.2010.11.024>.
- (26) Burton, A. W.; Ong, K.; Rea, T.; Chan, I. Y. On the Estimation of Average Crystallite Size of Zeolites from the Scherrer Equation: A Critical Evaluation of Its Application to Zeolites with One-Dimensional Pore Systems. *Microporous Mesoporous Mater.* **2009**, *117* (1–2), 75–90. <https://doi.org/10.1016/j.micromeso.2008.06.010>.
- (27) Gonçalves, N. S.; Carvalho, J. A.; Lima, Z. M.; Sasaki, J. M. Size-Strain Study of NiO Nanoparticles by X-Ray Powder Diffraction Line Broadening. *Mater. Lett.* **2012**, *72*, 36–38. <https://doi.org/10.1016/j.matlet.2011.12.046>.
- (28) Lu, Y.; Zhang, X.; Xiang, P.; Dong, D. Analysis of Thermal Temperature Fields and Thermal Stress under Steady Temperature Field of Diesel Engine Piston. *Appl. Therm. Eng.* **2017**, *113*, 796–812. <https://doi.org/10.1016/j.applthermaleng.2016.11.070>.
- (29) Harris, D. H.; Lutz, J. Thermal Barrier Coatings Technology for Diesel Engines. In *SAE Technical Papers*; 1988. <https://doi.org/10.4271/880437>.

- (30) Alvarez, F. X.; Jou, D.; Sellitto, A. Pore-Size Dependence of the Thermal Conductivity of Porous Silicon: A Phonon Hydrodynamic Approach. *Appl. Phys. Lett.* **2010**, *97* (3), 033103. <https://doi.org/10.1063/1.3462936>.
- (31) Kim, H.; Choi, D.; Kim, K.; Chu, W.; Chun, D. M.; Lee, C. S. Effect of Particle Size and Amorphous Phase on the Electrochromic Properties of Kinetically Deposited WO₃ Films. *Sol. Energy Mater. Sol. Cells* **2018**, *177*, 44–50. <https://doi.org/10.1016/j.solmat.2017.06.010>.
- (32) Thomas, R.; Ganesa-Pillai, M.; Aswath, P. B.; Lawrence, K. L.; Haji-Sheikh, A. Analytical/Finite-Element Modeling and Experimental Verification of Spray-Cooling Process in Steel. *Metall. Mater. Trans. A Phys. Metall. Mater. Sci.* **1998**, *29* (5), 1485–1498. <https://doi.org/10.1007/s11661-998-0364-y>.
- (33) Holmgren, D.; Källbom, R.; Svensson, I. L. Influences of the Graphite Growth Direction on the Thermal Conductivity of Cast Iron. *Metall. Mater. Trans. A Phys. Metall. Mater. Sci.* **2007**, *38* (2), 268–275. <https://doi.org/10.1007/s11661-006-9016-2>.
- (34) Gesele, G.; Linsmeier, J.; Drach, V.; Fricke, J.; Arens-Fischer, R. Temperature-Dependent Thermal Conductivity of Porous Silicon. *J. Phys. D. Appl. Phys.* **1997**, *30* (21), 2911–2916. <https://doi.org/10.1088/0022-3727/30/21/001>.
- (35) Aliasghari, S.; Němcová, A.; Skeldon, P.; Thompson, G. E. Influence of Coating Morphology on Adhesive Bonding of Titanium Pre-Treated by Plasma Electrolytic Oxidation. *Surf. Coatings Technol.* **2016**, *289*, 101–109. <https://doi.org/10.1016/j.surfcoat.2016.01.042>.
- (36) Aliasghari, S.; Ghorbani, M.; Skeldon, P.; Karami, H.; Movahedi, M. Effect of Plasma Electrolytic Oxidation on Joining of AA 5052 Aluminium Alloy to Polypropylene

Using Friction Stir Spot Welding. *Surf. Coatings Technol.* **2017**, *313*, 274–281.
<https://doi.org/10.1016/j.surfcoat.2017.01.084>.

(37) Cai, R.; Zhang, J.; Nie, X.; Tjong, J.; Matthews, D. T. A. Wear Mechanism Evolution on Brake Discs for Reduced Wear and Particulate Emissions. *Wear* **2020**, 452–453. <https://doi.org/10.1016/j.wear.2020.203283>.

6. CHAPTER 6 Pore-sealing Treatment of Plasma Electrolytic Aluminating Coating on Cast Iron

6.1 Introduction

Plasma electrolysis for surface engineering of metals has attracted researchers' attention because of its cost-effectiveness, environmentally friendliness and superior properties ¹. Based on the conductive properties of the oxides formed on the metal surface, plasma electrolysis could be divided into plasma electrolytic oxidation (PEO) and plasma electrolytic polishing (PEP) ^{2,3}. PEO is suitable for the "valve metals", which form n-type oxides or insulators like Al₂O₃, TiO₂, MgO, ZrO₂, and ZnO. On the other hand, PEP, i.e. anodic dissolution, dominates for the "non-valve metals" like steels, nickel and copper which form p-type oxides ⁴. The PEO process has been used for corrosion protection of aluminum and magnesium alloys ⁵⁻¹². Recently, several researchers have reported the application of PEO process on ferrous metals in the electrolyte contains sodium aluminate and sodium phosphate ¹³⁻¹⁶. Since the aluminate ions from the electrolyte contributed mainly to the plasma chemical reaction, this process could also be termed as plasma electrolytic aluminating (PEA) process ¹⁷. The hard-ceramic coatings produced by PEA process on the ferrous metals provide excellent wear resistance, good corrosion resistance and low thermal conductivity ¹⁸.

However, the PEA coatings are intrinsically highly porous. Extremely strong discharges could occasionally penetrate the coating and reach the substrate, leaving open pores and cracks across the coating. These open pores and cracks would impart the coating's corrosion performance, especially under the longtime exposure to corrosive media ¹⁹⁻²¹. Therefore, post-treatment is desired to seal these open pores and cracks. The advantages of

sol-gel technique include low processing temperature, good homogeneity, and environmental friendliness ²²⁻²⁶. The sol-gel method is a wet chemical technique and involving several stages: hydrolysis and polycondensation, drying, and sintering ²⁵⁻²⁷. Depending on the sintering temperature, the structure of sol-gel coatings may undergo changes. A sol-gel coating can be applied to the surface by dip-coating or spin-coating. Typically, the type of catalyst determines the pH of sols and affects the shapes (films, powders or monoliths) of sol-gel materials ²⁷. By properly selecting the synthesis parameters, a sol with moderate viscosity and an average particle size less than 20 nm could be obtained. Such a moderate viscosity and small particle size make the sol easily fill the pores of the coating prepared by PEA process.

Electroless nickel plating (EP) has a proven ability to provide improved corrosion resistance. The catalysts of this reaction are some metals, such as Co, Pd, Rh and Ni itself ²⁸⁻³⁰. Once an initial layer of nickel has formed on the surface, the reaction can proceed spontaneously. Electroless nickel plating could also proceed spontaneously on iron because an initial nickel layer could be obtained by a displacement reaction ³⁰. During electroless nickel plating of PEA coated iron samples, nickel is supposed to grow from the interface where the open pores and cracks locate. Eventually, the nickel could seal the open pores and cracks of the coating and thus enhance the corrosion resistance. The total volume of the pores and cracks on the PEA coating is relatively small, which would help to restrict the amount of actual usage of Ni metals and thus reduce the negative impact in environment. The electroless plated nickel with high hardness could enter into the tiny pores of the PEA coating and thus might be able to further improve the coating's hardness.

In this work, two post-treatment methods, electroless nickel plating and sol-gel dip coating, were used to seal the open pores of PEA coatings prepared on the iron substrate. The influence post-treatments on the corrosion resistance and thermal conductivities of the coatings were investigated.

6.2 Experimental setup

6.2.1 Preparation of PEA coatings

Compacted graphite iron (CGI, 0.2-1% Mn, 2.5-4% C, 1-3% Si, <0.25% S, <0.1% P, and Fe balance) samples ($\Phi 25.4 \text{ mm} \times 3 \text{ mm}$) were polished with #1200 abrasive paper, rinsed with distilled water and ultrasonically cleaned in ethanol. The samples were immersed in electrolyte (15-20 g/L NaAlO_2 as a precursor and 1-5 g/L Na_3PO_4 as a buffer dissolved in deionized water, pH=12, Sigma Aldrich) and positively biased in stainless steel vessel. A unipolar pulsed ($f = 1000 \text{ Hz}$, duty cycle is 0.2) power supply was used in present work. After the initiation of plasma discharges, the current density was kept at 0.15 A/cm^2 for 20 mins to produce coatings with thickness around $40 \text{ }\mu\text{m}$. After taking out from the electrolyte, all samples were thoroughly rinsed with deionized water and air dried at room temperature. Then some of these samples were used for electroless nickel plating and sol-gel dip coating, respectively.

6.2.2 Preparation of PEA-EP hybrid coatings

Before electroless nickel plating, the PEA samples were ultrasonically degreased in acetone. Electroless nickel bath contains 21 g/L nickel sulphate, 24 g/L sodium hypophosphite, 25 g/L lactic acid, 3 g/L propionic acid was operated at pH 4.7–4.9 and temperature $85 \pm 2 \text{ }^\circ\text{C}$ ³¹. The obtained Ni deposition rate was about $25 \text{ }\mu\text{m/h}$. To fully seal

the open pores/cracks, the specimens were plated for 1.5 h. After removal from the plating bath, the samples were thoroughly rinsed with distilled water and air dried. To simplify, samples only processed by plasma electrolytic aluminating process were named as PEA samples, while samples processed by plasma electrolytic aluminating and electroless nickel plating duplex treatment were named as PEA-EP samples.

6.2.3 Preparation of SiO₂ sol and PEA-SiO₂ hybrid coatings

SiO₂ sols were prepared by hydrolysis and condensation reactions of tetraethyl orthosilicate (TEOS, Sigma Aldrich, >98%) in the mixture of ethyl alcohol (EtOH, Sigma Aldrich, 99.7%) and water, with ammonia hydroxide (NH₄OH, Sigma Aldrich, 28%) as the catalyst. First, TEOS was added into a sealable glass container precisely. Second, EtOH and H₂O were added in the glass container and then immediately stirred for 10 min. Finally, NH₄OH were added in the glass container drop by drop. The final molar ratio of TEOS: EtOH: NH₄OH: H₂O was 1: 48: 0.09: 15. The resultant sols were stirred for 12 hours at 30 °C and then aged in sealed glass container at room temperature for 4 days. According to the literature²⁷, the average particle size of prepared sols should be ~ 16 nm. The prepared PEA coatings were cleaned with ethanol in an ultrasonic bath, rinsed with deionized water and then dry in air. The silica sol was applied on the PEA coatings by dip-coating method. The withdraw speed was 100 mm/min. After withdrawing from the sol, the samples were dried at 85 °C. To make sure all the open pores are sealed, the dip-coating process were repeated for 10 times. Finally, the samples were sintered at 450 °C for 2 hours under ambient atmosphere to densify the silica. After the heat treatment, the coating was polished to remove the loose surface layer (the surface roughness of polished hybrid coating was Ra

~ 1.0 μm). For the sake of simplicity, the samples with sol-gel treatment were named as PEA-SiO₂.

6.2.4 Materials characterization, corrosion test and thermal conductivity measurement

Phase structures of the coatings were determined by X-ray diffraction (XRD, PROTO AXRD), using Cu K α radiation in scans from 20° to 100° (10° to 100° for PEA-SiO₂ sample). The microstructures of coatings were observed by a scanning electron microscopy (SEM, Hitachi TM3030 Plus). Hardness was measured from the cross-sections of the coatings and substrate by a Vickers microhardness tester (Wilson VH1102) with a load of 25 g and a holding time of 12 s. Electrochemical impedance spectroscopy (EIS) in the frequency range between 10⁶ and 10⁻² Hz with ± 10 mV amplitude was measured by using the electrochemical workstation (BioLogic SP-150) after the test sample was immersed in 3.5 wt.% NaCl solution for 1~120 hours. Then, potentiodynamic polarization tests were carried out from -0.5 V to 0.5 V with respect to the corrosion potential (E_{corr}) at a scan rate of 1 mV/s. Ag/AgCl (KCl saturated) and Pt wire were selected as reference electrode and counter electrode, respectively. The working surface area for each specimen was controlled to be 0.5 cm². All EIS data were analyzed using EC-Lab software. The thermal conductivities were measured using the guarded heat flow method. A detailed explanation of the measurement could be found in previous study ¹⁸.

6.3 Results and discussion

6.3.1 Materials characterization of PEA, PEA-EP and PEA-SiO₂ samples

Figure 6-1 illustrates the processes of electroless nickel plating and sol-gel dip coating methods. The electroless nickel plating is a bottom-to-up process, during which the nickel grows from the substrate to the coating surface along the open pores and cracks, as illustrated in Figure 6-1a. Therefore, the surface pores were well retained and might serve as oil reservoirs during the lubricated sliding conditions. On the other hand, the sol-gel dipping is an up-to-bottom process, where the silica sol was applied on the sample surface and then filled the surface pores by capillary effect as shown in Figure 6-1b. After heat-treatment, the silica sol was transferred into fused silica and sealed all the surface pores (including the open pores and/or cracks). Thus, the sample surface is much smoother after the sol-gel dipping treatment.

The average hardness of the cast iron substrate, the PEA coating, the PEA-EP coating and the PEA-SiO₂ coating are 280 ± 20 HV, 822 ± 50 HV, 1150 ± 115 HV and 875 ± 67 HV, respectively. The PEA-EP coating has the highest hardness among all samples, which could be attributed that high hardness nickel filled into the pores of the PEA coating and thus provided additional load bearing capacity. It is well accepted that higher hardness is beneficial for improving wear resistance. It also needs to be pointed out that some surface pores could be retained after EP treatment. These surface pores could act as oil reservoirs during lubricated sliding or dimples to collect the wear debris during dry sliding, which are beneficial the tribological performance. Therefore, the PEA-EP sample should have the best wear resistance among all samples.

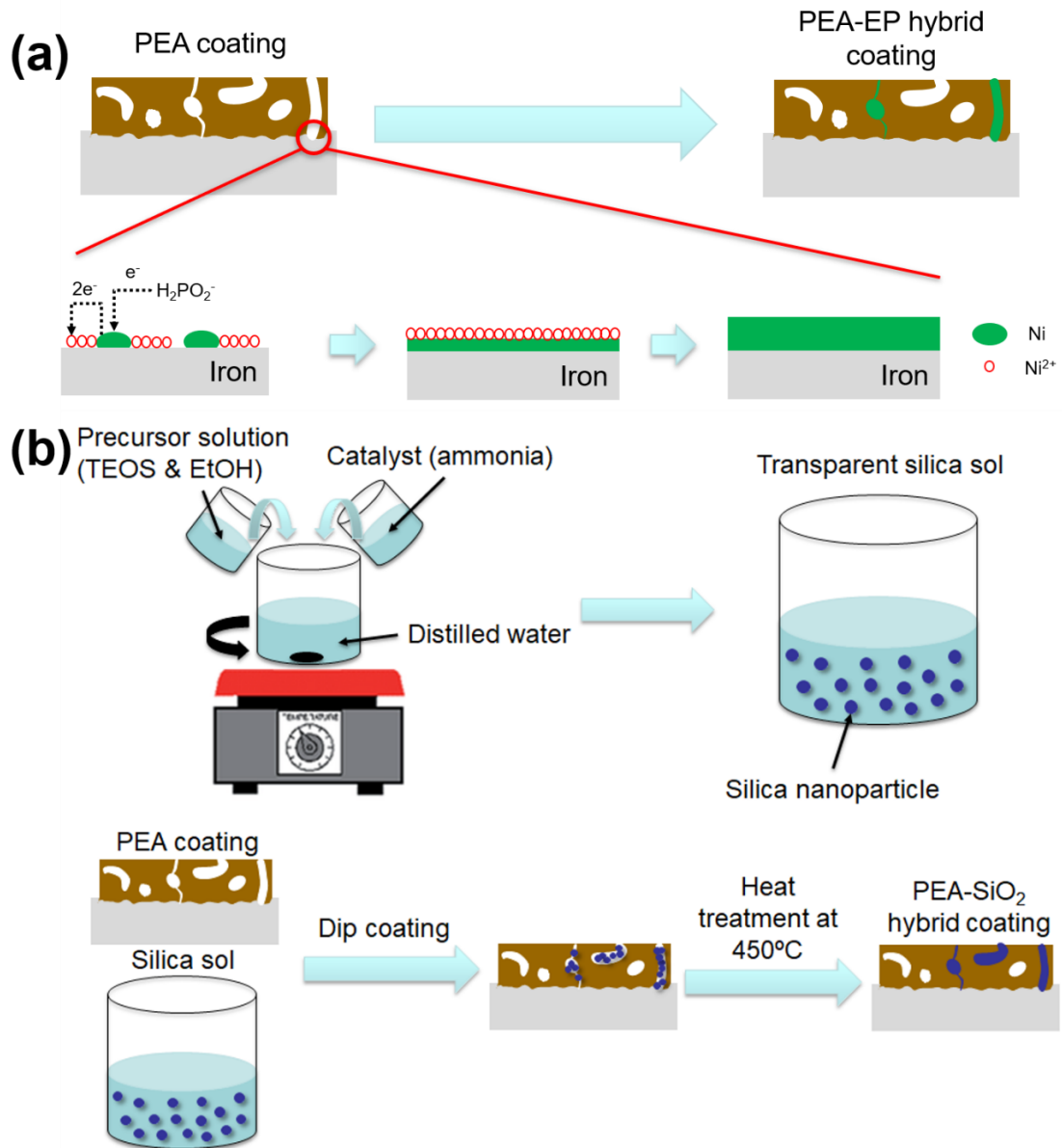


Figure 6-1 Illustration of the (a) electroless nickel plating and (b) sol-gel dip coating processes.

Figure 6-2 shows the microstructure of PEA, PEA-EP and PEA-SiO₂ samples. The PEA coating has a porous surface structure. Pores and cracks could be observed in Figures 6-2a and 6-2b. These pores/cracks might be the weak points of the coating served in corrosive environment since localized corrosion of the substrate cast iron might occur.

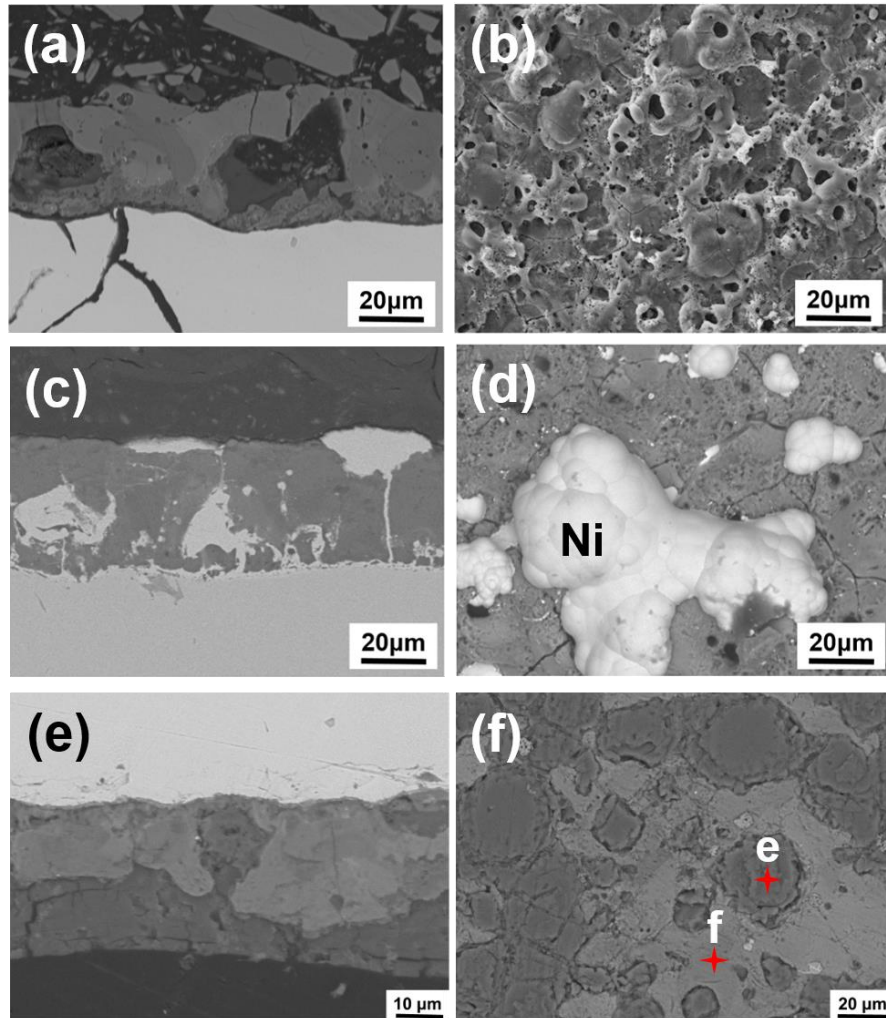
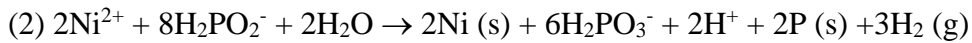
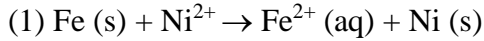


Figure 6-2 (a) and (b) SEM images of cross-section and surface of the PEA sample; (c) and (d) SEM images of cross-section and surface of the PEA-EP sample; (e) and (f) SEM images of cross-section of the as-sintered PEA-SiO₂ sample and surface of the polished PEA-SiO₂ sample.

Figures 6-2c and 6-2d demonstrate the cross-section and surface SEM images of the PEA-EP sample. As shown in Figure 6-2c, the pores and cracks were filled with metallic nickel. The nickel could grow to the coating surface at some location after a long-time EP

treatment, as shown in Figure 6-2d. As illustrated in Figure 6-1a, following reactions occurred during the EP treatment step by step ³⁰:



At the beginning of EP treatment, reaction (1) occurred, and the nickel seeds were formed at the coating-substrate interface. After these nickel seeds covered the interface, reaction (1) stopped, and reaction (2) started with these nickel seeds acted as catalysts. According to reaction (2), the nickel developed layer by layer along the open pores and cracks in the PEA coating. Phosphorus was deposited simultaneously with nickel to form Ni-P alloys ³¹. After long-time EP treatment, all open pores and cracks were filled electroless plated nickel.

Figure 6-2e shows the cross-section of as-sintered PEA-SiO₂ hybrid coating surface. The whole sample was covered by a silica layer. The open pores were filled with the silica. Some cracks could be found in the top silica layer, which could be attributed to the thermal stresses due to the heat treatment. After carefully grinding to remove the top silica layer, the surface morphology of the PEA-SiO₂ coating was revealed. As demonstrated in Figure 6-2f, all the surface pores of the PEA coating were filled by the silica. As demonstrated in Table 6-1, the EDS analysis at point e shows the Si/O ratio close to 0.5, which confirms that the dark gray particles are silica.

Table 6-1 EDS point analysis of the selected areas of the PEA-SiO₂ coating

Area	Fe (at. %)	Al (at. %)	Si (at. %)	O (at. %)
e	0.90	1.71	31.87	65.51
f	10.15	24.81	7.01	58.04

Figure 6-3 illustrates the XRD spectra of PEA, PEA-EP and PEA-SiO₂ samples. The peak at 31.4° represents the (220) planes of FeAl₂O₄ (JCPDS # 3-0894), while the peaks at 37.0°, 55.9°, 59.7° and 65.7° confirm the existence of Al₂O₃ (JCPDS # 46-1212). The iron peak at 45.1° might come from the substrate. The peak at 44.6° represents the (111) planes of Ni. However, there is no crystalline peak for SiO₂. A halo peak at ~20° indicates that SiO₂ exists as amorphous materials in the hybrid coating.

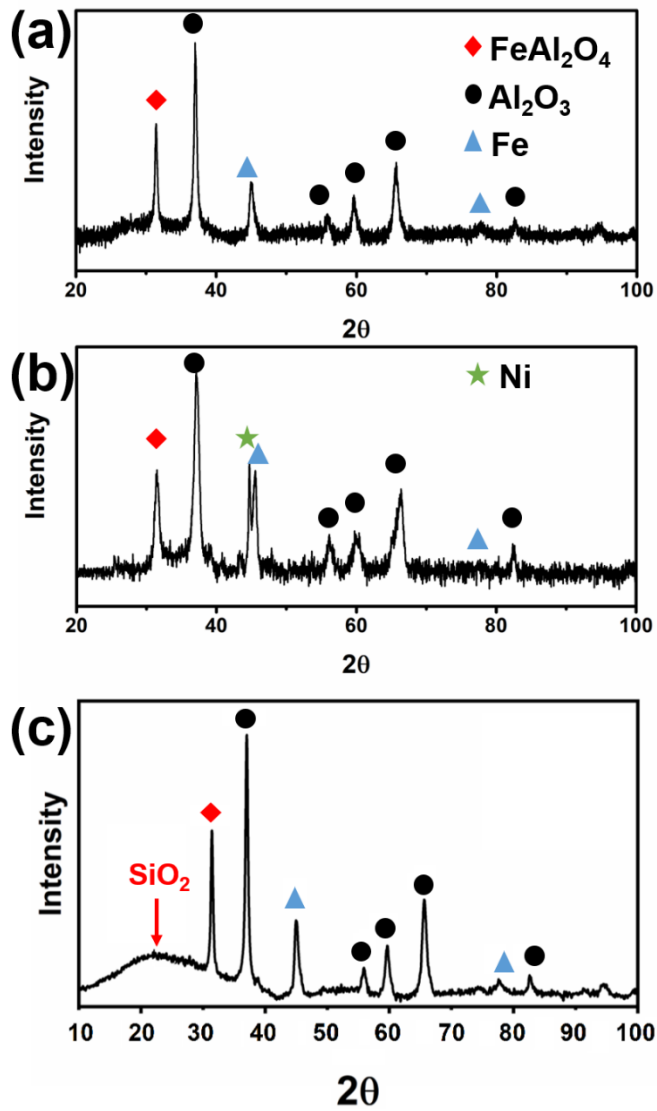


Figure 6-3 XRD spectra of the (a) PEA, (b) PEA-EP and (c) PEA-SiO₂ samples.

6.3.2 Electrochemical measurements

The electrochemical impedance spectra (EIS) of PEA, PEA-EP and PEA-SiO₂ samples after immersed in sodium chloride solution for 1 hour were illustrated in Figures 6-4a, 6-4c and 6-4e, respectively.

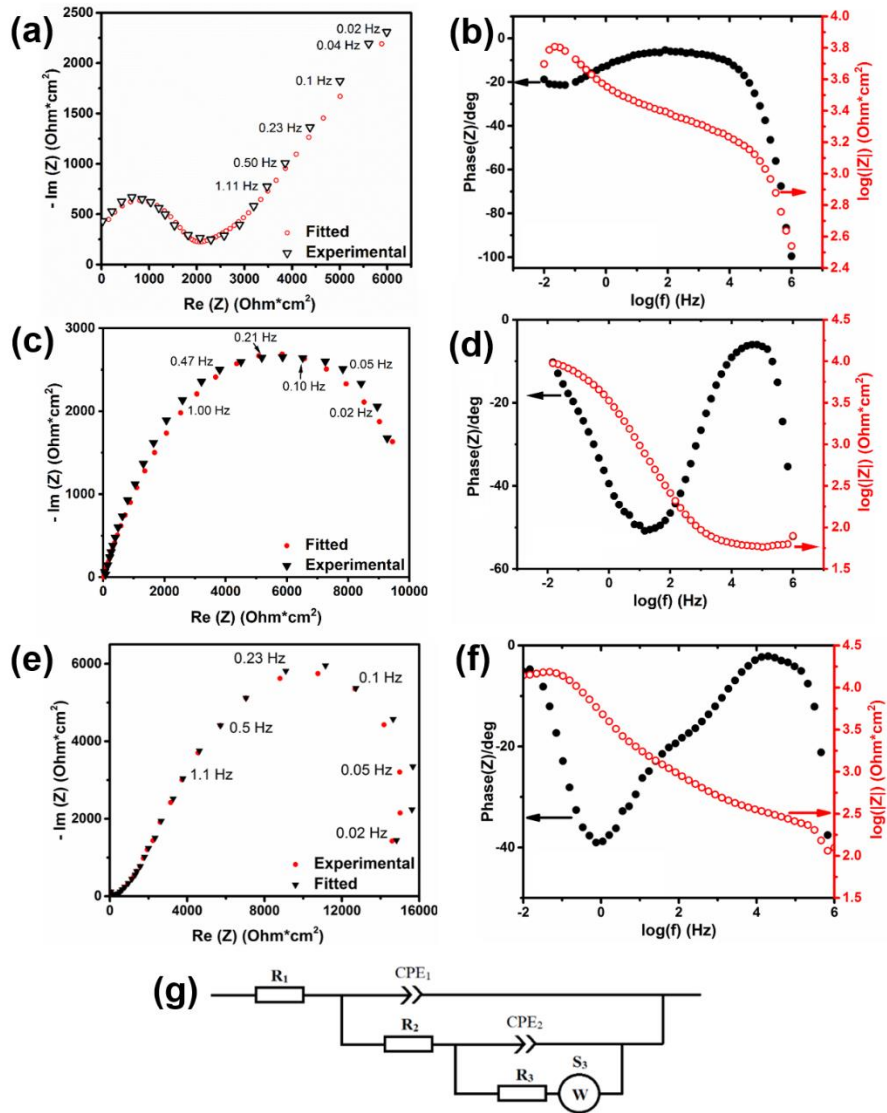


Figure 6-4 (a), (c) and (e) Nyquist plots of PEA, PEA-EP and PEA-SiO₂ samples after immersion in 3.5 wt.% NaCl solution for 1 hour; (b), (d) and (f) Bode plots corresponding to EIS spectra in (a), (c) and (e), respectively; (g) equivalent circuit.

The equivalent circuit model used for fitting the EIS curves is shown in Figure 6-4g. The goodness of the fit was determined by the chi-squared (χ^2) values in the range of 0.01–0.001 and the fitting parameters are summarized in Table 6-2. In Figure 6-4g, R_1 represents the solution resistance, R_2 denotes the charge transfer resistance at the coating–electrolyte interface, R_3 is associated with the resistance of the ceramic coating. Noticing the surface inhomogeneity, the constant phase element (CPE) was employed³². The impedance of CPE is expressed by the following equation³²:

$$Z_{CPE} = 1/[T(j\omega)^P] \quad (\text{Eq. 1})$$

where j is the imaginary unit, ω is the angular frequency defined as $\omega = 2\pi f$, f is the frequency in Hz, T is CPE constant; the value of P varies between 0 and 1. The values 0 and 1 of P imply the CPE of the circuit to be pure resistor and ideal capacitor, respectively. Furthermore, diffusion through the pores of the coating can be covered through Warburg diffusion element (S). The impedance of S can be expressed as follows^{33,34}:

$$Z_w = \frac{W}{\sqrt{i\omega}} \tanh\left(2\delta \sqrt{\frac{i\omega}{D}}\right) \quad (\text{Eq. 2})$$

where “ δ ” is the thickness of the diffusion layer, “ D ” is the diffusion coefficient, “ ω ” is the angular frequency W is the Warburg parameters, obtained from the EIS fitting curves and “ i ” is the imaginary number. Figures 6-4b, 6-4d and 6-4f show the Bode plots corresponding to the EIS spectra. As shown in Figure 6-4b, the $\log|Z|$ vs. $\log(f)$ plot discloses linear segment with a slope nearby $-1/2$ at high frequency domains, which means the existence of the Warburg diffusion element for PEA samples. Figures 6-4d and 6-4f, on the other hand, did not demonstrate linear segment with a slope nearby $-1/2$, which means that there is no Warburg diffusion element for PEA-EP and PEA-SiO₂

samples. The lack of Warburg diffusion element could be attributed to the pore-sealing effects.

All the EIS curves present depressed semicircles, suggesting CPE phenomenon instead of pure capacitive phenomenon. It is also noted that the PEA-SiO₂ sample exhibits the largest semi-circle among all samples and thus can be regarded as the highest corrosion resistance.

Table 6-2 Fitting parameters of the EIS curves.

Sample	PEA-1h	PEA-5d	PEA-EP-1h	PEA-EP-5d	PEA-SiO ₂ -1h	PEA-SiO ₂ -5d
R ₁ (Ω·cm ²)	15.6	14.8	16.2	15.6	15.8	16.2
CPE ₁ (F·s ^{P₁})	6.0E-10	2.7E-8	6.2E-5	6.8E-5	1.0E-7	1.3E-7
P ₁	0.71	0.99	0.64	0.65	0.74	0.75
R ₂ (Ω·cm ²)	1871	1267	3020	2850	9193	8851
CPE ₂ (F·s ^{P₂})	1.9E-4	7.7E-5	2.2E-4	1.8E-4	3.4E-4	3.3E-4
P ₂	0.26	0.14	0.56	0.57	0.57	0.55
R ₃ (Ω·cm ²)	4279	1157	10647	9566	27660	26840
S ₃ (Ω·s ^{-1/2})	2985	954	--	--	--	--

Figure 6-5 shows the EIS results after immersed in sodium chloride solution for different time. As shown in Figure 6-5a, the maximum impedance of PEA sample decreased from 6500 Ω to 2500 Ω as the immersion time increased from 1 hour to 5 days. The sharply decreased corrosion resistance of PEA sample after immersion could be explained by the degradation of R₃, as shown in Table 6-2. As mentioned before, the PEA coating has some open pores/cracks, which are the weak points. During the immersion tests, localized corrosion of the substrate cast iron might occur at these sites, leading to the degradation of corrosion resistance. On the other hand, the maximum impedences of PEA-EP and PEA-SiO₂ samples only decreased slightly, which indicates that the PEA-EP and PEA-SiO₂

hybrid coatings could provide better corrosion protection compared with the PEA coatings. The PEA-SiO₂ hybrid coating has the best corrosion performance among all samples.

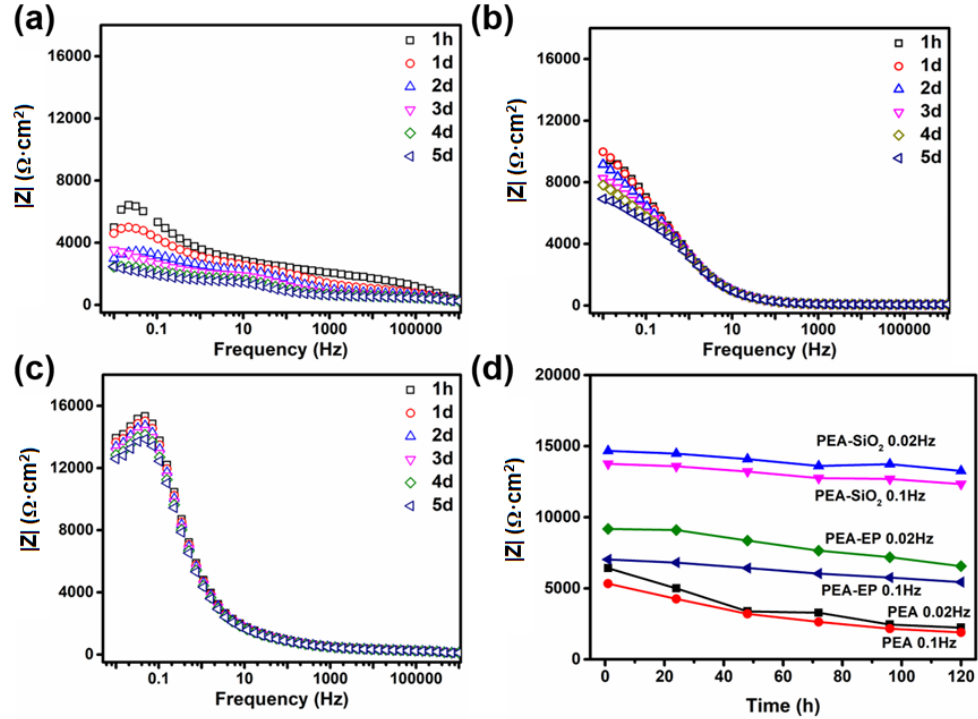


Figure 6-5 Impedance spectra of (a) PEA (b) PEA-EP and (c) PEA-SiO₂ samples after different immersion time in 3.5 wt.% NaCl solution, (d) variation of impedance with time at different frequencies.

To further evaluating the coatings' long-term corrosion behavior, potentiodynamic polarization tests were also conducted after immersed in the 3.5 wt.% NaCl solution for 5 days. As shown in Figure 6-6, the corrosion potential (E_{corr}), corrosion current density (i_{corr}), cathodic and anodic Tafel constants (β_c and β_a) could be obtained from the potentiodynamic polarization curves and the results are summarized in Table 6-3. The corrosion potentials are -0.86V, -0.63V and -0.43V for the PEA, PEA-EP and PEA-SiO₂ samples, respectively.

The higher corrosion potential means less thermodynamic tendency for corrosion to occur. Therefore, the PEA-SiO₂ sample is least likely to be corroded.

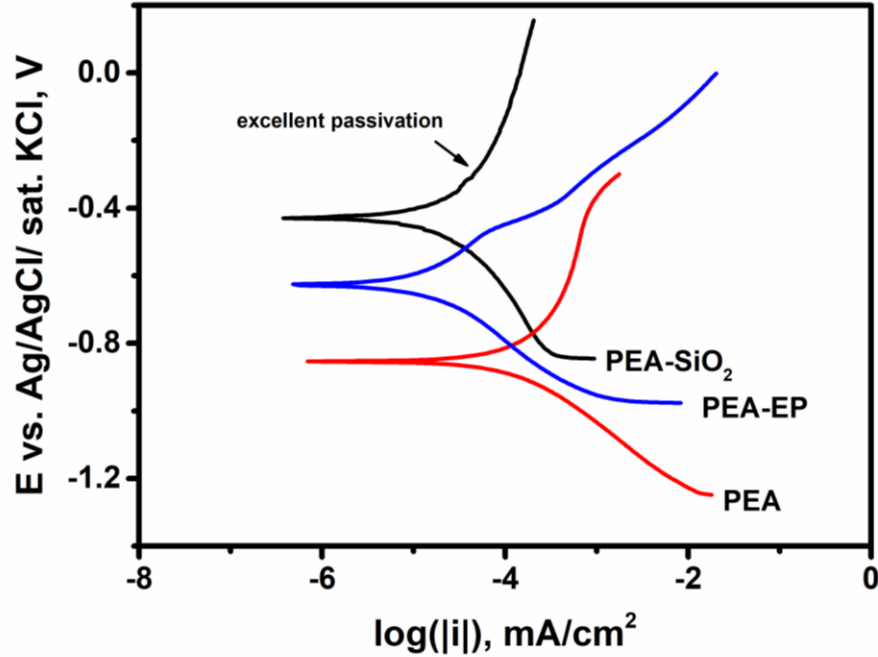


Figure 6-6 Potentiodynamic polarization curves of the PEA, PEA-EP and PEA-SiO₂ samples after immersed in 3.5 wt.% NaCl solution for 5 days.

Table 6-3 Kinetic parameters obtained from the polarization curves.

Sample	β_a (V/dec)	β_c (V/dec)	E_{corr} (V)	i_{corr} (A/cm ²)	R_p (k Ω ·cm ²)
PEA	0.514	0.243	-0.86	6.2E-6	11.58
PEA-EP	0.238	0.193	-0.63	1.5E-6	30.94
PEA-SiO ₂	0.314	0.256	-0.43	5.0E-7	126.03
Cast iron*	0.527	0.037	-0.88	4.5E-6	3.3

* Data was retrieved from Table 4-1.

The corrosion current densities were 6.2×10^{-6} A/cm², 1.5×10^{-6} A/cm² and 0.5×10^{-6} A/cm² for PEA, PEA-EP and PEA-SiO₂ samples, respectively. It has to be pointed out that the

potentiodynamic polarization curves were obtained after 5 days immersion in the 3.5 wt.% NaCl solution. The corrosion current densities for PEA and PEA-EP samples are close to each other and are close to the corrosion current density for fresh cast iron (4.5×10^{-6} A/cm² as shown in Figure 4-8 and Table 4-1 in Chapter 4), which means both PEA and PEA-EP treatments cannot provide excellent long-term protection for cast iron substrate against corrosion. On the other hand, the corrosion current density for PEA-SiO₂ sample after 5 days immersion in the 3.5 wt.% NaCl solution is 0.5×10^{-6} A/cm², which is much smaller than those for PEA and PEA-EP samples after immersion and is ~10 times smaller than that for the fresh cast iron. Thus, the PEA-SiO₂ treatment could provide excellent long-term protection for cast iron substrate against corrosion.

Polarization resistances (R_p) were determined with Stern-Geary equation ³⁵:

$$R_p = (\beta_a * \beta_c) / [2.303 * (\beta_a + \beta_c) * i_{corr}] \quad (\text{Eq. 3})$$

The polarization resistance of PEA-SiO₂ sample after 5 days immersion in the 3.5 wt.% NaCl solution ($126.03 \text{ k}\Omega \cdot \text{cm}^2$) is ~40 times higher than that of the fresh cast iron ($3.3 \text{ k}\Omega \cdot \text{cm}^2$). Excellent anodic passivation was also obtained for the PEA-SiO₂ sample, as shown in Figure 6-6.

The variation of open circuit potentials (E_{oc}) for blank cast iron and PEA-SiO₂ sample were shown in Figure 6-7. The large fluctuation of E_{oc} for blank cast iron might be attributed to the breaking of passivation layer by galvanic corrosion as well as pitting corrosion. The stable open circuit potential for PEA-SiO₂ sample indicates the uniform and steady corrosion, which could be explained by the excellent anodic passivation behavior as shown in Figure 6-6. Based on above analyses, the PEA-SiO₂ coating provides the best corrosion protection for the cast iron substrate.

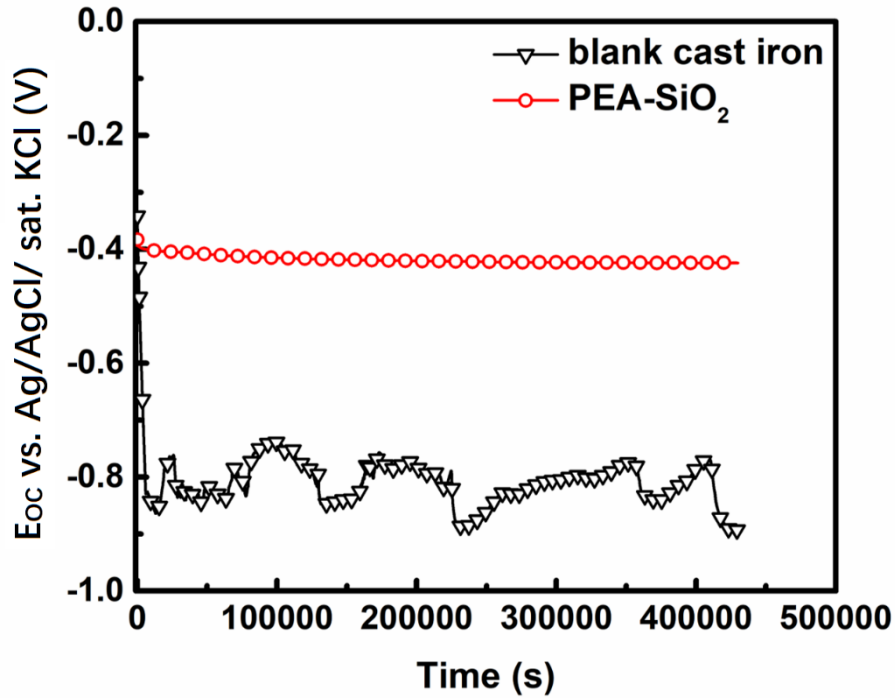


Figure 6-7 Variation of open circuit potentials (E_{oc}) for blank cast iron and PEA-SiO₂ sample.

6.3.3 Thermal conductivity measurements

The thermal conductivities of the PEA, PEA-EP and PEA-SiO₂ coatings were plotted in Figure 6-8. The thermal conductivities were 0.63 ± 0.12 W/(m·K), 1.44 ± 0.16 W/(m·K) and 0.8 ± 0.1 W/(m·K) for the PEA, PEA-EP and PEA-SiO₂ coatings, respectively. The PEA-EP and PEA-SiO₂ hybrid coatings could be regarded as nickel-filled or silica-filled ceramic composite. In the present work, the volume fractions of metallic nickel and fused silica were estimated to be ~30% and ~27%, respectively. The thermal conductivity of the hybrid coating could be estimated by Rayleigh model³⁶:

$$K_{eff}/K_m = 1 + 3\phi / [(K_1 + 2K_m)/(K_1 - K_m) - \phi] \quad (\text{Eq. 4})$$

where K_{eff} and K_m are the thermal conductivities of the hybrid coating and the ceramic matrix, i.e., PEA coating (0.63 W/m·K), respectively. K_1 the thermal conductivity of filler, i.e., metallic nickel (~80 W/m·K) and fused silica (~1.38 W/m·K); ϕ the volume fraction of the filler (0.3 and 0.27 for PEA-EP and PEA-SiO₂ coating, respectively). The predicted thermal conductivities of PEA-EP and PEA-SiO₂ coatings is ~1.3 and ~0.9 W/(m·K), respectively.

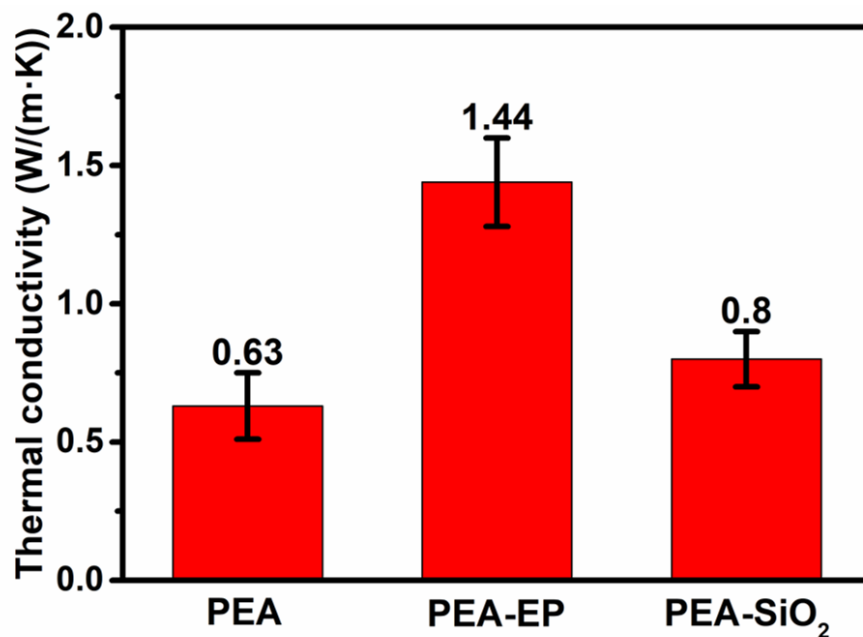


Figure 6-8 Thermal conductivities of PEA coating and PEA-EP and PEA-SiO₂ hybrid coatings.

6.3.4 Discussion

Based on above analyses, the PEA-EP and PEA-SiO₂ treatments are proposed for different engineering applications. For the PEA-EP sample, some surface pores were well retained and might serve as oil reservoirs during the lubricated sliding or dimples to collect the wear

debris during the dry sliding. Moreover, electroless plated nickel has high hardness which not only provides corrosion protection for the coating-substrate interface, but also is beneficial for improving wear resistance. The thermal conductivity of PEA-EP coating is pretty high. When a 20 μm -thick coating was applied on a 3 mm-thick cast iron substrate, the effect thermal conductivity (coating plus substrate) is $\sim 38 \text{ W}/(\text{m}\cdot\text{K})$, which is very close to that of the cast iron. Therefore, PEA-EP treatment is aimed for the application where high wear resistance, moderate corrosion resistance and high thermal conductivity are required, for instance the braking rotors.

For the PEA-SiO₂ sample, the surface roughness is significantly reduced. Due to the insulation property of SiO₂, the PEA-SiO₂ coating has the best corrosion performance among all samples and provides excellent long-term corrosion protection for cast iron substrate. The thermal conductivity of PEA-SiO₂ coating is low. When a 100 μm -thick coating was applied on a 3 mm-thick cast iron substrate, the effect thermal conductivity (coating plus substrate) is $\sim 16 \text{ W}/(\text{m}\cdot\text{K})$, which is much lower than that of the cast iron. The potential application of PEA-SiO₂ hybrid coating is thermal management of diesel steel pistons where high corrosion resistance, low thermal conductivity and low surface roughness are required.

The thermal shock resistance of PEA-EP and PEA-SiO₂ samples were also evaluated by repeatedly heating at 425°C and water quenched at 25°C for up to 100 cycles. The appearance of PEA-EP and PEA-SiO₂ samples are shown in Figure 6-9. After 100 cycles of thermal shock test, both the PEA-EP and PEA-SiO₂ samples seem to be intact, which implies superior thermal shock resistance.

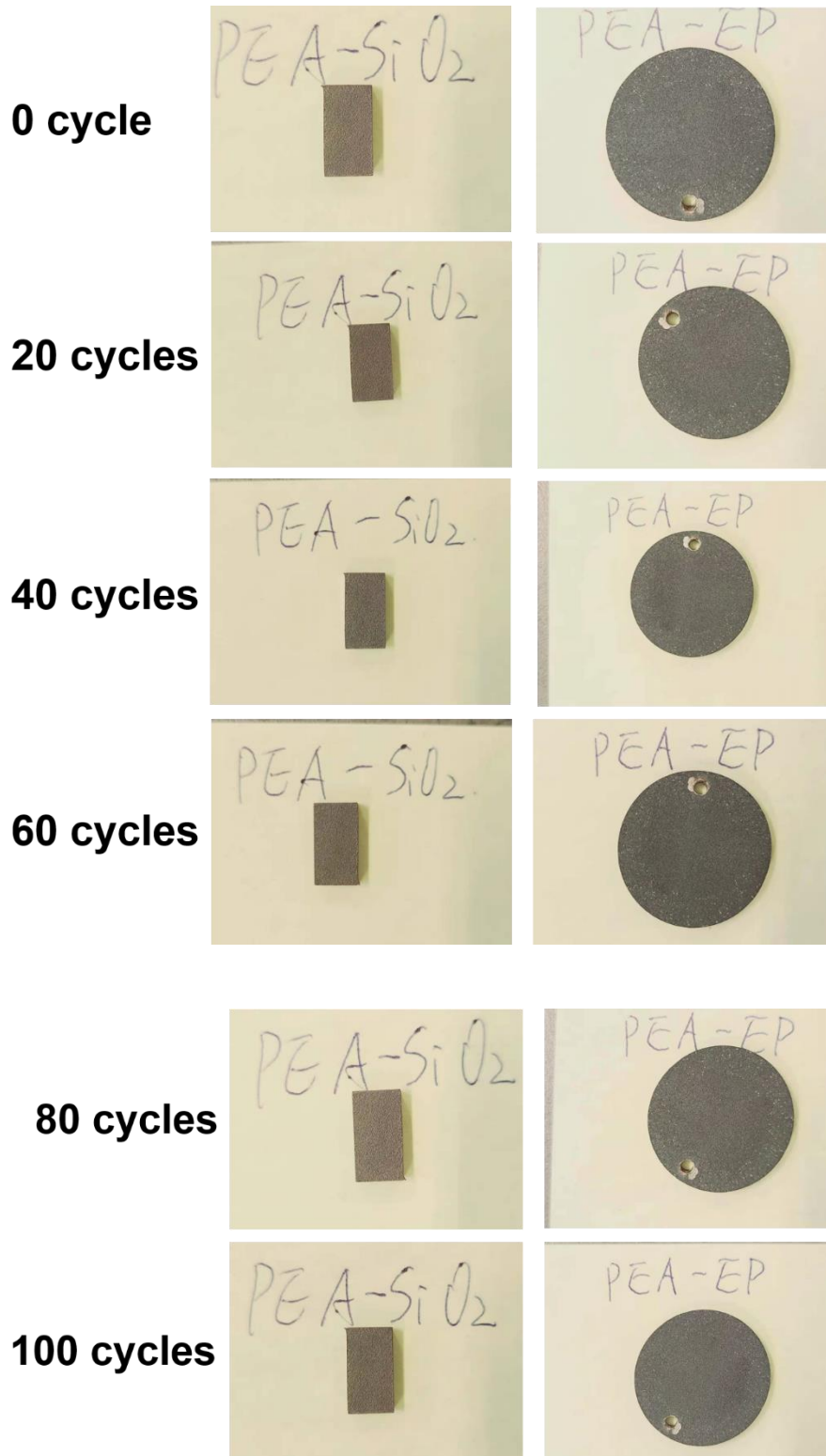


Figure 6-9 Optical images of the PEA-EP and PEA-SiO₂ samples after thermal shock tests.

6.4 Conclusions

Post-treatments, including electroless nickel plating (EP) and sol-gel dip coating, were applied to seal the open pores and cracks of PEA coatings. Both the PEA-EP and PEA-SiO₂ coatings could retain good corrosion resistance after immersed in sodium chloride solution for five days, while the PEA coating degraded due to localized corrosion of the iron substrate at these open pores and cracks. The PEA-SiO₂ coating demonstrates the best corrosion performance (polarization resistance of 126.03 kΩ·cm² after 5-day immersion in 3.5 wt. % NaCl solution) among all samples while the PEA-EP coating has the highest hardness (1150±115 HV). While the thermal conductivity of the PEA-EP coating is relatively high (1.44±0.16 W/(m·K)), the PEA-SiO₂ coating still has very low thermal conductivity (0.8±0.1 W/(m·K)). After cyclic thermal shock tests, both the PEA-EP and PEA-SiO₂ hybrid coatings seem intact.

REFERENCES

- (1) Yerokhin, A. L.; Nie, X.; Leyland, A.; Matthews, A.; Dowey, S. J. Plasma Electrolysis for Surface Engineering. *Surf. Coatings Technol.* **1999**, *122* (2–3), 73–93. [https://doi.org/10.1016/S0257-8972\(99\)00441-7](https://doi.org/10.1016/S0257-8972(99)00441-7).
- (2) Parfenov, E. V; Mukaeva, V. R.; Farrakhov, R. G.; Парфенов, Е. В.; Мукаева, В. Р.; Фарахов, Р. Г. Plasma Electrolytic Treatments for Advanced Surface Finishing Technologies. *Mater. Technol. Des.* **2019**, *1* (1), 34–41.
- (3) Belkin, P. N.; Kusmanov, S. A.; Parfenov, E. V. Mechanism and Technological Opportunity of Plasma Electrolytic Polishing of Metals and Alloys Surfaces. *Appl. Surf. Sci. Adv.* **2020**, *1*, 100016. <https://doi.org/10.1016/j.apsadv.2020.100016>.

- (4) Clyne, T. W.; Troughton, S. C. A Review of Recent Work on Discharge Characteristics during Plasma Electrolytic Oxidation of Various Metals. *Int. Mater. Rev.* **2019**, *64* (3), 127–162. <https://doi.org/10.1080/09506608.2018.1466492>.
- (5) Yerokhin, A. L.; Shatrov, A.; Samsonov, V.; Shashkov, P.; Pilkington, A.; Leyland, A.; Matthews, A. Oxide Ceramic Coatings on Aluminium Alloys Produced by a Pulsed Bipolar Plasma Electrolytic Oxidation Process. *Surf. Coatings Technol.* **2005**, *199* (2-3), 150–157. <https://doi.org/10.1016/j.surfcoat.2004.10.147>.
- (6) Matykina, E.; Arrabal, R.; Skeldon, P.; Thompson, G. E. Investigation of the Growth Processes of Coatings Formed by AC Plasma Electrolytic Oxidation of Aluminium. *Electrochim. Acta* **2009**, *54* (27), 6767–6778. <https://doi.org/10.1016/j.electacta.2009.06.088>.
- (7) Yerokhin, A. L.; Snizhko, L. O.; Gurevina, N. L.; Leyland, A.; Pilkington, A.; Matthews, A. Discharge Characterization in Plasma Electrolytic Oxidation of Aluminium. *J. Phys. D. Appl. Phys.* **2003**, *36* (17), 2110–2120. <https://doi.org/10.1088/0022-3727/36/17/314>.
- (8) Yerokhin, A. L.; Lyubimov, V. V.; Ashitkov, R. V. Phase Formation in Ceramic Coatings during Plasma Electrolytic Oxidation of Aluminium Alloys. *Ceram. Int.* **1998**, *24* (1), 1–6. [https://doi.org/10.1016/S0272-8842\(96\)00067-3](https://doi.org/10.1016/S0272-8842(96)00067-3).
- (9) Arrabal, R.; Matykina, E.; Viejo, F.; Skeldon, P.; Thompson, G. E.; Merino, M. C. AC Plasma Electrolytic Oxidation of Magnesium with Zirconia Nanoparticles. *Appl. Surf. Sci.* **2008**, *254* (21), 6937–6942. <https://doi.org/10.1016/j.apsusc.2008.04.100>.
- (10) Bala Srinivasan, P.; Liang, J.; Blawert, C.; Störmer, M.; Dietzel, W. Effect of Current Density on the Microstructure and Corrosion Behaviour of Plasma Electrolytic

Oxidation Treated AM50 Magnesium Alloy. *Appl. Surf. Sci.* **2009**, 255 (7), 4212–4218.
<https://doi.org/10.1016/j.apsusc.2008.11.008>.

(11) Liang, J.; Srinivasan, P. B.; Blawert, C.; Störmer, M.; Dietzel, W. Electrochemical Corrosion Behaviour of Plasma Electrolytic Oxidation Coatings on AM50 Magnesium Alloy Formed in Silicate and Phosphate Based Electrolytes. *Electrochim. Acta* **2009**, 54 (14), 3842–3850. <https://doi.org/10.1016/j.electacta.2009.02.004>.

(12) Duan, H.; Yan, C.; Wang, F. Growth Process of Plasma Electrolytic Oxidation Films Formed on Magnesium Alloy AZ91D in Silicate Solution. *Electrochim. Acta* **2007**, 52 (15), 5002–5009. <https://doi.org/10.1016/j.electacta.2007.02.021>.

(13) Wang, Y.; Jiang, Z.; Yao, Z.; Tang, H. Microstructure and Corrosion Resistance of Ceramic Coating on Carbon Steel Prepared by Plasma Electrolytic Oxidation. *Surf. Coatings Technol.* **2010**, 204 (11), 1685–1688.
<https://doi.org/10.1016/j.surfcoat.2009.10.023>.

(14) Wang, Y.; Jiang, Z.; Yao, Z. Preparation and Properties of Ceramic Coating on Q235 Carbon Steel by Plasma Electrolytic Oxidation. *Curr. Appl. Phys.* **2009**, 9 (5), 1067–1071. <https://doi.org/10.1016/j.cap.2008.12.004>.

(15) Li, Z.; Cheng, Y.; Kang, S. hang; Tu, W.; Cheng, Y. A Re-Understanding of the Breakdown Theory from the Study of the Plasma Electrolytic Oxidation of a Carbon Steel — A Non-Valve Metal. *Electrochim. Acta* **2018**, 284, 681–695.
<https://doi.org/10.1016/j.electacta.2018.07.201>.

(16) Yang, W.; Li, Q.; Liu, W.; Liang, J.; Peng, Z.; Liu, B. Characterization and Properties of Plasma Electrolytic Oxidation Coating on Low Carbon Steel Fabricated from

Aluminate Electrolyte. *Vacuum* **2017**, *144*, 207–216.
<https://doi.org/10.1016/j.vacuum.2017.08.003>.

(17) Zhao, C.; Zha, W.; Cai, R.; Nie, X.; Tjong, J. A New Eco-Friendly Anticorrosion Strategy for Ferrous Metals: Plasma Electrolytic Aluminating. *ACS Sustain. Chem. Eng.* **2019**, *7* (5), 5524–5531. <https://doi.org/10.1021/acssuschemeng.8b06839>.

(18) Zhao, C.; Sun, J.; Nie, X.; Tjong, J.; Matthews, D. T. A. Anodic Plasma Electrolytic Deposition of Composite Coating on Ferrous Alloys with Low Thermal Conductivity and High Adhesion Strength. *Surf. Coatings Technol.* **2020**, *398*, 126081. <https://doi.org/10.1016/j.surfcoat.2020.126081>.

(19) Duan, H.; Yan, C.; Wang, F. Effect of Electrolyte Additives on Performance of Plasma Electrolytic Oxidation Films Formed on Magnesium Alloy AZ91D. *Electrochim. Acta* **2007**, *52* (11), 3785–3793. <https://doi.org/10.1016/j.electacta.2006.10.066>.

(20) Wang, L.; Chen, L.; Yan, Z.; Wang, H.; Peng, J. Effect of Potassium Fluoride on Structure and Corrosion Resistance of Plasma Electrolytic Oxidation Films Formed on AZ31 Magnesium Alloy. *J. Alloys Compd.* **2009**, *480* (2), 469–474. <https://doi.org/10.1016/j.jallcom.2009.01.102>.

(21) Lee, K. M.; Shin, K. R.; Namgung, S.; Yoo, B.; Shin, D. H. Electrochemical Response of ZrO₂-Incorporated Oxide Layer on AZ91 Mg Alloy Processed by Plasma Electrolytic Oxidation. *Surf. Coatings Technol.* **2011**, *205* (13–14), 3779–3784. <https://doi.org/10.1016/j.surfcoat.2011.01.033>.

(22) Özer, N.; Cronin, J. P.; Yao, Y. J.; Tomsia, A. P. Optical Properties of Sol-Gel Deposited Al₂O₃ Films. *Sol. Energy Mater. Sol. Cells* **1999**, *59* (4), 355–366. [https://doi.org/10.1016/S0927-0248\(99\)00054-9](https://doi.org/10.1016/S0927-0248(99)00054-9).

- (23) Pezzato, L.; Rigon, M.; Martucci, A.; Brunelli, K.; Dabalà, M. Plasma Electrolytic Oxidation (PEO) as Pre-Treatment for Sol-Gel Coating on Aluminum and Magnesium Alloys. *Surf. Coatings Technol.* **2019**, *366*, 114–123. <https://doi.org/10.1016/j.surfcoat.2019.03.023>.
- (24) Tiwari, S. K.; Mishra, T.; Gunjan, M. K.; Bhattacharyya, A. S.; Singh, T. B.; Singh, R. Development and Characterization of Sol-Gel Silica-Alumina Composite Coatings on AISI 316L for Implant Applications. *Surf. Coatings Technol.* **2007**, *201* (16–17), 7582–7588. <https://doi.org/10.1016/j.surfcoat.2007.02.026>.
- (25) Parkhill, R. L.; Knobbe, E. T.; Donley, M. S. Application and Evaluation of Environmentally Compliant Spray-Coated Ormosil Films as Corrosion Resistant Treatments for Aluminum 2024-T3. *Prog. Org. Coatings* **2001**, *41* (4), 261–265. [https://doi.org/10.1016/S0300-9440\(01\)00138-2](https://doi.org/10.1016/S0300-9440(01)00138-2).
- (26) Capelossi, V. R.; Poelman, M.; Recloux, I.; Hernandez, R. P. B.; De Melo, H. G.; Olivier, M. G. Corrosion Protection of Clad 2024 Aluminum Alloy Anodized in Tartaric-Sulfuric Acid Bath and Protected with Hybrid Sol-Gel Coating. *Electrochim. Acta* **2014**, *124*, 69–79. <https://doi.org/10.1016/j.electacta.2013.09.004>.
- (27) Xia, B.; Yan, L.; Li, Y.; Zhang, S.; He, M.; Li, H.; Yan, H.; Jiang, B. Preparation of Silica Coatings with Continuously Adjustable Refractive Indices and Wettability Properties: Via Sol-Gel Method. *RSC Adv.* **2018**, *8* (11), 6091–6098. <https://doi.org/10.1039/c7ra12817g>.
- (28) Delaunois, F.; Petitjean, J. P.; Lienard, P.; Jacob-Duliere, M. Autocatalytic Electroless Nickel-Boron Plating on Light Alloys. *Surf. Coatings Technol.* **2000**, *124* (2–3), 201–209. [https://doi.org/10.1016/S0257-8972\(99\)00621-0](https://doi.org/10.1016/S0257-8972(99)00621-0).

- (29) Liu, Z.; Gao, W. The Effect of Substrate on the Electroless Nickel Plating of Mg and Mg Alloys. *Surf. Coatings Technol.* **2006**, *200* (11), 3553–3560. <https://doi.org/10.1016/j.surfcoat.2004.12.001>.
- (30) Loto, C. A. Electroless Nickel Plating – A Review. *Silicon*. Springer Netherlands April 1, **2016**, pp 177–186. <https://doi.org/10.1007/s12633-015-9367-7>.
- (31) Balaraju, J. N.; Kalavati; Rajam, K. S. Influence of Particle Size on the Microstructure, Hardness and Corrosion Resistance of Electroless Ni-P-Al₂O₃ Composite Coatings. *Surf. Coatings Technol.* **2006**, *200* (12–13), 3933–3941. <https://doi.org/10.1016/j.surfcoat.2005.03.007>.
- (32) Bisquert, J.; Garcia-Belmonte, G.; Bueno, P.; Longo, E.; Bulhões, L. O. S. Impedance of Constant Phase Element (CPE)-Blocked Diffusion in Film Electrodes. *J. Electroanal. Chem.* **1998**, *452* (2), 229–234. [https://doi.org/10.1016/S0022-0728\(98\)00115-6](https://doi.org/10.1016/S0022-0728(98)00115-6).
- (33) Bastidas, D. M. Interpretation of Impedance Data for Porous Electrodes and Diffusion Processes. *Corrosion* **2007**, *63* (6), 515–521. <https://doi.org/10.5006/1.3278402>.
- (34) Taylor, S. R.; Gileadi, E. Physical Interpretation of the Warburg Impedance. *Corrosion* **1995**, *51* (9), 664–671. <https://doi.org/10.5006/1.3293628>.
- (35) Shokouhfar, M.; Dehghanian, C.; Montazeri, M.; Baradaran, A. Preparation of Ceramic Coating on Ti Substrate by Plasma Electrolytic Oxidation in Different Electrolytes and Evaluation of Its Corrosion Resistance: Part II. *Appl. Surf. Sci.* **2012**, *258* (7), 2416–2423. <https://doi.org/10.1016/j.apsusc.2011.10.064>.

(36) Grandjean, S.; Absi, J.; Smith, D. S. Numerical Calculations of the Thermal Conductivity of Porous Ceramics Based on Micrographs. *J. Eur. Ceram. Soc.* **2006**, *26* (13), 2669–2676. <https://doi.org/10.1016/j.jeurceramsoc.2005.07.061>.

7. CHAPTER 7 Composite Coating on Cu Prepared by Plasma Electrolytic

Aluminating

7.1 Introduction

Copper and its alloys are some of the most versatile engineering materials. The largest end use of copper is in the building industry and civil engineering, including roofing, rainwater systems, oil and gas lines, etc. In unpolluted air, water and deaerated non-oxidizing acids, copper is a relatively stable metal, experiencing minimal corrosion issues. However, the corrosion-erosion, erosion by dispersed sediments and cavitation-erosion could be major problems of copper and its alloys whereby the naturally formed passive layers on copper-based substrates are damaged¹⁻⁴. To tackle the corrosion issues under mechanical stress conditions, protective coatings have been applied on the copper alloys surface, including electroless Ni-P coatings⁵⁻⁸, cold sprayed metal/ceramic composite coatings^{9,10}, high-velocity-oxy-fuel (HVOF) sprayed Fe-based amorphous coatings^{11,12} and metallic coatings¹³⁻¹⁶. It is well accepted that high hardness, high corrosion resistance and high adhesion strength of the protective coatings are beneficial for enhancing the erosion performance.

Plasma electrolytic oxidation (PEO) coatings demonstrate excellent combination of high hardness, high corrosion resistance and high adhesion strength to the substrate¹⁷, which make the PEO treatment a promising method to improve the erosion resistance. Recently, several researchers have reported the erosion resistance of aluminum alloys was improved by the PEO treatment^{18,19}. However, PEO treatment is not suitable for non-valve metals like Fe, Cu and Ni²⁰. Nevertheless, several papers were published on so-called PEO of carbon steel and cast iron in the electrolyte containing sodium aluminate and sodium

phosphate²¹⁻²⁴. Recent studies demonstrate that the aluminating species contribute mainly to the initial formation of a passive layer which is a pre-condition for the further generation of dielectric plasma discharging for plasma electrolysis whereby an alumina coating can finally be formed^{25,26}. Therefore, this process could also be termed as plasma electrolytic aluminating (PEA)²⁶.

In this work, PEA treatment was performed on pure copper without any pretreatment in an electrolyte containing sodium aluminate and sodium phosphate. A metal/ceramic composite coating with high hardness and excellent corrosion resistance was successfully obtained on the copper surface. The mechanism of coating deposition and the microstructure of the coating were studied in detail.

7.2 Experimental details

Pure copper samples ($\Phi 25.4$ mm \times 3 mm) were grinded and polished, followed by being ultrasonically cleaned in ethanol and rinsed with distilled water. During the PEA process, the samples (anode) were immersed in an electrolyte (15-20 g/L NaAlO₂, 1-5 g/L Na₃PO₄, pH=12, Sigma Aldrich) contained in a stainless-steel vessel (cathode). A pulsed DC current with a frequency of 1 kHz, duty cycle of 20% at constant voltage of 490 V was applied on the samples.

Surface morphologies and element-identification of the passive film and composite coating were studied by the scanning electron microscopy (SEM, Hitachi TM3030 plus) equipped with an energy dispersive X-ray spectrometer. Detailed compound compositions were determined by the X-ray photoelectron spectroscopy (XPS, Kratos AXIS Supra). The instrument work function was calibrated with a standard metallic gold reference sample to give binding energy (BE) of 83.95eV for metallic Au 4f_{7/2}. Charge neutralization were

performed by the Kratos charge neutralizer system for all analyses. XPS survey spectra with a pass energy of 160 eV followed by high-resolution spectra with a pass energy of 20 eV were obtained from an area of approximately 300 μm \times 700 μm . Phases of the prepared ceramic coating were determined by the X-ray diffraction (XRD, Rigaku SmartLab) using Cu K α radiation.

The hardness of the coating and substrate was measured by Vickers hardness tester (Wilson VH1102) with a load of 25 g and a holding time of 12 s. Tribological properties were evaluated by pin-on-disk sliding wear tests against SAE52100 steel balls (diameter 5.5 mm, hardness 848 HV) and WC-6Co balls (diameter 5.5 mm, hardness >1350 HV). The unlubricated sliding was performed with the load of 5 N at the sliding speed of 0.075 m/s. Potentiodynamic polarization tests were carried out from -0.5 V to 0.5 V with respect to the open circuit potential at a scan rate of 1.5 mV/s (BioLogic SP-150). Electrochemical impedance spectroscopy (EIS) in the frequency range between 10^6 and 10^{-2} Hz with ± 10 mV amplitude was also measured. All electrochemical tests were carried out in 3.5 wt.% NaCl solution at room temperature. Ag/AgCl (KCl saturated) and Pt were selected as reference electrode and counter electrode, respectively. The working surface area for each specimen was chosen to be 0.5 cm². All EIS data were analyzed using EC-Lab software. Thermal conductivities of prepared coating with different thickness were measured by the guarded heat flow method ²⁴.

7.3 Results and discussion

7.3.1 The discharge process and surface morphology evolution analyses

The average current density vs. time curve of the anode during the PEA process is illustrated in Figure 7-1 and could be divided into three stages. Representative samples

were taken for analysis during stage 2 (hereafter termed sample 1) and stage 3 (termed sample 2).

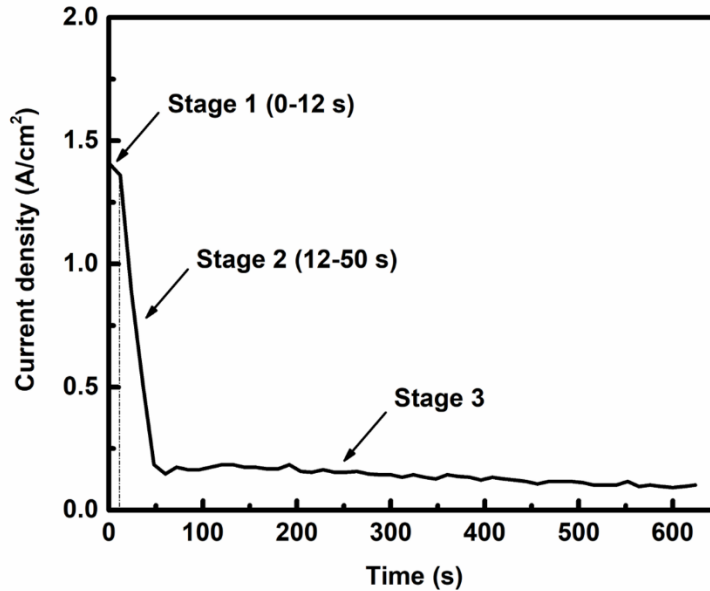


Figure 7-1 Average current density vs. time curve in the PEA process.

Stage 1 has a high current density of $\sim 1.35 \text{ A/cm}^2$ and is temporally the shortest stage. Observation of the process revealed that the sample surface was surrounded by numerous bubbles and no spark was observed in this stage. At the beginning of stage 2, tiny white-blue sparks were observed at the edges of the sample. The preferential formation of the sparks at sample edges can be attributed to the “edge effect” since electric flux lines are more concentrated at sample corners and edges^{25,27}. Then the sparks gradually spread to the center of the sample and changed from white-blue color into yellow color. Meanwhile, the current density decreased to $\sim 0.2 \text{ A/cm}^2$. During stage 3, the whole sample was covered by yellow sparks and the process lasted about 10 mins. The final coatings had a red tint color. Figure 7-2 demonstrates the SEM images of sample 1 (at 30 s, middle of stage 2) and sample 2 (at 10 min, end of stage 3). As shown in Figure 7-2a, the surface of sample 1

was covered with platelets of deposited materials, which could be the passive film. At this middle of the figure (denoted by B), evidence of plasma discharges was observed. Figure 7-2b reveals the porous surface structure of the final coating (sample 2). It is noted that white particles were embedded in the pores. Results of EDS analysis on areas A, B and C were summarized in Table 7-1.

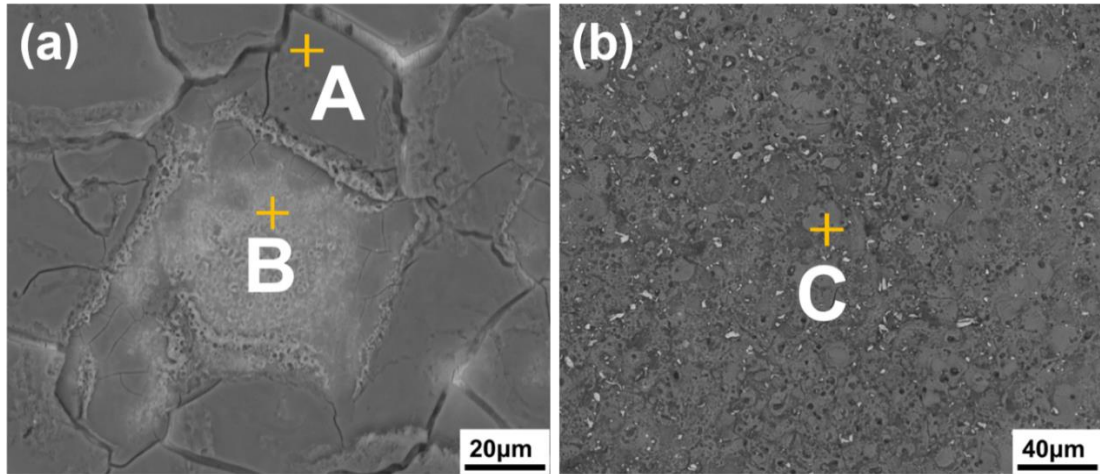


Figure 7-2 Surface SEM images of (a) sample 1 and (b) sample 2.

Table 7-1 Results of EDS point analyses on selected areas A, B and C.

	Cu (at. %)	Al (at. %)	O (at. %)	P (at. %)
Area A	0.51	23.50	70.26	5.74
Area B	8.64	26.01	61.14	4.22
Area C	7.70	35.48	56.20	0.62

Before the ignition of sparks, the passive film (area A) did not contain Cu, which means the substrate was not involved in the formation of passive film. However, with plasma discharges (areas B and C), Cu was incorporated into the coating, which could be attributed the evaporation of substrate materials driven by the high local thermal effects caused by sparks. To protect the passive film from washing away by running distilled water, sample

1 was not thoroughly rinsed. Therefore, the P detected by EDS analyses on areas A and B might come from the residue of electrolyte. An XPS survey scan on a sample retrieved during stage 2 of the PEA process after sputtering the top 20 nm shows only a negligible content of P (< 1 at. %), which could confirm that the P is from the residue of electrolyte. On the other hand, a sample retrieved after the full coating process was thoroughly rinsed with distilled water and the content of P detected with EDS is negligible. Therefore, it is possible to conclude that the phosphate was not incorporated into the coatings.

7.3.2 Coating formation mechanism analyses

To better understand the coating formation mechanism, XPS analyses were carried out on the surface of both samples 1 and 2. To evaluate the chemical state of Cu, both the Cu 2p spectra and the Cu L₃M_{4,5}M_{4,5} spectra were measured. The Cu 2p_{2/3}-Cu L₃M_{4,5}M_{4,5} Auger parameters were also used to determine the chemical state. Figure 7-3 demonstrates the XPS high resolution spectra obtained from the sample surface retrieved in stage 2 of the PEA process. As shown in Figure 7-3a, the peak at 74.60 eV accounts for the Al 2p_{3/2} line of Al(III) in Al(OH)₃²⁸, while the peak at 77.35 eV represents the Cu 3p_{3/2} line of Cu(ii) in Cu(OH)₂²⁹ or CuO³⁰. The sole peak at 531.75 eV in Figure 7-3b could be attributed to the O 1s line of hydroxide species^{31,32}. The Cu 2p_{3/2} spectra clearly demonstrated a “shake-up” satellite structure, as illustrated in Figure 7-3c. It is well accepted that the presence of shake-up satellite structure in Cu 2p spectra indicates the existence of Cu(II) species^{33,34}. Moreover, there is no splitting peaks for shake-up satellite structure, which means the Cu(II) species should come from Cu(OH)₂ instead of CuO³⁴. The shape of Cu LMM spectra (namely a lack of a distinct sharp peak which is typical for CuO) confirms this point³⁴.

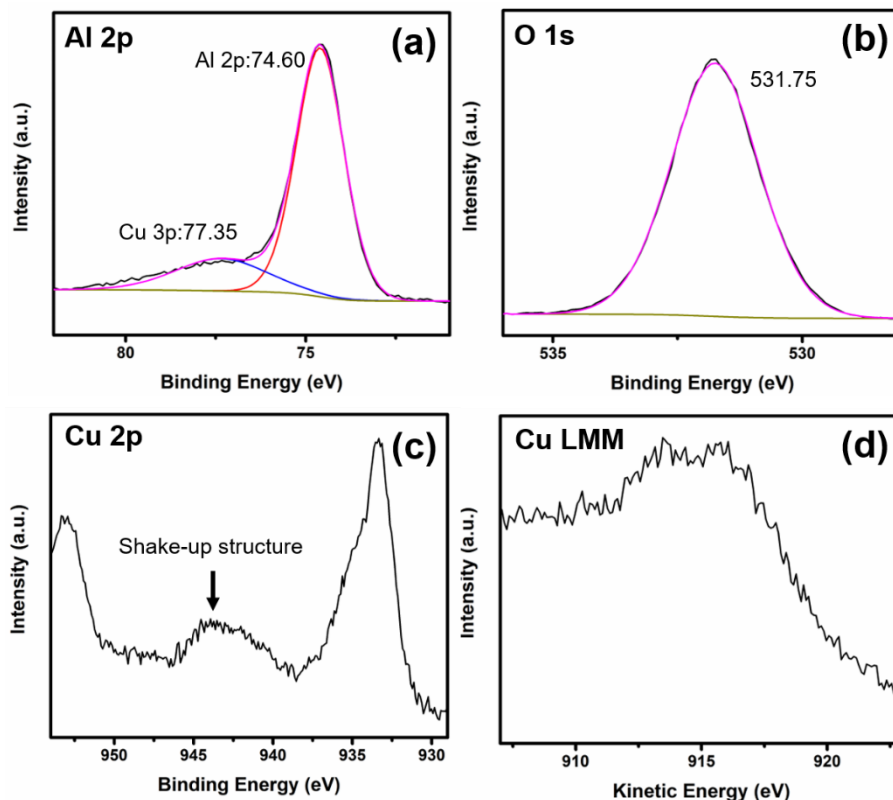
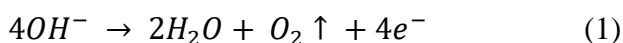
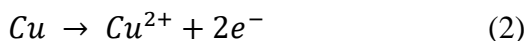


Figure 7-3 (a) Al 2p, (b) O 1s, (c) Cu 2p and (d) Cu LMM XPS high resolution spectra obtained from sample 1 surface.

As mentioned before, numerous gas bubbles were found nearby the anode, which could come from the oxygen evolution reaction in basic solution:

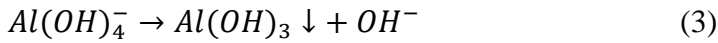


Meanwhile, another reaction is also possible for the anode:

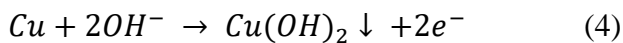


The standard electrode potentials of reactions (1) and (2) are 0.4 V and 0.34 V, which are very close. It needs to be mentioned that the concentration of OH^- anions (reducing agent) in our electrolyte is much higher than the standard state. Therefore, the reduction potential of reaction (1) will decrease according to the Nernst equation. Therefore, reaction (1)

occurred preferentially and released numerous oxygen bubbles at the anode surface. This oxygen evolution reaction consumed large amount of OH⁻ anions and caused a localized acidification of the electrolyte nearby the anode. As a result, Al(OH)₃ precipitated from the electrolyte:



The Al(OH)₃ nano- or micro-particles were deposited on the anode surface by an electrophoresis process and formed a passive film, as illustrated by area A in Figure 7-2a. This passive film would cause charge built-up at the interfaces and voltage across the film raised. After the critical voltage was reached, dielectric breakdown would occur, which led to the ignition of sparks at the edges of the sample, as shown by area B in Figure 7-2a. As mentioned before, the sparks gradually changed from white-blue color into yellow color and spread to the center of the sample during stage 2. As reported previously³⁵⁻³⁷, sparks with white-blue color at the beginning stage of PEO treatment is less intensified and its energy is smaller. Therefore, only small amount of Cu would be evaporated by the sparks and then reacted with excessive active species from the electrolyte to form the Cu(OH)₂ compounds:



The XPS high resolution spectra were obtained from an area of approximately 300 μm×700 μm, which means the spectra came from both area A and B. Therefore, the presence of both Al(OH)₃ and Cu(OH)₂ on the surface of sample 1 was confirmed by the XPS analyses. Figure 7-4 shows the XPS high resolution spectra obtained from sample 2 surface. The peak at 74.41 eV could be attributed to the Al 2p_{3/2} line of Al(III) in Al₂O₃^{28,38}, while the

peak at 77.05 eV represents the Cu 3p_{3/2} line of Cu(I) in Cu₂O^{29,39}. The peaks at 531.43 eV and 530.68 eV account for the O 1s lines of Al₂O₃^{31,40,41} and Cu₂O^{42,43}, respectively.

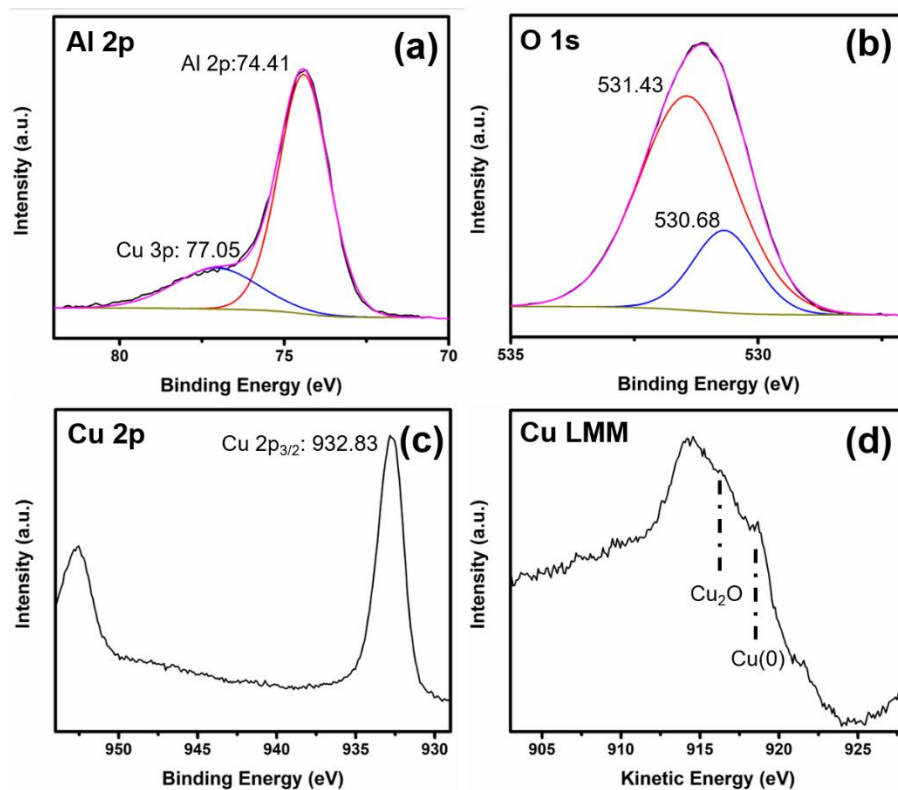


Figure 7-4 (a) Al 2p, (b) O 1s, (c) Cu 2p and (d) Cu LMM XPS high resolution spectra obtained from sample 2 surface.

As shown in Figure 7-4c, the main peak of Cu 2p_{3/2} was located at 932.83 eV. The shake-up satellite structure was diminished, which implies the lack of Cu(II) species. To further distinguish Cu(0) and Cu(I) species, the Cu LMM spectra was obtained. The shape of Cu LMM spectra obtained from sample 2 surface did not match well with either Cu(0) or Cu₂O standard spectra. However, two peaks could be found in the LMM spectra with kinetic energy at 916.25 eV and 918.51 eV. The calculated Cu 2p_{3/2}-Cu L₃M_{4,5}M_{4,5} Auger parameters were 1849.08 eV and 1851.34 eV, which matched with literature values for Cu(0) and Cu₂O³⁴. Therefore, the coating of sample 2 should contain metallic Cu, Cu₂O

and Al₂O₃. XRD analysis was also performed on sample 2, and the spectra was illustrated in Figure 7-5. As shown in Figure 7-5, crystalline peaks for metallic Cu, Cu₂O, α-Al₂O₃ and η-Al₂O₃ could be identified.

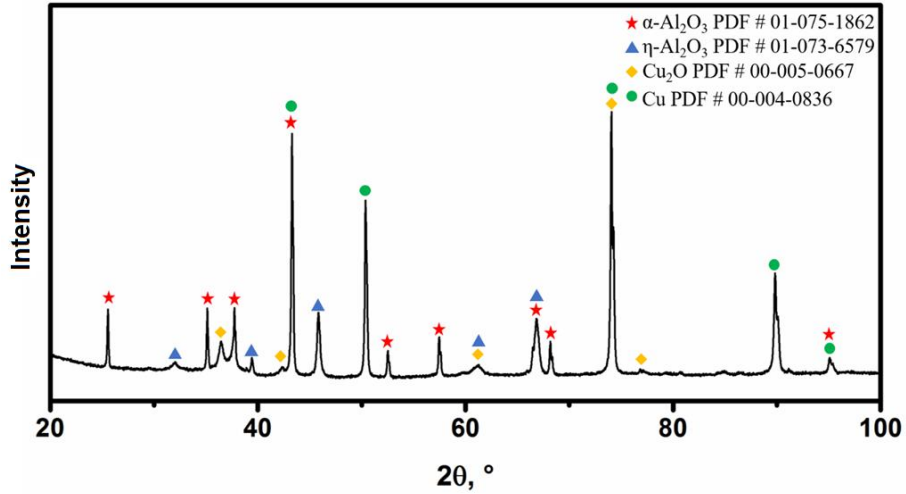
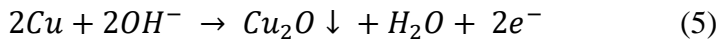


Figure 7-5 XRD spectrum for sample 2.

As mentioned before, the sparks have a yellow color during stage 3, which means the sparks are much stronger with higher energy^{35–37}. Large amount of Cu will be evaporated by these intensified sparks. When excessive Cu met with active species from the electrolyte in the discharge channels, part of the Cu would be oxidized:



and rest of the Cu would solidify into metallic Cu. It is plausible that Al₂O₃ originates from the plasma sinter reaction:

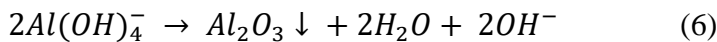


Figure 7-6 demonstrates the SEM surface and cross-section image of sample 2. The thickness was measured to be ~20 μm from the cross-section. Based on above analyses, the white particles should be the metallic Cu, as demarked with white circles in Figures 7-6a and 7-6b.

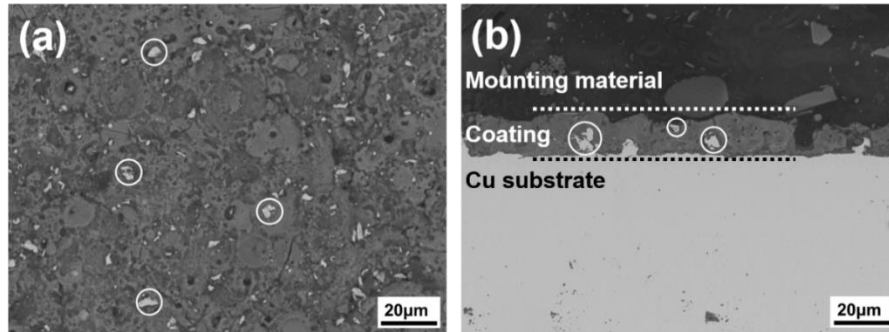


Figure 7-6 SEM images of (a) surface and (b) cross-section of the sample 2.

7.3.3 Hardness and wear tests

Hardness tests reveal that the micro hardness of the copper substrate and the coating are $98 \pm 15 \text{HV}$ and $1050 \pm 216 \text{HV}$, respectively. The friction coefficient curves are plotted in Figure 7-7. The friction coefficient of uncoated copper against steel ball ranges from 0.6 to 1.2, whereas this value is approximately 0.5 for the coated copper against steel ball and 0.3 for the coated copper against tungsten carbide ball, and the later ones are more stable.

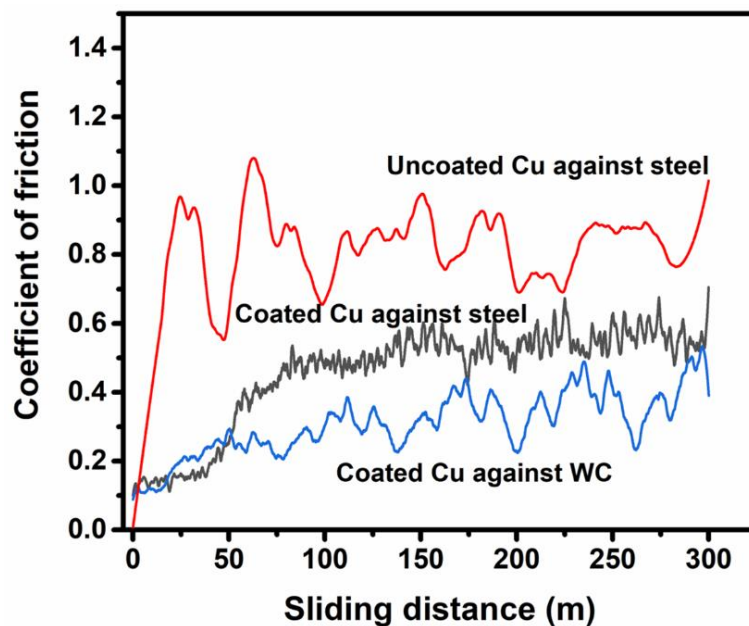


Figure 7-7 Friction coefficients vs. sliding distance for the uncoated sample against a SAE52100 steel ball and coated samples against SAE52100 steel and tungsten carbide balls.

Figure 7-8 summarizes the surface morphology of the wear tracks after the wear tests. As shown in Figures 7-8a and 7-8d, the worn surface of uncoated copper shows severe plastic deformation. Slight oxidation of the copper surface was verified with the EDS point analysis, as shown in the corresponding EDS spectra. The wear track width was $\sim 900 \mu\text{m}$ and the maximum depth was $\sim 40 \mu\text{m}$, as shown in the inset of Figure 7-8a. Adhesion of copper on the steel ball surface could be observed from Figure 7-8g. The steel ball was barely worn. Thus, the uncoated copper experienced severe ploughing wear, which could be attributed to its low surface hardness (98 HV) compared with the steel ball (848 HV). However, while annealed copper is a ductile metal, it has a strong work-hardening characteristic and therefore in the cyclic loading conditions of the pin-on-disk tribological test, it is expected that the surface of pure copper sample significantly work-hardened and the materials ductility reduced. This can be witnessed in the adhesion and fracture wear behavior which also played some roles in the wear process where the fractured Cu was partially transferred to the steel ball surface. Cumulatively, these observations also explain the highly fluctuating coefficient of friction for the pure copper sample and unstable tribological contact conditions.

Figures 7-8b and 7-8e demonstrate the surface morphology of coated copper sliding against the steel ball. Apparently, materials from the steel ball were transferred and adhered to the coating surface. Severe oxidation of the transferred iron was also verified by the EDS point analysis as shown in the corresponding EDS spectra. This observation reveals an evolution of the tribological contact, which can indicate why the friction coefficient increased from ~ 0.12 to ~ 0.5 after 50 m sliding distance, as shown in Figure 7-7. The low friction coefficient might come from the Cu_2O and metallic Cu, which could act as solid lubricant,

although such phenomena is generally associated with high temperature tribological contacts. A second hypothesis can be related to topographical evolution of the contact during “running-in”. This is supported by the similarity between the friction curves of the coated copper against both the steel and WC balls in the early stages of the wear process. However, the higher friction coefficient observed in the latter stages of the tribological test might come from the self-mating transfer layer against the steel ball surface. The wear track width was $\sim 400 \mu\text{m}$ while the wear depth could barely be measured as the transferred materials protected the coating underneath. The steel ball revealed a characteristic grooved wear scar as shown in Figure 7-8h, which indicates that abrasive wear occurred on the steel ball. The bright areas on the wear track represent iron oxide which came from the steel ball and then oxidized due to the frictional heating. Among the three tribotests, the lowest friction coefficient and narrowest wear track ($\sim 180 \mu\text{m}$) were found for the coated copper sliding against WC ball. Increased hardness of the counter material (i.e., employing a WC ball) resulted in a lower degree of material transfer. During the sliding test, only a small amount of wear debris was generated and became embedded in the pores of the coating. Therefore, severe three-body abrasive wear did not occur, and both the coating and the WC ball were insignificantly worn. It should be here emphasized that the PEA-coating on Cu indeed had a good mechanical integrity demonstrated by the sliding tribotests under a maximum Hertzian contact pressure of up to 1.6 GPa (for the WC ball case).

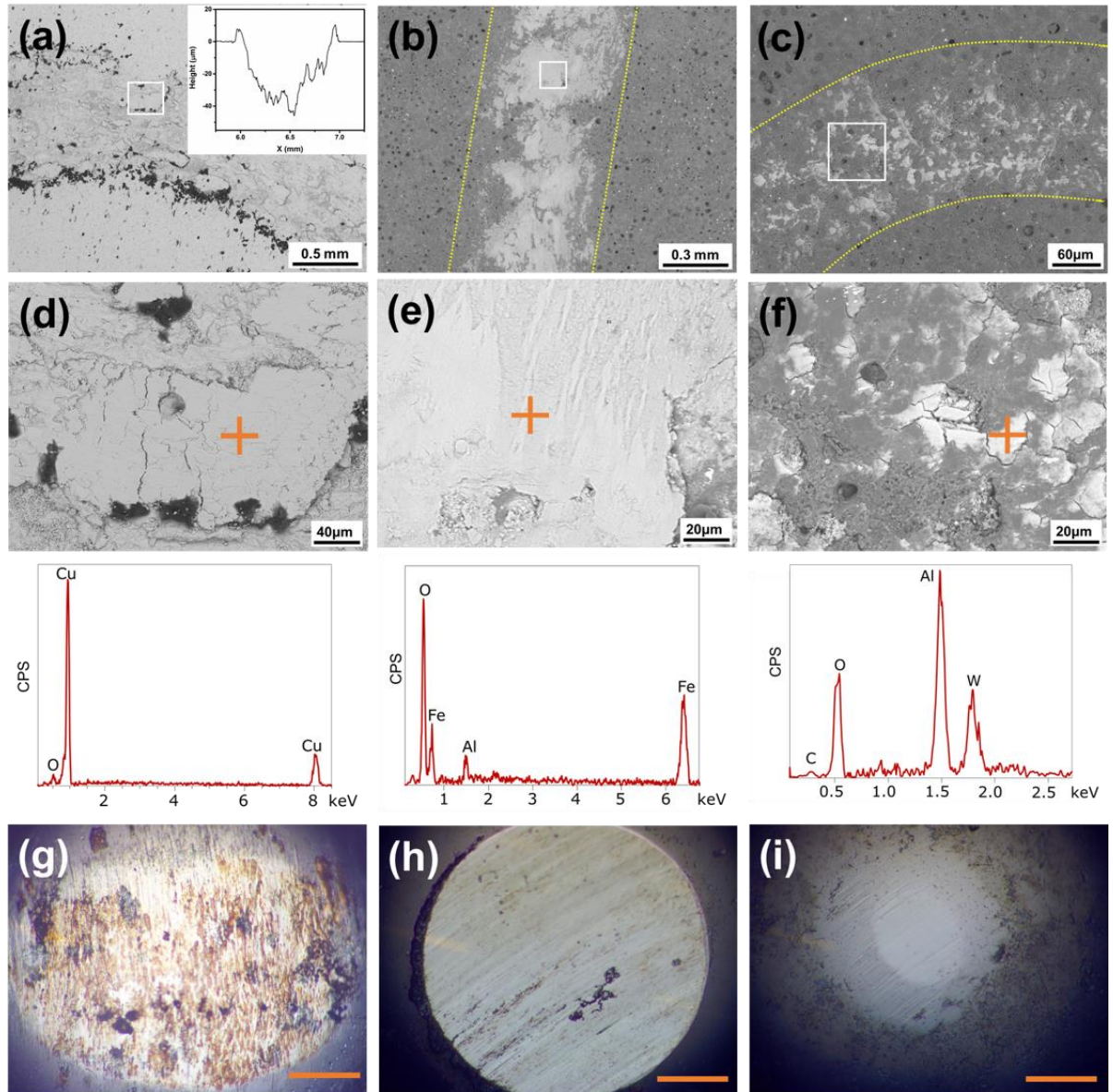


Figure 7-8 SEM images (BSE mode) of the wear track for (a) uncoated copper sliding against steel ball, (b) coated copper sliding against steel ball, and (c) coated copper sliding against tungsten carbide ball. (d), (e) and (f) are enlarged images of the white boxes in (a), (b) and (c), respectively. (g), (h) and (i) show the representative surfaces of the counter-balls, scale bar is 100 μm.

7.3.4 Corrosion tests

Figures 7-9a and 7-9b disclose the Nyquist plots of uncoated and coated samples in the 3.5% NaCl solution. The equivalent circuit models used for fitting the EIS curves are shown in Figures 7-9e and 7-9f. All the fitting parameters are summarized in Table 7-2. In Figure 7-9e, R_s represents solution resistance, R_0 denotes charge transfer resistance, CPE_0 denotes the double-layer capacitance at the metal-electrolyte interface. Noticing the surface inhomogeneity, the constant phase element (CPE) was employed to compensate for porosity and surface roughness^{44,45}.

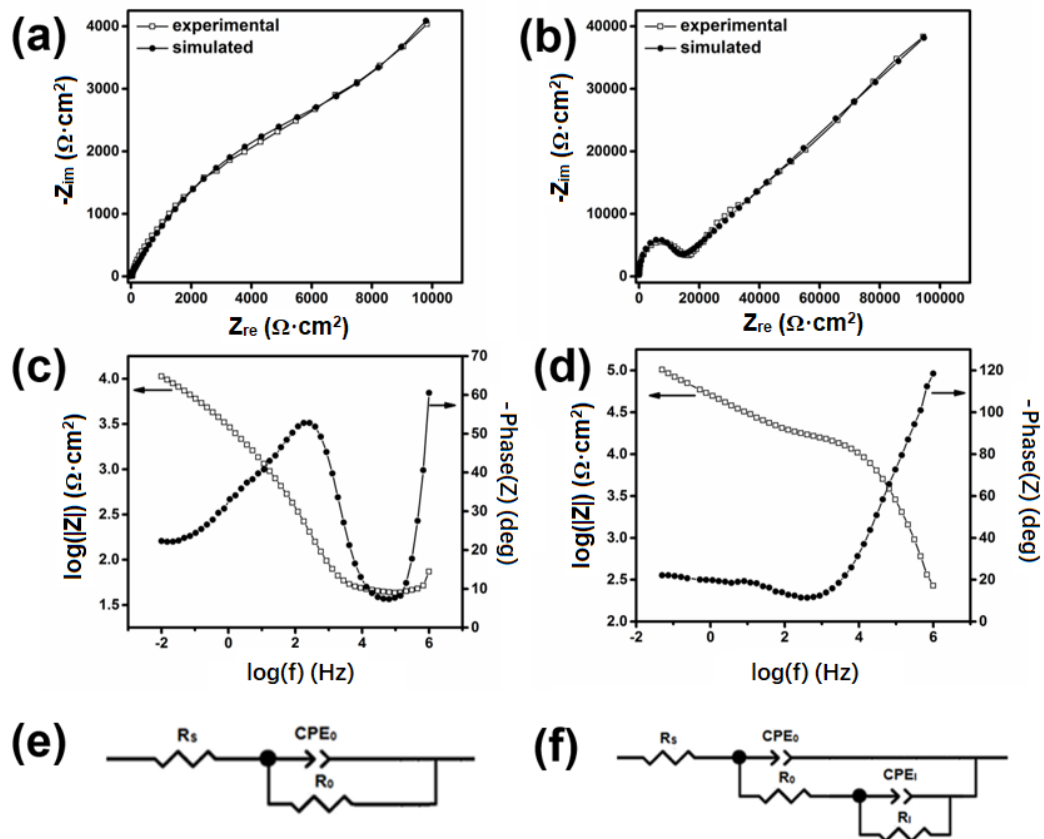


Figure 7-9 (a), (b) Nyquist plots of uncoated and coated copper samples in 3.5 wt.% NaCl solution; (c), (d) Bode plots of uncoated and coated copper samples; (e), (f) equivalent circuit used for fitting the EIS spectra in (a) and (b), respectively.

The impedance of CPE is expressed by the following equation ⁴⁴:

$$Z_{CPE} = 1/[T(j\omega)^P] \quad (7)$$

where j is the imaginary unit, ω is the angular frequency defined as $\omega = 2\pi f$, f is the frequency in Hz, T is CPE constant; the value of P varies between 0 and 1. The values 0 and 1 of P imply the CPE of the circuit to be pure resistor, and capacitor, respectively. In Figure 7-9f, R_s represents solution resistance, R_0 denotes the charge transfer resistance at the coating-electrolyte interface, R_1 is associated with the resistance of the coating material. CPE_0 and CPE_1 denote the double layer capacitance at the coating-electrolyte interface and the capacitance of the coating material.

Table 7-2 Fitted parameters from the EIS spectra.

Sample	Uncoated sample	Coated sample
R_s ($\Omega \cdot \text{cm}^2$)	12.91	18.75
R_0 ($\Omega \cdot \text{cm}^2$)	11034	9279
R_1 ($\Omega \cdot \text{cm}^2$)	--	2.0E6
CPE_0 ($\text{F} \cdot \text{s}^{P-1}$)	1.1E-4	1.1E-9
P_0	0.47	0.96
CPE_1 ($\text{F} \cdot \text{s}^{P-1}$)	--	1.4E-5
P_1	--	0.27

For the uncoated copper, the charge transfer resistance R_0 at the sample-electrolyte interface was $\sim 10^4 \Omega$. On the other hand, the coated copper possesses an inner layer resistance R_1 of $2 \times 10^6 \Omega$, which is much higher than the charge transfer resistance. Therefore, the corrosion resistance of the coated copper mainly relies on the compact inner ceramic layer.

The results of potentiodynamic polarization tests are presented in Figure 7-10. As shown in Figure 7-10, the PEO composite coating shifts the surface potential in noble direction and reduces the corrosion current density. From the Tafel curves, the corrosion potential (E_{corr}), corrosion current density (i_{corr}), cathodic and anodic Tafel constants (β_c and β_a)

could be obtained. The results are summarized in Table 7-3. Polarization resistances (R_p) were determined with Stern-Geary equation ⁴⁶:

$$R_p = \frac{\beta_a \times \beta_c}{2.303 \times (\beta_a + \beta_c) \times i_{corr}} \quad (8)$$

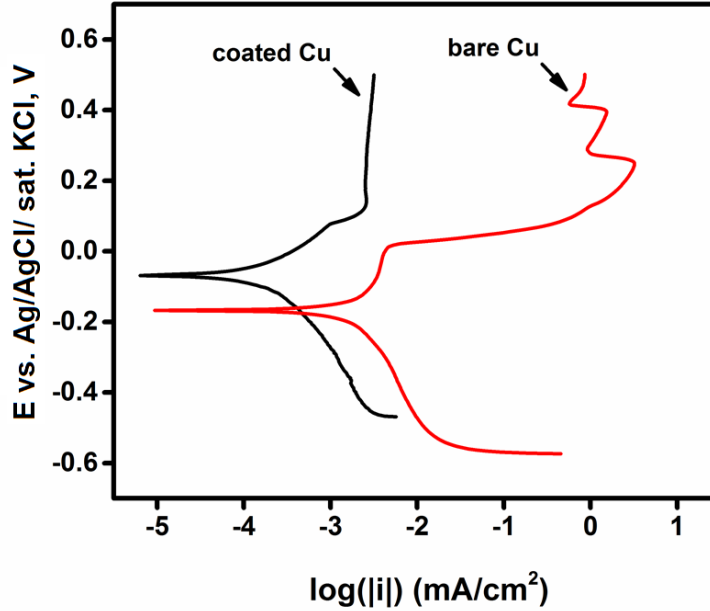


Figure 7-10 Potentiodynamic polarization curves of the coated and uncoated copper samples.

Table 7-3 Kinetic parameters obtained from the polarization curves.

Sample	E_{corr} (V)	i_{corr} (A/cm ²)	β_a (V/dec)	β_c (V/dec)	R_p (k Ω ·cm ²)
Uncoated Cu	-0.18	2.2E-5	0.70	0.37	4.73
Coated Cu	-0.04	2.5E-7	0.12	0.24	141.7

Firstly, the corrosion potential of coated sample was higher than the blank sample, indicating a decreased thermodynamic tendency of corrosion. Secondly, the anodic section of the coated sample was moved towards lower current density, indicating that the anodic reactions were restrained by composite coating. Efficient and stable passivation protection of the sample was also obtained. Moreover, the corrosion current density measured by the

polarization tests was 2.2×10^{-5} A/cm² for uncoated sample, which was two orders higher than the corrosion current of the coated sample (2.5×10^{-7} A/cm²). The polarization resistance of coated sample was 141.7 kΩ·cm², which was much higher than the uncoated copper sample (4.73 kΩ·cm²).

7.3.5 Thermal conductivities of the PEA coatings

Figure 7-11 demonstrates the measured thermal conductivities of the composite coatings with different thicknesses. The coatings' thermal conductivities increased from ~ 3.8 W/(m·K) @ 25 μm to ~ 5.1 W/(m·K) @ 60 μm.

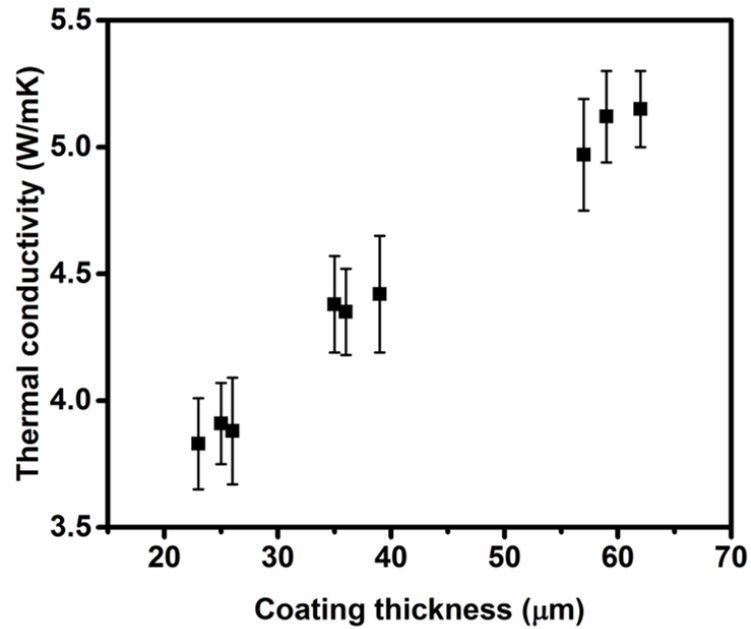


Figure 7-11 Thermal conductivities of the coatings with different thicknesses.

These values are much higher than the alumina coatings prepared by PEO processes on aluminum alloys and PEA process on irons and steels^{24,47,48}. The relatively high thermal conductivity could be attributed to the presence of metallic Cu in the composite coating. As discussed above, these metallic Cu comes from the intensified sparks. It is well-known that the intensity of sparks increased with increasing coating thickness. Thus, the content

of metallic Cu would also increase with increasing coating thickness, which was confirmed by the cross-sectional images.

7.4 Conclusions

(1) A composite ceramic coating was successfully prepared on pure copper by plasma electrolytic aluminating process.

(2) The Al(OH)₃ passive film formed on the copper surface was indispensable for ignition of stable plasma discharges. XPS and XRD analyses indicate that the coating prepared by a prolonged PEA treatment contains metallic Cu, Cu₂O, and Al₂O₃.

(3) The hardness of coating is 1050±216 HV, which is 10 times of the pure copper. The wear mechanism against SAE52100 steel balls changed from ploughing wear of the copper for the uncoated sample to abrasive wear of the ball for the coated sample.

(4) The composite coating shows effective corrosion protection of the pure copper in 3.5% NaCl solution. Stable passivation protection was achieved. The corrosion potential and corrosion current density of the coated sample are -0.04 V and 2.5×10⁻⁷ A/cm², respectively. The polarization resistance of the copper increased from 4.73 kΩ·cm² to 141.7 kΩ·cm².

(5) The coatings' thermal conductivities increased from ~3.8 W/(m·K) @ 25 μm to ~ 5.1 W/(m·K) @ 60 μm. The relatively high thermal conductivity could be attributed to the presence of metallic Cu in the composite coating.

REFERENCES

(1) Levy, A. Solid Particle Erosion and Erosion-Corrosion of Materials. *Choice Rev. Online* **1996**, 33 (05), 2760. <https://doi.org/10.5860/CHOICE.33-2760>.

- (2) Rajahram, S. S.; Harvey, T. J.; Wood, R. J. K. Erosion–Corrosion Resistance of Engineering Materials in Various Test Conditions. *Wear* **2009**, *267* (1–4), 244–254. <https://doi.org/10.1016/j.wear.2009.01.052>.
- (3) Malka, R.; Nešić, S.; Gulino, D. A. Erosion–Corrosion and Synergistic Effects in Disturbed Liquid-Particle Flow. *Wear* **2007**, *262* (7–8), 791–799. <https://doi.org/10.1016/j.wear.2006.08.029>.
- (4) Kwok, C.; Cheng, F.; Man, H. Synergistic Effect of Cavitation Erosion and Corrosion of Various Engineering Alloys in 3.5% NaCl Solution. *Mater. Sci. Eng. A* **2000**, *290* (1–2), 145–154. [https://doi.org/10.1016/S0921-5093\(00\)00899-6](https://doi.org/10.1016/S0921-5093(00)00899-6).
- (5) Jiang, B.; Jiang, S. L.; Ma, A. L.; Zheng, Y. G. Erosion-Corrosion Behavior of Electroless Ni-P Coating on Copper-Nickel Alloy in 3.5 Wt.% Sodium Chloride Solution. *J. Mater. Eng. Perform.* **2014**, *23* (1), 230–237. <https://doi.org/10.1007/s11665-013-0763-0>.
- (6) Calderón, J. A.; Jiménez, J. P.; Zuleta, A. A. Improvement of the Erosion-Corrosion Resistance of Magnesium by Electroless Ni-P/Ni(OH)₂-Ceramic Nanoparticle Composite Coatings. *Surf. Coatings Technol.* **2016**, *304*, 167–178. <https://doi.org/10.1016/j.surfcoat.2016.04.063>.
- (7) Jiang, B.; Jiang, S. L.; Ma, A. L.; Zheng, Y. G. Effect of Heat Treatment on Erosion-Corrosion Behavior of Electroless Ni-P Coatings in Saline Water. *Mater. Manuf. Process.* **2014**, *29* (1), 74–82. <https://doi.org/10.1080/10426914.2013.852222>.
- (8) Tamilarasan, T. R.; Sanjith, U.; Siva Shankar, M.; Rajagopal, G. Effect of Reduced Graphene Oxide (RGO) on Corrosion and Erosion-Corrosion Behaviour of Electroless Ni-P Coatings. *Wear* **2017**, *390–391*, 385–391. <https://doi.org/10.1016/j.wear.2017.09.004>.

- (9) Szala, M.; Łatka, L.; Walczak, M.; Winnicki, M. Comparative Study on the Cavitation Erosion and Sliding Wear of Cold-Sprayed Al/Al₂O₃ and Cu/Al₂O₃ Coatings, and Stainless Steel, Aluminium Alloy, Copper and Brass. *Metals* **2020**, *10* (7), 856. <https://doi.org/10.3390/met10070856>.
- (10) Hu, H. X.; Jiang, S. L.; Tao, Y. S.; Xiong, T. Y.; Zheng, Y. G. Cavitation Erosion and Jet Impingement Erosion Mechanism of Cold Sprayed Ni–Al₂O₃ Coating. *Nucl. Eng. Des.* **2011**, *241* (12), 4929–4937. <https://doi.org/10.1016/j.nucengdes.2011.09.038>.
- (11) Wang, Y.; Zheng, Y. G.; Ke, W.; Sun, W. H.; Hou, W. L.; Chang, X. C.; Wang, J. Q. Slurry Erosion–Corrosion Behaviour of High-Velocity Oxy-Fuel (HVOF) Sprayed Fe-Based Amorphous Metallic Coatings for Marine Pump in Sand-Containing NaCl Solutions. *Corros. Sci.* **2011**, *53* (10), 3177–3185. <https://doi.org/10.1016/j.corsci.2011.05.062>.
- (12) Zheng, Z. B.; Zheng, Y. G.; Sun, W. H.; Wang, J. Q. Erosion–Corrosion of HVOF-Sprayed Fe-Based Amorphous Metallic Coating under Impingement by a Sand-Containing NaCl Solution. *Corros. Sci.* **2013**, *76*, 337–347. <https://doi.org/10.1016/j.corsci.2013.07.006>.
- (13) Tan, K. S.; Wharton, J. A.; Wood, R. J. K. Solid Particle Erosion–Corrosion Behaviour of a Novel HVOF Nickel Aluminium Bronze Coating for Marine Applications—Correlation between Mass Loss and Electrochemical Measurements. *Wear* **2005**, *258* (1–4), 629–640. <https://doi.org/10.1016/j.wear.2004.02.019>.
- (14) Hong, S.; Wu, Y.; Gao, W.; Zhang, J.; Zheng, Y.; Zheng, Y. Slurry Erosion-Corrosion Resistance and Microbial Corrosion Electrochemical Characteristics of HVOF Sprayed WC-10Co-4Cr Coating for Offshore Hydraulic Machinery. *Int. J. Refract. Met. Hard Mater.* **2018**, *74*, 7–13. <https://doi.org/10.1016/j.ijrmhm.2018.02.019>.

- (15) Hong, S.; Wu, Y.; Zhang, J.; Zheng, Y.; Zheng, Y.; Lin, J. Synergistic Effect of Ultrasonic Cavitation Erosion and Corrosion of WC–CoCr and FeCrSiBMn Coatings Prepared by HVOF Spraying. *Ultrason. Sonochem.* **2016**, *31*, 563–569. <https://doi.org/10.1016/j.ultsonch.2016.02.011>.
- (16) Liu, Y.; Hang, Z.; Xi, N.; Chen, H.; Ma, C.; Wu, X. Erosion-Corrosion Behavior of HVOF WC-Co Coating in Cl^- and SO_4^{2-} Containing Solutions. *Appl. Surf. Sci.* **2018**, *431*, 55–59. <https://doi.org/10.1016/j.apsusc.2017.06.107>.
- (17) Yerokhin, A. L.; Nie, X.; Leyland, A.; Matthews, A.; Dowey, S. J. Plasma Electrolysis for Surface Engineering. *Surf. Coatings Technol.* **1999**, *122* (2–3), 73–93. [https://doi.org/10.1016/S0257-8972\(99\)00441-7](https://doi.org/10.1016/S0257-8972(99)00441-7).
- (18) Algahtani, A.; Mahmoud, E. R. I. Erosion and Corrosion Resistance of Plasma Electrolytic Oxidized 6082 Aluminum Alloy Surface at Low and High Temperatures. *J. Mater. Res. Technol.* **2019**, *8* (3), 2699–2709. <https://doi.org/10.1016/j.jmrt.2019.02.017>.
- (19) Barik, R. C.; Wharton, J. A.; Wood, R. J. K.; Stokes, K. R.; Jones, R. L. Corrosion, Erosion and Erosion–Corrosion Performance of Plasma Electrolytic Oxidation (PEO) Deposited Al_2O_3 Coatings. *Surf. Coatings Technol.* **2005**, *199* (2–3), 158–167. <https://doi.org/10.1016/j.surfcoat.2004.09.038>.
- (20) Clyne, T. W.; Troughton, S. C. A Review of Recent Work on Discharge Characteristics during Plasma Electrolytic Oxidation of Various Metals. *Int. Mater. Rev.* **2019**, *64* (3), 127–162. <https://doi.org/10.1080/09506608.2018.1466492>.
- (21) Wang, Y.; Jiang, Z.; Yao, Z. Preparation and Properties of Ceramic Coating on Q235 Carbon Steel by Plasma Electrolytic Oxidation. *Curr. Appl. Phys.* **2009**, *9* (5), 1067–1071. <https://doi.org/10.1016/j.cap.2008.12.004>.

- (22) Yang, W.; Li, Q.; Liu, W.; Liang, J.; Peng, Z.; Liu, B. Characterization and Properties of Plasma Electrolytic Oxidation Coating on Low Carbon Steel Fabricated from Aluminate Electrolyte. *Vacuum* **2017**, *144*, 207–216. <https://doi.org/10.1016/j.vacuum.2017.08.003>.
- (23) Wang, Y.; Jiang, Z.; Yao, Z.; Tang, H. Microstructure and Corrosion Resistance of Ceramic Coating on Carbon Steel Prepared by Plasma Electrolytic Oxidation. *Surf. Coatings Technol.* **2010**, *204* (11), 1685–1688. <https://doi.org/10.1016/j.surfcoat.2009.10.023>.
- (24) Zhao, C.; Sun, J.; Nie, X.; Tjong, J.; Matthews, D. T. A. Anodic Plasma Electrolytic Deposition of Composite Coating on Ferrous Alloys with Low Thermal Conductivity and High Adhesion Strength. *Surf. Coatings Technol.* **2020**, *398*, 126081. <https://doi.org/10.1016/j.surfcoat.2020.126081>.
- (25) Li, Z.; Cheng, Y.; Kang, S.; Tu, W.; Cheng, Y. A Re-Understanding of the Breakdown Theory from the Study of the Plasma Electrolytic Oxidation of a Carbon Steel — A Non-Valve Metal. *Electrochim. Acta* **2018**, *284*, 681–695. <https://doi.org/10.1016/j.electacta.2018.07.201>.
- (26) Zhao, C.; Zha, W.; Cai, R.; Nie, X.; Tjong, J. A New Eco-Friendly Anticorrosion Strategy for Ferrous Metals: Plasma Electrolytic Aluminating. *ACS Sustain. Chem. Eng.* **2019**, *7* (5), 5524–5531. <https://doi.org/10.1021/acssuschemeng.8b06839>.
- (27) Cheng, Y.; Zhu, Z.; Zhang, Q.; Zhuang, X.; Cheng, Y. Plasma Electrolytic Oxidation of Brass. *Surf. Coatings Technol.* **2020**, *385*, 125366. <https://doi.org/10.1016/j.surfcoat.2020.125366>.

- (28) Taylor, J. A. An XPS Study of the Oxidation of AlAs Thin Films Grown by MBE. *J. Vac. Sci. Technol.* **1982**, *20* (3), 751–755. <https://doi.org/10.1116/1.571450>.
- (29) McIntyre, N. S.; Cook, M. G. X-Ray Photoelectron Studies on Some Oxides and Hydroxides of Cobalt, Nickel, and Copper. *Anal. Chem.* **1975**, *47* (13), 2208–2213. <https://doi.org/10.1021/ac60363a034>.
- (30) Robert, T.; Offergeld, G. Spectres de Photoélectrons X de Composés Solides de Cuivre Relation Entre La Présence de Raies Satellites et l'état d'oxydation Du Cuivre. *Phys. Status Solidi* **1972**, *14* (1), 277–282. <https://doi.org/10.1002/pssa.2210140134>.
- (31) Wagner, C. D.; Passoja, D. E.; Hillery, H. F.; Kinisky, T. G.; Six, H. A.; Jansen, W. T.; Taylor, J. A. Auger and Photoelectron Line Energy Relationships in Aluminum–Oxygen and Silicon–Oxygen Compounds. *J. Vac. Sci. Technol.* **1982**, *21* (4), 933–944. <https://doi.org/10.1116/1.571870>.
- (32) McIntyre, N. S.; Sunder, S.; Shoesmith, D. W.; Stanchell, F. W. Chemical Information from XPS—Applications to the Analysis of Electrode Surfaces. *J. Vac. Sci. Technol.* **1981**, *18* (3), 714–721. <https://doi.org/10.1116/1.570934>.
- (33) Biesinger, M. C.; Payne, B. P.; Grosvenor, A. P.; Lau, L. W. M.; Gerson, A. R.; Smart, R. S. C. Resolving Surface Chemical States in XPS Analysis of First Row Transition Metals, Oxides and Hydroxides: Cr, Mn, Fe, Co and Ni. *Appl. Surf. Sci.* **2011**, *257* (7), 2717–2730. <https://doi.org/10.1016/j.apsusc.2010.10.051>.
- (34) Biesinger, M. C. Advanced Analysis of Copper X-Ray Photoelectron Spectra. *Surf. Interface Anal.* **2017**, *49* (13), 1325–1334. <https://doi.org/10.1002/sia.6239>.
- (35) Yerokhin, A. L.; Snizhko, L. O.; Gurevina, N. L.; Leyland, A.; Pilkington, A.; Matthews, A. Discharge Characterization in Plasma Electrolytic Oxidation of Aluminium.

J. Phys. D. Appl. Phys. **2003**, *36* (17), 2110–2120. <https://doi.org/10.1088/0022-3727/36/17/314>.

(36) Hussein, R. O.; Nie, X.; Northwood, D. O. An Investigation of Ceramic Coating Growth Mechanisms in Plasma Electrolytic Oxidation (PEO) Processing. *Electrochim. Acta* **2013**, *112*, 111–119. <https://doi.org/10.1016/j.electacta.2013.08.137>.

(37) Hussein, R. O.; Nie, X.; Northwood, D. O.; Yerokhin, A.; Matthews, A. Spectroscopic Study of Electrolytic Plasma and Discharging Behaviour during the Plasma Electrolytic Oxidation (PEO) Process. *J. Phys. D. Appl. Phys.* **2010**, *43* (10), 105203. <https://doi.org/10.1088/0022-3727/43/10/105203>.

(38) Nefedov, V. I. A Comparison of Results of an ESCA Study of Nonconducting Solids Using Spectrometers of Different Constructions. *J. Electron Spectros. Relat. Phenomena* **1982**, *25* (1), 29–47. [https://doi.org/10.1016/0368-2048\(82\)85002-0](https://doi.org/10.1016/0368-2048(82)85002-0).

(39) Ertl, G.; Hierl, R.; Knözinger, H.; Thiele, N.; Urbach, H. P. XPS Study of Copper Aluminate Catalysts. *Appl. Surf. Sci.* **1980**, *5* (1), 49–64. [https://doi.org/10.1016/0378-5963\(80\)90117-8](https://doi.org/10.1016/0378-5963(80)90117-8).

(40) Strohmeier, B. R. Gamma-Alumina (Γ -Al₂O₃) by XPS. *Surf. Sci. Spectra* **1994**, *3* (2), 135–140. <https://doi.org/10.1116/1.1247774>.

(41) Paparazzo, E. XPS and Auger Spectroscopy Studies on Mixtures of the Oxides SiO₂, Al₂O₃, Fe₂O₃ and Cr₂O₃. *J. Electron Spectros. Relat. Phenomena* **1987**, *43* (2), 97–112. [https://doi.org/10.1016/0368-2048\(87\)80022-1](https://doi.org/10.1016/0368-2048(87)80022-1).

(42) Haber, J.; Machej, T.; Ungier, L.; Ziólkowski, J. ESCA Studies of Copper Oxides and Copper Molybdates. *J. Solid State Chem.* **1978**, *25* (3), 207–218. [https://doi.org/10.1016/0022-4596\(78\)90105-6](https://doi.org/10.1016/0022-4596(78)90105-6).

- (43) Deroubaix, G.; Marcus, P. X-Ray Photoelectron Spectroscopy Analysis of Copper and Zinc Oxides and Sulphides. *Surf. Interface Anal.* **1992**, *18* (1), 39–46. <https://doi.org/10.1002/sia.740180107>.
- (44) Bisquert, J.; Garcia-Belmonte, G.; Bueno, P.; Longo, E.; Bulhões, L. O. Impedance of Constant Phase Element (CPE)-Blocked Diffusion in Film Electrodes. *J. Electroanal. Chem.* **1998**, *452* (2), 229–234. [https://doi.org/10.1016/S0022-0728\(98\)00115-6](https://doi.org/10.1016/S0022-0728(98)00115-6).
- (45) Rezaei Niya, S. M.; Hoorfar, M. On a Possible Physical Origin of the Constant Phase Element. *Electrochim. Acta* **2016**, *188*, 98–102. <https://doi.org/10.1016/j.electacta.2015.11.142>.
- (46) M. Stern and A. L. Geary Electrochemical Polarization- A Theoretical Analysis of the Shape of Polarization Curves. *J. Electrochem. Soc.* **1957**, *104* (12), 751. <https://doi.org/10.1149/1.2428472>.
- (47) Curran, J. A.; Kalkancı, H.; Magurova, Y.; Clyne, T. W. Mullite-Rich Plasma Electrolytic Oxide Coatings for Thermal Barrier Applications. *Surf. Coatings Technol.* **2007**, *201* (21), 8683–8687. <https://doi.org/10.1016/j.surfcoat.2006.06.050>.
- (48) Curran, J. A.; Clyne, T. W. The Thermal Conductivity of Plasma Electrolytic Oxide Coatings on Aluminium and Magnesium. *Surf. Coatings Technol.* **2005**, *199* (2–3), 177–183. <https://doi.org/10.1016/j.surfcoat.2004.11.045>.

8. Chapter 8 Discussion, Conclusions, and Future Works

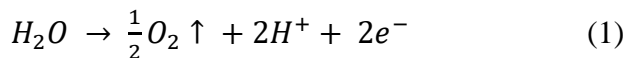
8.1 Discussion

8.1.1 Electrolyte species

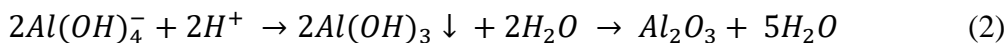
In chapter 3, influence of PEA process parameters, including the concentration of NaAlO_2 in the electrolyte (C), the frequency (f) and duty cycle (δ) of the DC power supply, was evaluated by Taguchi experimental design and ANOVA analysis. It has revealed that the most influential parameter is the concentration of NaAlO_2 . In this study, we have found that the passive films formed on Fe and Cu consist of FeAl_2O_4 and $\text{Al}(\text{OH})_3$, respectively. Therefore, the sodium aluminate is the precursor, which is indispensable. Concentrated sodium aluminate could effectively decrease the critical voltage for the initiation of plasma discharges. Medium voltage PEA process ($< 600 \text{ V}$) was successfully applied on the Fe and Cu substrates in the concentrated sodium aluminate solution.

Sodium phosphate also has significant effect on the deposition of passive layer and the coating. As shown in Figure 3-2, the passive film formed in the solution containing 20 g/L of NaAlO_2 and 5 g/L Na_3PO_4 is smooth and homogeneous while the passive film formed in the solution containing 40 g/L of NaAlO_2 and 5 g/L Na_3PO_4 is rough and inhomogeneous. The coatings formed in these two electrolytes are also strongly different as shown in Figure 3-3, which shows the coating formed in the latter one is very rough and loose.

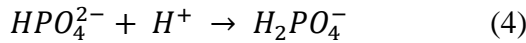
During the coating deposition process, oxygen evolution reaction caused the decreasing of pH values:



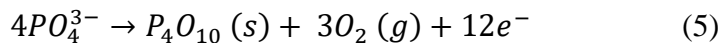
Followed by the precipitation of aluminum hydroxide and sintering of alumina:



It is well known that the hydrolysis products of aluminate ions strongly rely on the pH values: the monomer aluminate ions prevail when $\text{pH} > 13$; at $\text{pH} 9.3\text{-}12.8$ the polymers with the composition $[\text{Al}(\text{OH})_4]_n(\text{OH})_2^{(n+2)-}$ are formed. When $\text{pH} < 9.3$, rapid precipitation of aluminum hydroxide would dominate. The formation of aluminate polymers is desired, which means the localized pH value near the anode surface should be $9.3\text{-}12.8$. There are two pH-related hydrolysis reactions for phosphate ions in the electrolyte:



The $\text{p}K_a$ values for reactions (3) and (4) are 12.37 and 7.20, respectively. Therefore, the phosphate ions are able to stabilize the localized pH value near the anode surface and promote the formation of aluminate polymers instead of uncontrolled rapid precipitation of aluminum hydroxide. The phosphate ions could also prompt the formation of phosphate-aluminate complexes, which are beneficial for the uniform deposition of aluminum hydroxide. EDS analysis demonstrated that the passive layer formed on iron substrate contains high amount of Fe (10~15 at. %), Al (20~25 at. %) and O (50~60 at. %) with minor amount of P (2~3 at. %). This minor amount of P could come from the phosphate-aluminate complexes. On the other hand, the amount of P is negligible in the final coating (< 1 at. %), which means the P was removed during the plasma sintering reaction (phosphate-aluminate complexes \rightarrow alumina).

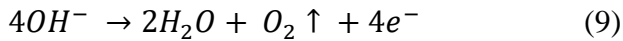
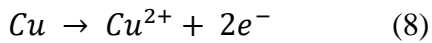
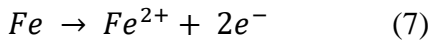


In summary, the sodium aluminate is the precursor of the passive layer and the coating. Concentrated sodium aluminate enables the PEA process to be performed under medium voltage (< 600 V). Sodium phosphate could improve the quality of the coating by acting as buffer and complexing agent.

8.1.2 Influence of substrate materials

In this project, two different non valve metals, i.e., Fe and Cu, were chosen as the substrate for PEA treatment. As investigated in Chapters 4 and 7, the iron substrate was incorporated into the passive film (FeAl_2O_4) while the copper substrate did not participate in the formation of passive film ($\text{Al}(\text{OH})_3$). This difference could be attributed to the difference of reduction potentials of Fe and Cu.

Before the ignition of sparks, the possible anodic reactions in the basic electrolyte include:

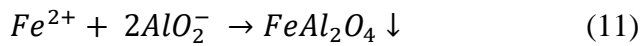


The standard electrode potentials for these three reactions are -0.45 V, 0.34 V and 0.40 V. From the principle of electrochemistry, the reaction with lower potential occurred preferentially.

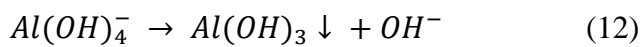
The standard electrode potential of reactions (8) and (9) are very close. Since our electrolyte is strongly basic, the concentration of hydroxides species (OH^-) is much higher than the standard state. The reduction potential of reaction (9) will decrease following the Nernst equation:

$$E = E^0 - \frac{RT}{zF} \ln \frac{[\text{Red}]}{[\text{Ox}]} \quad (10)$$

where E is the reduction potential, E^0 is the standard electrode potential, R is the gas constant, T is the temperature, z is the ion charge (moles of electrons), F is the Faraday constant, $[Red]$ and $[Ox]$ are the activities of reduction agent and oxidation agent, respectively. Thus, it is possible that the reduction potential of reaction (9) is lower than that of reaction (8) in our strongly basic electrolyte. However, the reduction potential of reaction (7) is much lower than that of reaction (9), which cannot be compensated by increasing the concentration of OH^- . Therefore, when PEA process was applied on Fe, reaction (7) occurred which means the iron substrate participated in the formation of passive film:



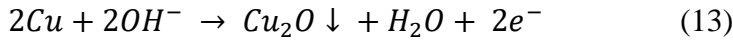
On the other hand, when PEA process was applied on Cu, reaction (9) occurred preferentially. This reaction consumed large amount of OH^- and caused localized acidification of the electrolyte near the anode (if the consuming rate of OH^- by reaction (9) is higher than the supplying rate by diffusion in electrolyte, and this is the reason that a high current density is needed during the formation of passive film). Then the aluminum hydroxide will precipitate on the anode surface:



The copper substrate was not incorporated into the passive film.

Another difference of PEA treatment on Fe and Cu is the phase structure of the coating. The coating prepared on pure copper contains metallic Cu while metallic Fe was not found in the coating prepared on Fe. This phenomenon could be attributed to the difference of vapor pressure of Fe and Cu. It is well known that Cu has much higher vapor pressure than Fe, which means Cu is much easier to be evaporated by the sparks. During the PEA

treatment on pure copper, large amount of Cu was evaporated by occasionally strong sparks. When excessive Cu met with the active species of the electrolyte, part of them was oxidized:



Rest of the Cu will be condensed into metallic copper particles and be embedded in the coating. This process is somewhat like the “droplet” defects in the PVD coatings, when arcing on the target occurred due to poor process control. On the other hand, Fe is less likely to be evaporated by the sparks. Only a small amount of Fe was evaporated by occasionally strong sparks and reacted with excessive active species in the electrolyte to form the hercynite ($FeAl_2O_4$) and/or iron oxides. Therefore, no metallic iron particle was found in the coating.

8.1.3 Post-treatments

Two different post-treatments, i.e., electroless nickel plating and sol-gel silica coating, were applied on the PEA treated iron samples to further increase the corrosion resistance. Although both post-treatments significantly improved the corrosion performance of the PEA treated iron samples, there are several differences.

The electroless nickel plating is a bottom-to-up process, during which the nickel grows from the substrate to the coating surface along the open pores and cracks, as illustrated in Figure 8-1(a). Therefore, the surface pores were well retained and might serve as oil reservoirs during lubricated sliding or dimples to collect the wear debris during the dry sliding. Moreover, electroless plated nickel has high hardness which not only provides protection for the ceramic coating-metal substrate interface, but also is beneficial for improving the wear resistance. The thermal conductivity of PEA-EP coating (~ 1.44 W/m·K) is pretty high because of the presence of metallic Ni. When a 20 μ m-thick coating

was applied on a 3 mm-thick cast iron substrate, the effective thermal conductivity (coating plus substrate) is $\sim 38 \text{ W}/(\text{m}\cdot\text{K})$, which is very close to that of the cast iron. Therefore, the PEA-EP coating is aimed for the application where high wear resistance, moderate corrosion resistance and high thermal conductivity are required, for instance the braking rotors.

On the other hand, the sol-gel dipping is an up-to-bottom process, where the silica sol was applied on the sample surface and then filled the surface pores by capillary effect. After heat-treatment, the silica sol was transferred into fused silica and sealed all the surface pores (including the open pores and/or cracks). Thus, the sample surface is much smoother. Due to the insulation property of SiO_2 , the PEA- SiO_2 hybrid coating has the best corrosion performance among all samples and provides excellent long-term corrosion protection for cast iron substrate. The thermal conductivity of PEA- SiO_2 hybrid coating is also lower ($\sim 0.8 \text{ W}/\text{m}\cdot\text{K}$). The potential application of PEA- SiO_2 hybrid coating is thermal management of cast steel pistons (used for heavy duty diesel engines) where high corrosion resistance, low thermal conductivity and low surface roughness are required.

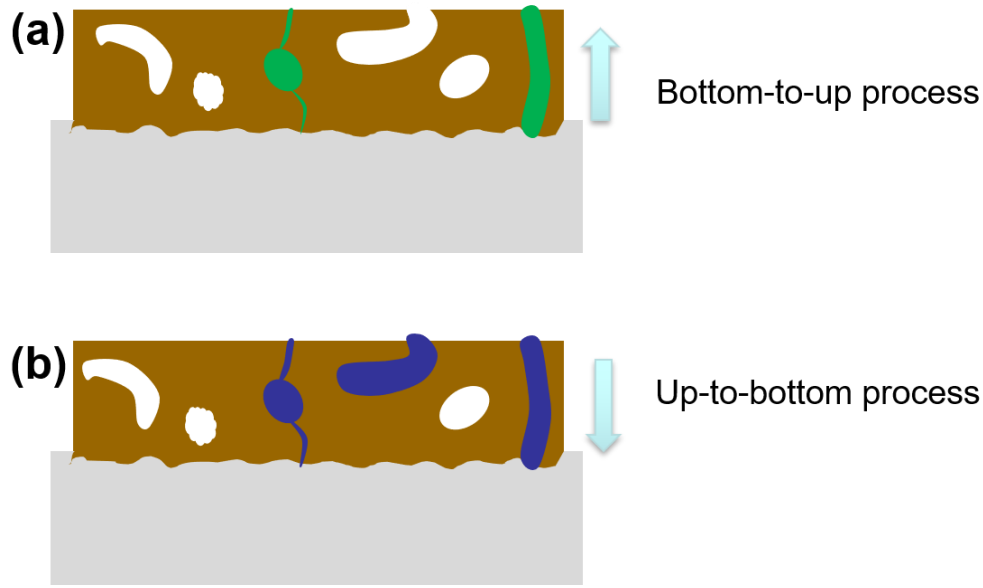


Figure 8-1 Illustration of (a) electroless nickel plating, (b) sol-gel dipping.

8.2 Conclusions

1. Ceramic coatings with multiple functions have been successfully deposited on the surface of non-valve metals, including Fe and Cu, by the plasma electrolytic aluminating (PEA) treatment in electrolyte contains sodium aluminate and sodium phosphate.
2. Incorporation of aluminate species is the key to the formation of passive films, which is indispensable for the initiation of sparks. Based on the reduction potentials of Fe and Cu, two different passive films were formed: FeAl_2O_4 passive film was formed on iron surface with the participation of iron substrate, while $\text{Al}(\text{OH})_3$ passive film was formed on copper surface without the incorporation of copper substrate.
3. Taguchi experimental design and ANOVA analysis were carried out for evaluating the influence of selected process parameters: the concentration of NaAlO_2 in the electrolyte (C), the frequency (f) and duty cycle (δ) of the DC power supply. It has been

demonstrated that C has the most significant influence on all coating properties. While f has stronger effect on the coating's hardness and polarization resistance, δ is more influential on the coating's thickness. The maximum multi-response S/N ratio (53.86) was achieved by confirm experiment with optimum level of A2B3C1 ($C = 20$ g/L, $f = 1000$ Hz and $\delta = 0.2$), which had an average hardness of 822 HV, polarization resistance of $296 \text{ k}\Omega\cdot\text{cm}^2$ and thickness of $35 \text{ }\mu\text{m}$.

4. The coating deposited on Fe mainly consists of Al_2O_3 and FeAl_2O_4 . The adhesive strength and thermal conductivity were measured to be > 60 MPa and $\sim 0.5 \text{ W}/(\text{m}\cdot\text{K})$, respectively. After cyclic thermal shock tests, the coating retained its porous structure without spallation. The low thermal conductivity of the coating deposited on Fe could be attributed to the nanograins and amorphous materials.
5. Post-treatments, including electroless nickel plating (EP) and sol-gel dip coating, were applied to seal the open pores and cracks of PEA coatings. Both the PEA-EP and PEA- SiO_2 coatings could retain good corrosion resistance after immersed in sodium chloride solution for five days, while the PEA coating degraded due to pitting corrosion at these open pores and cracks. The PEA- SiO_2 coating demonstrates the best corrosion performance among all samples while the PEA-EP coating has the highest hardness. While the thermal conductivity of the PEA-EP coating is relatively high, the PEA- SiO_2 coating still has very low thermal conductivity. After cyclic thermal shock tests, both the PEA-EP and PEA- SiO_2 hybrid coatings seem intact.
6. The coating deposited on pure copper contains metallic Cu, Cu_2O , and Al_2O_3 . The hardness and polarization resistance of the coating were 1050 ± 216 HV, $141.7 \text{ k}\Omega\cdot\text{cm}^2$ and $\sim 5.1 \text{ W}/(\text{m}\cdot\text{K})$, respectively. The coating has excellent wear and corrosion

resistance, which might be used for wear-corrosion protection of copper alloys. The coatings' thermal conductivities increased from $\sim 3.8 \text{ W}/(\text{m}\cdot\text{K})$ @ $25 \mu\text{m}$ to $\sim 5.1 \text{ W}/(\text{m}\cdot\text{K})$ @ $60 \mu\text{m}$. The relatively high thermal conductivity could be attributed to the presence of metallic Cu in the composite coating. The amount of Cu particles increased with increased coating thickness, which could be attributed to intensified plasma discharges.




8.3 Future work

1. The tribological performance of PEA-EP hybrid coating needs to be investigated in detail. Performance of the PEA-EP and PEA-SiO₂ hybrid coatings during the dyno-tests could be another interest of research.
2. Simulated erosion-corrosion tests on PEA treated copper samples is needed and might provide a new method to enhance the erosion-corrosion performance of copper alloys.
3. The possibility of using PEA coating on pure copper as the insulation layer is another interest of study.
4. Applying PEA process on other non-valve metals like Ni and Zn could also be part of the future work.


APPENDICES

COPYRIGHT RELEASES FROM PUBLICATIONS

CHAPTER 4



Home Help Email Support CHEN ZHAO ▾



A New Eco-friendly Anticorrosion Strategy for Ferrous Metals: Plasma Electrolytic Aluminating
Author: Chen Zhao, Wei Zha, Ran Cai, et al
Publication: ACS Sustainable Chemistry & Engineering
Publisher: American Chemical Society
Date: Mar 1, 2019
Copyright © 2019, American Chemical Society

PERMISSION/LICENSE IS GRANTED FOR YOUR ORDER AT NO CHARGE

This type of permission/license, instead of the standard Terms & Conditions, is sent to you because no fee is being charged for your order. Please note the following:

- Permission is granted for your request in both print and electronic formats, and translations.
- If figures and/or tables were requested, they may be adapted or used in part.
- Please print this page for your records and send a copy of it to your publisher/graduate school.
- Appropriate credit for the requested material should be given as follows: "Reprinted (adapted) with permission from (COMPLETE REFERENCE CITATION). Copyright (YEAR) American Chemical Society." Insert appropriate information in place of the capitalized words.
- One-time permission is granted only for the use specified in your request. No additional uses are granted (such as derivative works or other editions). For any other uses, please submit a new request.

BACK CLOSE WINDOW

© 2020 Copyright • All Rights Reserved | [Copyright Clearance Center, Inc.](#) | [Privacy statement](#) | [Terms and Conditions](#)
Comments? We would like to hear from you. E-mail us at customer@copyright.com



Anodic plasma electrolytic deposition of composite coating on ferrous alloys with low thermal conductivity and high adhesion strength

Author: Chen Zhao, Jiayi Sun, Xueyuan Nie, Jimi Tjong, D.T.A. Matthews

Publication: Surface and Coatings Technology

Publisher: Elsevier

Date: 25 September 2020

© 2020 Elsevier B.V. All rights reserved.

Please note that, as the author of this Elsevier article, you retain the right to include it in a thesis or dissertation, provided it is not published commercially. Permission is not required, but please ensure that you reference the journal as the original source. For more information on this and on your other retained rights, please visit: <https://www.elsevier.com/about/our-business/policies/copyright#Author-rights>

BACK

CLOSE WINDOW

VITA AUCTORIS

NAME: Chen Zhao

PLACE OF BIRTH: Anhui, China

YEAR OF BIRTH: 1994

EDUCATION: Northwestern Polytechnical University, B.Sc.,
Xian, China, 2014

University of Windsor, M.A.Sc., Windsor, ON,
2017